Determination of energy and mass of cosmic rays using air shower radio emission

Zur Erlangung des akademischen Grades eines
DOKTORS DER NATURWISSENSCHAFTEN
bei der Fakultät für Physik des
Karlsruher Instituts für Technologie (KIT)

genehmigte

DISSERTATION

von

Dipl. Phys. Nunzia Palmieri
aus Turin

Tag der mündlichen Prüfung: 30 November 2012

Referent: Prof. Dr. J. Blümer,
Koreferent: Prof. Dr. M. Feindt,
Betreuer: Dr. T. Huege

”[...] I am fain to compare myself with a wanderer on the mountains who, not knowing the path, climbs slowly and painfully upwards and often has to retrace his steps because he can go no further — then, whether by taking thought or from luck, discovers a new track that leads him on a little till at length when he reaches the summit he finds to his shame that there is a royal road, by which he might have ascended, had he only had the wits to find the right approach to it. In my works, I naturally said nothing about my mistake to the reader, but only described the made track by which he may now reach the same heights without difficulty.”

Hermann von Helmholtz
Beveridge, W. I. B., 1955, The Art of Scientific Investigation

Abstract

Determination of energy and mass of cosmic rays using air shower radio emission

Coherent radio emission in the MHz frequency range arises from extensive air showers generated in the atmosphere by cosmic rays with sufficiently high energy. In the last decades the detection techniques as well as the understanding of the emission mechanisms of this electromagnetic radiation have made remarkable progress. Achieving the information of fundamental air-shower parameters, and attaining a certain quality in their reconstruction, both remain the principal goals of the radio detection. The main purpose of the radio detection is to become competitive with the already well-established Cherenkov and fluorescence detection methods, which, in contrast to the radio technique, are limited to dark and moonless nights.

The present work explores a simulation-based method which leverages the slope of the radio lateral distribution in order to obtain crucial attributes of cosmic ray air showers. It aims to determine both the energy and the mass of a primary cosmic ray.
In this thesis former results achieved with outdated simulations are revised and the method improved. An enhanced investigation on REAS3 simulations, adapted to represent a realistic experimental set-up and acceptance is elaborated. In addition, a direct application to real experiments, such as LOPES at the Karlsruhe Institute of Technology (KIT) and AERA at the Pierre Auger Observatory, is performed.

The main results of the study are:
$*$ The geomagnetic origin of the radio emission is confirmed as the predominant contribution to the radio emission from air showers, except for well-defined incoming directions for which the geomagnetic contribution quickly decreases and the charge-excess effect becomes significant.
$*$ The radio lateral distribution function is verified not to be an exponential. Other functions are suggested to interpret the radio data especially at large distances (> 200 m) from the shower axis. However, the homogeneous exponential function is proved to sufficiently well describe the radio data at the distances probed by the LOPES experiment.
$*$ A particular, zenith-angle-dependent distance is identified to be the most suited place for the primary energy estimation. An upper-limit to the uncertainty of the reconstructed energy with the LOPES data is provided.
$*$ The slope of the radio lateral distribution is employed to infer composition information from radio-only data. The depth of the shower maximum ($X_{\max}$) is reconstructed for the LOPES events and the values are within the range expected for the cosmic ray composition in this energy range. By combining two independent radio methods, an uncertainty on the reconstructed $X_{\max}$ (~ 30 g/cm^2) comparable with the values of the most advanced fluorescence detectors is provided.

Zusammenfassung

Bestimmung von Masse und Energie kosmischer Strahlen mittels der Luftschauer-Radioemission

Kohärente Radioemisionen im MHz-Frequenzbereich entstehen in ausgedehnten Luftschauern, die in der Atmosphäre durch kosmische Strahlen mit ausreichend hoher Energie ausgelöst werden.
In den letzten Jahrzehnten haben die Detektortechnik und das Verständnis der Emissionsmechanismen beachtliche Fortschritte gemacht. Die Rekonstruktion fundamentaler Parameter des ursprünglichen kosmischen Teilchens mit ausreichender Qualität bleibt das prinzipielle Ziel der Radiomessung. Damit würde die Messtechnik wettbewerbsfähig mit den bereits etablierten Cherenkov- und Fluoreszenz-Methoden, die im Gegensatz zur Radiomessung auf Dunkelheit und mondlose Nächte beschränkt sind.

Die vorliegende Arbeit erforscht eine simulationsbasierte Methode, die die Steigung der Radio-Lateralverteilung ausnutzt, um wichtige Eigenschaften der aus kosmischer Strahlung resultierenden Luftschauer zu bestimmen. Sie zielt darauf ab, Energie und Masse des Primärteilchens zu rekonstruieren.
In dieser Arbeit wurden frühere Resultate aus unvollständigen Simulation überprüft und weiterentwickelt, indem verbesserte REAS3-Simulationen an einen realistischen Versuchsaufbau und geometrische Akzeptanz angepasst wurden. Anschließend wurde die direkte Anwendung auf Experimente, wie LOPES am KIT und AERA am Pierre Auger Observatorium untersucht.

Die wichtigsten Resultate dieser Arbeit sind:
$*$ Radioemissionen geomagnetischen Ursprungs dominieren die Radioemission aus Luftschauern, ausser für wohldefinierte Eintrittsrichtungen, für die der geomagnetische Anteil schnell abnimmt und der Ladungsüberschuss-Effekt Bedeutung gewinnt.
$*$ Die Funktion der Radio-Lateralverteilung ist nicht exponentiell. Einige Funktionen werden alternativ vorgeschlagen, um die Radioergebnisse insbesondere bei grossen Entfernungen von der Schauerachse ($>$ 200 m) zu interpretieren. Für die Ausdehnung des LOPES-Experiments jedoch genügt die homogene Exponentialfunktion zur Beschreibung der Ergebnisse.
$*$ Eine bestimmte, vom Zenitwinkel abhängige Entfernung wird als der günstigste Ort zur Bestimmung der Energie des Primärteilchens identifiziert. Für LOPES-Daten wird eine obere Schranke der Unsicherheit der rekonstruierten Energie angegeben.
$*$ Die Steigung der Radio-Lateralverteilung wird verwendet, um Kompositionsinformationen ausschliesslich aus Radiomessungen zu rekonstruieren. Die atmosphärische Tiefe des Luftschauermaximum ($X_{\max}$) wird für LOPES-Ereignisse rekonstruiert, und die Ergebnisse liegen innerhalb der Erwartungen für die Zusammensetzung der kosmischen Strahlung in diesem Energiebereich. Indem man zwei voneinander unabhängige Radio-Methoden kombiniert, lässt sich eine Unsicherheit auf $X_{\max}$ ($\sim$ 30 g/cm^2), vergleichbar mit den fortgeschrittensten Fluoreszenz-Detektoren, erreichen.

Contents

1 Introduction

The discovery of the cosmic radiation by Victor Hess (Hess, 1912) at the beginning of the 20th century laid the foundation for a new field of research. Mainly consisting of protons, these particles have an energy spectrum which extends over eleven orders of magnitude, up to 10^{20} eV, where the flux decreases quickly resulting in extremely few particles for these highest energies (Gaisser, 1990).
Despite the almost hundred years of investigation, fundamental questions are yet partially unsolved: sources and origin as well as acceleration mechanisms are still under discussion (Blümer et al., 2009). Several models are proposed that try to explain the peculiar features of the cosmic ray spectra, and different astronomical environments are suggested as possible cribs for the highest energetic particles. Detailed information about the mass composition for the complete energy range would uphold or invalidate some of the theories about the creation and propagation of cosmic rays, mentioned above. Nevertheless, this is a goal quite difficult to achieve and knowing the exact composition for the whole cosmic ray flux is still a big challenge.
The detection of cosmic rays with energies larger than 10^{15} eV is possible only with indirect measurements: the primary particle interacts in the atmosphere with nuclei and secondaries are generated (Extensive Air Showers). Fluorescence (Arqueros et al., 2008) and Cherenkov (Hinton, 2004, Lidvansky, 2005) light, and electromagnetic radiation (Jelley et al., 1965) are created as well. Lighter elements, such as protons, interact deeper in the atmosphere than heavier cosmic rays, e.g. iron, thus their depth of the shower maximum (X_{max}) results larger in comparison.
Information about energy, direction and type of the primary is preserved and carried by the secondaries through the complete journey before they reach the ground. Thereby, these important parameters about the primary can be reconstructed.
Particle detector experiments achieve the information about the type of primary by the ratio of muons and electrons which reach the ground (Gaisser, 1990). The fluorescence detection method can accurately reconstruct the longitudinal development of the shower in the air, thus it has an easy access to the primary mass by the X_{max} reconstruction (Abraham et al., 2010b). Likewise, Cherenkov and radio detection methods may achieve information about X_{max} since they measure the signal integrated over all the atmosphere.
For the radio detection, the capability to measure X_{max} has been deeply investigated only lately, with the most recent hint for a success in the experimental data (Apel et al., 2012a). Two independent approaches for the determination of X_{max} are feasible: on the one hand by measuring the shape of the radio wavefront (Schröder, 2010). On the other hand, for a pure geometrical effect, by looking at the slope of the radio lateral distribution function (LDF), which is predicted to be by itself an indicator of the depth of the shower maximum (Huege et al., 2008).
The latter method (slope method) is investigated in the following dissertation, with the goal of a better precision in the X_{max} reconstruction compared to previous results

(Schröder, 2010).
For both primary energy and X_{max} determination from the radio LDF, only (outdated) simulations (Huege et al., 2008) existed so far. The results discussed in Huege et al. (2008) were exemplary but the method could not be directly applied to any radio experiment. Moreover, the REAS2 simulations turned out to be incomplete, thus not describing the detected radio data.
An updated investigation on the radio LDF with the more complete REAS3 simulations (Ludwig and Huege, 2011b) is performed in this work, and, for the first time, the slope method is shown in practice, on the basis of LOPES data.
First, a composition signature in the LOPES measurements is proposed. Second, the most suited distance from the shower core, i.e. intersection between the shower axis and the ground, where a more precise value for the primary energy reconstruction is achievable with radio-only measurements is discussed (Chapter 9). Finally, Chapter 10 addresses the applicability of the slope-method on the last generation of radio antenna arrays (AERA experiment).

2 Cosmic rays

The first experimental evidence for cosmic rays dates back to the early 20th century. Precisely in 1912, Victor Hess discovered an increase of ionizing radiation with height during balloon ascents (Hess, 1912). For this discovery he was awarded the Nobel Prize in 1936.
This radiation, which penetrates the atmosphere from outer space, covers different orders of magnitude in flux and in energy (see fig. 2.1). Even the most sophisticated and modern ground-based particle accelerators (e.g. LHC at CERN) can not reach energies comparable with the highest cosmic ray energies.
This cosmic radiation consists of ionized nuclei, mainly protons but also alpha particles and heavy nuclei. Knowing the exact composition for the complete energy spectrum is still a big challenge. This would help in understanding both the sources and the underlying acceleration mechanisms.

In section 2.1 the two main features of the energy spectrum of cosmic rays will be introduced and the objects (galactic and extragalactic) discussed as possible sources will be listed (see also Blümer et al. (2009)).
Due to the fast decreasing flux of the cosmic rays with increasing energy, various detection methods have been developed and improved since almost the beginning of the previous century. A short overview about the indirect detection methods of cosmic rays, i.e. of the secondary particles in the Extensive Air Showers (EAS), is given in the last part of this chapter.

2.1 Energy spectrum

The cosmic ray spectrum falls steeply and extends over eleven orders of magnitude in energy, from 1 up to 10^{11} GeV. The flux of primary particles decreases from more than 1000 particles per second and square meter at GeV energies to less than one particle per square kilometer and century in the tail of the spectrum.
This spectrum is described by a rather featureless power-law with a spectral index γ:

$$\frac{dN}{dE} \propto E^{\gamma}$$

This indicates a non-thermal acceleration process for such particles.

By scaling the flux with a power of particle energy, such as in **fig.** 2.1, some structures become clear. At energies around 10^{15} eV the slope of the spectrum steepens and the index γ changes from -2.7 to -3.1 ($knee$ region); a further steepening (second or heavy $knee$) is visible around 10^{17} eV (Apel et al., 2011b). Finally the spectral index drops again to -2.7 around 10^{18} eV ($ankle$).
The understanding of the origin of such features will improve the knowledge about the

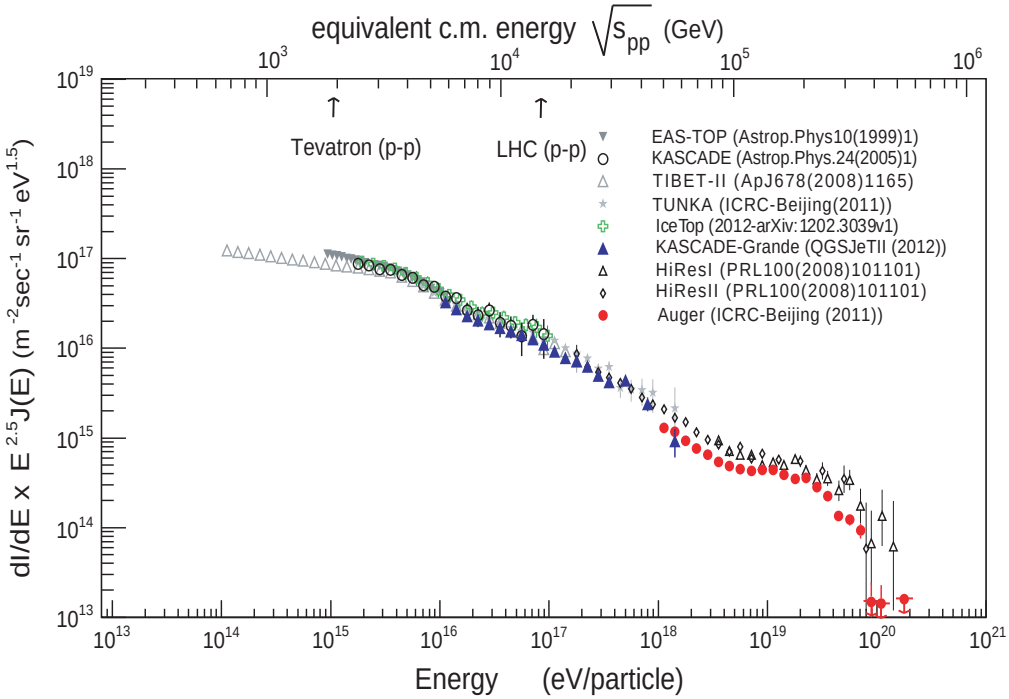

Figure 2.1: *Cosmic ray energy spectra. The KASCADE-Grande data are taken from Apel et al. (2012c)*

sources and the acceleration mechanism of cosmic rays.

Mainly three models can explain the $knee$ region:

The first associates these energies with the upper limit of acceleration by sources in the Milky Way. Supernova remnants are considered plausible acceleration sites. With an explosion rate of three Supernovae per century in the Galaxy and with an average energy of 10^{51} erg released in each explosion, only $\sim 15\ \%$ of the energy from one Supernova is enough to explain the observed cosmic ray energy density (Baade and Zwicky, 1934). The mechanism of acceleration was proposed by Fermi (first order Fermi acceleration) (Fermi, 1949). This mechanism involves interactions of particles with strong shock fronts, powered by Supernova explosions and propagating into the interstellar medium from the Supernova remnants.

The second explanation is the leakage of cosmic rays from our Galaxy. Due to the magnetic field in the Milky Way (in average B $\sim$3 μG), particles with charge Z move describing helical trajectories with radius r_L (Larmour radius). A proton with energy E_{18}=10^{18} eV has a Larmour radius ($r_L \approx E_{18}/ZB$ $\sim$350 pc) comparable with the thickness of the galactic disk. As a consequence, for energies larger than $\sim 10^{17}$ eV the galactic magnetic field is not strong enough to confine the cosmic rays.

The third explanation is based on particle interactions. For energies larger than 10^{15} eV exotic interactions may occur. A new interaction channel would retain part of the total energy of the cosmic ray air shower with the production of heavier particles (Kazanas and Nicolaidis, 2003). Thus, the reconstructed energy would be underesti-

mated.

The LHC (Large Hadron Collider) experiment at CERN (LHC, 2008) has extended the c.m. energy range reachable in the laboratory for hadronic interaction and new data are now available. The LHC measurements strongly support the interpretation of the $knee$ as due to a feature in the cosmic ray flux and a hardening of the cosmic ray spectrum (d'Enterria et al., 2011). The LHC data disfavour both a possible fast changing in the hadron interaction properties and the creation of exotic particles.
In addition, the first and second models are upheld by both a change of the cosmic ray composition to heavier nuclei experimentally observed (Apel et al., 2009) and the presence of the heavy $knee$ in the energy spectrum (Apel et al., 2011b).

The energies of the $ankle$ are generally associated to cosmic rays of extragalactic origin, which present a harder spectrum and dominate at such energies.
The $ankle$ itself may be the transition region from galactic to extragalactic cosmic rays (transition model) (Allard et al., 2005).

Another theory predicts the transition region not around $\sim 10^{18}$ eV but at the second $knee$ (dip model) (Berezinsky et al., 2005). In this model the $ankle$ would be generated by the Bethe-Heitler process (pair production by $p + \gamma_{CMB} \rightarrow p + e^+e^-$) and, as a consequence, the particles for energies above the $ankle$ would be only protons. The transition model is supported by Pierre Auger data, that hint on existing heavy nuclei at such large energies (Abraham et al., 2010a).

At energies larger than $5 \cdot 10^{19}$ eV the flux of cosmic rays drops drastically. A possible explanation is the GZK cut-off effect (Greisen, 1966, Zatsepin and Kuzmin, 1966): All hadronic particles with larger energies suffer energy losses during propagation, interacting with the photons of the cosmic microwave background (CMB). In the case of protons, the Δ^+ resonance is formed (Stecker and Salamon, 1999), precisely:

$$p + \gamma_{CMB} \rightarrow \Delta^+ \rightarrow p + \pi^\circ$$

For the nuclei, photo-disintegration is predicted (Stecker and Salamon, 1999).
Due to the GZK effect, the mean free path length of protons with energy larger than 10^{20} eV is only 50 Mpc. Therefore, this is also the maximum distance from the Solar system of the sources where such energetic cosmic rays may originate.

Another possible explanation for the suppression of the cosmic ray flux at larger energies is linked with the maximum energy reachable in the potential extragalactic accelerator environments, such as AGN, GRBs or radio lobes of specific galaxies (Medvedev, 2007).

Besides the explanations for the cut-off in the cosmic rays flux already presented above, different, non-acceleration, scenarios are also proposed. In these so-called top-down models decays of super-heavier objects are predicted, such as topological defects (Hill, 1983) or dark matter (Berezinsky et al., 1997). Severe constraints on the top-down models are placed by the Pierre Auger Observatory measurements and a recently updated photon flux further support the bottom-up processes (Settimo, 2011).

2.2 Extensive air showers

In the 1930s Pierre Auger was the first who realized that particles recorded almost at the same time on the ground are secondaries generated in the atmosphere from a primary cosmic ray (Auger, 1938). The detectors used at that time were simple Wilson chambers and Geiger-Müller counters placed at large distance far from each other and working in coincidence. This first setup is the precursor of the modern and more sophisticated experiments for the detection of extensive air showers (EAS) such as the Pierre Auger Observatory (Abraham et al., 2004a).

When ultra high energetic cosmic rays enter the atmosphere and interact with nuclei, secondary particles are produced in sequence, generating the so-called extensive air showers.
The cascades of secondaries are classified as electromagnetic cascade, when induced by high energy gammas or electrons, and as hadronic cascade if the primary is a nucleus or a hadron.

The electromagnetic showers contain only electrons, positrons and gamma particles, produced by Bremsstrahlung and pair-production processes. A simplified model was presented by Heitler (Heitler, 1944). After a radiation length d ($\simeq$ 37 g/cm^2 in air), positrons and electrons above a critical energy ($\simeq$ 85 MeV) lose half of their energy by emitting a photon, while the gammas produce other electrons and positrons after the same length. At the maximum development of the shower ($X_{\max}$) the total number of generated particles is proportional to the energy of the primary cosmic ray. When the energy of the individual particles becomes smaller than the critical energy, ionization losses become predominant and electrons (and positrons) are absorbed in the atmosphere.

A similar simplified model can be applied to hadronic air showers (Matthews, 2005). The interaction probability of the primary cosmic ray depends on its inelastic cross-section in the air, which, in turn, is a function of the primary energy. Due to the several interaction channels and cross-sections possible, even for the same type of cosmic ray of a specific energy the interaction height is not fixed. Thus, shower-to-shower fluctuations arise.

The secondary particles in hadronic cascades are grouped in three main components: The **hadronic** component, which carries a large fraction of the air shower energy. Due to the high momenta, the hadrons in the cascade (π^+, π^-, π°, kaons but also protons and neutrons) are assembled around the shower axis. Charged pions above 100 GeV can interact or they decay (mean lifetime $\sim$2.6$\cdot 10^{-8}$ s) generating the **muonic** component. Muons in the air showers are generated not only by charged pions, but also by decaying kaons. The most energetic ones ($>$100 GeV) originate in the first stage of the air shower development and penetrate the complete atmosphere almost without losing their energy by ionization or Bremsstrahlung. On the contrary, low energy muons decay into electrons (or positrons) and neutrinos. The **electromagnetic** component of the hadronic air shower is generated principally by neutral pions, which decay almost instantaneously into two photons, thus inducing electromagnetic sub-showers.

Together with the production of up to billions of particles, air showers emit several kinds of radiation, such as fluorescence light (Arqueros et al., 2008), Cherenkov (Lidvansky, 2005) light, and radio emission in both MHz (Huege, 2004) (c.f. Chapter 3) and GHz (Facal San Luis et al., 2012, Šmída et al., 2011, 2012) frequency ranges.

Properties of the primary cosmic rays, such as the energy, the mass, and the direction are traceable backwards. Mainly muons and electromagnetic particles are used for such a purpose.
The primary energy is proportional to the sum of muon (N_μ) and electron (N_e) number (Matthews, 2005) and can be easily estimated. Moreover, the number of electrons (and positrons) at a certain observation level is smaller for showers initiated by heavier nuclei than for a proton-generated cascade with the same primary energy; simultaneously the N_μ is larger. Thus, the ratio of the muonic and electromagnetic components N_μ/N_e can be used to trace the mass of a primary cosmic ray (Weber et al., 1999, Antoni et al., 2003a).
Information about the type of the primary are retained in other, at least two, characteristics of air showers: the lateral profile and the position of the maximum development of the shower ($X_{\max}$).
The latter is sensitive to the type of the primary particle since, on average, lighter particles, such as photons, interact more deeply in the atmosphere than nuclei. $X_{\max}$ is sensitive directly to the mass of the primary. In a simplified model, where a particle with energy E_o and mass A is supposed to behave in atmosphere as a group of A nucleons of energy E_o/A, $X_{\max}$ is proportional to $\simeq (\ln E_o - \ln A)$. In a typical shower of primary energy $\sim 10^{17}$ eV the depth of the shower maximum is at $\simeq$580 g/cm^2 for an iron primary and $\simeq$690 g/cm^2 for a proton initiated shower.
In Antoni et al. (2005) it is shown how the lateral distribution of the individual muonic and electromagnetic component differs for different primary particles. Moreover, in this dissertation, the link between the $X_{\max}$ and the radio lateral distribution will be investigated.

2.3 Detection methods

With the current technologies, direct measurements of cosmic rays are possible for primary energies up to 10^{14} eV. The detection occurs at large distance from the ground, with balloon-borne and satellite-borne detectors, and instruments installed on space stations. An overview can be found in (Sparvoli, 2008).
On the contrary, for ultra-high energy cosmic rays only indirect measurements are possible. Different techniques for the detection of extensive air showers are described in (Haungs et al., 2003), and in the following they are briefly introduced.

Particle detectors measure the secondary particles from air showers which reach the ground. The hadrons are detected with calorimeters while, for the muonic component the detectors are usually buried in the ground or shielded with lead, in order to screen them from the electromagnetic component.
The most common particle detectors are scintillators and water Cherenkov tanks. The latter are employed as surface detectors at the Pierre Auger Observatory (Abraham et al., 2004b), in Argentina. The KASCADE (Antoni et al., 2003b) and KASCADE-Grande (Apel et al., 2010b) experiments employed plastic and liquid scintillators as well as a calorimeter. Muons tracking was performed by gas detectors. A detailed overview about the existing particle detectors is given in (Blümer et al., 2009).

The particle counters are deployed on a wide area, at a certain distance from each other depending on the energy threshold to which the experiment is sensitive. Among the advantages of particle detectors are: almost 100 $\%$ duty cycle and the simple determination of the arrival direction of the air showers, by looking at the relative arrival time of the particles in the different detectors.

As disadvantages: the high instrumental cost and the large uncertainties relative to the primary energy determination, which is based on hadronic interaction models designed for lower energies with the information from ground-based acceleration data (Knapp et al., 2003, Menjo et al., 2011).

Fluorescence detectors (Arqueros et al., 2008) observe the light emitted in atmosphere by excited nitrogen molecules. The excitation occurs with the transit of ultrarelativistic particles and the emission of ultraviolet photons takes place when the molecules de-energize.
The integrated intensity of the fluorescence light is proportional to the energy of the primary cosmic ray within a low uncertainty of $\simeq 20$ $\%$. In addition, by detecting the longitudinal development of the air shower also the $X_{\max}$ is determined with high precision ($\simeq 20$ g/cm^2) (Abraham et al., 2010c).
The big disadvantage of the fluorescence detectors is their limitation to dark and moonless nights, which reduces the duty cycle to almost 10 $\%$ (Abraham et al., 2010c).

Besides the Pierre Auger Observatory, fluorescence detectors are installed at the Telescope Array (Matthews et al., 2009). In both experiments, fluorescence and surface detectors measure air showers in coincidence, employing a hybrid detection mode.

Cherenkov detectors measure the Cherenkov light emitted in the atmosphere by relativistic particles. As well as for fluorescence light, the detection of Cherenkov light is bound to cloudless and dark nights.
Mainly exploited for the detection of gamma-induced showers at energies $\sim$ TeV (Hinton, 2004, Lidvansky, 2005), Cherenkov detectors have been recently used also for the observation of EAS below 10^{18} eV, such as at the TUNKA experiment, in Siberia (Budnev et al., 2009).

Radio detectors measure the radiation emitted in the atmosphere at radio frequencies. In the last years, the detection in the MHz range of coherent radio pulses was established and has become a complementary detection method mainly due to its high duty cycle (almost 95 $\%$ Apel et al. (2011c)). Indeed, radio detection is limited only by lightnings during thunderstorms and, generally, by high and unstable atmospheric electric fields (Buitink et al., 2007) and high human-made noise. In the following, further details are presented.

Recently, measurements of the radio emission from air showers also in the GHz frequency range have been performed. So far, this method is still under investigation in several small experiments, such as CROME, located in Karlsruhe (Šmída et al., 2011).

3 Radio emission from cosmic ray air showers

In the previous decade, a large interest in the radio detection of cosmic ray air showers was revived. More and more sophisticated experiments have evolved and their need to better interpret the data has hugely grown. The necessity of a deeper understanding of the emission mechanisms led to the development of several simulation approaches and models.

In the next section, the main emission processes which induce radio emission from air showers and the principal characteristics of a radio pulse are described.
A general summary of the theoretical interpretation is briefly presented, with the major focus on the REAS approach (Ludwig and Huege, 2011b). For a detailed overview we refer the reader to (Huege et al., 2010).
Moreover, some important results obtained with the old REAS2 code (Huege et al., 2007), concerning the derivation of air shower parameters using only radio detection, will be reviewed.

3.1 Radio emission processes

The radio emission is a complex phenomenon, due to the creation/annihilation and acceleration of the electromagnetic charged particles in an air shower. Many mechanisms contribute to the total emission, even though the geomagnetic one is considered to be predominant.

The most appropriate and physical way to look at this phenomenon is to consider the radio emission as a whole, and not separated in contributions from the different mechanisms. This is exactly the approach used in the latest version of the REAS code (REAS3, Ludwig and Huege (2011b)) with the end-point formalism (James et al., 2010), as it will be discussed in section 3.2.
Some of the processes which contribute to the total radio emission are described below:

Transverse current (Kahn and Lerche, 1966)
The (relativistic) charged particles in air showers experience the presence of the Earth's magnetic field in the atmosphere. The Lorentz force acts on them by separating negative from positive charges. The consequent deflection of electrons and positrons, together with the development of the shower induce a time-varying transverse current, and radio emission is generated. The emitted radiation is linearly polarized (cf. Chapter 5) on the plain perpendicular to both the Earth's magnetic field and the direction of the shower. This effect is considered to be the predominant mechanism for the total radio emission.

Varying dipole (Werner and Scholten, 2008)
The transverse currents in one air shower result in an electric dipole. Since the dipole

strength changes during the shower development, a further radio emission contribution is created.

Charge excess (Askaryan, 1962)
In extensive air showers, the number of electrons exceeds the number of positrons mainly due to the knock-out of electrons from air molecules, but also due to the anti-particle annihilation. During the shower development, the amount of charge excess varies as well as the total number of particles in the air showers. This leads to linearly polarized contribution, with the electric field vector oriented radially (see fig. 3.1).
The variation of the net charge excess was proposed the first time by Askaryan as explanation of the radio emission from cosmic ray air showers. Nowadays it is considered to be the main effect among the non-geomagnetic mechanisms for the radio emission.

Refraction index effect (de Vries et al., 2012, Ludwig and Huege, 2011a)
The refractive index (n) of the atmosphere plays an important role in the radio emission from cosmic ray air showers. The radio source moves faster than the wave-propagation velocity in the medium. As a consequence, a shock wave is induced and all the radio emission is collimated in a Cherenkov-like cone. Although n is not much larger than unity, the time-travel between the source and the observer is delayed enough and the radio emission from two consecutive stages of the air shower development can reach the observer at the same time. This results in a compression (or decompression) and delayed radio pulse observed at ground. The refractive index effect vanishes with increasing distance from the shower core, relative to the air-shower geometry.

Geosynchrotron effect (Huege and Falcke, 2003)
In an air shower, the Lorentz force acts on electrons and positrons created and these are not only separated from each other, but also accelerated. This effect produces a synchrotron-like emission contribution, which is recently considered of minor importance for the total radio emission from air showers.

Atmospheric electric fields
The electric field generated in the Earth's atmosphere can accelerate the charged particles of an air shower as well as the magnetic field.
Under normal atmospheric conditions the electric field strength is generally of few hundred V/m near ground (on average $\sim$6 V/m) and this seems to not influence the radio emission from air showers. In contrast, during thunderstorms, the atmospheric electric field strength rises up to $\sim$ 10000 V/m and the radio emission generated becomes stronger even than the geomagnetic one (Buitink et al., 2007).

A fundamental feature of the total radio emission from an air shower is the coherence of the signal at MHz frequencies. The thickness of the shower front, i.e. of few meters, is smaller than the wavelength of the radio emission for frequencies lower than 100 MHz. As a consequence, the individual contribution at such frequencies adds up coherently and a radio pulse with a time-range of $\sim$ 10 ns is emitted.

The refractive index in the air, which varies in accordance with the atmospheric depth, is predicted to have a noteworthy impact on the radio signal (Ludwig, 2011). The travel time of the emission (from the radio source to the observer) as well as the electric field amplitude arising due to acceleration of the charged particles result influenced. Thus a change in the coherent condition is expected.

The simulated strength of the radio electric field presents a proportionality with both

the number of electrons and positrons in the shower maximum (Huege et al., 2008) and with the energy of the primary cosmic ray (Huege and Falcke, 2005b). The energy correlation with radio data from the LOPES experiment is subject of investigation in the next chapters.

The radio pulse amplitude depends on the arrival direction of the shower, precisely on the geomagnetic angle, i.e. the angle between the shower axis and the Earth's magnetic field direction, and an investigation on its polarization is of large interest. This would contribute to a better understanding of the emission processes (cf. section 12.1).

The dependence of the radio field strength on the lateral distance to the shower axis is still under study; especially for distances larger than 200 m, there is an open discussion on possible functions which may describe the radio lateral distribution.
At short distances (30-200 meters), the exponential function seems to be sufficient, as it will be discussed in Chapter 6 for the LOPES experiment.

A predicted influence on the radio lateral distribution comes from the charge-excess radiation (Ludwig and Huege, 2011b, de Vries et al., 2010). In contrast to the geomagnetic contribution, the net charge-excess radiation is characterized by an electric field vector oriented radially from the shower axis (see **fig.** 3.1). The electric field vectors of the geomagnetic and charge-excess contributions are, thus, not always oriented in the same direction, and, depending on the observer position, they combine in a constructive or destructive way (Marin, 2011). A detailed analysis on the radio lateral distribution function will lead to a better understanding of the radio emission processes from air showers.

The slope of the radio lateral distribution function is predicted to be by itself an indicator of the depth of the shower maximum, thus, indirectly, of the mass of the primary particles. An investigation lead on this topic can be found as well in the next chapters.

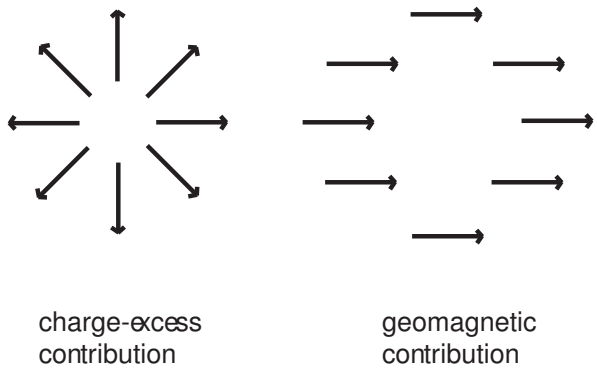

Figure 3.1: *The charge-excess radiation (left side) as well as the geomagnetic radiation (right side) are linearly polarized. The electric field vector is, in the first case, radially oriented (left side), while, in the case of geomagnetic contribution, oriented always in the same direction with respect to the position of the geomagnetic field*

3.2 Modeling approaches

The two interpretations of the radio emission from cosmic ray air showers by Askaryan (1962, 1965) (charge excess) and by Kahn and Lerche (1966) (transverse current) both became the milestones for several models which have been developed in the following decades.
In 2001, a new interpretation was proposed by Falcke and Gorham (2003), later further elaborated with an analytical formulation by Huege (Huege and Falcke, 2003). This geo-synchrotron model describes the radio emission again due to the acceleration of the electrons and positrons in the Earth's magnetic field, but as a synchrotron-like radiation.

The REAS[1] code (Huege and Falcke, 2005a, Huege et al., 2007) created by Huege in the following years, has the big advantage to simulate the radio emission from a realistic distribution of particles based on individual Monte Carlo air shower simulations with CORSIKA (Heck et al., 1998).
The predictions from REAS2 have been used for a first comparison with the experimental data, provided, in particular, by the LOPES experiment (Falcke et al., 2005, Horneffer et al., 2009).

A macroscopic approach was proposed with MGMR (**M**acroscopic **G**eo-**M**agnetic **R**adiation) (Scholten et al., 2008, Werner and Scholten, 2008) by Scholten, Werner and Rusydi. In this model, the induced transverse current, the induced dipole moments, the charge excess and the influence of the refractive index of the atmosphere are included.

More and more models were proposed in the recent years and contradictions among them clearly appeared, in particular concerning the radio pulse shape.
Two groups of models could be identified, one predicting unipolar pulses (as REAS2), the other predicting bipolar radio pulses (as MGMR).
The disagreement was solved only recently (Huege et al., 2010) and it was due to a radio component missing in the unipolar-pulse-models. REAS2, thus, resulted to be incomplete and inconsistent.

The missing radiation was successfully implemented with the end-point formalism (James et al., 2010) in the version REAS3.0, released in 2010 by Ludwig and Huege (2011b). The current version of REAS (REAS3) does not imply a specific radio emission mechanism. REAS3 is now comparable also with the MGMR predictions and it potentially incorporates the complete radio emission which arises from the underlying charge particle motion.
REAS3 as well includes the effect on the radio emission of the refractive index in the air - properly treated only in the recently released version REAS3.1. Nevertheless, minor improvements are still under investigation. The latest comparison of the REAS3 simulations with the LOPES experimental data, have already shown a sensible agreement in the radio lateral distribution (Ludwig, 2011).

An implementation of the end-point formalism directly in CORSIKA is, currently, under development (CoREAS) (Huege, 2012).

[1] **R**adio **E**mission from **A**ir **S**howers

3.3 Primary energy and X_{max} investigation with REAS2

The dependence of the "geo-synchrotron" radio emission - as it was modeled in the REAS2 code - on the energy and the depth of the shower maximum was analyzed by Huege et al. (2008)
The method of investigation shown in the paper and the correlated results will be used as guideline for the analysis of the slope method applied to a realistic case (cf. Chapter 7 and Chapter 10) and for the further comparisons with the LOPES experimental data (cf. Chapter 8 and Chapter 9).
This section will lead the attention to the main aspects of this investigation and focus on the principal results obtained.

In the paper Huege et al. (2008) the radio lateral distribution of several events, simulated as gamma, proton, and iron primaries, with a specific incoming direction were compared (see **fig.**3.2). One noteworthy characteristic of these lateral profiles was that all intersect at a specific distance from the shower core, defined as "flat" region. At such a distance, the filtered field strength was almost independent of X_{max} and thus of shower-to-shower fluctuations. In other words, the "flat" region was characterized by the minimum RMS spread of the amplitudes from the different events (for details we refer to section 7.2.1). In **fig.**3.3 a quantitative view of the filtered electric field strength in this peculiar region is shown in relation to the X_{max} of the primaries. On the left side, the filtered peak amplitudes of the events with the same primary energy (coming from the south and with an inclination of 45 degree from the zenith), are shown. The amplitude distribution is quite flat, confirming the independence of X_{max}, but a kind of steps between the primaries are clearly visible. These steps are due to the radio emission connected only to the electromagnetic component of the shower and, depending on the primary type, a different portion of the total primary energy is given to the electromagnetic particles. Similar steps are expected as well in Chapter 8 and Chapter 9 when the normalization for the total energy is used to compare the LOPES detected events.
On the right side of **fig.**3.3, the primaries present an energy in the range between 10^{18} and 10^{20} eV, thus an energy normalization was required in order to facilitate a comparison. The normalization to the electromagnetic energy, i.e. the energy contribution from the electromagnetic component of the air shower, is reported as example. As expected from the above discussion, the smallest spread (RMS $\sim 3\%$) is reached for this normalization. Further investigations pointed out that the "flat" region and, more in general, the RMS spread of the amplitudes at all the distances, depends on the inclination of the shower, on the altitude of the experimental site and on the frequency-band used to filter the radio pulse (Huege et al., 2008).

For a given observer frequency and zenith angle, the filtered electric field strength in the well-defined "flat" region can be used to directly read off the electromagnetic energy E_{em}, with the linear relation

$$E_{\mathrm{em}} = aA_{\mathrm{flat}} \left[\mathrm{GeV} \frac{\mathrm{m}}{\mu \mathrm{V}} \right]$$

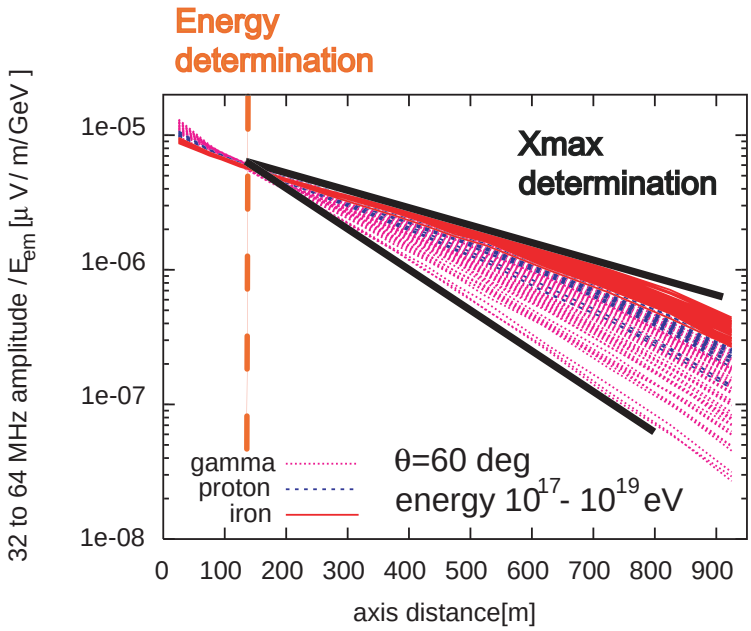

Figure 3.2: *Comparison of radio LDFs from gamma-, proton-, and iron-initiated showers simulated with REAS. A characteristic distance from the shower axis ($flat$ region) where the lateral profiles intersect, is predicted. In this region the investigation on the primary energy would be affected by the only shower-to-shower fluctuations. The slope of each LDF carries information on the shower $X_{\max}$. (Adapted from Huege et al. (2008))*

with A_{flat} the radio pulse amplitude in the "flat" region, as shown also in **fig.**3.4. The theoretical accuracy on the E_{em} reconstruction was predicted to be less than 3%, not considering experimental uncertainties; this value was achievable on a shower-to-shower basis and without an a priori knowledge of the primary mass or $X_{\max}$.

Defining the "steep" region at another distance, chosen arbitrarily far from the shower core, the ratio of the filtered electric field strength in the "flat" and "steep" regions (A_{flat}/A_{steep}) directly inferred the $X_{\max}$ value, which can be related to the mass of the primary.
The correlation between $X_{\max}$ and A_{flat}/A_{steep}, shown in **fig.**3.5, is described by the formula

$$X_{\max} = a \left[\ln \left(b \frac{A_{\text{flat}}}{A_{\text{steep}}} \right) \right]^{c} \ [\text{g/cm}^2]$$

Taking into account the deviation of the individual shower points from the fit, an RMS spread of 15.9 g/cm^2 (Huege et al., 2008) was obtained for all the simulated events of one specific geometry. This uncertainty included the shower-to-shower fluctuation, but no experimental error.

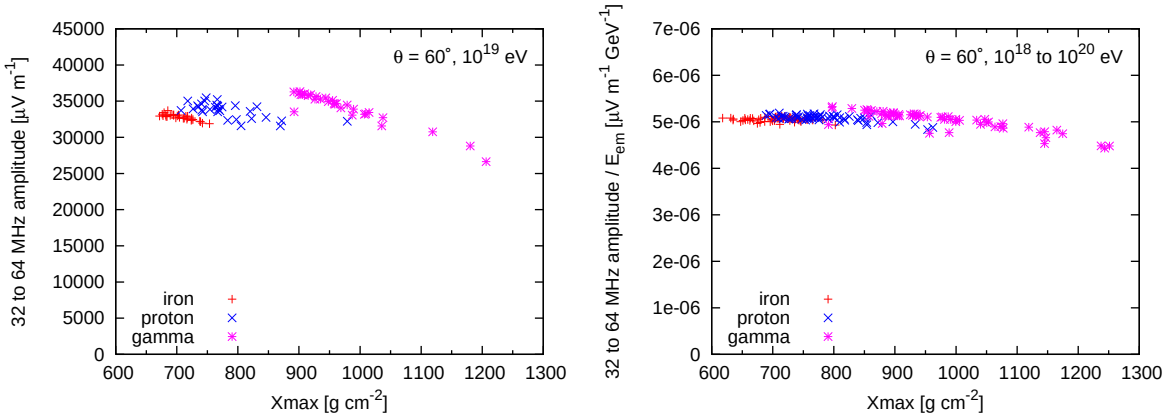

Figure 3.3: *Peak filtered radio field strengths in the "flat" region. The filtered radio pulses of only the events with 10^{19} eV primary energy are shown in the left part. The filtered field strengths of all the events in the primary energy range 10^{18}-10^{20} eV are normalized with the electromagnetic energy (right). Figure from (Huege et al., 2008)*

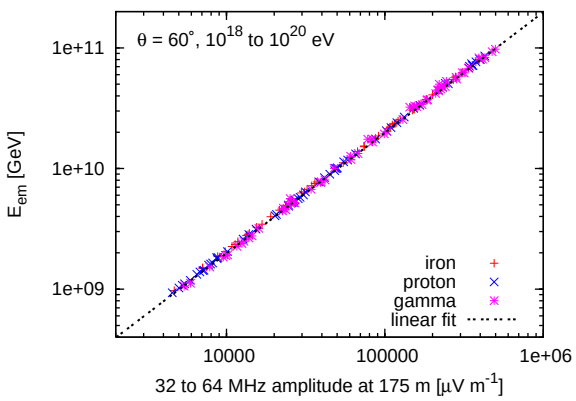

Figure 3.4: *Linear correlation of the filtered radio pulse measured in the "flat" region and the electromagnetic energy (a = 197900). Figure from (Huege et al., 2008)*
.

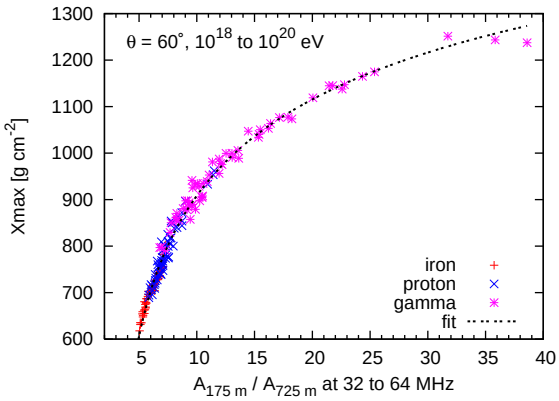

Figure 3.5: *The ratio of the peak field strengths in the "flat" and "steep" regions yields direct information on the $X_{\max}$ (a=856.1, b=0.3149, c=0.4340)(Huege et al., 2008)*

3.4 Outlook

The results in the paper by Huege et al. (2008), only briefly reviewed in the last section, show the possibility to derive important shower parameters, such as the primary energy and depth of the shower maximum, with radio-only measurements, and, at least in principle, low uncertainties in spite of shower-to-shower fluctuations.

The availability of the more complete REAS3 code, and both an improved agreement between the LOPES and the REAS3 simulated lateral distribution function (Ludwig, 2011), as well as the recent LOPES results concerning the $X_{\max}$ sensitivity (Apel et al., 2012a), suggest to revise the analysis presented above (cf. Chapter 7). Indeed, the latest version of the REAS code incorporates almost the total complexity of the radio emis-

sion; thus, the included charge excess contribution will affect the lateral distribution function and, eventually, some of the results described above.
Nevertheless, the main outcome concerning the radio lateral slope as indicator of the depth of the shower maximum is expected to be still valid. This is due to a pure geometrical effect. Iron nuclei interact earlier in the atmosphere, so their X_{max} is further away from the observer compared to the X_{max} of the lighter elements. The radio lateral distribution function slope is expected to be flatter for heavier- and steeper for lighter-primaries.

Investigating the "flat" region for a specific experimental set-up, such as LOPES or AERA (cf. Chapter 8 and Chapter 10), will, moreover, evaluate the applicability of this method of investigation to the real recorded data: to test whether it is feasible to reconstruct both the energy and the mass type of the primaries, and to define the related uncertainties.

4 The LOPES and the AERA experiments

As early as the 1960s, the first radio signals associated with extensive air showers were detected in the MHz regime (Jelley et al., 1965). Several mechanisms were proposed to interpret the phenomenon, among them the "Askaryan radiation" (Askaryan, 1962, 1965) and the geomagnetic radiation (Kahn and Lerche, 1966).
After basic results, the field of radio detection suffered a lack of interest principally due to the limited technology available at that time and to the concurrent development of other detector techniques, such as the fluorescence and Cherenkov light detections.
With the progress in digital signal processing and the availability of more advanced technology together with the intrinsic advantage (almost 100 $\%$ duty cycle and a moderate cost for the antenna detectors), the radio detection method experienced a revival in the last decade.

The CODALEMA (Ardouin et al., 2005, 2006) and the LOPES (Falcke et al., 2005, Horneffer et al., 2009) experiments have been playing a pioneering role. Many results have been achieved, such as the confirmation of the geomagnetic origin of the radio emission (Horneffer, 2006, Isar et al., 2009, Ardouin et al., 2009), the exponential behavior of the lateral distribution function (Apel et al., 2010a, Ravel, 2010), the influence of the atmospheric electric field (Buitink et al., 2007), the reconstruction of the shower-core position (Bellètoile, 2011), and the recent evidence of the charge excess contribution in the radio data (Marin, 2011). The LOPES and CODALEMA success led several air shower experiments to extend their detectors with digital radio antenna arrays.
The most prominent among those is the Pierre Auger Observatory, in Argentina, with the AERA [1] project, which is a second-generation digital-radio-antenna array (Huege, 2009a, Fliescher, 2010).
Apart from the already mentioned above, several other radio experiments were developed in the last years, with the main purpose of optimizing the radio technique and understanding the details of the radio emission from air showers, such as LOFAR (Falcke et al., 2006), Tunka (Budnev et al., 2009), TREND (Ardouin et al., 2011), etc..
An overview of the currently operating radio experiments is available in the ARENA proceedings (ARENA, 2010).

In the following, the experiments of interest for this dissertation (LOPES section 4.1 and AERA section 4.2) are briefly introduced.

[1] **A**uger **E**ngeneering **R**adio **A**rray

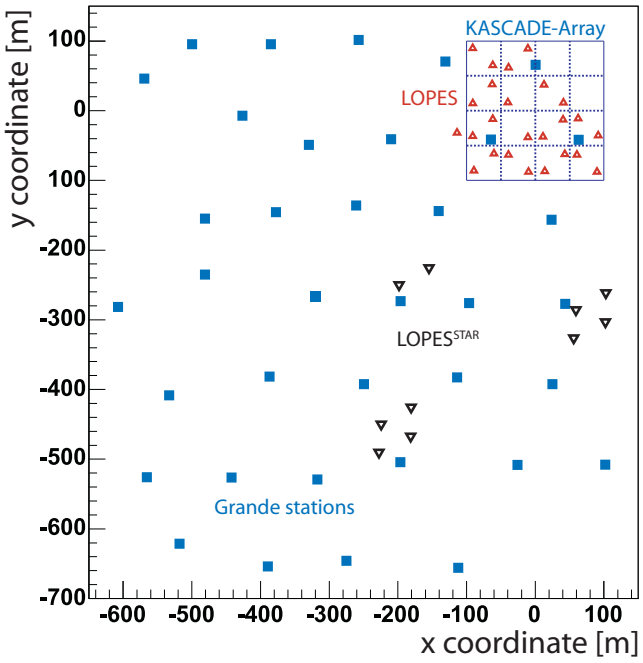

Figure 4.1: *The KASCADE-Grande experiment. On the top-right, in red, the LOPES antenna array.*

4.1 The LOPES experiment

LOPES [2] (Falcke et al., 2005, Horneffer et al., 2009, Huege, 2010) is a digital radio interferometer, co-located with the KASCADE-Grande experiment (Antoni et al., 2003b, Apel et al., 2010b), at the KIT (Karlsruhe Institute of Technology), Germany (see **fig.**4.1). LOPES read-out and setup are performed with the aim to detect radio signals in the primary energy range approximately of 10^{16}-10^{18} eV.
Built in 2003, LOPES was extended several times in order to test different setups and antenna types, and to address different questions about the radio emission from cosmic ray air showers.
The first antennas were designed as prototypes for the LOFAR experiment, a digital low-frequency interferometer for radio astronomy (Röttgering et al., 2003, Falcke et al., 2006).

Built with the purpose of the "proof-of-principle", LOPES offers the possibility to correlate the observables of the radio measurements with the shower parameters provided by the particle detector arrays KASCADE (Antoni et al., 2003b) and KASCADE-Grande (Apel et al., 2010b).

In the following sections an overview of the LOPES setups and software used for the analysis is presented.

[2] **LO**FAR **P**rototyp**E** **S**tation.

Figure 4.2: *LOPES antenna in use up to end of 2009*

4.1.1 LOPES setup

The experimental configuration of LOPES, the layout and the antenna type changed several times.
In the first phase (LOPES 10), the LOPES setup consisted of 10 inverted V-shape dipole antennas of the kind shown in **fig.**4.2.
In 2005, LOPES was extended to 30 antennas of the same kind, all aligned in the east-west direction (LOPES 30-EW). The purpose was to extend the covered area in order to provide large baselines for an accurate LDF study, and to raise the experimental sensitivity.
At the end of 2006, half of the antennas were rotated by 90° in order to investigate also the north-south component of the radio pulse (LOPES 30-Pol). The layout consisted of 10 antennas measuring the EW direction, other 10 the NS direction, and 5 antennas able to measured simultaneously in the EW and NS directions.
The LOPES configuration was then extended with other types of antennas, a log-periodic antenna consisting of dipoles (LPDA) and a SALLA antenna (Short Aperiodic Loaded Loop Antenna) (Krömer et al., 2009), based on the idea of developing an antenna system able to operate independently and self-triggering (Asch, 2009) (LOPES$^{\mathrm{STAR}}$)[3].
A new antenna type was introduced in spring 2010, and the 30 inverted V-shape antennas were exchanged for half-wave dipoles, forming a tripole antenna in each station (LOPES 3D). This latest setup is targeted to measure all three components of the electric field vector (Huege, 2010, Huber, 2011).

The electronics used for the digital read out of the radio signal is summarized in **fig.**4.3. Every antenna contains a low noise amplifier (LNA). Via a coaxial cable, the signal is transmitted from the antenna to an analogue electronics board, where it is again

[3] **S**elf-**T**riggered **A**rray of **R**adio **D**etectors

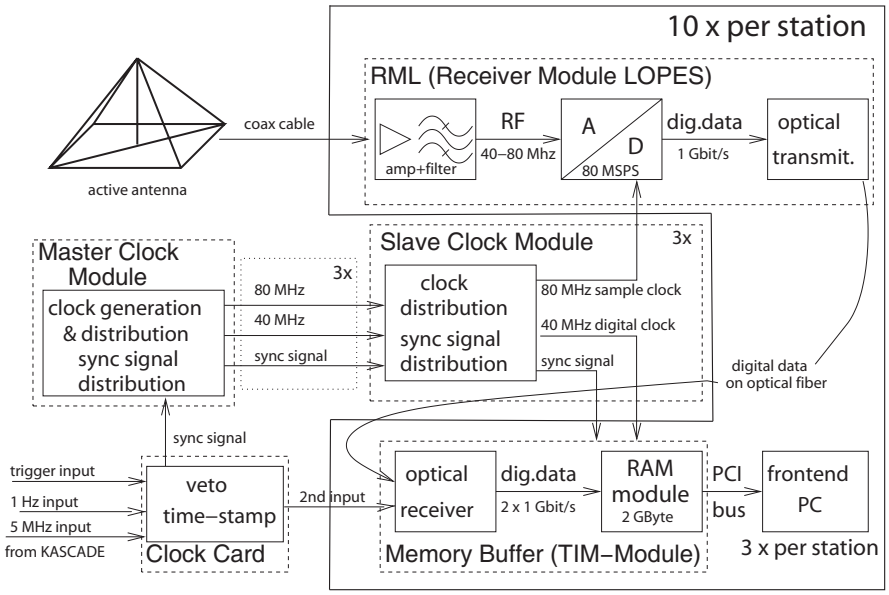

Figure 4.3: *LOPES hardware setup Nehls (2008)*

amplified, filtered and digitized. The board amplifies the signal by +16 dB and filters it to 43-74 MHz with a pass-band filter. The FM radio-transmitter frequencies ($\gtrsim$80 MHz) and the atmospheric-noise frequencies ($\lesssim$40 MHz) are, thus, suppressed.
The re-amplified and filtered signal is sampled with a 12 bit ADC at the sampling frequency of 80 MHz (i.e. 12.5 ns samples) in the 2nd Nyquist domain. The application of a limited band-width filter is fundamental to have the complete information of a radio signal, using a limited sampling frequency. This, according to the Nyquist theorem (Nyquist, 1928), must be at least twice the used bandwidth, exactly as in the case of the LOPES experiment.

The read-out of the LOPES traces is triggered by both KASCADE (Antoni et al., 2003b) and KASCADE-Grande (Apel et al., 2010b). In the first case, the trigger condition is fulfilled if at least 10 of the 16 KASCADE clusters have recorded a signal, while in the case of KASCADE-Grande the condition holds when hexagons 9, 10 and 13, which include stations in the center of the Grande array, have triggered (Nehls, 2008).

The KASCADE experiment consists of 252 detector stations arranged on a rectangular grid in a 200x200 m^2 area. KASCADE provides both the number of electrons (Ne) and muons (Nμ) present in the air shower. Electrons and gammas are detected by unshielded liquid scintillator. Muon-detectors are shielded against the electromagnetic component with iron-lead-absorber, which allows only muons with energy larger than 250 MeV to penetrate.
The Grande array, much wider (0.5 km^2), measures the complete number of charged particles in the shower (N_{ch}) by using plastic scintillators.

LOPES trigger rate is of about two events each minute and the dead-time is circa one second, implying almost 3000 LOPES events per day.
After the read-out, the LOPES data are stored as well as the KASCADE and KASCADE-

Grande information in order to perform, in a second step, a correlation between radio and particle detectors measurements.

For the LOPES setup the static atmospheric electric field on the ground is monitored with an electric field mill (Nehls, 2008). This device is mounted quite in the center of the KASCADE array and it measures the vertical component of the atmospheric electric field. Even an electric field of $\sim$ 3000 V/m may generate an amplification in the radio signal from air showers (Ender, 2009). Such an event must be excluded from the analysis of radio emission from cosmic rays but it can be used for lightning studies Apel et al. (2011c). The electric field meter is used as lightning detector and operates for the LOPES DAQ as discriminator between good weather condition (electric field of few 100 V/m) and thunderstorm condition (electric field up to 100 kV/m).

4.1.2 Data analysis procedure

Software (CR-Tools, 2004) has been developed to fulfill the requirements of the LOPES experiment, in particular some of the general tasks such as selection of the radio events, reconstruction of the properties of the recorded radio pulses, and correlation of the radio results with the KASCADE-Grande reconstruction for the same event.
The high, largely human-made, noise level at the LOPES site requires an analysis procedure consisting of several highly sophisticated steps, mostly done with the LOPES standard analysis pipeline (CR-Tools).

CR-Tools are part of the open-source LOFAR software package (CR-Tools, 2004).
In its pipeline are included: corrections for instrumental effects (amplitude calibration (Nehls et al., 2008), correction for cables and electronics delays (Schröder, 2010), correction for the pulse distortion due to the frequency band-filter (Schröder, 2010), application of the simulated antenna gain pattern, etc.), treatment of the data (mitigation of narrow band RFI, up-sampling (Asch, 2009), correction of the pulse height for the noise (Schröder et al., 2010b), etc.) and determination of radio pulse parameters (CC-beam, reconstruction of the lateral distribution function, i.e. LDF, etc.).

Interferometric analysis
The LOPES project has successfully implemented modern interferometric methods to measure the radio emission from extensive air showers. The capability to form a cross-correlation beam, which involves several steps briefly summarized in the following, improves the signal-to-noise ratio and the reconstruction accuracy of the properties of cosmic ray primaries.

· *Absolute amplitude calibration* (Nehls et al., 2008). An absolute amplitude calibration is applied to the LOPES data. The frequency-dependent amplification factors for each LOPES channel are estimated with measurement campaigns, performed over several years with a calibrated external reference source. By comparing the emitted power of the reference antenna and the received power at each LOPES station, a frequency-dependent gain factor can be calculated. The relative uncertainties concerning the amplitude calibration are: the absolute scale of the amplitude for the emitted reference signal (34 $\%$) (Nehls, 2008), which plays no role when several LOPES events are compared with each other, the simulation of the antenna gain pattern, used for the calculation of the amplification factor (7.5 $\%$), the uncertainty on the measured power (2.5 $\%$), and

environmental effects (5 %) (Schroeder, 2011).

· *Narrow band RFI suppression* A digital filtering algorithm is applied in the frequency-spectra of each antenna in order to suppress narrow-band radio interferences (RFI). This step increases the signal-to-noise ratio of the radio event and does not affect the broad-band cosmic ray radio signal.

· *Time calibration* For a reliable interferometric analysis, high precision of the relative timing between the antennas is a fundamental prerequisite, e.g. when forming a cross-correlation beam into the air shower direction (see also CC-beam). Nowadays, this is performed by using an external reference signal from the beacon antenna (Schröder et al., 2010a) and an accuracy of ~ 1 ns is achieved.

· *Up-sampling* Since LOPES measures in the 2nd Nyquist domain (Nyquist, 1928), the whole frequency information between 43 and 74 MHz is contained in the recorded signal. Thus, the raw data can be up-sampled to a higher sampling rate. This procedure results in a band-limited interpolation, in the time-domain, between the sampled data points with 12.5 ns spacing. The up-sampling is performed by the zero-padding method applied in the frequency-domain (Bracewell, 1986, Asch, 2009). In a normal data acquisition mode, for each event, 2^{16} data points in each trace are recorded, which correspond to about 0.8 ms.

· *Beam-forming* (Horneffer et al., 2007, Horneffer, 2006) A digital beam-forming is applied to the radio pulses in order to achieve the sensitivity in the arrival direction of the incoming cosmic ray: The traces of all the antennas are shifted in time so to overlap, according to the antenna position at ground (geometrical delay). A spherical radio wave front is usually assumed in the analysis. An investigation about a wave-front with conical shape was recently performed (Schröder, 2010). Afterwards, the traces are manipulated to calculate either a P-beam or a CC-beam (explained in the following). Both the direction of the beam-forming (Nigl et al., 2008) and the curvature radius (i.e. the distance between the radio source and the core of the air shower) are obtained with a simplex fit optimization in an iterative process. In the first iteration, the arrival direction and the first curvature radius (usually of few km) are taken from the KASCADE-Grande reconstruction and from a scan, respectively. The quantity maximized in the iterative procedure is a Gaussian fit of the CC-beam.

· *CC-beam* and *P-beam* (Horneffer et al., 2007, Horneffer, 2006) After beam-forming, the CC-beam is calculated with the following equation:

$$\mathrm{CC[t]} = \pm\sqrt{\mid \frac{1}{\mathrm{N_{pairs}}} \sum_{i=1}^{N-1} \sum_{j>i}^{N} s_i[t] s_j[t] \mid} \tag{4.1}$$

with N the number of antennas, $\mathrm{N_{pairs}}$ the number of unique antenna pairs and $s_N[t]$ the time shifted data of the denoted antenna.
Then the CC-beam is block-averaged over 37.5 ns in order to suppress fine structures and fitted with a Gaussian function.
The height of the Gaussian fit is referred to as the total coherent radio signal.
A power beam (P-beam) is obtained by averaging the squared values of all the antennas and taking the square root. In other words, the P-beam is the quantity which represents the total power received in all the antennas together.
An example of the calculated P-beam, CC-beam, and Gaussian fit for a LOPES event is

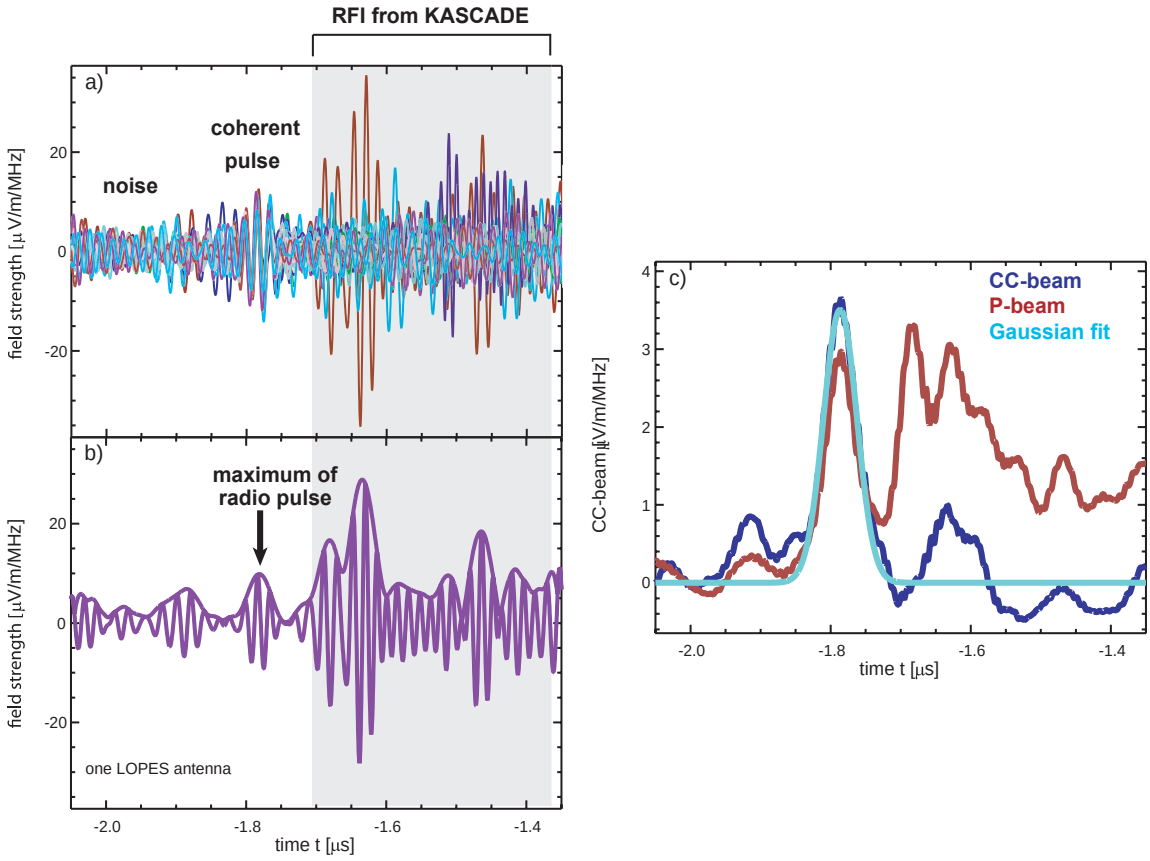

Figure 4.4: *Example of a LOPES event: a)Electric field strength traces of all the antennas, b)trace recorded in one antenna with a Hilbert envelope, used to define the maximum amplitude, c)CC-beam and P-beam.*

shown in **fig.**4.4.

LDF reconstruction

The LOPES analysis pipeline makes possible not only an interferometric combination of the traces, but also the study of the radio pulse in the individual antenna.

A LDF reconstruction requires high quality cuts, mainly concerning the recorded radio amplitudes, since the signal-to-noise ratio in each individual antennas is lower compared to the one for the CC-beam.

The digital cross-correlation beam-forming plays a crucial role also for the reconstruction of the lateral distribution of amplitudes (Chapter 6). Indeed, in the LDF investigation, the CC-beam is used for both the selection of events with a clear radio signal (c.f. section 4.1.3) and for the identification of the exact time of the radio pulse ($t_{cc-beam}$).

In each LOPES antenna, the signal is defined as the maximum instantaneous amplitude ϵ: after applying a Hilbert envelope to the up-sampled trace, ϵ corresponds to the local maximum of the Hilbert envelope closest to the CC-beam time ($t_{cc-beam}$) (Schröder et al., 2010b) previously determined, as shown in **fig.**4.4. A measurement of a radio signal is possible in all the antennas. For further details on the LDF recon-

Table 4.1: *Preselection*

successful reconstruction by KASCADE	$0.4 <$ shower age < 1.4
core position inside KASCADE array	r=$\sqrt{x^2+y^2} < 90$ m
zenith angle	$\theta < 45^\circ$
primary energy	E $> 10^{17}$eV
atmospheric electric field[1]	$\lvert \mathrm{E_{atms}} \rvert < 3000$ μV/m
total events	977

Table 4.2: *Selections - EW signal*

	Selection1	Selection2
CR-Tools version	rev. 4950	rev. 6250
high signal-to-noise	P-beam > 80 % $\frac{\mathrm{CC_{amplitude}}}{\mathrm{RMS(CC-beam)}} > 9$	P-beam > 80 % $\frac{\mathrm{CC_{amplitude}}}{\mathrm{RMS(CC-beam)}} > 9\frac{\sqrt{\mathrm{N_{ANT}}}}{30}$
quality cuts on the LDF fit	$\mathrm{R_0} > 0$ m $\mathrm{R_0} < 1000$ m $\epsilon_{fit} > 0$ μV/m/MHz $\epsilon_{fit} < 1000$ μV/m/MHz	$\mathrm{R_0} > 0$ m $\mathrm{R_0} < 1000$ m $\epsilon_{fit} > 0$ μV/m/MHz $\epsilon_{fit} < 200$ μV/m/MHz amplitude at 0 m > 5 μV/m/MHz $0 < \chi^2/\mathrm{ndf} < 5$
Events	160	253
Events with $\theta < 40^\circ$		238
Events with $\lvert \mathrm{P_{EW}} \rvert < 0.2$		229

struction please see also Chapter 6.

4.1.3 LOPES data selection

Two different selections of LOPES events will be presented here, each of them used to optimize specific aspects of the investigation. Since the main part of the LOPES analysis is focused on the correlation between the slope of the lateral distribution function (LDF) and the primary cosmic ray type (cf. Chapter 7, Chapter 8, Chapter 9), high quality cuts on the LDF fit parameters are generally required.

The data taking covers the period from December 2005 to October 2009, which includes two different setups of the LOPES experiment (LOPES 30-EW and LOPES 30-Pol).
Only the signals recorded in the EW-oriented antennas are considered in the analysis due to both higher statistics and larger signal-to-noise ratios in comparison to the NS-oriented antennas.

The events are triggered by both the KASCADE (Antoni et al., 2003b) and Grande (Apel et al., 2010b), and, as a first step, some standard KASCADE quality cuts are ap-

[1] Reliable measurements available only from August 2006

plied (Table 4.1): The core position of the shower, namely the intersection point of the shower axis and the ground, is required close to the LOPES array (R<90 m). This cut avoids the analysis of tails of the lateral distribution functions, which have, in general, a lower signal-to-noise ratio in the antennas. In other words, this cut allows to have higher quality of the fit of the radio lateral distribution.
Several further cuts are applied on the parameters reconstructed by KASCADE, which is based on KRETA[4] version 1.18/05. Among these, a restriction on the inclination of the shower ($\theta < 45°$) is required, to avoid large uncertainties on the reconstruction.
The energy of a primary cosmic ray is obtained using the KASCADE-Grande formula (Wommer, 2007), since the KASCADE experiment is optimized only for lower energies ($\lesssim 10^{16}$ eV) - KASCADE-Grande performs a primary energy reconstruction in the range 10^{16}-10^{18} eV. Nevertheless, due to the proximity of the core position of the selected events to the KASCADE detector array, both the muons and electrons number recorded by KASCADE are used as input parameters for the energy formula.

Moreover, a cut on the atmospheric electric field measured on the ground is required. It is known, in fact, that the radio pulse is strongly influenced by not only nearby thunderstorms (Nehls et al., 2008) but, more in general, by a high electric field in the atmosphere (Ender, 2009).

The radio specific cuts, for two independent selections (Selection1 and Selection2), used for different purpose respectively in Chapter 7 and Chapter 8, are summarized in Table 4.2:
The events are processed with the standard LOPES pipeline (CR-Tools pipeline, svn revisions 4950 and 6250) (CR-Tools, 2004). The main difference between the two versions consists in the treatment of the noise, properly introduced only in the latest period (Schröder et al., 2010b). Nevertheless, the net average effect on the electric field in the antennas, thus on the slope of the LDF (cf. Chapter 6), is expected to be of only 7% (Schröder et al., 2010b).

High coherency is required for the signal in each antenna, setting the fraction of the correlated power (amplitude of CC-beam/amplitude of P-beam) to be larger than 80 % (**fig.**4.6, right side). In this way, events with high signal-to-noise ratio due to random coherency are cut away. Values of the correlated power larger than 100 % are caused by improper treatment of the noise: the subtraction of an averaged noise causes the P-beam amplitude to be smaller than the CC-beam one.

Both selections are characterized by generally high quality cuts on the LDF fit parameters. More in details, Selection2 constitutes slightly stronger cuts on the LDF fit reconstruction (slope parameter R_0, amplitude parameter ϵ_{fit} and amplitude reconstructed at 0 m from the shower core), but less restrictive ones on the minimum signal-to-noise ratio (CC-amplitude / root mean square of the CC-beam) (cf. Chapter 4). This is set to 9 in both selections, but a further normalization factor on the number of antennas, i.e. $\sqrt{N_{ANT}}$, is applied for Selection2. The reason for $\sqrt{N_{ANT}}$ is related to the proportionality of the CC-amplitude with the number of the antennas (N_{ANT}) which record a radio pulse, and the proportionality of the noise, for a non-interferometric array, with $\sqrt{N_{ANT}}$ (**fig.**4.6, left side).

The main goal of Selection2 is to increase the statistics in comparison with Selec-

[4]Kascade Reconstruction for Ex-Tensive Air showers.

tion1. This is done by maximizing the number of the selected events with a slightly lighter cut on the signal-to-noise ratio in each antenna, but discriminating from the unsuccessful radio LDF fit with a stronger cut on the amplitude parameter.
A direct comparison between the two selections is presented in **fig.**4.5 from top to bottom, clockwise, for the azimuth angle, zenith angle and energy distributions, with 160 events for Selection1 and 259 events for Selection2.

Further cuts on the zenith angle and on the so-called **P** vector component (cf. Chapter 5) are necessary for the investigation on the slope method applied to the LOPES data (Chapter 8 and Chapter 9).
The first restricts θ to 40° in order to avoid an analysis on a too low statistics typical of the zenith range between 40 and 45 degree of such selection; the second sets the minimum for the east-west component $\mathrm{P_{EW}}$, which will be used for the electric field normalization in the lateral distribution function fit (see also section 8.1).

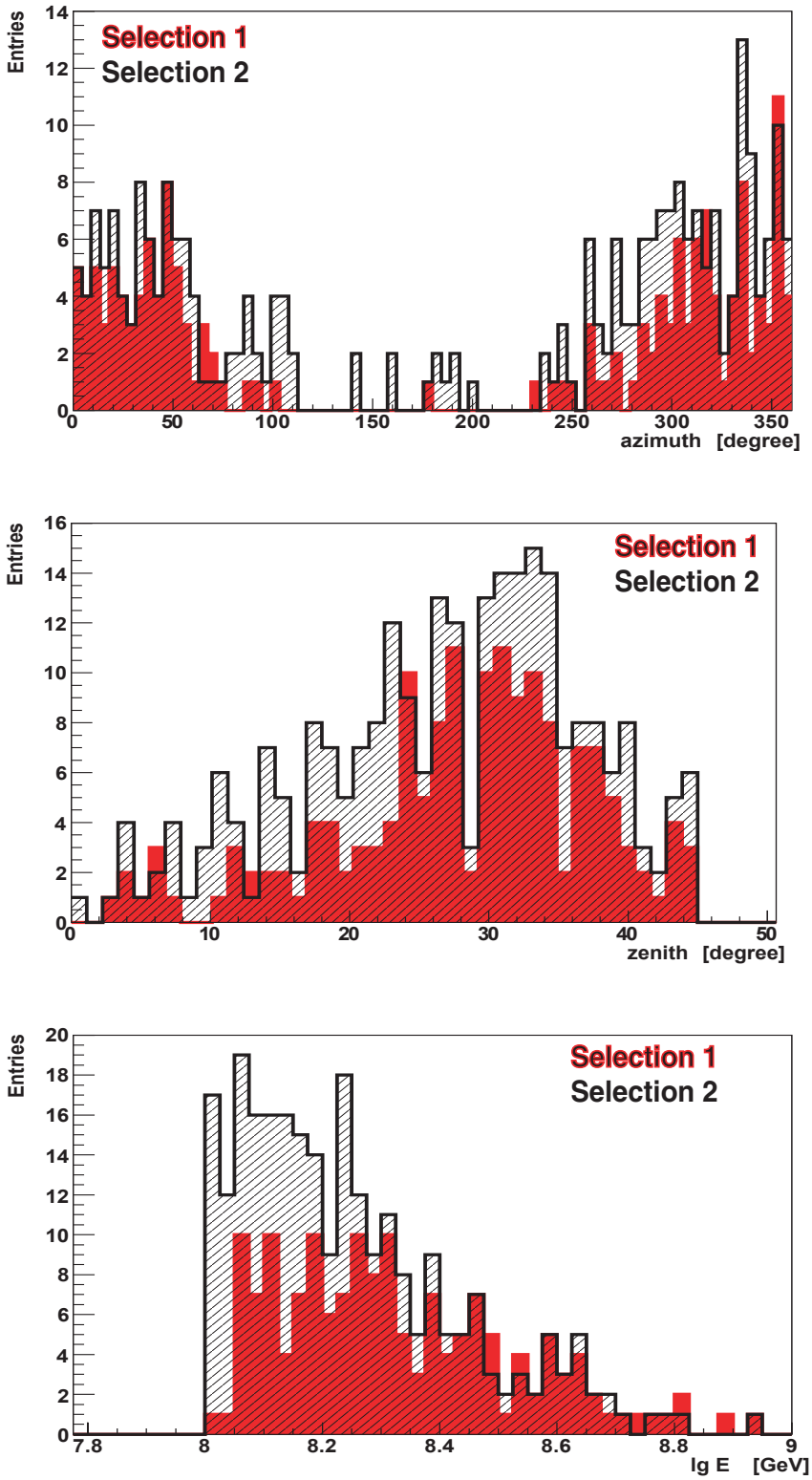

Figure 4.5: *From top to bottom, azimuth and zenith angle and primary energy distributions for the LOPES selected events.*

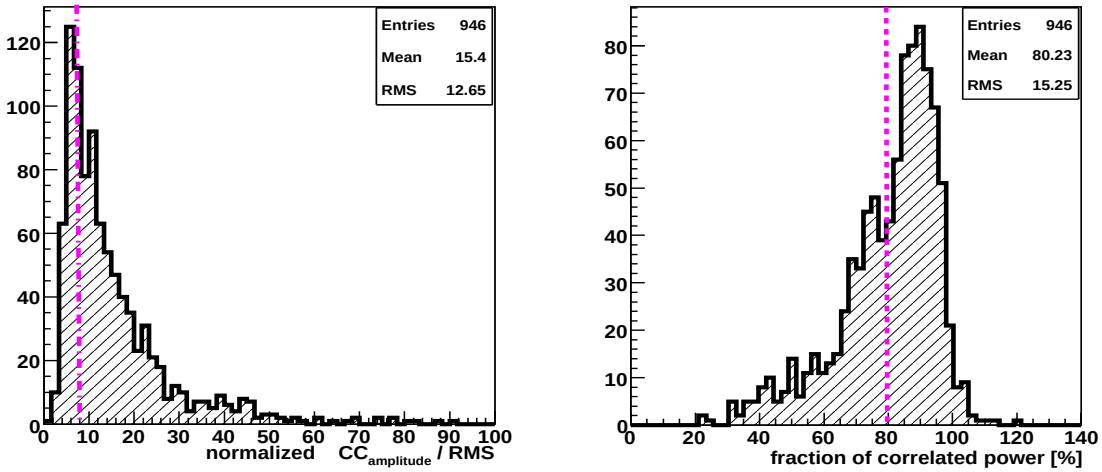

Figure 4.6: *Cuts on the CC-beam. Left: normalized signal-to-noise ratio, i.e. CC-amplitude/CC-RMS . Right: fraction of the correlated power, i.e. amplitude of CC-beam/amplitude of P-beam*

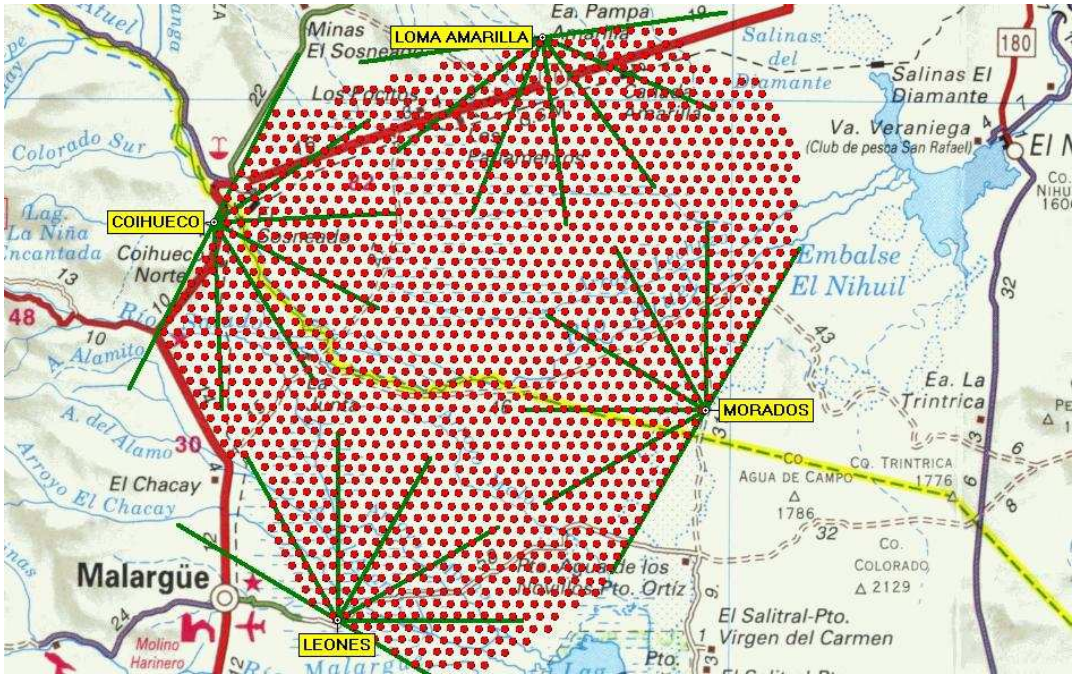

Figure 4.7: *Map of the Pierre Auger Observatory in Argentina. The SD detectors are represented by the red points, while the FD telescope by the green lines.*

4.2 The AERA project at the Pierre Auger Observatory

In Western Argentina, in the vast plain called Pampa Amarilla, the southern site of the Pierre Auger Observatory was completed in 2008 (Abraham et al., 2004a) (**fig.**4.7). Pierre Auger is the world's largest observatory which features a hybrid approach for the detection of ultra-high energy cosmic rays (UHECR).

The Surface Detector array (SD) consists of 1600 water Cherenkov detector tanks, covering the complete area of 3000 km^2, with 1.5 km spacing (Abraham et al., 2004b). The SD collects information from all the charged particles of the air showers which reach the Earth's surface ($\sim$ 1400 m a.s.l.).

The Fluorescence Detectors (FD) observe the atmosphere above the SD with 24 optical telescopes, grouped in four buildings. The purpose of FD is to observe the longitudinal development of extensive air showers by detecting both the fluorescence light emitted by the nitrogen molecules, which are excited by the secondary particles in the showers, and the Cherenkov light induced by them (Abraham et al., 2010c).
The combination of these two detection methods in so-called "hybrid" measurements allows a unique reduction of the uncertainties in the reconstruction of the air shower parameters, such as the energy and the mass of the primaries (Abraham et al., 2010a,b).

Lately the Pierre Auger Observatory has been extended with other detectors in order to decrease the primary energy threshold, up to $\sim 10^{17}$ eV and to allow a super-hybrid detection approach. These detectors are all situated in the same area close to the fluorescence detector installation at Coihueco: HEAT (Mathes, 2011), a high elevation

telescope, AMIGA (Platino, 2009), underground scintillators for muons detection and infill array of SD at only 750 m spacing, AERA (Fliescher, 2010), for the radio detection.

The Auger Engineering Radio Array (AERA) is intended to investigate the feasibility of the radio detection method on a large scale.
In the final stage, the 20 km^2 array will consist of circa 160 autonomously-operating radio stations **fig.**4.8. In 2010, phase 1 was concluded and 24 radio stations were built as well as the CRS (Central Radio Station) and a beacon reference antenna was set.
The core of AERA is in the infill array, at $\sim$6 km distance in the line of sight of the fluorescence detector Coihueco; this peculiar position was chosen in order to allow for a maximum number of events to be detected in coincidence with the other detectors.
The major goals proposed for AERA are:

* Explore the potential of the radio detection technique, such as the self-triggering on the radio pulse and the digital interferometry on large scales.

* Improve the understanding of the radio emission mechanism up to high primary energies (10^{19} eV).

* Perform a detection of the radio events in coincidence with the other detectors in the super-hybrid mode. The radio reconstruction for the primary parameters, such as the incoming direction, the energy and the mass, will be investigated and cross-checked with the other Auger detector reconstructions. This will indicate whether radio detection can compete with the established detection methods.

Another advantage of the AERA experiment is the possibility to analyze the radio data within the $\overline{\text{Off}}\underline{\text{line}}$ standard software framework of the Pierre Auger Observatory (Argirò et al., 2007), properly extended for this purpose (Abreu et al., 2011). The radio implementation in $\overline{\text{Off}}\underline{\text{line}}$ is fundamental for the combined super-hybrid reconstruction. Moreover, the $\overline{\text{Off}}\underline{\text{line}}$ offers interfaces for the radio data and simulations from the different codes available at the moment, such as REAS3 (Ludwig and Huege, 2011b), MGMR (Scholten et al., 2008), and ReAires (DuVernois et al., 2005).

4.2.1 AERA setup

In the first phase, the dense core of AERA has been covered with 24 antenna stations, which have a mutual distance of 150 m. The phases 2 and 3 are planned to deploy, respectively, 52 stations in the area around the dense core, at a distance of 250 m, and 85 stations in the outer region, with 375 m spacing. The graded AERA layout is intended to maximize the number of detectable events over a wide primary energy range, $10^{17.5}$-10^{19} eV.

The sheer size of the AERA setup does not allow a direct transfer of the data between stations and CRS (Central Radio Station) with cables, but the continuous radio signal

must be digitized directly at the antenna station and the data can be transferred wireless to the CRS only in the case of possible cosmic ray events. Thus, AERA requires highly advanced technology to realize an efficient trigger and a fast and reliable wireless transfer of the radio information.

For AERA radio-telescope array, the concept of autonomous station has been developed (Revenu, 2011). **fig.**4.8 is picked as example for the AERA stations currently in use.
It consists of one antenna (two channels), solar panels and an aluminum box containing the electronics and the digitizer. The antennas in phase 1 are logarithmic period dipole antennas (LPDA) (Seeger, 2010) and, in each station, they are aligned in north-south and in east-west direction, in order to allow the investigation of two electric field vector components. Each antenna has both low-gain and high-gain channels.
For the individual local station, the analogue electronics, which include the Low Noise Amplifier and filters, are designed to detect radio pulses from cosmic rays in the frequency range 30-80 MHz (Stephan, 2010). The filtered signal is digitized with 12 bit ADCs, at a sampling rate of 200 MHz, and it is stored in the local AERA station electronics. A Field-Programmable Gate Array is used for the trigger and the management of the data storage (Aminaei, 2010).
A GPS antenna is used for time synchronization between different AERA stations and only interesting data are selected and collected by a central data acquisition (DAQ).
A high-speed, low-power wireless communication system, still under development, will be used to connect the single AERA stations and the central DAQ (Kelley, 2011). In the current phase, fiber optics are used instead.

Since the end of January 2012, some[5] already existing AERA stations have been equipped with new electronics. A ring-buffer allows receiving SD triggers with a latency of up to ~ 7 seconds. This readjusted setup has been testing an external SD-trigger and aims to be complementary to the AERA self-trigger in use. For more details please see also (Melissas, 2012).

As well as for the LOPES experiment, a beacon reference antenna (Schröder et al., 2009, Konzack et al., 2010) is used to monitor and correct the relative timing between the stations, reaching an uncertainty of only 1 ns.
Moreover, the atmospheric electric field at ground is constantly analyzed, to detect thunderstorm-like conditions (Melissas et al., 2011).
Subsequently, the collected data will be analyzed with the $\overline{\text{Off}}\underline{\text{line}}$ pipeline (Abreu et al., 2011, Fliescher et al., 2010).

4.2.2 Prototype stations

Prototype setups at the Balloon Launching Station (BLS) as well as at the Central Laser Facility (CLF), have been used as precursors of AERA to explore the radio detection at the Pierre Auger Observatory. Different antenna types and electronics have been tested since 2007 (van den Berg, 2009, Coppens, 2009, Revenu, 2010a, Fuchs et al., 2011).
The setup used at the BLS during the year 2007 is briefly described below. For a de-

[5] 24 antennas till the end of July

Figure 4.8: *AERA station with wired LPDA.*

tailed description we refer to (Coppens, 2009).

Three antenna stations (Pole1, Pole2 and Pole3) were used, arranged to form an equilateral triangle, with a baseline of 100 m. At each station, two antennas were located, aligned respectively in the north-south and in the east-west direction.
At Pole1 and Pole2 the LPDA antennas were employed, while Pole3 was first arranged with a wire-LPDA (with copper wires instead of the aluminum rods) and, later, with a LOFAR antenna, which consists of two inverted V-shape dipoles.
These antenna stations were connected to the BLS by RG213 coaxial cables, 160 m long each.
The complete setup was at circa 500 m from the closest SD-tank “Olaia”.
In order to lower the energy threshold of the SD and detect local showers, an additional particle detector was placed close to the BLS. It consisted of two scintillator plates at a distance of 10 m from each other. These scintillators provided the external trigger for the read-out of the antennas.
After the trigger, the measured voltage at each antenna was recorded for a total of 10 µ s, 2 µ s before the trigger and 8 µ s after.
The radio signal was amplified twice, with a pre-amplifier of 22 dB (Krömer, 2008) placed directly at the antenna stations and with a 31 dB amplifier after the cable.
Two high-pass and two low-pass frequency filters were used, reducing the frequency window to 25-70 MHz.
Before sending to a central computer in the BLS, the recorded radio signal was digitized using a 12 bit ADC.
The search for coincidences with the SD was performed by looking at the GPS timestamps of the events recorded by the radio antennas and the SD tank “Olaia”. One event is considered in coincidence if the radio setup was triggered within 10 µs -time-window from an SD event.

The BLS events recorded in 2007 have been analyzed with the RDAS software, which includes the simulation of the antenna response and was available at the time when the analysis was performed.

RDAS tool (**R**adio **D**etector **A**rray **S**imulation) [6] (Fliescher, 2008) is a freely available software. Unlike the $\overline{\text{Off}}\underline{\text{line}}$ package, RDAS is not suited for hybrid analysis. Nevertheless it allows a basic analysis of the radio data and includes simulations of the radio detector response.

The basic idea is to analyze the radio data on the channel voltage level: the measured data are taken without removing detector effects, while the simulated events are compared after applying the detector effects.

The software consists of mainly three blocks, one for the detector description, one as a module collection and the last for the event information. Such a design tries to follow the $\overline{\text{Off}}\underline{\text{line}}$ framework structure.

For the characteristics of the LPDA antennas available at the BLS setup, simulations were performed with the Nec2 antenna modeling software (Burke and Poggio, 1977, 1981, 1983), which provides the antenna properties.

The detector simulation and the reconstruction processes for REAS simulations and recorded data are done in a series of modules:

- The "ReadReas" module handles the REAS simulations. The galactic noise is also simulated and it can be added to the traces at the observer position. The noise is generated with the "GalacticNoise" module, based on the parametrization of the galactic noise made by Cane (Cane, 1979).

- A number of modules are used to simulate additional characteristics of the radio station apart from the antenna.
  The "Cable" module applies the frequency-dependent attenuation for a given length of a coaxial cable, which, in this case, is 160 m. The "Amplifier" module amplifies the data of the total gain 53 dB. Finally, the "DAQfilter" module filters the signal to the bandwidth 25-75 MHz (HP25-LP75). This last module is applied a second time to the REAS traces with a pass-band from 50 to 70 MHz (SBP-60) as well as to the recorded data, in order to improve the BLS data quality.

- The noise level in the time-domain and the radio pulse are determined.
  For the measured data, the signal is expected to lie within a certain time window of the recorded traces. Due to the trigger condition of the BLS specific setup, this time range is exactly 2.4-3.1 µ s. The "SizeRecData" module constrains the search for the radio pulse to this specific time window. Moreover, it determines the noise level in another arbitrarily chosen time window, which, for the analysis described in Chapter 5, is set to 0-2 µ s.

- A search for the maximum amplitude is performed to find the radio signal within a given trace, for both recorded or simulated voltages. The signal-to-noise ratio is recognized to be a powerful tool to determine whether the trace carries information of the radio pulse from a cosmic ray. In RDAS, the signal-to-noise is defined as a power quantity. In other words, it is the ratio between the squared

[6] the documentation is available at (RDAS Software, 2008)

Table 4.3: *BLS data selection- May-November 2007*

	Events
coincidence with SD	313
signal in all the three poles	234
RDAS version 217	
SNR > 14 [9]	24
Δdirection (SD - Radio) $< 20^{\circ}$	21
ΔR / R $< 25\%$	21

amplitude peak and the squared noise standard deviation. The module "ReconstructionStar" (Asch et al., 2008) allows to arbitrarily set the minimum value for the signal-to-noise which is required for the signal trace to be considered in the reconstruction.

The radio pulses processed with the different modules, which pass the first criteria selection, i.e. signal-to-noise ratio, are allowed to participate in the reconstruction of air shower parameters, such as the incoming direction.

4.2.3 Data selection

The radio events detected during 2007 with the three poles at the Balloon Launching Station (BLS) are used for the polarization analysis of section 12.2.
The data taking covers the period between May and November, and 313 events were recorded in coincidence with the Auger Surface Detector (SD). Based on the SD data, the direction, the core position, as well as the primary energy of these showers are reconstructed by CDAS (Central Data Acquisition Software) (CDAS, 2008)

Of these 313 hybrid events, recorded by both radio and SD detectors, only 234 show a signal in all the three poles. These are processed with RDAS in order to simulate the antenna detector response.
Within the RDAS modules, a first selection on the signal-to-noise ratio is applied. Only traces with SNR larger than 14 are allowed to participate in the reconstruction of the air shower parameters.
In each channel, the SNR is defined as a power quantity

$$\mathrm{SNR} = \frac{\mathrm{A}^2_{\mathrm{signal}}}{\sigma^2_{\mathrm{noise}}} \tag{4.2}$$

with $\mathrm{A}^2_{\mathrm{signal}}$, the squared signal amplitude calculated as the maximum peak of the trace, and $\sigma^2_{\mathrm{noise}}$ the squared standard deviation of the noise.
This step is done with the module ReconstructionStar and SeizeRecData respectively for the simulated and recorded events.

The radio reconstruction of the shower direction, which is based on a plane-wave fit, requires a clear detected signal in all the three poles, thus the SNR cut implies a trace

[9] in one channel per pole

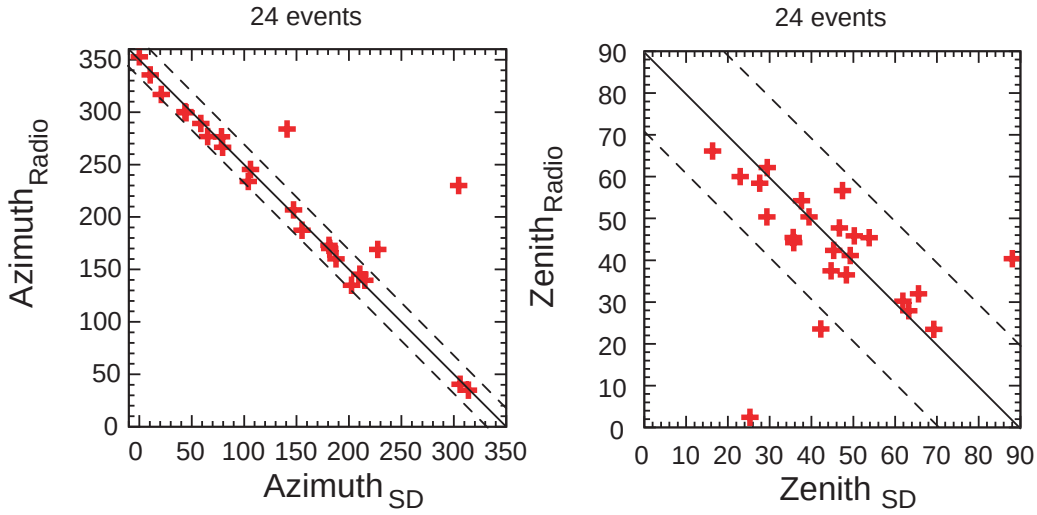

Figure 4.9: *Direct comparison of the Radio and SD direction reconstruction for the selected 21 events. The dash-lines represent a discrepancy of 20 degrees in the SD and Radio reconstructions.*

with high signal-to-noise in at least one channel per pole.
A direct comparison between the azimuth and zenith angle of the events reconstructed by both SD and radio detectors, allows to methodically reject all the radio mis-reconstructions or RFI (Radio Frequency Interference). In this way, only for 24 events of 234, the incoming direction of the showers is successfully reconstructed by RDAS.
In **fig.**4.9, the direct comparison between the values for both the zenith and the azimuth angles given by SD and RDAS is presented. In general the direction reconstructed by the radio detectors is compatible with the SD values. Nevertheless, a further cut is imposed in order to reduce the discrepancy between SD and radio to a value not larger than 20°. Three of the 24 events are, thus, removed.

Another possible selection criterion concerns the relative error on the distance R between the core of the air shower and the antenna (ground-based coordinate system). Both the values for R and the absolute error ΔR are given by SD. Since the largest value of ΔR/R is smaller than 25% no cut is required.
A total of 21 events are available for the analysis.

5 Geomagnetic contribution to the radio emission from extensive air showers

Since the interest in radio emission from cosmic ray air showers has been revived, many efforts have been made in trying to understand the radio emission mechanism.
The coherent radio emission from the time-varying electrons and positrons in the cascade, drifted by the presence of the Earth's magnetic field **B**, is considered to be the predominant contribution (Allan, 1971).

This idea is supported by the data analysis of several experiments, such as LOPES (Horneffer et al., 2007, Isar et al., 2009), CODALEMA (Ardouin et al., 2009) and the RAuger setup at the Pierre Auger Observatory (Revenu, 2010b): A dependence of the strength of the radio pulse on the geomagnetic angle α [1] was recorded. Moreover, with antennas aligned in the east-west direction, a general suppression of the events coming respectively from the south for CODALEMA and LOPES and from the north for the RAuger setup was noticed, according to the theoretical expectation for the geomagnetic emission (see also next section).

Among all the other contributions not dependent on the magnetic field **B**, thus called non-geomagnetic emissions, the predominant seems to be connected with the variation of the net charge excess in the air shower (Askaryan, 1962).
The charge excess radiation, as well as the geomagnetic emission, is linearly polarized. The main difference among these two contributions concerns the electric field vector (fig. 3.1): on the one hand, the geomagnetic emission is characterized by an electric field oriented in the same direction per each event, depending on both the direction of the Earth's magnetic field and the direction of the shower axis. On the other hand, the electric field vectors of the charge excess radiation is oriented radially from the shower axis.
The major outcome is that these two contributions add up destructively or constructively according to the observer position.

In this chapter we will focus first on the expectation for purely geomagnetic emission, in the individual electric field components, for the specific case of the LOPES and AERA experiment sites.
Moreover, further hints, which allow to treat the total detected radio pulse as predominantly due to the geomagnetic emission mechanism, will be discussed.

[1] α is the angle between the incoming direction of the shower and the magnetic field vectors. For α of 0° or 180°, the two vectors are parallel to each other, while for α of 90° the vectors are orthogonal.

5.1 The vector of the Lorentz force

The electrons and positrons created in the cosmic ray air shower, experience the presence of the Earth's magnetic field **B**. As a result, an electric current is induced in the direction perpendicular to both the shower axis and the magnetic field vector. Due to the time-varying number of charges within the development of the air shower, a total radio emission proportional to **P** $\sim$ **v** x **B**, with **v** the velocity in the direction of the shower axis, is generated (Jackson, 1975).

The normalized **P** vector is proportional to the geomagnetic angle α, precisely

$$\frac{\mid \mathbf{P} \mid}{\mid \mathbf{v} \mid \cdot \mid \mathbf{B} \mid} \sim \sin(\alpha) \tag{5.1}$$

and the whole generated radiation (linearly polarized) lies along the **P** vector direction, thus orthogonally to both the shower axis (**v**) and the magnetic field.
The individual components of the unitary vector **P** along the east-west (EW), the north-south (NS) and the vertical (VE) direction, are easily reconstructed through the cross product, generally expressed with

$$\frac{1}{\mid \mathbf{P} \mid}\begin{pmatrix} \mathrm{P_{EW}} \\ \mathrm{P_{NS}} \\ \mathrm{P_{VE}} \end{pmatrix} = \frac{1}{\mid \mathbf{P} \mid}\begin{pmatrix} \mathrm{v_{NS}}(\theta,\phi)\mathrm{B_{VE}}(\theta_\mathrm{B},\phi_\mathrm{B}) - & \mathrm{v_{VE}}(\theta,\phi)\mathrm{B_{NS}}(\theta_\mathrm{B},\phi_\mathrm{B}) \\ \mathrm{v_{VE}}(\theta,\phi)\mathrm{B_{EW}}(\theta_\mathrm{B},\phi_\mathrm{B}) - & \mathrm{v_{EW}}(\theta,\phi)\mathrm{B_{VE}}(\theta_\mathrm{B},\phi_\mathrm{B}) \\ \mathrm{v_{EW}}(\theta,\phi)\mathrm{B_{NS}}(\theta_\mathrm{B},\phi_\mathrm{B}) - & \mathrm{v_{NS}}(\theta,\phi)\mathrm{B_{EW}}(\theta_\mathrm{B},\phi_\mathrm{B}) \end{pmatrix} \tag{5.2}$$

where the azimuth ϕ and the zenith θ define the direction of the incoming shower, while ϕ_B and θ_B give the direction of the field **B**. This is the general definition, which does not imply any particular axis coordinate system.
For the specific case of the LOPES coordinate system where θ = θ_L, ϕ = ϕ_L = 0° indicates the shower coming from the north and ϕ_L = 90° from the east, eq.5.2 becomes

$$\frac{1}{\mid \mathbf{P} \mid}\begin{pmatrix} \cos(\theta_\mathrm{L})\sin(\theta_\mathrm{B}) - \sin(\theta_\mathrm{L})\cos(\phi_\mathrm{L}) \\ \sin(\theta_\mathrm{L})\sin(\phi_\mathrm{L})\cos(\theta_\mathrm{B}) \\ -\sin(\theta_\mathrm{L})\sin(\phi_\mathrm{L})\sin(\theta_\mathrm{B}) \end{pmatrix} \tag{5.3}$$

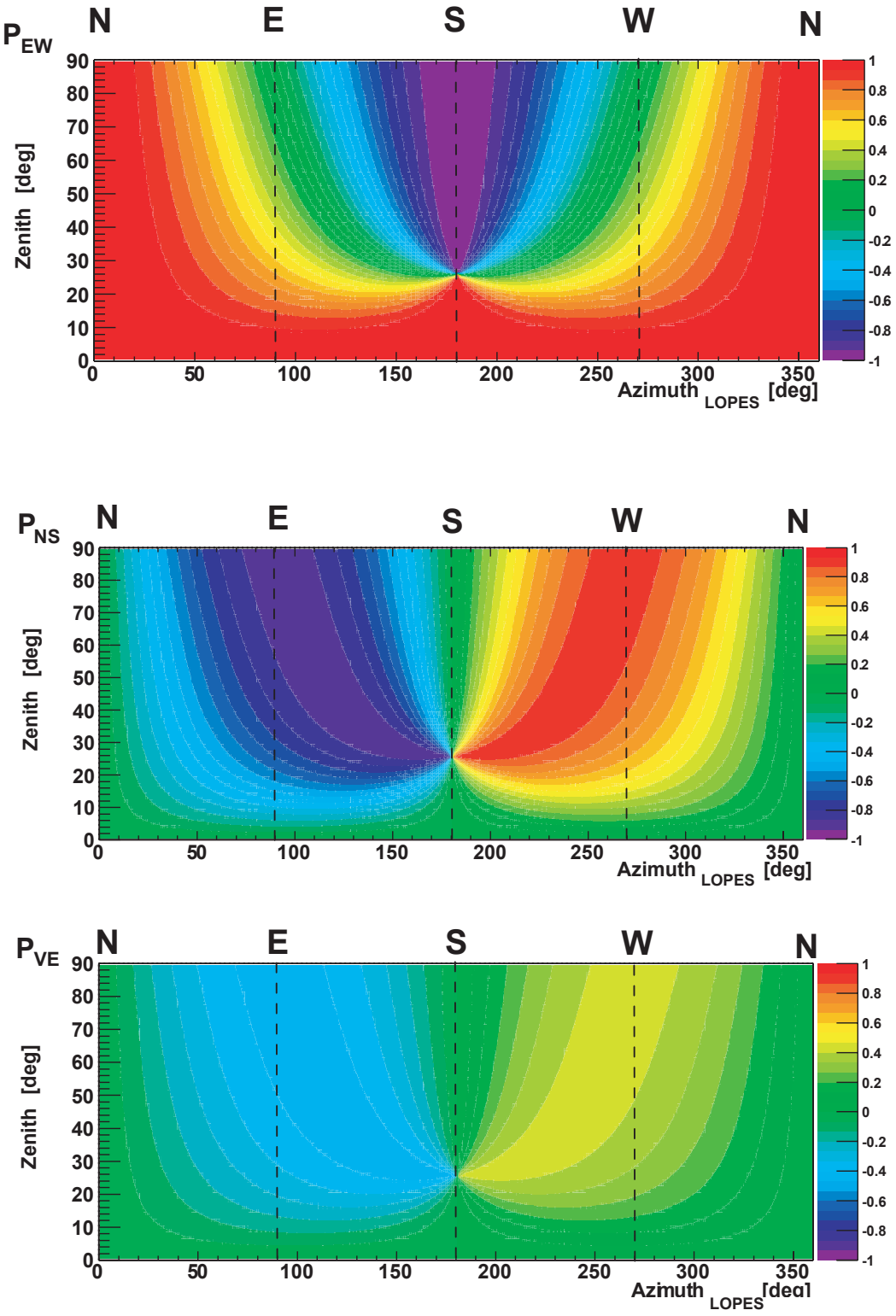

Figure 5.1: ***P*** *vector components calculated in the east-west, north-south and vertical direction, for the magnetic field information of the LOPES experiment site. For the LOPES coordinate system of the azimuth angle 0° = coming from the north, 90° = coming from the east.*

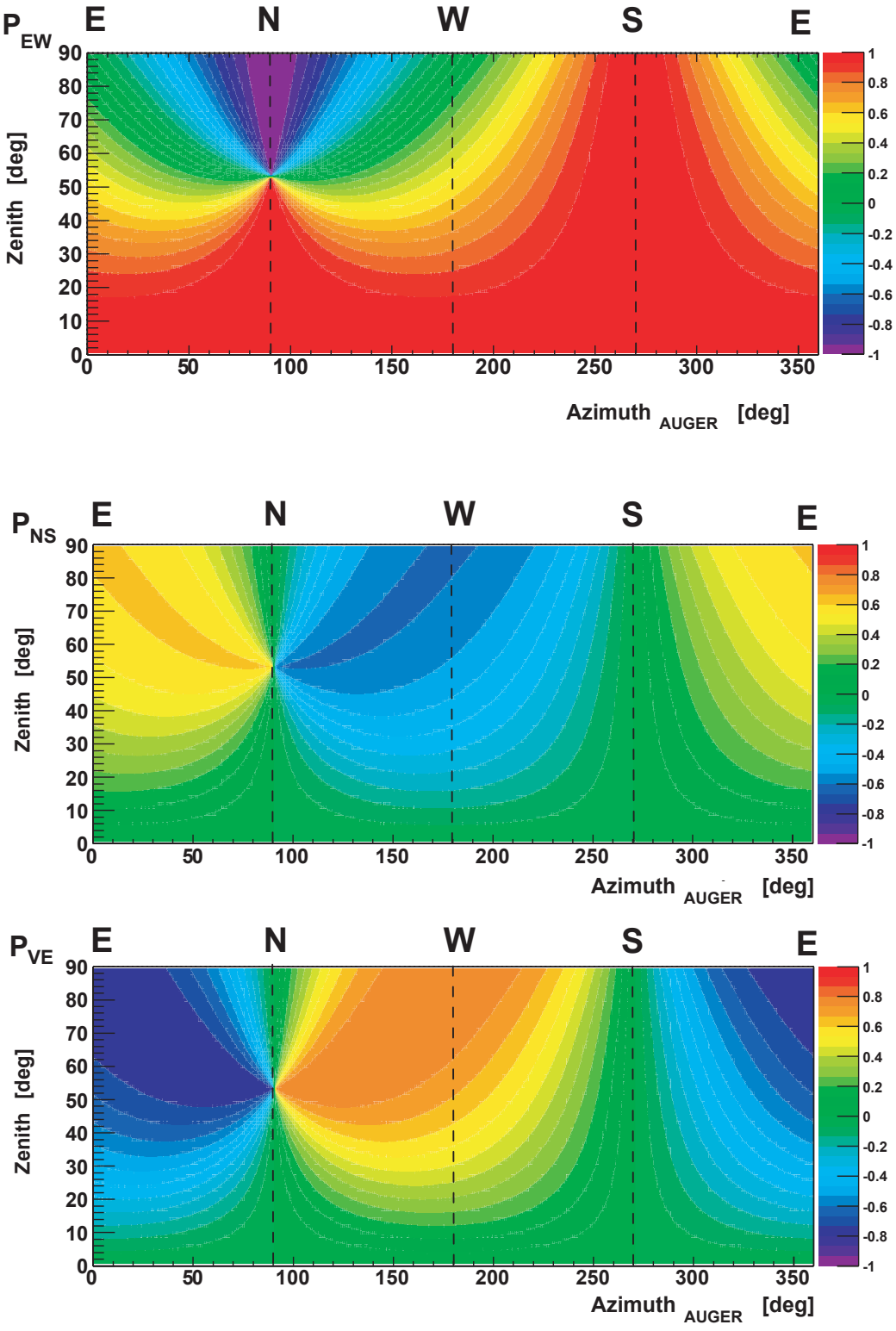

Figure 5.2: *Same as in* ***fig.****5.1, but for the Malargüe site. For the Auger coordinate system of the azimuth angle 0° = coming from the east, 90° = coming from the north.*

The Earth's magnetic field is considered specifically for the LOPES experiment site (0.45 gauss intensity, $\sim$ 25 degrees inclination, pointing downwards to the north) and for the Pierre Auger Observatory site (0.23 gauss intensity, $\sim$ 53 degrees inclination, pointing upwards to the north)(NOAA, 2011).
The **P** vector components are calculated in **fig.**5.1 and **fig.**5.2 with the direction of the incoming shower covering the complete sky, thus varying the shower zenith angle between 0 degrees (vertical shower) and 90 degrees (shower coming from the horizon), and the azimuth between 0 and 360 degrees.

Taking the case of the LOPES site as example (**fig.**5.1), one can immediately notice that for showers coming from the north (0 and 360 degree in the LOPES coordinate system) **P** is completely oriented in the EW direction, independent of the zenith angle. For events coming from the south (180 degrees) a flip in the sign for the EW component occurs when the shower direction is parallel to the magnetic field direction ($\sim$ 25 degrees). Moreover, in that point all the three components of the **P** vanish since the direction of the shower becomes parallel to the magnetic field.
Similar features are shown also in **fig.** 5.2. According to the orientation of the geomagnetic field in the southern hemisphere, showers coming from the south (270 degrees in the Auger coordinate system) are characterized by a **P** vector totally oriented in the EW direction, independent of the zenith angle. A flip in the sign for the EW component is shown in the opposite incoming direction (north in the specific case of Auger), i.e. when the incoming direction is parallel to the geomagnetic field vector. The **P** contribution vanishes for showers oriented in the same direction of the geomagnetic field (showers coming from the north, with zenith angle of 53 degrees). It is interesting to notice how the vertical component of the **P**, which is expected to be quite weak in the LOPES site due to the the magnetic field in Karlsruhe mainly oriented in the vertical direction, becomes of the same magnitude as the NS component for the AERA site (5.2).

5.2 Geomagnetic contribution in the radio data

A flip in the sign for each individual **P** vector component is clearly visible in **fig.**5.1 and **fig.**5.2. This is dependent on both the geomagnetic field vector and the incoming direction of the event.
The agreement in the first order between radio measurements and the predicted **P** behavior (Horneffer et al., 2007, Isar et al., 2009, Ardouin et al., 2009, Revenu, 2010b) implies the expectation of a sign dependence of the unlimited bandwidth electric field components, i.e. the unfiltered radio pulse detected in the west (EW), north (NS) and vertical (VE) directions.
In **fig.**5.3 an unfiltered radio pulse is taken as example from a REAS3 simulated event. The component in the EW direction of the total radio pulse shows a positive sign, while in the NS and VE directions the pulse has a negative sign according to the specific arrival direction of the event.
Nevertheless, there is no clear motivation to suppose that the sign is preserved in the pass-band filtered signal. In **fig.** 5.4 the signal in the EW components of **fig.**5.3 is filtered with the ideal rectangular filter 43-74 MHz.

CODALEMA claimed a correlation between the incoming direction of the cosmic ray primaries and the sign of the radio signal, i.e. 23-83 MHz pass-band filtered pulses,

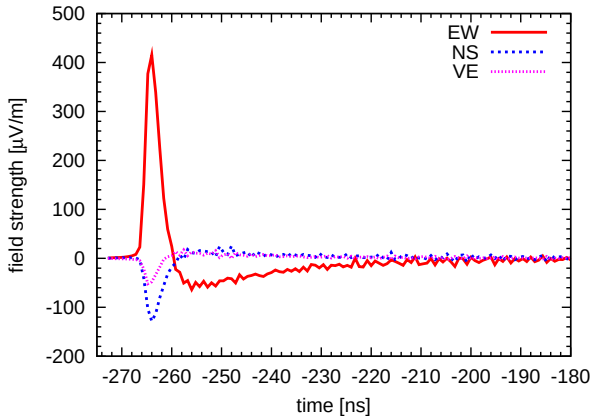

Figure 5.3: *REAS3 unfiltered pulse. The trace in the EW channel shows a positive sign, while in the NS and vertical channels the sign is negative.*

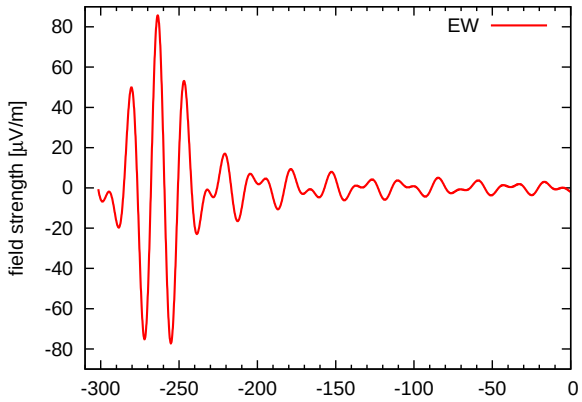

Figure 5.4: *The signal in the EW channel of* ***fig.****5.3 is filtered with an ideal rectangular filter (43-76 MHz)*

recorded in the EW and NS directions (Ardouin et al., 2009, Riviere et al., 2009). Namely, showers coming from the north generally have positive pulses while signals from the south are generally negative.

A similar analysis on the LOPES measurements is proposed in Appendix A: Chapter.12 - **"Polarity of the signal"**.
With this investigation a clear suppression of the signal coming from the south is seen for the LOPES detected events. This reconfirms, once again, the geomagnetic emission mechanism as the main radio emission process.
Despite no obvious reason exists for a signal sign preservation in the filtered pulse, also the LOPES data seems to confirm the CODALEMA results concerning a dependence of the sign on the arrival direction of the events: According to the specific "negative regions" of **fig.**12.1, LOPES measurements present *negative* detected events with a significance double than for the *positive* events. This result is confirmed in both the east-west and north-south detections. However, with a stronger cut on the event selection the

statistics is drastically reduced, and no conclusive statement about the signal-sign in the LOPES data is possible.

Further proofs concerning the geomagnetic origin of the radio emission as the predominant contribution are discussed in the second part of Appendix A: section 12.2.
A recent analysis of LOPES data has already shown interesting correlations of the radio pulse polarization with air shower parameters, in particular with the shower azimuth angle (Isar, 2010). Taking into account the LOPES results, a similar investigation is proposed, using one of the first radio data set collected within the Pierre Auger Observatory (BLS data - cf. section 4.2.3).

Despite a general geomagnetic-like trend for both data and REAS3 simulations, the discrepancy with the **P** vector predictions becomes larger for a specific incoming direction, namely, when a pure geomagnetic component is expected to be weak in one of the two channels. In other words, for events coming from the south (small or null P_{NS} signal) and from the north (small or null P_{EW} signal), the charge excess contribution is of the same order of magnitude of the geomagnetic one, and it can not be any longer ignored.

The findings discussed above on measurements of both LOPES and BLS setup confirm that using the **P** vector as a first order approximation for the radio detected pulse does not lead to large deviations. This statement remains valid as long as the direction of the shower is considered. A careful treatment for those events with arrival direction from the north (or from the south according to the polarization taken into account) and the inclination of the magnetic field must be applied.

5.3 Outlook

The expectation for a pure geomagnetic contribution to the radio emission (**P** vector), as well as a direct comparison with experimental data are discussed.
The **P** vector can be considered a first order approximation for the radio detected pulses. Meanwhile, for specific arrival directions where the charge excess influence to the radio emission is expected to be of the same order of the geomagnetic contribution, a careful treatment of the events is necessary.
Such conclusions will have an influence on the radio pulse amplitude normalization in the slope method analysis (cf. Chapter 7). As next step, an accurate study on the LDF fit function is mandatory and it is developed in the following chapter.

6 The lateral distribution function

The lateral distribution function (LDF) describes the variation of the radio electric field as a function of the distance from the shower axis.
An accurate analysis of the radio LDF provides several advantages. First of all, it allows a better understanding and a precise modeling of the radio emission from the air showers. Second, it gives a hint for the spacing of future radio antenna array experiments. Moreover, it provides information about the energy and the mass of the primary cosmic ray, because its slope is sensitive to the depth of the shower maximum (Huege et al. (2008) and cf. section 3.3).

In relation to previous comparisons with the outdated REAS2 code, a recently improved, but still not complete, agreement in the lateral distribution function between LOPES events and their REAS3 simulations is discussed in Ludwig (2011).
This improvement is due to two main reasons: on the one hand, the latest version of the REAS code (REAS3), released in 2010, is more complete and it potentially includes the total complexity of the radio emission from cosmic ray air showers (Ludwig and Huege, 2011b).
On the other hand, the experimental data analysis has been refined. This is mainly connected to the new noise treatment, which corrects the systematic bias introduced by the noise and affects the slope and the height of the lateral distribution function (Schröder et al., 2010b).

The investigation of the depth of the shower maximum through the slope of the radio LDF (slope method) requires the identification of an appropriate function which properly describes the radio LDF.
For the LOPES experiment, an exponential function has been used so far. Nevertheless, there are clear hints that, the radio lateral distribution is more complex. Indeed, a flattening towards the shower core was experimentally observed in Apel et al. (2010a). Moreover, mainly due to the charge excess contribution, the radio amplitude should depend also on the azimuthal position of the observer (antenna) (de Vries et al., 2010, Ludwig and Huege, 2011b).
As a consequence, the radio LDF may be better described by a multidimensional (more than 1 spatial dimension) function, which would take into account the azimuthal position of observer with regard to the shower axis.

In the next part, based on an analysis on both REAS3 simulations and LOPES data, it will be discussed why an exponential function is a good approximation for the distance range probed by the LOPES experiment, i.e. < 200 m.

6.1 Lateral distribution function of LOPES data

For each individual LOPES antenna, the maximum instantaneous amplitude ϵ is used to quantify the radio pulse (see also section 4.1.2, ***The LDF reconstruction***).
ϵ is taken at the maximum of the Hilbert envelope (Schröder et al., 2010b) of the up-sampled electric field strength, closest to the pulse time known from the interferometric cross-correlation analysis.

The uncertainty on the radio pulse ($\Delta\epsilon$) is calculated as the root sum of squared uncertainties, due to the noise and the calibration uncertainty of $\lesssim 5\%$ (Schröder, 2010). Three types of error concerning the amplitude calibration are not considered in the LDF analysis (cf. section 4.1.2): first the one related to the absolute scale of the electric field strength (34%)(Nehls, 2008), which is a systematic uncertainty of the emitted reference signal used during the calibration campaign; second, the error connected to the simulated antenna gain pattern, used for the evaluation of the calibrated measurements (7.5%) (Nehls, 2008) and finally the error due to the environmental effects (4.5%) (Schroeder, 2011). The last two are not taken into account for the lateral distribution analysis of the single event since their effects occur on a time scale of minimum one hour. These uncertainties must be included in the comparison of the LOPES data with simulations or other experiment results, but can be omitted in the analysis of a single event LDF, since all the antennas are affected in the same way.

The distance (d) of the antenna to the shower axis is calculated in the shower-plain coordinate system, thus it is the projection on the shower plain of the lateral distance antenna to core position.
The uncertainty on d depends not only on the uncertainty of the core position given by KASCADE (4 m) but also on the geometry reconstruction accuracy ($<$0.3 degrees) (Antoni et al., 2003b).
The lateral distribution of the LOPES data is fitted with an exponential function

$$\epsilon(d) = \epsilon_{100} \cdot \exp\left(-\frac{d - 100\mathrm{m}}{R_0}\right) \tag{6.1}$$

with the two free parameters, ϵ_{100}, which is the amplitude of the electric field at the distance of 100 m (d_{100}) from the shower axis, and R_0, the slope parameter.
The fitting procedure is optimized using a χ^2 minimization with ROOT 5.20 [1].

Several reasons supported the idea to fit the data at 100 m and not at 0 m, as it was done in the previous LOPES analysis (Apel et al., 2010a): First of all, 100 m is roughly the mean lateral distance of a typical LOPES event. Consequently the ϵ_{100} is close to measured amplitude values and not derived on extrapolation. Second, the LDF fit at 0 m (d_0) led to a correlation between ϵ_0 and R_0 parameters. With the LDF fit at 100 m (d_{100}) the ϵ_{100} - R_0 correlation seems strongly reduced (Schröder, 2010).
Moreover, the resulting values for ϵ_{100} are in general more precise, as it is shown in **fig.**6.1 where the relative errors on the amplitude parameter for the same events fitted respectively at 100 m and at 0 m are compared. On the other side the variable R_0 shows no qualitative difference (see **fig.**6.2). In both the figures the continuous line represents the one-by-one correspondence.

[1] http://root.cern.ch

The slope parameter R_0 for the Selection2 is presented in **fig.**6.5, with a mean value of 168 m and a standard deviation of the distribution of 93 m.

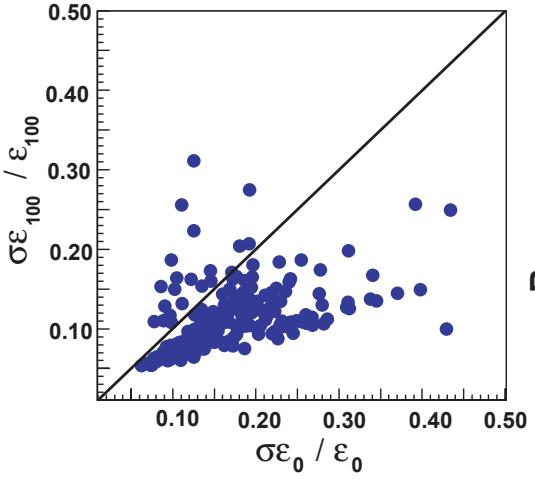

Figure 6.1: *Comparison of the amplitude parameter uncertainty for the exponential fit computed at 0 m and at 100 m*

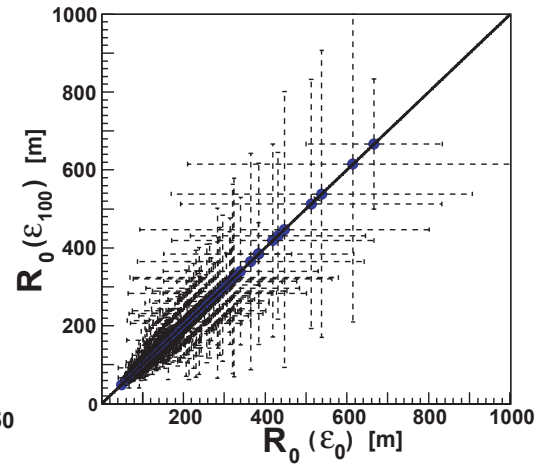

Figure 6.2: *The R_0 parameter does not depend on whether the fit is evaluated at 0 m or at 100 m*

.

The curvature k of a radio wave-front indirectly gives a hint about the primary types: protons interact deeper in the atmosphere, i.e. closer to the observer, compared to iron-like cosmic rays. This results in a curvature k of the radio wave-front larger for proton than for iron-initiated showers. Defining $r \sim 1/k$ the curvature radius, proton-showers have a curvature radius r smaller than iron-showers.

A first indication of the mass composition signature in the radio data can be pointed out by looking at the correlation between the exponential index of the lateral distribution function (i.e. R_0) and the curvature radius r of the shower front. Indeed, a source further away from the observer (iron-like air showers) implies a slowly decreasing lateral function, i.e. large values of R_0. In contrast, smaller values of R_0 would indicate a shorter distance between the radio source and the observer, favoring proton initiated showers.

The curvature radius is reconstructed for each event by the CR-tool pipeline (cf. section 4.1.2), by using a spherical-wave fit.

Unfortunately, the shown relation is quite faint (**fig.**6.3), and this could be related to: the large uncertainty on R_0, the inaccuracy in the curvature radius reconstruction with the LOPES CR-pipeline, and the assumption of a spherical shape of the radio wavefront.

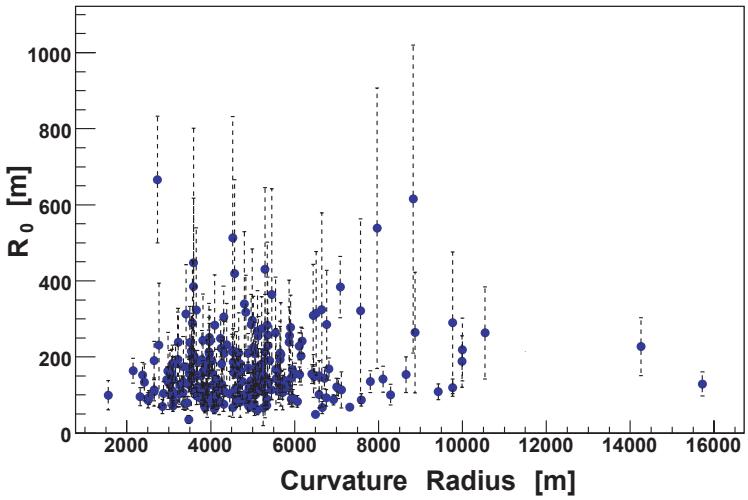

Figure 6.3: *No significant dependence of the LDF slope on the curvature radius of a spherical wave-front, reconstructed with the CR-tool pipeline. (Selection2)*

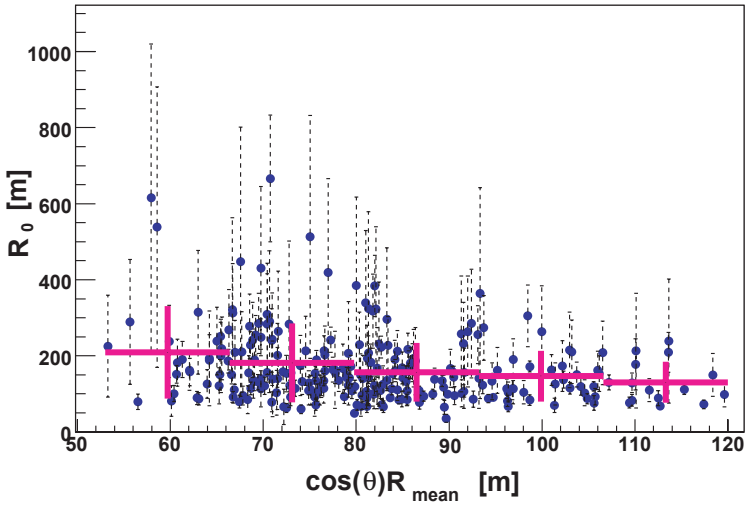

Figure 6.4: *The slope of the LDF tends to increase in relation to the inclination of the shower and the distance to the shower axis. (Selection2)*

The R_0 dependence on the inclination of the shower, expected due to a pure geometrical effect (cf. Chapter 3) is shown in **fig.**6.4.
As already seen in Apel et al. (2010a), the correlation between R_0 and the zenith angle combined with the mean lateral distance R_{mean}, emphasizes that flatter LDF slopes (i.e. larger values for R_0) are expected - independent of the primary particle type - for highly inclined showers and when the radio pulse is detected close to the core position.
By definition, the slope of an exponential function remains constant with increasing the

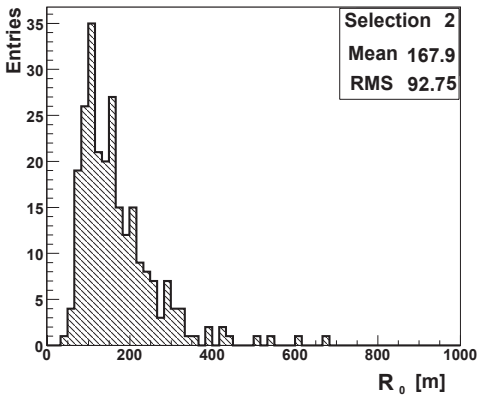

Figure 6.5: *The slope parameter R_0 for the LOPES events in Selection2*
.

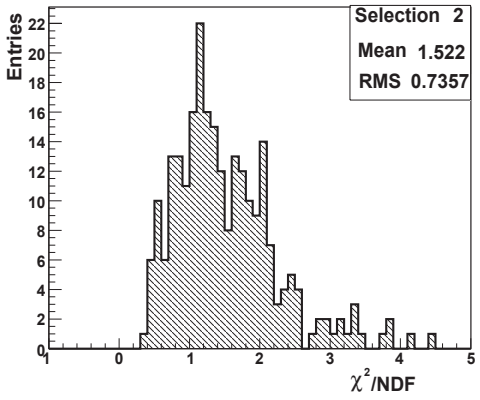

Figure 6.6: *χ^2 values for the LDF fit, when the exponential function 6.1 is used. (Selection2)*

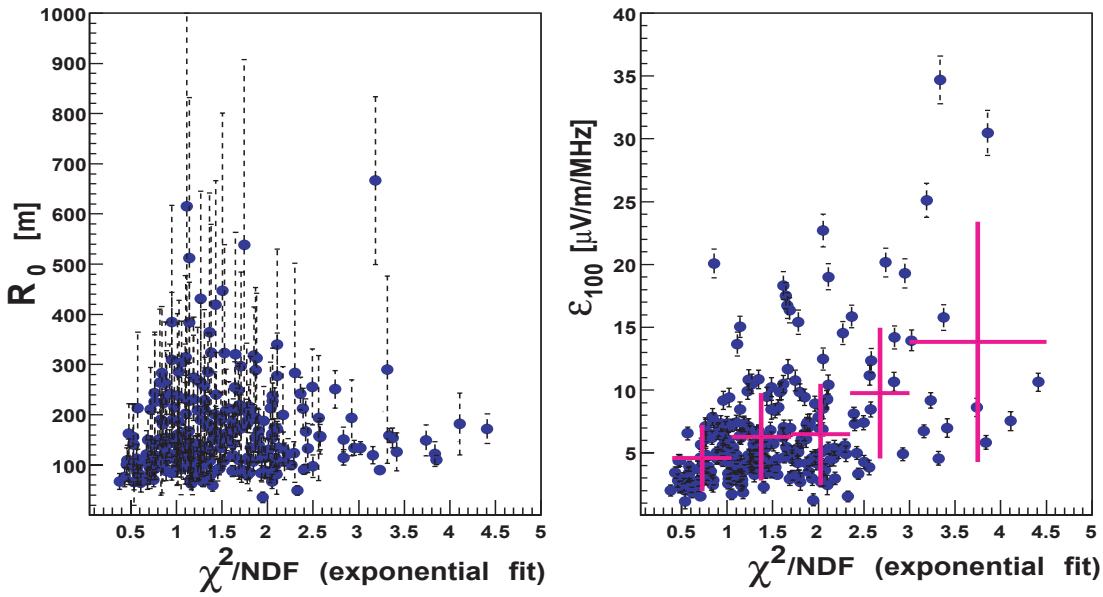

Figure 6.7: *Left site: The χ^2 values show no clear dependence with the R_0 parameter. Right side: The goodness of the LDF fit decreases at larger values of the ϵ_{100} parameter, i.e. for recorded radio pulses far from the noise level. (Selection2)*

distance from the origin.
This is one clear hint that the detected LDF needs a more complex than an exponential function to be properly described.

The exponential fit applied to the LOPES LDF shows a mean of the reduced χ^2 of 1.5 (**fig.**6.6), which is a quite acceptable value; at the first glance, this would suggest that the exponential function describes well enough the behavior of the detected electric

field amplitudes for the LOPES data.
No clear tendency appears between the χ^2 and the R_0 parameter **fig.**6.7 (left side).
In contrast, a correlation with the amplitude parameter ϵ_{100} (right side) indicates how the goodness of the fit decreases by going far from the noise level with larger values of ϵ_{100}. Further investigation on the quality of the fit are, thus, required.

Hints in the recorded data of the LOPES experiment - e.g. the flattening of the LDF close to the shower core and the large χ^2 values for events far from the noise level - suggest that the radio lateral distribution is a complex function. To argue whether the exponential function can be considered a good approximation to describe the LOPES LDF, a quantitative analysis on the residuals of the lateral fit is discussed in the next section.

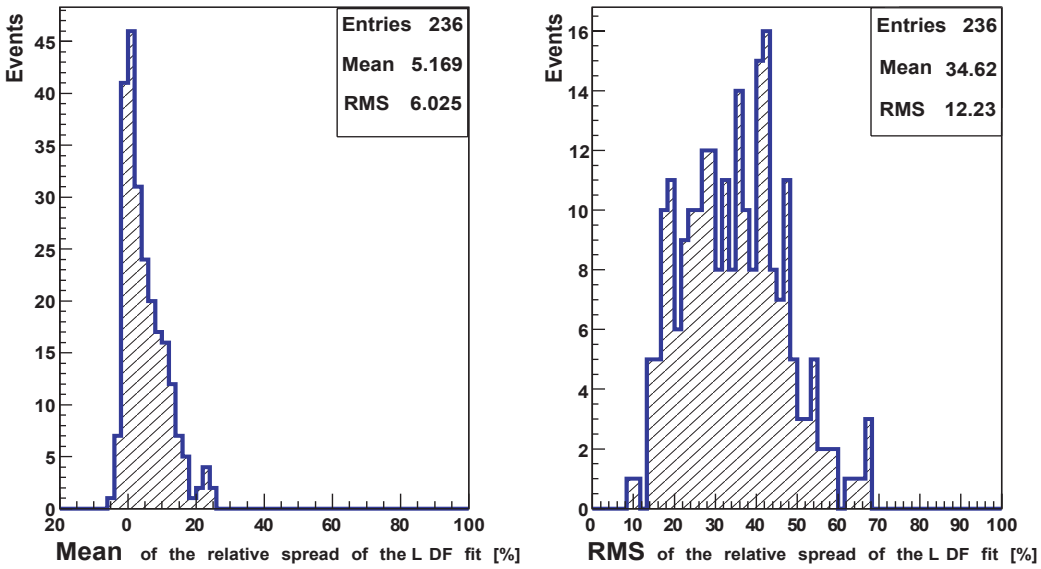

Figure 6.8: *Mean and RMS values of the dispersion around the exponential fit of the radio LDFs. The whole LOPES selection (Selection2) is considered.*

6.1.1 Residuals analysis [2]

A statistical analysis on the LDF residuals is presented in the following, in order to judge whether the exponential function is a sufficient approximation to describe the radio lateral distribution of individual LOPES events.

For each event, the relative deviation between the radio pulse amplitude in the antenna, $\epsilon(d)$, and the fitted exponential function at the same distance d, $\epsilon_{\rm fit}(d)$, is calculated: $\epsilon(d)$-$\epsilon_{\rm fit}(d)$/$\epsilon_{\rm fit}(d)$.
The distribution of these relative deviations is examined in order to evaluate the goodness of the fit. Negative values of the relative deviation represent the points "under" the fit.
A distribution not centered around zero, but with a large value of the Mean, generally indicates a systematic shift of the data from the fit. In this case, the exponential fit most probably failed for that specific event.
On the other side, a large value for the RMS of the distribution, is an indication of the spread of the points around the fitted function.
Both the Mean and the RMS of this distribution are taken for each event. The Mean and RMS values for the whole LOPES selection (Selection2) are shown in **fig.**6.8.

In general, by looking at the Mean quantity, a systematic shift of the data points from the exponential fit is noticed, with an average value for the whole selection of 5 $\%$ (**fig.** 6.8, left part). It must be stressed that this Mean value different from zero does not imply a failure of the fitting procedure with the χ^2 minimization. For this investigation,

[2] Paper in preparation: (Apel,W.D. and others (LOPES Coll.), *Radio lateral distribution of cosmic ray air showers - a comparison of LOPES measurements and REAS3 simulations)*

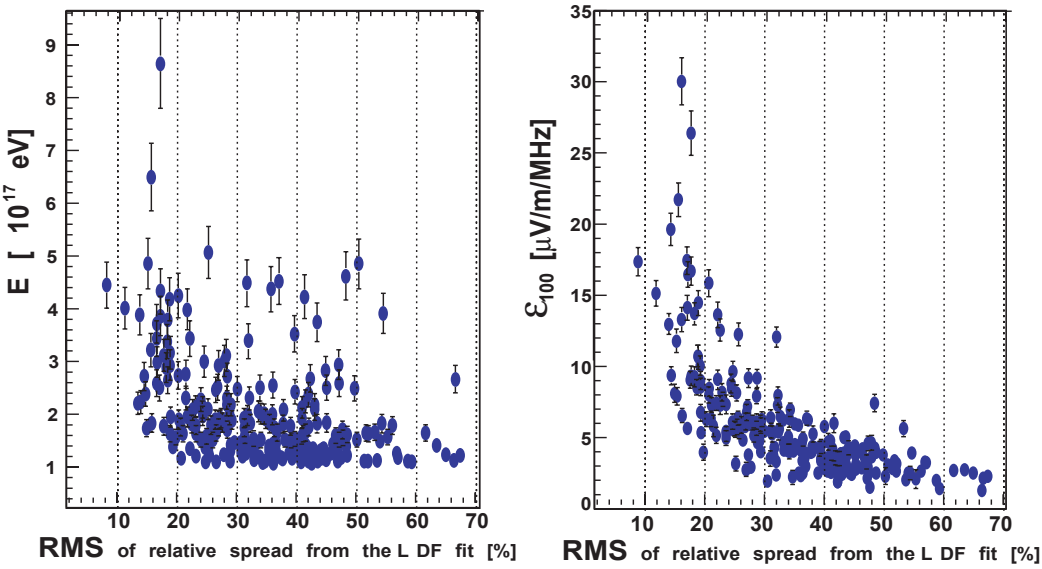

Figure 6.9: *A minimum value of the (RMS) dispersion of ∼14 % is found even at high signal-to-noise ratio, i.e. large ϵ_{100} and large primary energy. (Selection2)*

in fact, the uncertainty on the amplitude is not considered and, moreover, the relative and not absolute distance point–fit is taken into account. This 5 % value is a first index to quantitatively judge the goodness of the exponential fit, and it is of the same order of magnitude of the uncertainty on the recorded amplitude.

Concerning the RMS, a mean value of 35 % in the complete selection is obtained, with a tail of the distribution that reaches 70 % (**fig.** 6.8, right part).
Also for the RMS it is important to notice that in the computation of the relative dispersion point-fit, the uncertainty on the amplitude $\epsilon_{\text{fit}}(d)$ is not taken into account, which could partially explain the large value for the RMS.
The expected value for the average RMS is of the same order as the calibration uncertainty for the LOPES data, thus around 5 %. Nevertheless, the RMS does not fall below a certain minimum value ($\sim$ 14 %) even for the events far from the noise level, thus with higher primary energies (left side of the figure 6.9) and larger amplitude parameter ϵ_{100} (right side of the figure).

Both the Mean (5 %) and the minimum RMS ($\sim$ 14 %) are quite different from the values presented in (Apel et al., 2012b), which are respectively of 1.5 % and 10 %, stressing quite significant dependence on the selection criteria applied for the LOPES data. For the paper, in fact, a higher signal-to-noise ratio in the antennas and less restrictive cuts on the LDF fitting parameters were required.
The minimum RMS limit ($\sim$ 14 %) is an explanation of the large χ^2 values discussed above: even far from the noise level, and for same distances from the shower axis but at different azimuthal angles, the electric field amplitudes recorded with the antennas

varies considerably. This implies an intrinsic difficulty in fitting the lateral distribution function with a one-spatial dimension function.
This can arise from the influence of the charge excess contribution to the air shower radio emission (cf. Chapter 3).
A similar effect was seen in the data of the Nançay Decametric Array experiment, where an inhomogeneity of the electric field strength was detected at small scale distance ($<$ 100 m) (Lecacheux and Bellètoile, 2009).

The unexpected large RMS values are a further indication that the one spatial dimensional (1D) fit is not enough to well describe the radio lateral behavior, and, therefore, the investigation of a possible multidimensional fit must be seriously taken into account. Nevertheless, the large RMS would only partially affect the analysis on the slope method (cf. Chapter 7). Indeed, the antenna spacing of the LOPES experiment allows to average out this effect, and the slope of the radio LDF is only marginally influenced.
A comparison with the expectation from the REAS3 simulated LDF concerning the Mean and the RMS of the relative dispersion are discussed in the following section.

6.2 Lateral distribution function of REAS3 simulations - exponential fit

The lateral distribution fit will be investigated in this section with REAS3 simulations of the LOPES events, mainly for two reasons: the simulations are easier to handle since no uncertainty is considered neither in the radio pulse nor in the antenna-core position distance, and the agreement between detected and simulated LDF for the LOPES events is improved (Ludwig, 2011).

For each event in the LOPES selection (Selection2), REAS3 simulations have been performed (for detail please see Chapter 8). The simulated radio pulse amplitude at each antenna position, $\epsilon_{\mathrm{SIM}}(d)$, is determined as the maximum of the simulated electric field strength in the east-west polarization, divided by the effective LOPES bandwidth (31 MHz) (cf. section 4.1.1).
Since a systematic difference in the slope is expected between heavier and lighter primaries, the LDF of events both simulated as proton and iron initiated air showers will be separately treated.

As an example of a typical behavior, a LOPES event with a primary energy of $1.2{\cdot}10^{17}$ eV, zenith angle $\theta \sim 23$ degrees and azimuthal angle $\phi_{\mathrm{LOPES}} \sim 1$ degrees reconstructed by KASCADE (event coming from the north), is presented in **fig.**6.10, left side, as proton and as iron initiated air showers; the lateral distribution is, again, fitted with the exponential function of eq.6.1.
The result of the reduced χ^2 is smaller than 0.2 in both cases, suggesting the correctness of such a function in describing the simulated radio lateral distribution.
An analysis on the residuals for the REAS3 simulated lateral distributions follows.

6.2.1 Residuals analysis for the REAS3 simulations

The approach of the residual analysis is used also for the REAS3 simulations. As a first step, a visual interpretation is performed, using the absolute distance point–fit. In a sec-

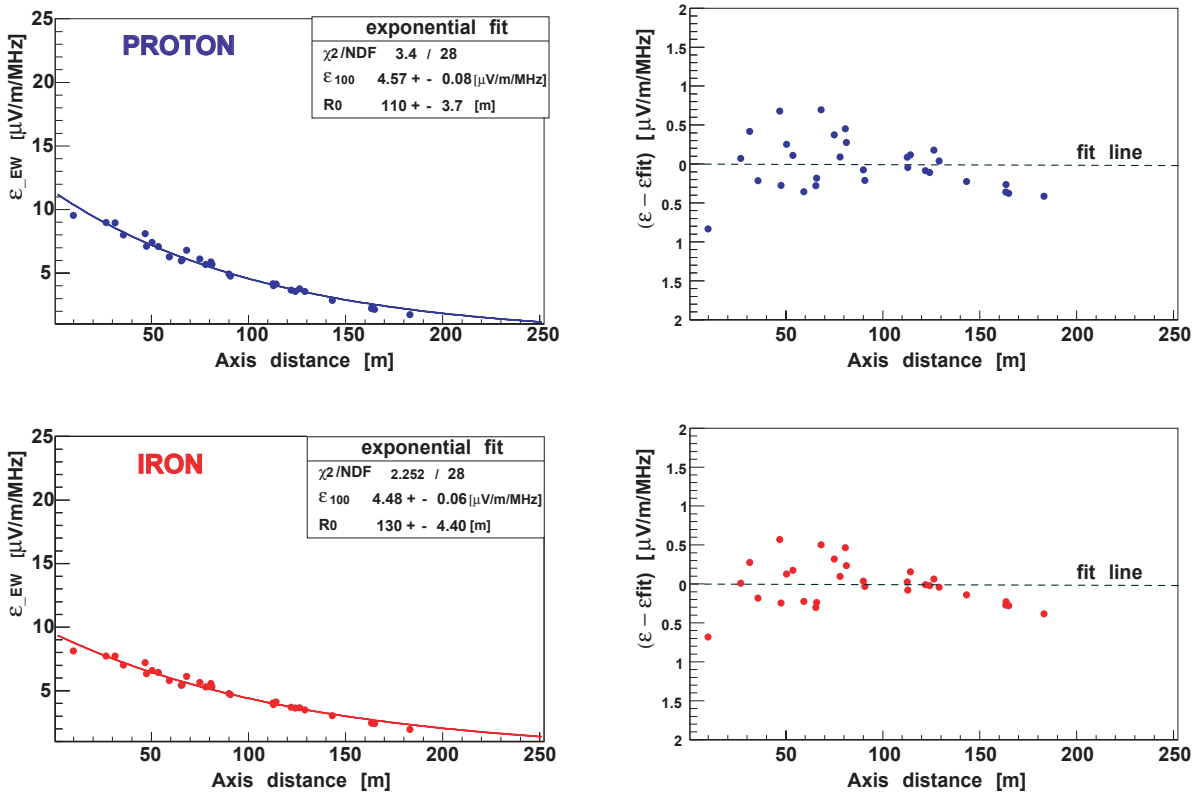

Figure 6.10: *Exponential fit of the LDF for a typical LOPES event simulated as proton (TOP) and as iron (BOTTOM) primary. On the right part a visualization of the absolute residuals distributions.*

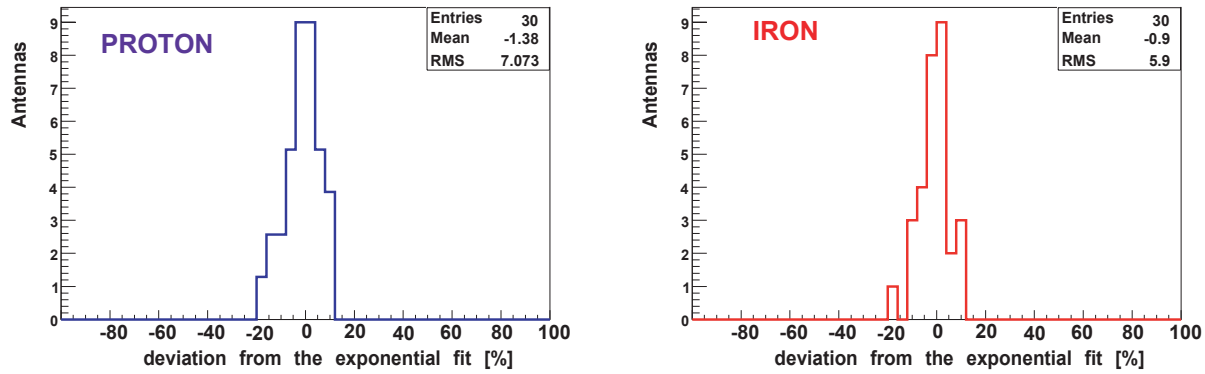

Figure 6.11: *Distributions for the relative residuals of the single event of* ***fig.****6.10 taken as example.*

ond step, the same investigation done for the LOPES LDF is performed, thus analyzing the relative distance point-fit and the Mean and RMS values of the distributions.

The absolute vertical distance (residual) of each point from the regression line, i.e.

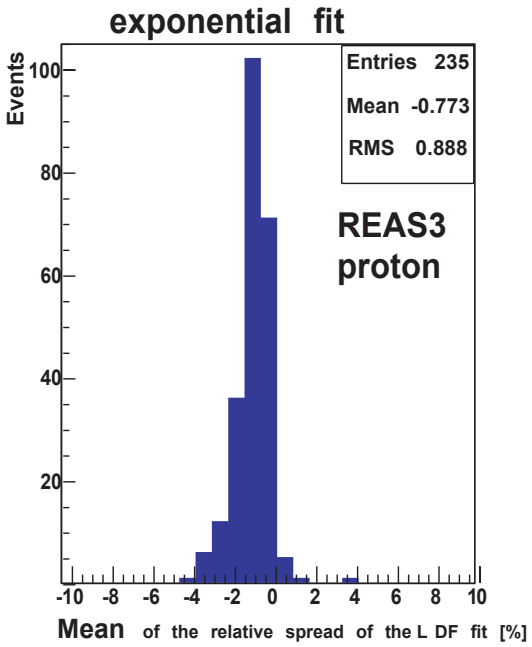

Figure 6.12: *Systematic shift from the LDF fit, for the whole set of simulations (Selection2). The events are simulated as proton primaries. The exponential function is used to fit the LDFs*
.

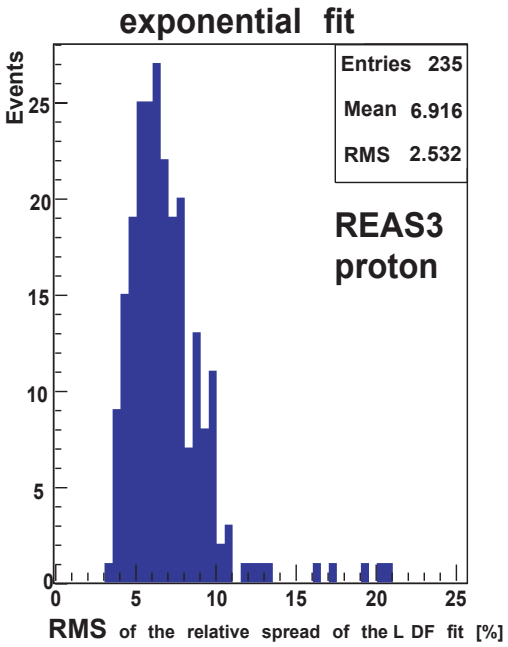

Figure 6.13: *Relative spread around the LDF fit (i.e. RMS of **fig.** 6.11), for the whole set of simulations of Selection2. The events are simulated as proton primaries. The exponential function is used to fit the LDFs*

$\epsilon(d)$ - $\epsilon_{\rm fit}(d)$ is considered. Plotting this quantity directly provides a visual interpretation of the goodness of the fit. Assuming that the chosen fitting function is the correct model to interpret the data, the residuals should approximate the numerical uncertainties, so they should appear to behave randomly. On the other side, if the residuals display a systematic pattern, it is a clear sign that the model fits the data poorly. For a proper visual interpretation the absolute and not the relative distance point-line is considered.

By looking at a typical event taken as example in **fig.**6.10, right part, a random behavior of the residuals is shown only in the distance range 30-200 m.
The systematic pattern for distances smaller than 30 m indicates that also REAS3 simulations predict a flattening of the LDF slope close to the shower axis, similar to what the LOPES data show (Apel et al. (2010a) and **fig.**6.4)

A visual interpretation of the residual is not sufficient to judge the exponential fit. In consistency with the analysis done for the experimental LDF in section 6.1.1, a statistical investigation on the relative dispersion around the LDF fit is presented.
The relative deviation point–fit $\epsilon(d)$ - $\epsilon_{\rm fit}(d)/\epsilon_{\rm fit}(d)$ is computed for each antenna distance d and its distribution is considered, as presented in **fig.**6.11 for the typical event taken as example.

For both proton and iron simulations of the example-event, the value of the Mean of

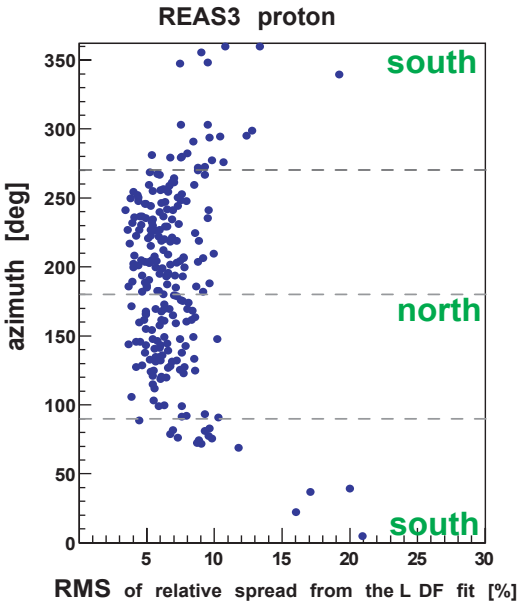

Figure 6.14: *Events from the south have the largest values of the weighted dispersion around the LDF fit. No noise is included in REAS3 simulations.*

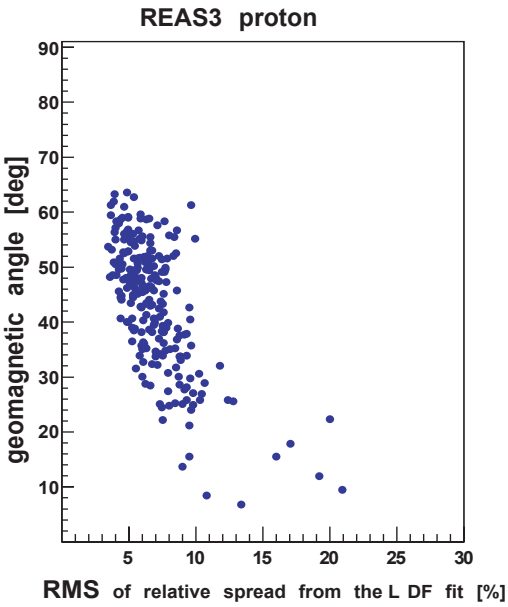

Figure 6.15: *Events with smaller geomagnetic angle have the largest values of the weighted dispersion around the LDF fit.*

the distribution, respectively of $\sim$ -1.38 % and -0.9 %, quantifies the small systematic shift of the points from the exponential behavior. Again, the negative values are due to the points "under" the fit.
Since iron and proton generated events differ only slightly, later on, the plots for the proton-events are picked as example.
By looking at the whole selection, shown in **fig.**6.12 only for proton, the average Mean values of the relative deviation distributions for proton and iron are respectively of -0.8 % and -0.6 %.
One can affirm that the systematic deviation from the fit for each simulated event is small, and the exponential function can be considered good enough to describe the data for the distance range of individual LOPES events.

Of big interest is to look at the RMS values for the complete selection (**fig.**6.13) with the aim to compare with the values for the LOPES data. For each individual REAS3 event the RMS indicates the intrinsic spread of the electric field strength which is, in this case, not affected at all by the noise.
The magnitude of RMS is, thus, an indicator of the variations of the radio pulse amplitude in the individual antennas, which is mainly due to the influence of the charge excess contribution (cf. Chapter 3).
Evidence which supports this idea is shown in **fig.**6.14 and **fig.**6.15; in **fig.**6.14 it appears clearly that the large values for the RMS are due to events coming from the south (0 and 360 degrees in the REAS coordinates system (Huege, 2011)). Indeed, for these events,

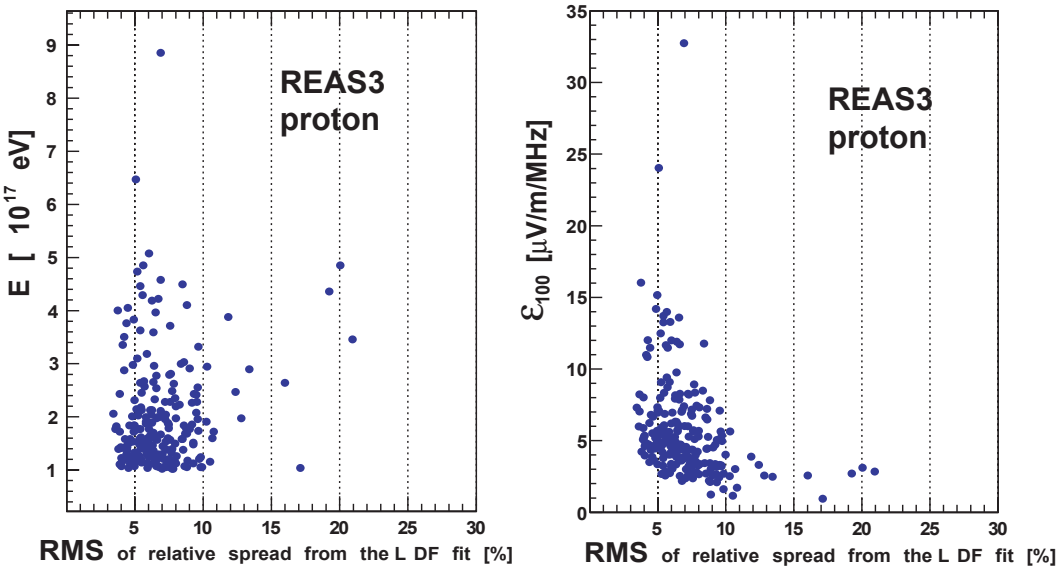

Figure 6.16: *The minimum RMS value, for high primary energies (left) and for large ϵ_{100} parameter values (right), thus far from the noise level, is of the same order as the calibration uncertainty (5%).*

according to the zenith angle, the radio emission is dominated by the charge excess contribution, since the geo-magnetic angle (α) is close to zero. The correlation is even more clear by looking at the behavior of the RMS values with regard to the geomagnetic angle (**fig.**6.15). Events with small α show larger values for the RMS spread.
For the whole selection, the average influence of the charge-excess contribution on the radio lateral distribution function predicted by the REAS3 simulations is of at most 6-7 % (precisely the average RMS for proton and iron is respectively of 6.9 % and 5.9 %) (**fig.**6.13). Since this value is quite small and comparable to the calibration uncertainties of the LOPES data (5 %), the one dimension (1D-) exponential function (eq.6.1) can generally be considered good enough for the description of the radio lateral distribution behavior.

It must be stressed that the REAS3 prediction for the average spread of the points around the fit, however, seems to only partially describe the LOPES data results, where a mean RMS of 35 % and a minimum RMS of $\sim$ 14 % even for events far from the noise level was found (**fig.**6.9).
Considering that the RMS values for the same simulated events with the largest primary energy and/or largest ϵ_{100} reconstructed parameters (**fig.**6.16) are around 5-7 %, one can affirm that only half of the experimental relative dispersion around the LDF fit can be attributed to the charge excess contribution.

Possible reasons for this inconsistency between simulations and experimental data about both the Mean and the RMS values of the dispersion are listed below: first of all, the discrepancy can be referred to an underestimation of the calibration uncertainty, i.e. 5 %, in the detected radio pulse ($\Delta\epsilon$) for the LOPES experiment; second, due to the

comparison with the results in (Apel et al., 2012b), it might be attributed to the data selection used. A higher signal-to-noise cut will possibly reduce the discrepancy between data and simulations. Moreover, the inconsistency could also stress the incompleteness of the simulation code (REAS3.0) in describing the detected data. For instance, in this set of REAS3 simulations, the refractive index of the atmosphere was set to unity (a realistic atmospheric refractive index was properly implemented only in REAS3.1, unavailable at the time of writing).

6.3 REAS3 - A comparison of alternative fitting functions

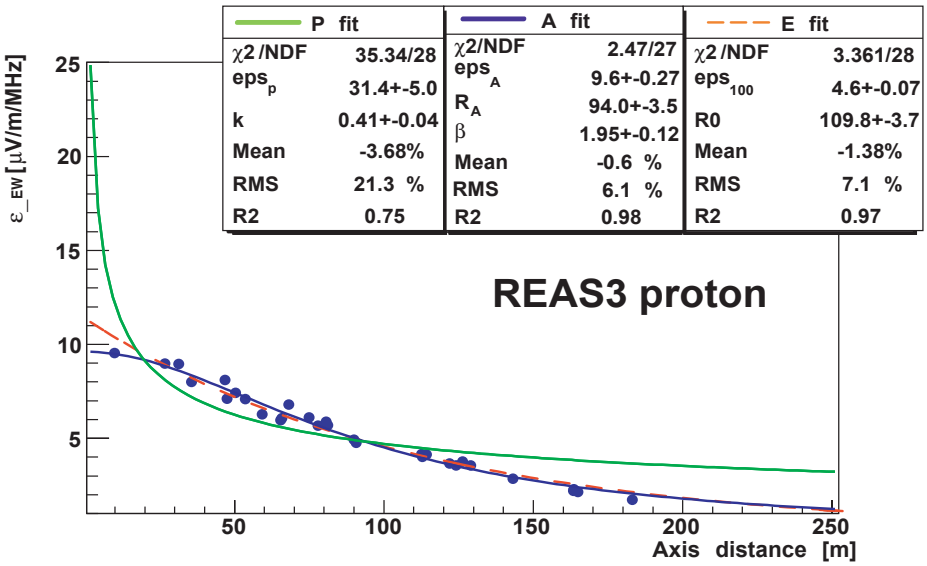

Figure 6.17: *REAS3 simulated LDF for the same event of* ***fig.****6.10, fit with the three functions.*

By comparing with other possible functions, the following shows the uniform exponential function to appropriately describe the radio LDF.
This procedure concerns only (REAS3) simulated radio LDF, since the noise and the large error-bars in the detected LOPES amplitudes do not allow a precise study of the LDF fit.
The purpose is to reduce the systematic shift found for the relative deviation from the LDF fit, thus the Mean values of the distribution (**fig.**6.12).

The three functions taken into account for the LDF fit are:

- P fit : $\epsilon(d) = \epsilon_{\mathrm{p}} \cdot (\frac{d}{\mathrm{m}})^{\mathrm{k}}$, with ϵ_{p} [μV/m/MHz] and k as free fitting parameters
- E fit : $\epsilon(\mathrm{d}) = \epsilon_{100} \cdot \exp\left(\frac{\mathrm{d}-100\mathrm{m}}{\mathrm{R}_0}\right)$, with ϵ_{100} [μV/m/MHz] and R_0 [m] as free fitting parameters
- A fit : $\epsilon(\mathrm{d}) = \epsilon_{\mathrm{A}} \frac{1}{1-\left(\frac{\mathrm{d}}{\mathrm{R_A}}\right)^{\beta}}$, with ϵ_{A} [μV/m/MHz], R_A [m] and β as free fitting parameters

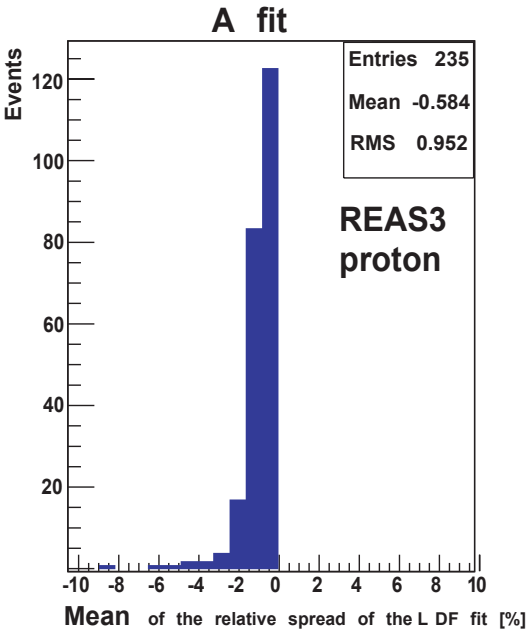

Figure 6.18: *Systematic shift from the LDF fit, for the whole set of simulations of Selection2. Values comparable to E-fit in **fig.**6.12. The events are simulated as protons. (A fit)*

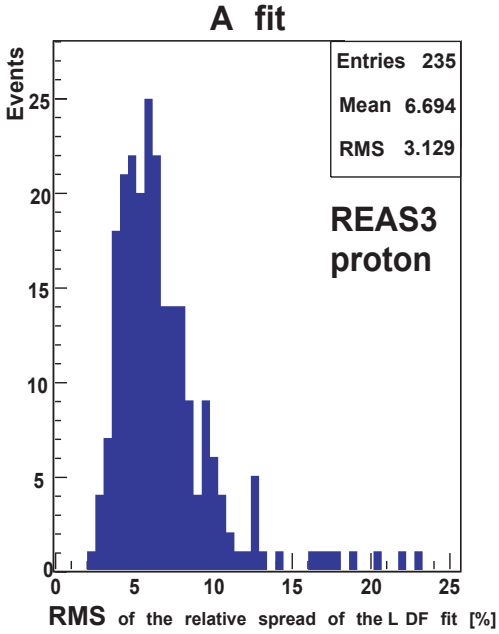

Figure 6.19: *Weighted spread around the LDF fit, for the whole set of simulations of Selection2. Values comparable to E-fit in **fig.**6.13. The events are simulated as protons. (A fit)*

These are respectively a power-law function (P fit) similar to what has already been investigated in (Apel et al., 2010a), the exponential (E fit) and a more complicated function (A fit), with three free fitting parameters (Badescu, 2010).
The advantage for the last A fit is that it turns to a power-law function for larger distance, which is expected from the theoretical point of view (Scholten et al., 2008).

$$\lim_{d\to inf} \epsilon(d) \approx \epsilon_A \left(\frac{d}{R_A}\right)^{-\beta}$$

The same typical event, taken as example in the previous section (cf. **fig.**6.10), is now fitted with the three functions; only the proton simulated event (**fig.**6.17) is reported since no big difference among proton and iron generated air showers is found.
As it immediately appears by eye, the power-law fit completely fails in fitting the data, for the distance range of the LOPES event.
The case is different for the other two functions, especially for the A fit which seems to describe best the behavior of the electric field amplitude in the antennas even for the distance range 0-30 m, where a flattening of the LDF slope is experimentally expected (**fig.**6.4) (Apel et al., 2010a).

The relative deviation of the points around the LDF fit is computed also for the A function. The Mean and RMS of the distribution are taken again into account to have a first indication of potential improvements, in comparison with the exponential fit case

(**fig.**6.12 and **fig.**6.13).
On average, the A fit presents a Mean value slightly smaller, for proton of -0.58 $\%$ (**fig.**6.18) and for iron of -0.26 $\%$, compared to the systematic shift of the exponential function (respectively of $\sim$ -1.38 $\%$ and -0.9 $\%$). The negative sign is, again, due to the amplitudes smaller than the fit values. The same occurs for the average RMS for proton of $\sim$ 6.7 $\%$ (**fig.**6.19) and for iron of $\sim$ 5.1 $\%$ (the RMS values for the exponential fit are respectively of $\sim$ 6.9 $\%$ and 5.9 $\%$), thus a slightly smaller dispersion of the points around the fit appears using the three parameters function (A fit).

The values reported above exhibit a behavior almost similar for iron and protons primaries. Nevertheless, proton-initiated showers show an average MEAN and RMS dispersion values of 1-2$\%$ systematically bigger than for iron-initiated showers. In other words, iron-showers are characterized by less variations in the radio pulse amplitudes. As consequence, the iron LDF profile can be more easily and better described by both an exponential and the A fit function, compared to the proton events.

A method to directly compare, event by event, the E fit and A fit functions, is provided by the R-square coefficient from the non-linear regression, which is presented in the next section.

6.3.1 Goodness of the fit analysis

The R-square coefficient provides a measure of how well future data are likely to be predicted by the used model (GraphPad, 2011). Its value is between 0 and 1, with R^2 close to zero indicating that the fit curve explains the data no better than a horizontal line going through the mean of all y-values, while R^2=1 meaning that all the data points are on the fitted function.
One should carefully give a meaning to the absolute R^2 value for an individual function used to fit the data, since this coefficient is not a solid indicator of the quality of the individual fit. Anyway, for the specific case of a comparison between models applied to the same events - in this case a comparison between the A fit and the E fit - the R^2 coefficients indicates which of the two functions predicts best the future outcome.

Considering the different number of the free parameters for the analyzed functions, it is mandatory to use the adjusted coefficient $R^2_{\rm adj}$ in which the number of degrees of freedom is taken into account:

$$R^2_{\rm adj} = 1 - \left(\frac{n-1}{n-p-1}\right)\frac{\Sigma_{i=0}^{n}(y_i - f_i)^2}{\Sigma_{i=0}^{n}(y_i - \overline{y}_i)^2} \tag{6.2}$$

y_i are the fitted points, the $\Sigma_{i=0}^{n}(y_i - f_i)^2$ is the regression sum of squares with f_i the value of the individual points projected on the fitted line, $\Sigma_{i=0}^{n}(y_i - \overline{y}_i)^2$ is the total sum of squares, with $\overline{y}_i$ the horizontal line passing through the mean y value, p is the number of free fitting parameter and n-1 the degrees of freedom.
The adjusted $R^2_{\rm adj}$ coefficients for the exponential and the A fits, for each individual event, are compared in **fig.**6.20 and **fig.**6.21, respectively for proton and iron REAS3 simulated showers. The continuous line represents the one-by-one correspondence.

In both cases, a slight shift towards larger R^2_{adj} coefficient values for the A fit is noticeable, hinting towards the A fit to be a better description of the radio lateral distribution (as it was already noticed above).
Nevertheless, the general improvement consists of only a small percentage.
Moreover, the A fit is a three parameters function. One parameter more than the exponential function will result in a larger difficulty in fitting the measured data.
In regard with the last two remarks, the "easier to handle" exponential function is preferable and it is considered to generally well describe the radio lateral distribution for the LOPES experiment array, thus for distances smaller than 200 m.

6.4 Outlook

Clear hints in the LOPES data reveal that the radio lateral distribution for each individual event is more complex than the used (1D)-exponential and it may be better described by a multidimensional (more than 1 spatial dimension) function.
A statistical analysis on the LDF residuals for both recorded and simulated data was performed and the exponential is, all in all, judged as a sufficient approximation to describe the radio lateral distribution at the distances probed by the LOPES experiment: The systematic deviation from the fit is small and comparable to the calibration uncertainties ($\sim 5\%$). REAS3 predictions for the average spread of the points around the fit, however, seem to only partially describe the LOPES data results. Possible causes for this behavior were discussed. Nevertheless, the large RMS will not affect the slope method analysis performed in the next chapters, thus the homogeneous exponential function is used.

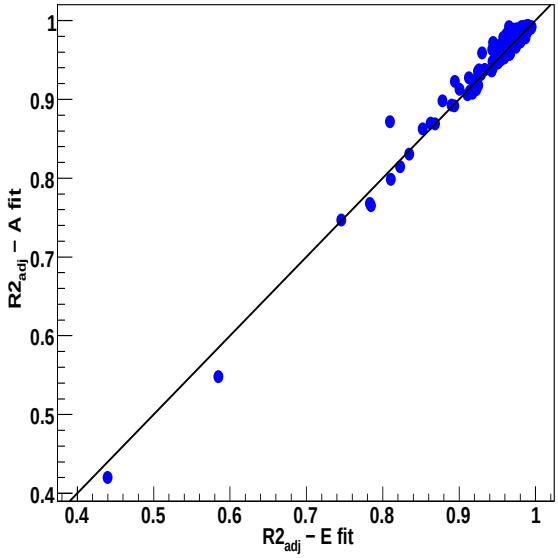

Figure 6.20: *Direct comparison of the R^2_{adj} coefficient computed once for the exponential, once for the A functions. (REAS3 proton primaries)*

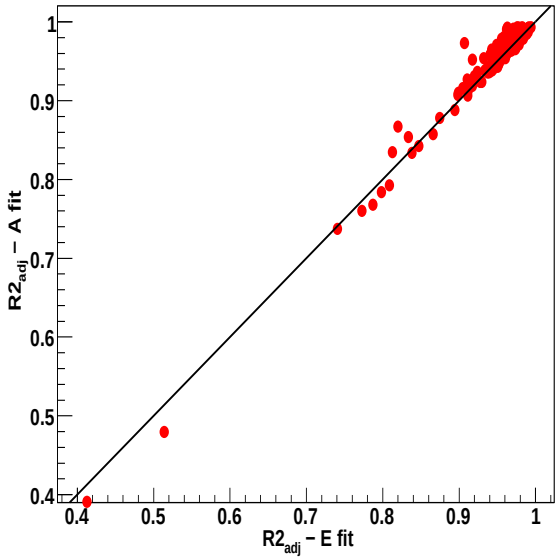

Figure 6.21: *Same as in **fig.**6.20, but for the REAS3 iron primaries.*

7 The slope method based on REAS3 simulations

Several simulation models for the radio emission from cosmic ray air showers have been developed in the last few years (Huege, 2009b). Irrespective of some differences in the results, almost all models predict the LDF slope to be a strong indicator for the cosmic ray mass (Ludwig and Huege, 2011b, Scholten et al., 2008), due to a pure geometrical effect: Iron nuclei interact earlier in the atmosphere compared to lighter cosmic rays. The depth of the shower maximum (X_{max}) depends mainly on the first interaction. An X_{max} at a larger geometrical distance from the observer (like for iron-generated showers, as well as for inclined showers) implies a flatter radio LDF compared to proton-generated or vertical showers.

An analysis on the simulated radio LDF slope was done in Huege et al. (2008) with the former REAS2 code (Huege and Falcke, 2005a, Huege et al., 2007), showing the possibility to derive important shower parameters, such as the primary energy and depth of the shower maximum, with radio-only measurements. Some results are reviewed in section 3.3 and are used as guideline for the investigation presented here.
The purpose of the paper (Huege et al., 2008) was a general investigation which studied four specific shower geometries. The results of Huege et al. (2008) are exemplary, leaving the direct application to any of the radio experiments still to be elaborated.
In addition, the REAS2 code turned out to be incomplete and not fully consistent. The updated version of the code, REAS3, available since 2010, considers almost the entire complexity of the radio emission from the complete air shower development.

Furthermore, the improved noise treatment (Schröder et al., 2010b) included in the LOPES analysis pipeline (cf. Chapter 4), and the careful study on the systematic bias and uncertainties on the detected radio amplitude, now allow a precise study of the LOPES lateral distributions.

A sign of the refinement of the REAS3 code and the improvements in the LOPES LDF analysis is the significantly better agreement between REAS3 simulated and LOPES detected lateral distribution functions (Ludwig, 2011).

This insight leads to the conclusion that an updated LDF analysis with the new REAS3 code is mandatory.
The general goals of the following chapter are: First, to verify and improve the previous REAS2 analysis (cf. section 3.3) with the updated REAS3 simulations. Divergences in the results, mainly due to the charge excess contribution to the radio emission (omitted in REAS2), will be pointed out. Moreover, a dependence on the hadronic interaction model used to simulate the air showers in atmosphere is discussed.
Second, the application of the slope method to the detected LOPES data needs to be

validated.
For such a purpose, the events in Selection1 (cf. section 4.1.3) are considered.

7.1 REAS3 simulations adapted to a realistic case

One important issue in this investigation is to create a set of REAS3 simulations which describe accurately a realistic situation for the LOPES experiment.
The following aspects have been taken into account:

- **Simulations of the LOPES detected events**
  CORSIKA (Heck et al., 1998) and REAS3 (Ludwig and Huege, 2011b) are used to simulate, respectively, the particle cascade and the radio emission from the electromagnetic component of air showers, induced by a cosmic ray primary. For these simulations the interaction models used are QGSJetII (Ostapchenko, 2006) and UrQMD (Bass et al., 1998), as high energy and low energy interaction models. In this first part of the analysis, we refer to the events in Selection1 (cf. section 4.1.3). The information related to the energy, the incoming direction and the core position of each event detected by the LOPES experiment (reconstructed by KASCADE(-Grande)) are used as input parameters for the simulations. In this way, also the geometrical acceptance of the LOPES experiment is taken into account.
  Moreover, the geomagnetic field, which is important for the radio emission in air showers, is set to the intensity and inclination values valid for the LOPES site (cf. Chapter 5).

- **LOPES antenna array**
  The REAS3 simulated electric field is filtered with an ideal rectangular bandpass filter of 43-74 MHz, in order to reproduce what is measured by the LOPES antenna setup.
  Each observer position (i.e. each antenna) for the simulated events correspond to the LOPES antenna in the array. In other words, for a single simulated event, 25 observer positions (see fig.4.1) are located with respect to the shower axis of the specific event just as the LOPES antennas .
  For most of the events the core of the shower occurs to lie in between the antennas. Accordingly, the LDF for each event, which is the electric field amplitude in relation to the distance from the shower axis, is considered not only in one specific azimuthal direction.
  In this way, the influence of the charge excess contribution in the different directions can be investigated.

- **Shower-to-shower fluctuations**
  REAS3 takes the needed information about the electrons and positrons in the air shower from CORSIKA, collected into histograms created by the interface program COAST[1] (Lafèbre et al., 2009).
  For each selected LOPES event one complete simulation with CORSIKA is performed, once as proton, once as iron-generated showers, with no pre-selection of

[1] **CO**RSIKA d**A**ta acces**S** **T**ools: C++ code providing simple and standardized access to CORSIKA data.

a typical shower.
Shower-to-shower fluctuations, which affect the data, are thus included.

7.2 The slope method approach

The slope method approach is investigated here by using as guideline the analysis shown in Huege et al. (2008), but applied to the REAS3 simulations of the LOPES detected events, as described in the previous section.

For each of the 30 simulated antennas, REAS gives the three vector components of the electric field in the east-west, north-south and vertical directions. The amplitude is determined as the maximum of each component of the electric field.
In the following, we will refer to the total absolute value $|\overrightarrow{\epsilon_{\mathrm{TOT}}}|$, i.e. the square root of the quadratic sum of all the three electric field components.

The 30 absolute amplitude points of each event need to be interpolated with a proper function. The slope method applied to study the mass sensitivity in the radio lateral slope does not require a specific function to fit the radio LDF. This is a big advantage if one considers that the radio lateral distribution is not yet fully understood at larger distances than 200 m from the shower axis. According to the conclusion in Chapter 6, a homogeneous 1D-exponential function (eq.6.1) is sufficiently accurate to describe the LDF for the LOPES events, thus it is used in the following analysis.

In addition to $\mathrm{X_{max}}$, another factor of big influence on the lateral slope is the zenith angle of the air shower. This dependence, expected again due to a pure geometrical effect, is experimentally seen in Apel et al. (2010a) and in fig.6.4.
To reduce the dependence of the LDF-slope on the zenith angle, and better focus on the effects of the primary composition, five zenith angle bins are separately considered.

The comparison of the radio lateral functions for the LOPES events requires a normalization of the electric field amplitude in the antennas. Indeed, the LOPES selection presents a primary energy in the range 10^{17}-10^{18} eV and an isotropic arrival direction.

The $\sin(\alpha)$, with α the geomagnetic angle, can be considered a good approximation for the arrival direction normalization when the total absolute value $|\overrightarrow{\epsilon_{\mathrm{TOT}}}|$ is considered. Indeed, further proof for the geomagnetic induction effect as the major mechanism for the radio emission has been discussed in Chapter 5.

Concerning the energy, three different normalizations are separately investigated:

$$\frac{\epsilon_{\mathrm{TOT}}}{\sin(\alpha)\mathrm{E}}\ ,\ \frac{\epsilon_{\mathrm{TOT}}}{\sin(\alpha)\mathrm{E_{cal}}} \text{ and } \frac{\epsilon_{\mathrm{TOT}}}{\sin(\alpha)\mathrm{E_{em}}}$$

the first with the primary energy (E) used as input parameter for the REAS3 simulations, the second with the calorimetric energy ($\mathrm{E_{cal}}$), i.e. the energy deposited by the particles in the atmosphere, and finally with the electromagnetic energy ($\mathrm{E_{em}}$), i.e. the energy deposited in the atmosphere by the electromagnetic component of the shower. While, for the LOPES experiment, the primary energy is directly given by the KASCADE reconstruction, the $\mathrm{E_{cal}}$ and $\mathrm{E_{em}}$ are calculated after the particle information

given by CORSIKA.
E_{cal} is the quantity measured by fluorescence light detectors (Risse and Heck, 2004). The E_{em} does not consider the energy deposited in the ground and the energy carried away by the hadronic and muonic components. Since the radio emission comes primarily from the electrons and the positrons moving in the atmosphere, it should be best correlated to E_{em} Huege et al. (2008) (cf. section 3.3).

7.2.1 The *flat* region

The proper normalizations, previously discussed, allow a comparison of several LDFs from the LOPES selection (Selection1).
The simulations of the 54 events in the first zenith angle bin, i.e. less than 19.4 degrees, are presented in fig.7.1. The distance from the shower axis is taken in the shower-plane coordinates system, i.e. the plane perpendicular to the shower axis, with a maximum of 350 m, taking into account the dimension of the LOPES array.
The differences between iron and proton simulated LDFs are clearly seen by eye for all the three energy normalizations.

One expects to find a specific region, the $flat$ region (Huege et al., 2008) (cf. section 3.3), where all the LDF profiles intersect, independent of the shower X_{max}. In our case this distance, that from now on we will refer to as d_{flat}, is not distinctly identifiable. The main reason are the variations of the pulse amplitudes, for each single event, even at the same distance from the shower axis. This is a clear outcome of both the realistic simulation of the LOPES antenna array, and the expected influence of the charge excess contribution on the total simulated electric field when several azimuthal directions from the shower axis are taken into account.
Therefore, the profile of the relative spread of the fits is computed and the minimum RMS value is taken. For the first zenith bin, the RMS spread is shown in relation to the distance from the shower axis for each of the three energy normalizations (fig.7.1, right part).

The maximum value of the RMS is obtained for the furthest distance (around 350 m) and it is almost the same ($\sim$ 50 $\%$) in all the three normalizations.
The minimum RMS value is quite small and varies between 6 $\%$ and 8 $\%$.
The normalization for the total primary energy shows the largest values (8$\%$) for the RMS spread of the fits (Table 7.1), which is, by all means, an expected effect (Huege et al., 2008).
Indeed, as already discussed in section 3.3, the iron and proton primaries transfer a different amount of the same primary energy to the electromagnetic component, which is of interest for the radio emission. Much larger fluctuations among the electric field strengths and larger values even for the minimum of the spread of the fits are expected. In contrast, the lowest RMS spread is observed, as expected, for the electromagnetic energy normalization.

In **fig.**7.2, the distributions of the normalized field strength in the $flat$ region is shown in relation to X_{max}. Again, it is clearly visible how the radio amplitudes spread reduces best for the electromagnetic energy normalization (bottom part). Nevertheless, the $steps$

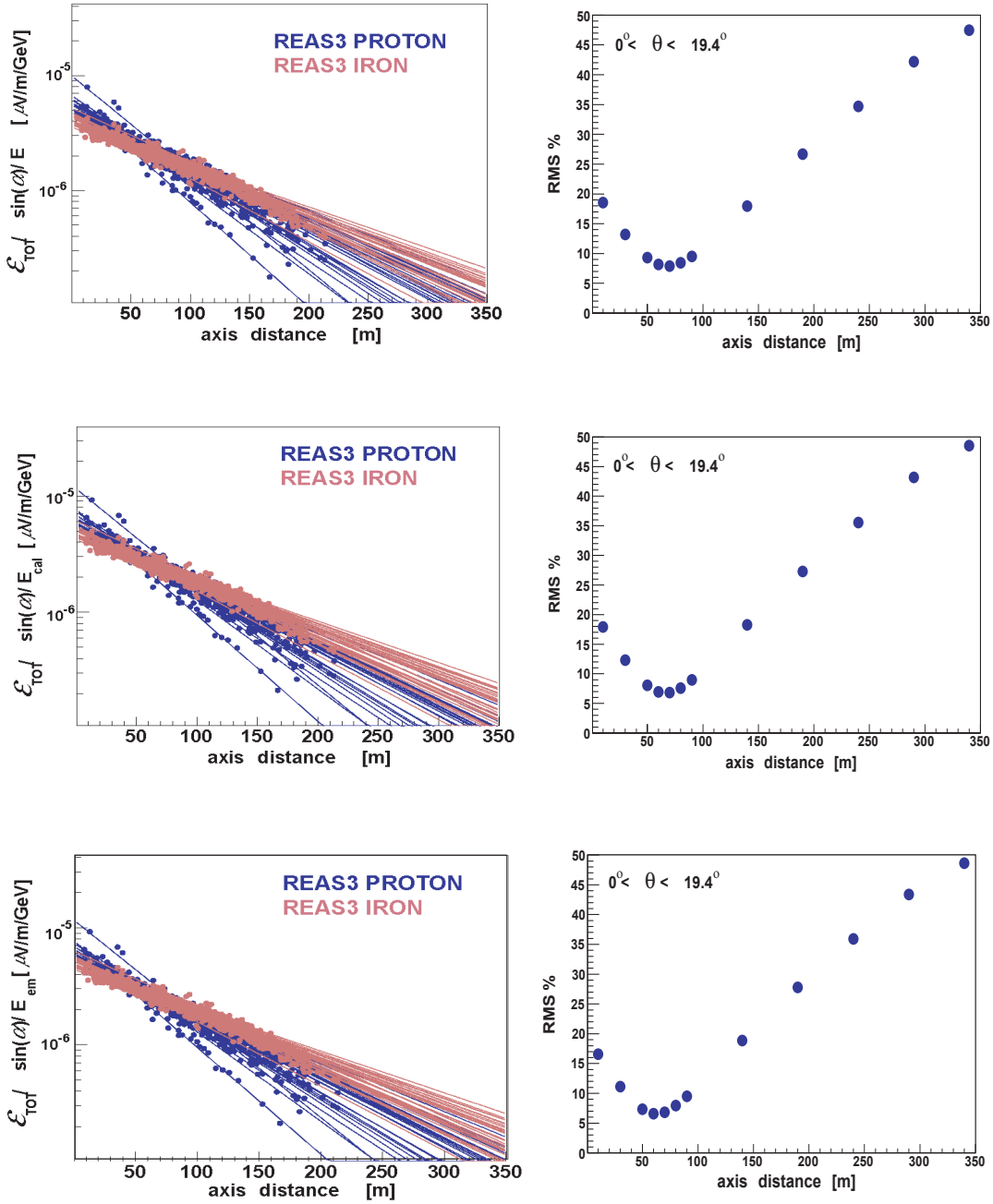

Figure 7.1: *Left part: LDF for proton (blue) and iron (red) REAS3–simulated LOPES events in the first zenith angle bin. The total electric field is normalized, respectively from top to bottom, by the total, the calorimetric and the electromagnetic energy, as well as the geomagnetic angle. Right part: RMS of the electric field fits, calculated at 12 distances from the shower axis.*

between the primaries expected for the E normalization (Huege et al., 2008), as previously introduced with **fig.**3.3 top left, are not so evident here.

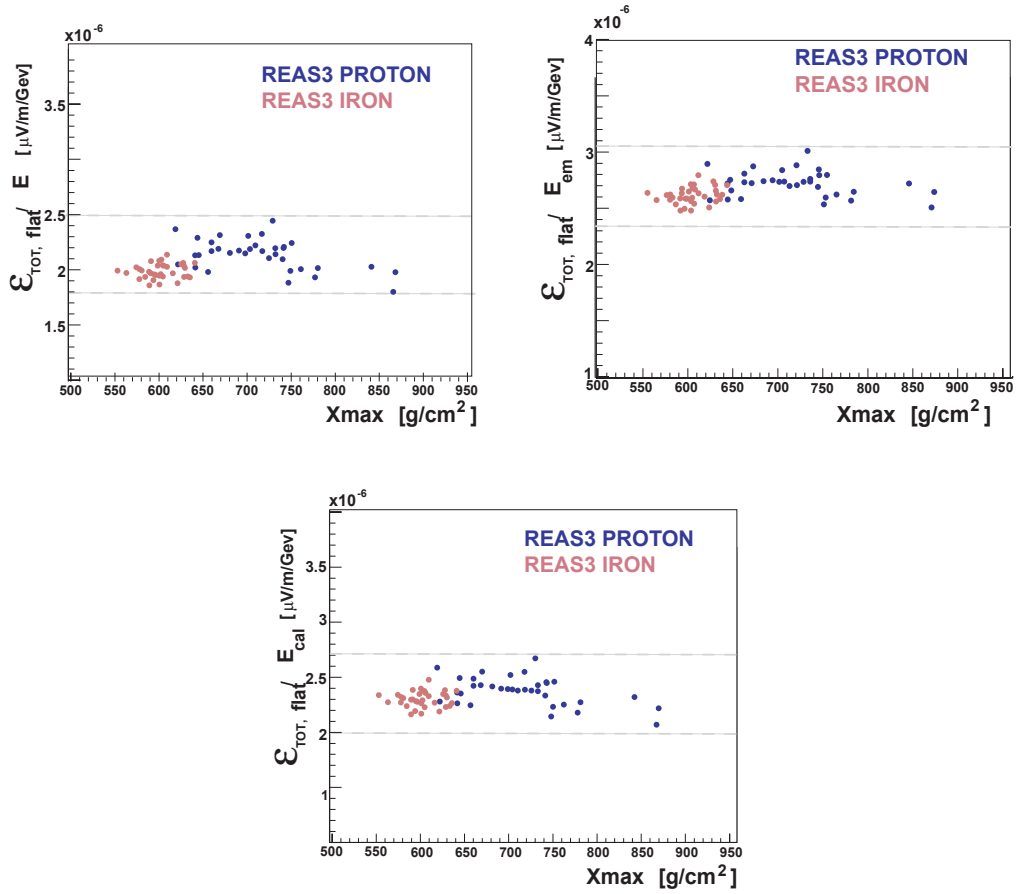

Figure 7.2: *Total electric field strength for proton (blue) and iron (red) simulated events taken in the $flat$ region and normalized, respectively from top to bottom, clockwise, by the total, the calorimetric and the electromagnetic energy. The electric field amplitude in the $flat$ region is independent on the shower $X_{\max}$*

Even though the E normalization presents the largest values for the minimum RMS spread for all the zenith angle bins considered, this is, on average, no more than few percent larger compared to the other two normalizations. Therefore, the three normalizations used for these selected LOPES events do not widely differ.
In spite of shower-to-shower fluctuations, realistic simulations predict that radio measurements can possibly determine directly the total energy of primary cosmic rays with a precision of 6 % and 8 %.

A relevant result comes with the electromagnetic energy normalization. The characteristic lower RMS-spread (Table 7.1 and **fig.**7.3) stress the expected dependence of radio signals on the electromagnetic component of the air shower. The smallest RMS reaches on average a value of almost 3 %. This emphasizes the potentiality of the radio detection to provide with extremely high precision the electromagnetic-component of the primary energy. As a consequence, the radio detection, combined with a different detection method which provides the total primary energy reconstruction, allows to disentangle between the hadronic interaction models proposed in last decades for

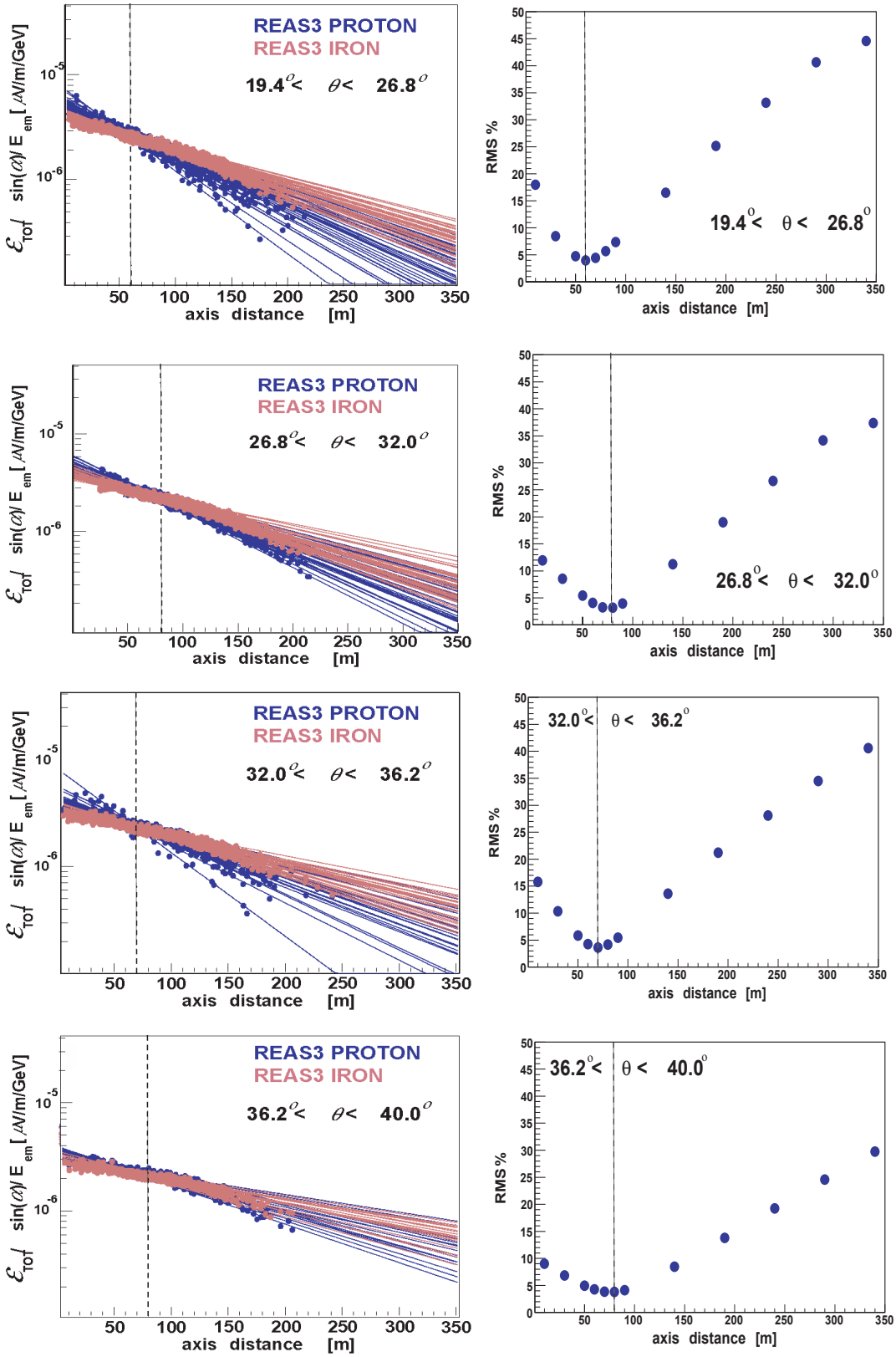

Figure 7.3: *Total electric field strength for proton (blue) and iron (red) simulated events taken in the $flat$ region and normalized by the electromagnetic energy in all zenith angle bins (from top to bottom, from the second to the fifth zenith angle bins).*

describing the air-shower development in the atmosphere.

A clear evidence of the shower inclination influence on the lateral slope can be seen by comparing the plots in the different zenith angle ranges (**fig.** 7.3). The more the showers have larger inclinations, the more they collimate. This results in an overall smaller RMS spread also for larger distances.

The values for the distance where the minimum RMS happens, d_{flat}, changes between 60 and 90 m far from the shower axis, increasing with the zenith angle and in dependence of the energy normalization used. One needs to take into account that, especially for larger zenith angles, the values for the RMS dispersion in the distance-bins contiguous to d_{flat} vary of a small quantity (less than 0.5 $\%$).
As remarkable result, the $flat$ region is found to lie inside the LOPES array, at the maximum distance of d=90 m, i.e. R=132 m in the ground coordinates system [2], for the most inclined showers.
An uncertainty of 5 m must be considered for the d_{flat} values, due to the chosen distance binning.

7.2.2 The *steep* region

The $steep$ region is defined to be another distance from the shower axis, where the electric field amplitude carries the information about $X_{\max}$.
This is chosen to be at the arbitrary value of 170 m far from the $flat$ region, so d_{steep} will lie in the range of 230 - 250 m.
The constant value of 170 is set taking into account different factors: First of all the primary energy of the events in the selection, which does not exceed 10^{18} eV, and implies a radio signal decreasing fast to small values for distances of only a few hundred meters. Second, the small range of the LOPES antenna array. Third, the indications for the exponential function to fail in describing the data at distances larger than $\sim$ 200 m (cf. Chapter 6).
The ratio of the electric field amplitudes in the $flat$ and $steep$ region, $\frac{\epsilon_{\mathrm{flat}}}{\epsilon_{\mathrm{steep}}}$, provides information on the slope of each individual LDF, thus this ratio is used to trace the $X_{\max}$ of the single event.

7.3 Dependence of the radio lateral distribution on the hadronic interaction model

The interpretation of measurements of cosmic ray air showers and the reconstruction of the primary cosmic ray parameters, such as energy, incoming direction and shower maximum depth (X_{max}), are strongly dependent on simulations.
Different interaction models are used to simulate air-showers. The production of the different particles and antiparticles in the atmosphere needs to be modeled in detail, thus the simulations require a deep knowledge about the theoretical and phenomenological

[2] For the conversion between shower-plain system and ground system the transformation $\mathrm{R(d)} = \mathrm{d}(\sqrt{1-\cos(\Delta\varphi)^2 \cdot \sin(\theta)^2})^{-1}$ has been used

Table 7.1: *Distance of the $flat$ region*

zenith angle		E_{cal}		E_{em}		E	
$\Delta\theta$	entries	d_{flat} [m] $\pm$ 5 m	RMS % min	d_{flat} [m] $\pm$ 5 m	RMS% min	d_{flat} [m] $\pm$ 5 m	RMS% min
0.°-19.4°	54	70	6.82	60	6.58	70	7.91
19.4°-26.8°	70	70	4.59	60	4.01	70	6.41
26.8°-32°	76	80	3.49	80	3.20	80	5.21
32°-36.2°	54	70	4.25	70	3.61	80	5.93
36.2°-40°	36	80	4.51	80	3.80	90	6.56

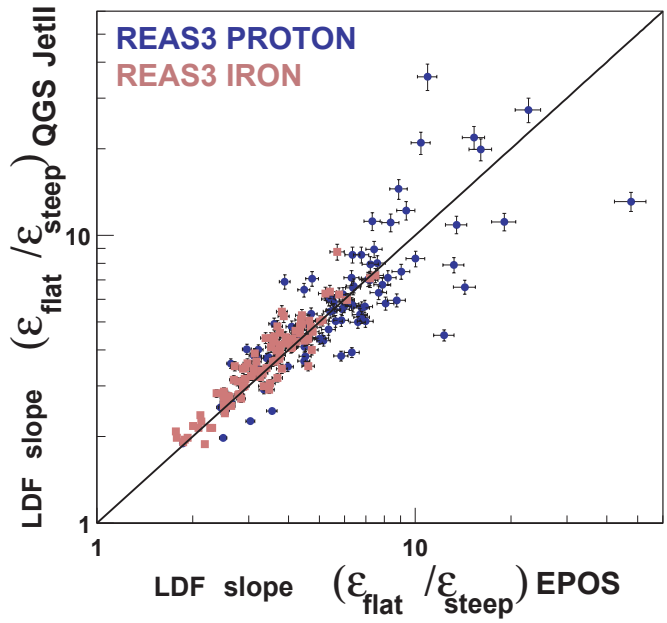

Figure 7.4: *Event-by-event comparison of the radio LDF slopes for the REAS3 simulations using once QGSJetII and once EPOS interaction models. (Selection1).*

description of the processes inside the cascade.

The possible dependence of the radio detection on hadronic interaction models is investigated in the following. EPOS 1.99 (Pierog and Werner, 2009) and QGSJetII (Ostapchenko, 2006) are used for the air shower simulations of the LOPES selected events.
The main difference between the two models lies in the number of high energy muons produced in the cascade, which directly affect the position of the air-shower maximum in the atmosphere, differently for iron and proton initiated showers (Pierog et al., 2009).

For primary energies of interest for our investigation, i.e. between 10^{17}-10^{18} eV, the iron X_{max} is predicted to happen deeper in the atmosphere for QGSJetII (Ostapchenko, 2006) compared to EPOS 1.99.
The proton induced showers for the EPOS 1.99 model show a higher elongation (i.e.

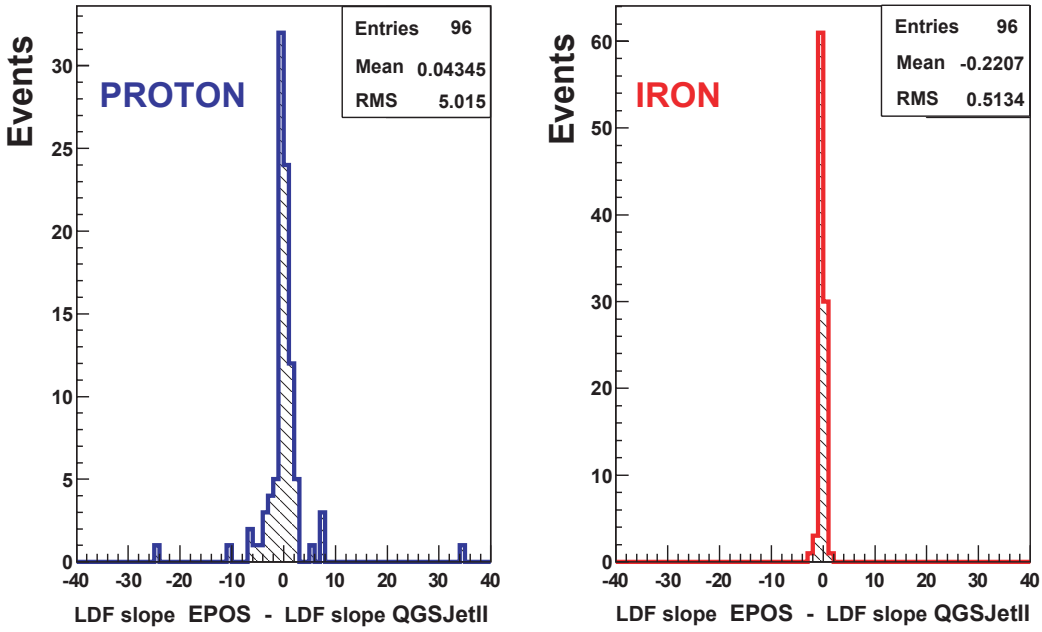

Figure 7.5: *QGSJetII- and the EPOS1.99- simulated lateral distribution function slope for the proton (left) and iron (right) simulated events.*

X_{max}) than QGSJetII (Pierog et al., 2009).
The X_{max} dependence on the particle interaction model is expected to have influence also on the predictions for the radio lateral distribution function.

All the LOPES detected events in Selection1 are simulated a second time as discussed in section 7.1 but with the EPOS 1.99 hadronic interaction model, once as proton, once as iron initiated showers.
The ratio $\epsilon_{flat}/\epsilon_{steep}$, with ϵ_{flat} and ϵ_{steep} the total electric field amplitudes extrapolated from the LDF fit in the $flat$ and $steep$ regions, is used as indicator of the LDF slope for each single event.

In **fig.**7.4 a direct event by event comparison is shown and, as expected, the proton simulated points (blue) scatter much more than the iron simulated events (red), due to the larger fluctuations.
A general agreement between the radio LDF slopes of the two interaction models appears, apart from the slight systematic shift for the iron events towards larger values for the QGSJetII simulated slope.
This is, anyway, in perfect agreement with the expectations, since the QGSJetII X_{max} for iron nuclei is predicted larger, i.e. closer to the observer, which implies larger values for the LDF slope. Moreover the iron showers fluctuate much less, therefore the differences between the iron X_{max} predicted by EPOS 1.99 and by QGSJetII may have a visible effect also on the radio LDF slope.
On the other hand, this effect could be due to the low statistic.

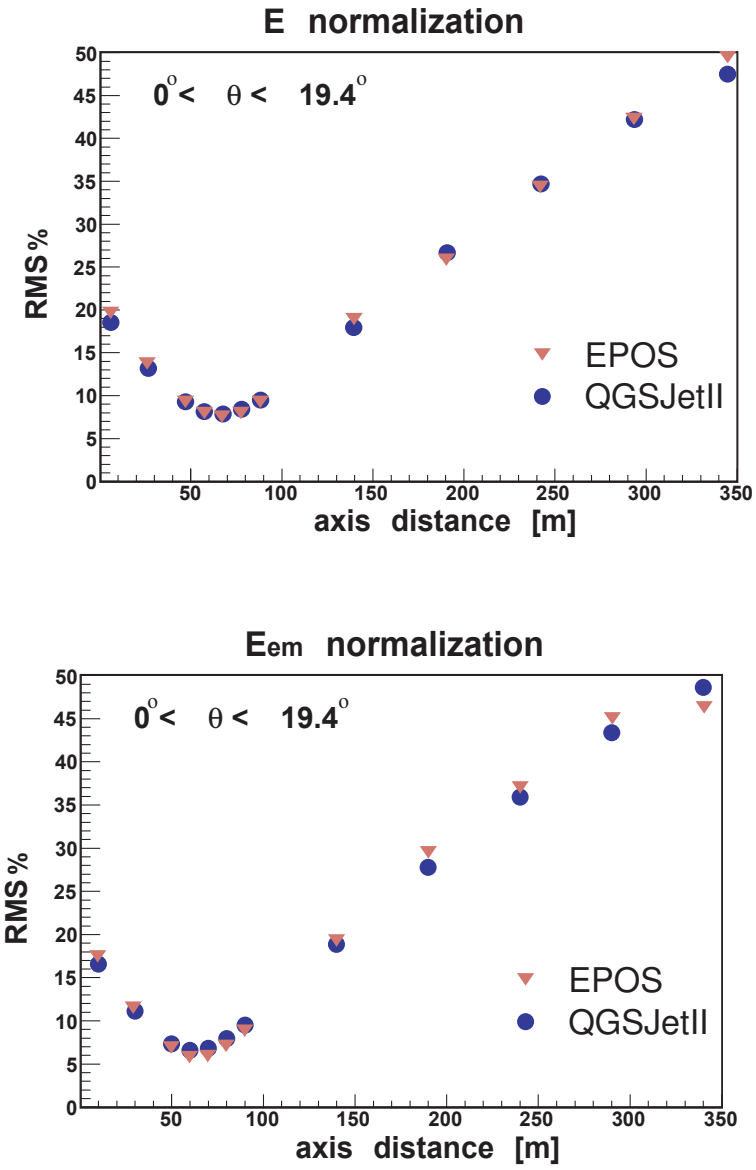

Figure 7.6: *RMS of the radio lateral distribution functions of the events in the first zenith angle bin for both EPOS and QGSJetII hadronic interaction models. The electric field is normalized by the total primary energy (left) and by the electromagnetic energy (right).*

Quantitatively speaking, a distribution for the differences between EPOS and QGSJet radio slopes is presented in **fig.**7.5, for proton and iron separately. The mean and the standard deviation for both the primaries are quite small, confirming the general agreement. The difference between EPOS 1.99 and QGSJetII is not significant at 3 σ. Indeed, the means are, for both protons and irons, smaller than three times the quantity RMS/$\sqrt{\text{entries}}$.

Table 7.2: *Distance of the $flat$ region - EPOS interaction model.*

zenith angle		E		E_{em}	
$\Delta\theta$	entries	d_{flat} [m] $\pm$ 5 m	RMS % min	d_{flat} [m] $\pm$ 5 m	RMS% min
0.°-19.4°	54	60	7.7	60	5.9
19.4°-26.8°	70	70	6.3	60	4.2
26.8°-32°	76	80	7.1	70	4.1
32°-36.2°	54	90	6.9	70	4.4
36.2°-40°	36	90	6.8	80	3.8

In the specific case of the slope method analysis, it is important to consider the possible dependence of the overall RMS spread of the radio LDF fits on the hadronic interaction model. Moreover, possible divergences in the d_{flat} value reconstruction must be investigated.
The RMS spread profile of the total electric field values in relation to the distance from the shower axis of **fig.**7.1, right part - events in the first zenith angle bin - is compared with the EPOS 1.99 simulated RMS profile (**fig.**7.6). Both the total (top side) and electromagnetic (bottom side) energy normalizations are taken into account.
A quite nice overlapping can be noticed, especially for the region of interest where the RMS minimum value takes place. This result is quite unexpected since the two interaction models vary in the different amount of electromagnetic particles generated in the air showers. The result is most probably due to the large RMS spread of the fits - e.g. connected to the charge excess influence - compared to (Huege et al., 2008) which would prevent to distinctly see the effect of the different energy normalizations.
In Table 7.2 all the relevant values in the whole zenith angle range for the simulations based on the EPOS 1.99 interaction model are summarized.

In conclusion, a nice agreement is found between the minimum RMS values for the two hadronic interaction models, for both the total and electromagnetic energy normalizations. Moreover, a solidity of the predicted d_{flat} region, which is, also in the case of the EPOS 1.99 model, found to be in the range 70-90 m and 60-80 m, respectively for the E and the E_{em} normalization, in dependence on the shower inclination, is clearly seen.
One can affirm that the hadronic interaction model used to simulate the air shower cascade for the REAS3 simulations only slightly affects the radio lateral slope in the primary energy range of this selection. As a consequence, the hadronic interaction model has almost no influence on the d_{flat} identification.

7.4 Primary energy determination

The importance of the $flat$ region was already discussed in Huege et al. (2008) and section 3.3: in d_{flat}, the peak electric field, normalized with the energy and the arrival direction of the shower, independent of the primary particle type, shows no correlation with the shower maximum depth and has almost the same value for all the events.
Such a distance is characteristic of the detectors considered and it can be compared

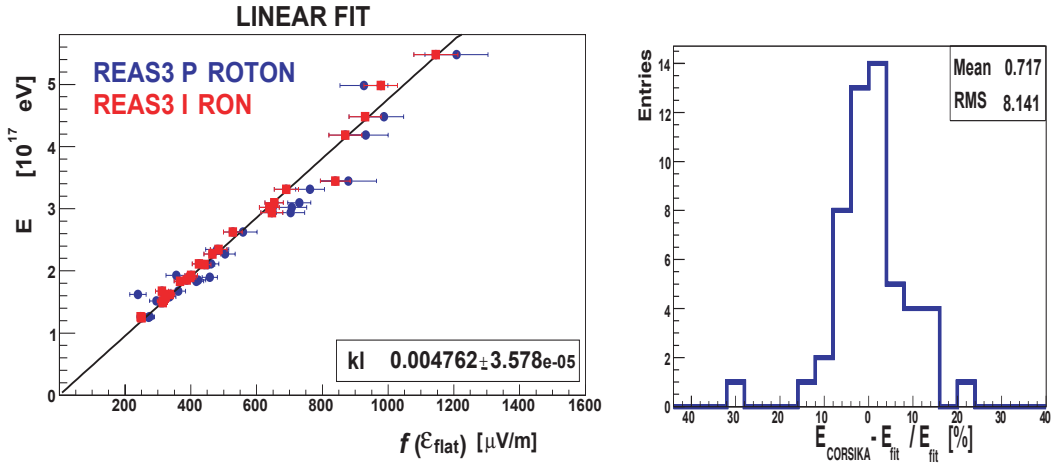

Figure 7.7: *Linear correlation between the electric field in the $flat$ region and the total primary energy, for the events in the first zenith angle bin. Both proton (points) and iron (squares) primaries are simulated. On the right part, the relative dispersion around the fit.*

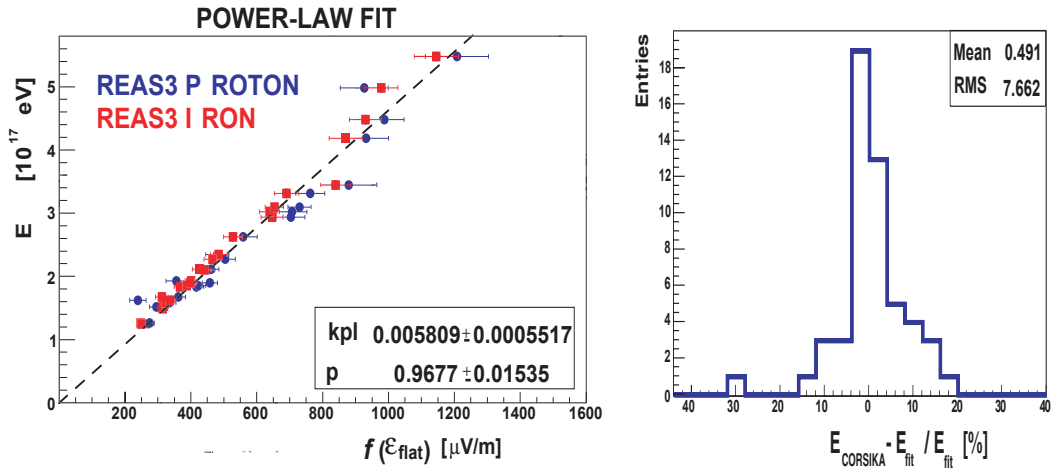

Figure 7.8: *Same as in **fig.**7.7 but with a power-law fit.*

to both S(1000) for the Pierre Auger Observatory experiment (Sommers, 2005) and S(500) for the KASCADE-Grande experiment (Toma, 2010). Respectively the water Cherenkov signal in the SD at 1000 m and the charge particle density at 500 m from the shower axis.

From the theoretical point of view, one should expect a direct correlation between the amplitude of the radio filtered pulse - normalized with the arrival direction - in this specific region and the energy of the shower, especially the electromagnetic energy (Huege et al. (2008), cf section 3.3).
Since no big difference between all the three normalizations introduced in section 7.2

Table 7.3: *Reconstructed parameters and RMS spread of the energy fit. Both linear and power-law fits are considered.*

zenith angle	E				
$\Delta\theta$	linear fit		power-law fit		
	$(k_{\rm l})$e-3 [GeV]	RMS[%]	$(k_{\rm pl})$e-3[GeV]	p	RMS[%]
1	4.762 ± 0.0036	8.14	5.8 ± 0.55	0.97 ± 0.009	7.66
2	4.901 ± 0.0026	6.48	6.0 ± 0.45	0.97 ± 0.01	6.24
3	5.968 ± 0.0027	5.09	6.8 ± 0.33	0.98 ± 0.008	5.47
4	5.642 ± 0.0026	6.27	6.0 ± 0.37	0.99 ± 0.01	6.28
5	5.996 ± 0.0025	6.41	7.1 ± 0.37	0.97 ± 0.009	6.41
$\Delta\theta$	$\rm E_{em}$				
	linear fit		power-law fit		
	$(k_{\rm l})$e-3 [GeV]	RMS[%]	$(k_{\rm pl})$e-3 [GeV]	p	RMS [%]
1	4.759 ± 0.0035	6.75	5.7 ± 0.53	0.97 ± 0.015	6.46
2	4.901 ± 0.0026	4.16	6.0 ± 0.45	0.97 ± 0.012	4.59
3	5.968 ± 0.0027	3.27	6.8 ± 0.33	0.99 ± 0.008	3.25
4	5.642 ± 0.0026	3.60	6.1 ± 0.37	0.99 ± 0.01	3.62
5	5.996 ± 0.0025	3.93	7.2 ± 0.37	0.97 ± 0.009	3.93
$\Delta\theta$	$\rm E_{cal}$				
	linear fit		power-law fit		
	$(k_{\rm l})$e-3 [GeV]	RMS[%]	$(k_{\rm pl})$e-3 [GeV]	p	RMS[%]
1	4.759 ± 0.0035	6.87	5.7 ± 0.5	0.97 ± 0.015	6.74
2	4.901 ± 0.0026	4.53	6.0 ± 0.4	0.97 ± 0.012	3.93
3	5.968 ± 0.0027	3.70	6.8 ± 0.3	0.98 ± 0.008	3.58
4	5.642 ± 0.0026	4.42	6.0 ± 0.4	0.99 ± 0.01	4.28
5	5.996 ± 0.0025	4.56	7.2 ± 0.4	0.97 ± 0.009	4.56

is observed, the expected linear correlation could be generally applied not only for the electromagnetic energy.

The measured or simulated radio pulse height ϵ_{flat}, normalized by sin(α), will immediately give information about the shower energy, using eq.7.1. The proportionality constant $k_{\rm l}$ [GeV] will depend on both the shower geometry (inclination) and on the energy component that is to be reconstructed, such as primary energy, electromagnetic energy, or calorimetric energy.

$$\mathrm{E}, \mathrm{E_{cal}}, \mathrm{E_{em}} = \frac{k_{\rm l}}{\sin(\alpha)} \left(\frac{\epsilon_{flat}}{\mu \mathrm{V/m}} \right) \tag{7.1}$$

The normalized radio pulse height f is simply an exponential function of the distance

$$\mathrm{f} = \frac{\epsilon_{\rm flat}}{\sin(\alpha)} = \frac{\epsilon_{\rm fit}}{\sin(\alpha)} \cdot \exp - \left(\frac{d_{\rm flat}}{R_0} \right) \tag{7.2}$$

The error on the normalized ϵ_{flat} is calculated with the Gaussian error propagation formula,

$$\sigma_{\rm f} = \sqrt{\left(\frac{\partial \mathrm{f}}{\partial \mathrm{d}_{flat}} \sigma \mathrm{d}_{flat} \right)^2 + \left(\frac{\partial \mathrm{f}}{\partial R_0} \sigma R_0 \right)^2 + \left(\frac{\partial \mathrm{f}}{\partial \epsilon_{\rm fit}} \sigma \epsilon_{\rm fit} \right)^2 + \left(\frac{\partial \mathrm{f}}{\partial \alpha} \sigma \alpha \right)^2} \tag{7.3}$$

where the covariance terms are neglected, and an uncertainty of 5 m is associated with d_{flat}, due to distance bin range used.
For the first zenith angle bin the correlation between the electric field in the $flat$ region and the total primary energy, fit with the linear function 7.1, are shown in **fig.**7.7. The figures relative to the calorimetric and electromagnetic energy for the other zenith bins are shown in Appendix B: section 13.1.1. On the right part of the figure, the relative deviation of the points from the linear fit, defined as ($\text{energy}_{\text{point}}$-$\text{energy}_{\text{fit}}$/$\text{energy}_{\text{fit}}$), are presented.
The RMS of the relative deviation is quite small and, even for the total primary energy, is of only 8 $\%$. This is the intrinsic energy uncertainty for the radio measurement due to shower-to-shower fluctuations.

From the experimental point of view, with the LOPES30 setup data, a power-law correlation between the total primary energy reconstructed by KASCADE or KASCADE-Grande and the electric field detected in the east-west polarization was found. Precisely $\epsilon_{\text{east}} \simeq \text{E}^{0.95\pm0.04}$ (Link, 2011).
In coherence with the experimental observation, also the power-law must be taken into account as fitting function, in order to test any possible improvement in the primary energy - ϵ_{flat} correlation.
The same simulated events are thus to be fitted also with the second function (**fig.** 7.8),

$$\text{energy} = \frac{k_{\text{pl}}}{\sin(\alpha)} \left(\frac{\epsilon_{flat}}{\mu\text{V/m}} \right)^{p} \tag{7.4}$$

with p and k_{pl} [GeV] the two free fitting parameters. The p value is expected around 1.05, i.e. 1/0.95, from the experimental data analysis (Link, 2011).

For the whole zenith angle range (0°-40°), no relevant differences between the two fits can be detected. The k_{pl} and k_{l} values of the two functions are comparable in each of the three energy normalizations and the p parameter reconstructed is close to 1 (see also Table 7.3).
Over the whole zenith angle range, a mean uncertainty of 6 $\%$ for the linear fit and 4 $\%$ for the power-law fit is found, i.e. the mean of the RMS values (Table7.3).

In summary, the linear function can be considered a good approximation for the analyzed correlation between the energy of an air shower and the filtered radio pulse in the $flat$ region. Moreover, as already pointed out, no big differences between the total (E) and partial (E_{em} and E_{cal}) energies is noticed.

7.5 X_{max} determination

The expected correlation between the atmospheric depth of the shower maximum (X_{max}) and the slope of the radio lateral distribution function is tested for the REAS3 simulations of the LOPES events (Selection1).

The ratio $\epsilon_{\text{flat}}/\epsilon_{steep}$ is viewed in relation to the X_{max} of the air shower, provided by the CORSIKA simulations (QGSJetII interaction model).

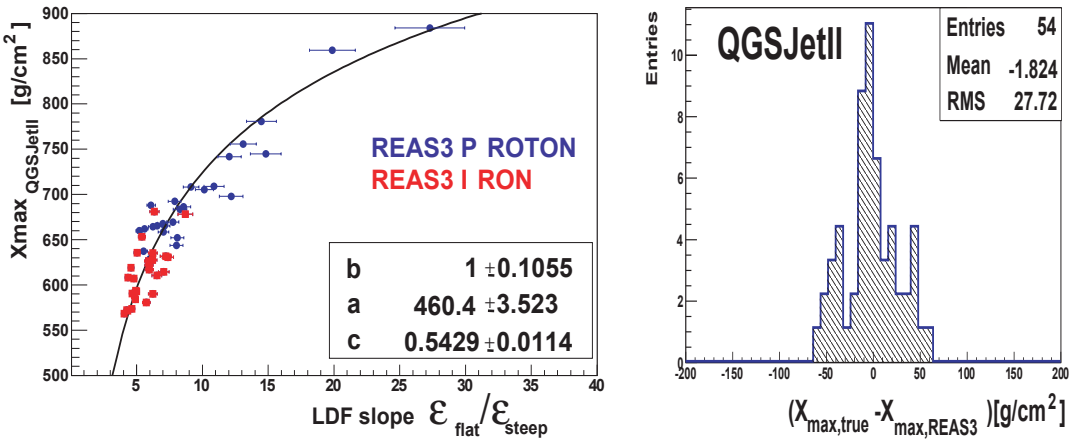

Figure 7.9: *Ratio of the simulated filtered radio pulse in the $flat$ and $steep$ region in relation to the depth of the shower maximum. Proton (points) and iron (squares) simulations, for the events in the first zenith bin are shown. In Appendix B (section 13.1.2) the figures of the other zenith bins are reported.*

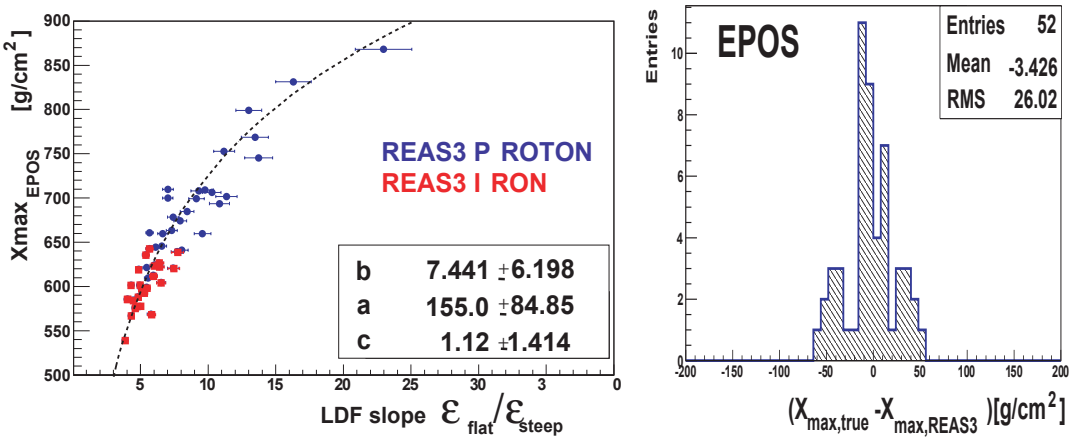

Figure 7.10: *Same as **fig.**13.6 but with EPOS interaction model simulations.*

The exponential function used to fit the LDF implies the $\epsilon_{\rm flat}/\epsilon_{steep}$ ratio to be exponential too, of the kind

$$\frac{\epsilon_{\rm flat}}{\epsilon_{\rm steep}} = \epsilon_{\rm ratio} = \exp - \left(\frac{\Delta d}{R_0}\right) \tag{7.5}$$

where R_0 is the fitting parameter and Δd is the distance between the $flat$ and the $steep$ regions, which, by definition for this LOPES analysis, is the constant value of 170 m (cf section 7.2.2).
The ratio can be considered as not influenced by the energy normalizations used so far, thus no further distinction by energy normalization is made.
A correlation between the $X_{max,CORSIKA}$ and the radio LDF slope is clearly visible.

Table 7.4: *X_{max} fitting function parameters and reconstruction uncertainty for the LDF slope of the total electric field strength $\epsilon_{\rm TOT}$. QGSJetII interaction model*

	E			
$\Delta\theta$	a	b	c	ΔX_{max}
0.°-19.4°	460.4 ± 3.5	1. ± 0.1	0.54 ± 0.01	28
19.4°-26.8°	266 ± 13.5	3.3 ±0.27	0.88±0.03	27
26.8°-32°	18 ±2	88.9 ±10.7	2. ±0.4	34
32°-36.2°	499.3 ±16.8	1.4 ±0.09	0.62±0.02	36
36.2°-40°	12.6 ±0.87	47±4.6	2.5±0.04	46

Table 7.5: *X_{max} fitting function parameters and reconstruction uncertainty found for the LDF slope of the total electric field strength $\epsilon_{\rm TOT}$. EPOS 1.99 interaction model*

	E			
$\Delta\theta$	a	b	c	ΔX_{max}
0.°-19.4°	155 ± 84.8	7.4 ±6.19	1.12 ±1.41	26
19.4°-26.8°	524 ± 2.1	1.0 ± 0.03	0.49±0.01	24
26.8°-32°	561 ±1.6	1.0 ±0.02	0.48± 0.01	37
32°-36.2°	605 ±1.4	1.0 ±0.03	0.48±0.01	34
36.2°-40°	34.3 ±2.8	20.7±2.2	2.16±0.03	41

The function

$$X_{max} = a \left[\ln \left(b \frac{\epsilon_{\rm flat}}{\epsilon_{\rm steep}} \right) \right]^c \tag{7.6}$$

used in Huege et al. (2008) (cf. section 3.3), fits the REAS3 simulated events (**fig.** 7.9, for the events in the first zenith angle bin). The correlations and fit for all the other zenith bins are reported in Appendix B: section 13.1.2 (**fig.** 13.6).

For this specific investigation and for the purpose of a comparison with the detected data in the next chapters, the b parameter is required to be, at least, $\geqslant$1. This restriction aims to avoid a bias in the application of the formula on LOPES measurements and to prevent that LOPES events can not be reconstructed. Indeed, the minimum value of $\frac{\epsilon_{\rm flat}}{\epsilon_{\rm steep}}$ ratio is heavily connected to the b parameter: $\left(\frac{\epsilon_{\rm flat}}{\epsilon_{\rm steep}}\right)_{\rm min}$=1/b. Values of b smaller than 1 constrain to apply the $X_{\rm max}$-formula only to LOPES events with a LDF-slope $\left(\frac{\epsilon_{\rm flat}}{\epsilon_{\rm steep}}\right)_{\rm LOPES} > 1$[3], excluding from the reconstruction all the flatter LDF-slope.

For the $X_{max,CORSIKA}$– LDF-slope correlation, the distribution of the deviation from the fit is calculated as well. The RMS spread is found to be 27-46 g/cm^2, with the larger values usually arising from the most inclined showers. This can be referred to as the intrinsic uncertainty of the slope method in reconstructing the shower maximum depth. These values are large if compared to the RMS found in the REAS2 paper (Huege et al.,

[3]Requiring $b \geqslant 1$ imply the, not fully correct, assumption to expect the minimum $\frac{\epsilon_{\rm flat}}{\epsilon_{\rm steep}}$ = 1

2008) (15-20 g/cm^2). Basically, this can be attributed to the simulation of a realistic case, namely the simulated antenna array of the LOPES experiment and the inclusion of the charge excess contribution for the total radio emission mechanism in REAS3. The radio lateral slope, reconstructed with the exponential fit of the electric field in the antennas, is affected by this contribution.
One possible way to reduce the uncertainty on the lateral slope would be the use of a multi-dimensional fitting function.

The three fitting parameters a, b and c obtained for each zenith angle range, are summarized in Table 7.4, with the corresponding uncertainty of the reconstruction method, i.e. the RMS spread from the fit.

At this point, the comparison between the values obtained using the two hadronic interaction models introduced above is of interest.
The values of the a, b and c parameters reconstructed for the events simulated with both QGSJetII and EPOS 1.99 interaction models are compared.
Even though the slope of the radio lateral distribution function is found to not strongly depend on the hadronic interaction model used for the particle cascade simulations (section 7.3), the reconstruction of X_{max} with the slope method, i.e. the a, b and c fitting parameters, is influenced by the $true$ X_{max} values given by the simulations. These values are quite different for EPOS 1.99 and QGSJetII interaction models.
In Table 7.5, the values obtained for the EPOS 1.99 interaction model, are shown.

The function eq.7.6 works for the QGSJetII as well as for the EPOS 1.99 interaction models, for all the zenith angle ranges.
Comparing the reconstructed fitting parameters, they are found to be sensitive to the number of analyzed events, to the zenith angle and to the hadronic interaction model.

The influence of the shower inclination on the radio lateral slope is affecting the goodness of the fit and the a, b and c fitting parameters, which vary from one zenith bin to another.
It is interesting to notice how the influence of the zenith angle on the slope is getting strong very fast, rendering it more difficult to distinguish between the primaries at only 40°, i.e. the last bin in this selection. For further discussion see also next section.

7.5.1 Zenith angle dependence

In the previous part, the events in different zenith ranges are separately looked at, in order to emphasize the primary mass dependence of the radio lateral slope.
However, it is convenient to investigate which kind of dependence is expected between the $\epsilon_{\rm flat}/\epsilon_{steep}$ ratio and the shower zenith angle.

The LDF slopes for the entire selection, i.e. 0°-40° zenith angle, are shown for the proton simulated (points) and iron simulated (squares) showers in relation to the cosine of the zenith angle (**fig.**7.11). A correlation is noticed.
In spite of large values for the $\epsilon_{\rm flat}/\epsilon_{steep}$, i.e. steeper lateral distribution function slopes, are clearly characteristic of the light element, the iron and proton profiles are approaching each other for events with a larger zenith angle. Even at 35° (i.e. cos(θ)$\simeq$ 0.82), the

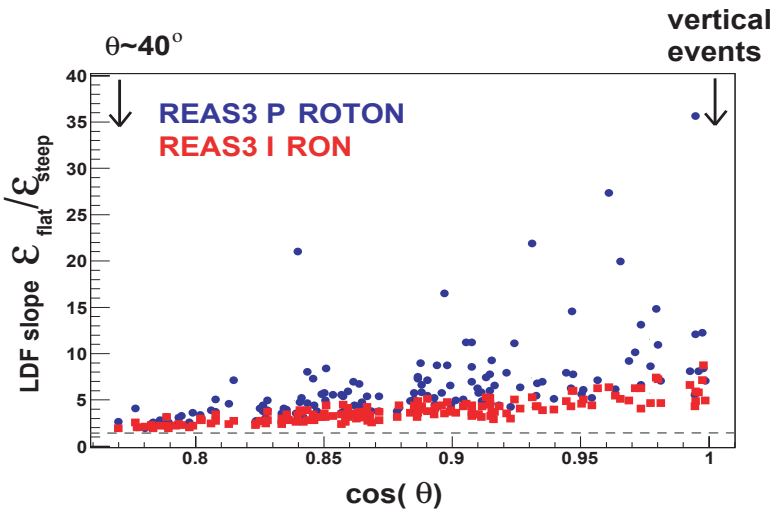

Figure 7.11: *Slope of the radio lateral distribution function in relation to the shower zenith angle, for the proton (circles) and iron (squares) simulated events in the whole selection. The profiles for protons (magenta) and irons (green) are drown as well.*

flattening of the radio lateral slope due to the inclination of the shower seems to become important and makes it much more difficult to distinguish the mass-composition effect.

It is though essential to stress that this analysis is made for the LOPES selection and setup, so the results can not be directly applied to other radio experiments.
The altitude of the LOPES experimental site (roughly sea level) and the frequency band filter (40-80 MHz) used, have both an influence on the value of the electric field in the $flat$ and $steep$ regions and on their positions far from the shower axis (Huege et al., 2008). This makes the d$_{flat}$ derived here a LOPES-specific value.
Moreover, the shower energy range detected by KASCADE-Grande, and the small LOPES array limit the choice for the distance of the $steep$ region at only 170 m from the identified $flat$ region. Larger primary energies and wider radio experimental arrays may possibly achieve larger $\epsilon_{\text{flat}}/\epsilon_{steep}$ values, and see the influence of the mass composition even at larger zenith angles.

7.6 Outlook

The objectives previously proposed for this chapter are achieved. The slope method analysis introduced in section 3.3 is revisited with REAS3 simulations of recorded LOPES events.

The influence of the charge excess contribution is visible, but does not prevent the identification of the $flat$ region for the primary energy investigation. This region is identified inside the LOPES array and its values are solid in comparison with several shower inclinations, different energy normalizations, and the two chosen hadronic in-

teraction models.

The minimum RMS spread of the LDF fits is quite small. Thus, an investigation on the primary energy of the cosmic ray with the LOPES experiment is possible within quite small predicted uncertainties ($\sim 8\%$ for the most inclined showers). Moreover, a linear correlation is expected between the radio amplitude in the $flat$ region and the primary energy reconstructed for the LOPES measurements.

The slope of the radio LDF simulated with REAS3 continues to show a clear dependence on the $X_{\max}$ even for the simulations of a realistic experimental setup.

Adequate parameters for both the primary energy and the $X_{\max}$ reconstruction with the LOPES measurements still remain to be identified. Higher statistics are demanded and a further step in the simulations is performed and discussed in the next chapter.

8 The slope method applied to refined simulations of LOPES measurements

The slope method analysis was successfully investigated with REAS3 simulations adapted to a realistic experimental acceptance and setup (LOPES experiment). Significant outcomes were discussed in the previous chapter and the application of the slope method to the LOPES experimental data was dealt with as well.

For a direct comparison with the experimental data (cf. Chapter 9) more precise parameters for the energy and $X_{\max}$ reconstructions are necessary. On the one hand, higher statistics in the selection are required: The LOPES events in Selection2 are exploited. In addition, a further step in order to reduce the shower-to-shower fluctuations is suggested: Among the simulated showers, one is chosen which represents best the shower reconstructed by the KASCADE particle detector experiment. For a precise description of this methodology of air shower selection we refer to (Ludwig, 2011). Some details of the process are given below:

Two REAS3 simulations (one for proton, one for iron) are performed for each event of Selection2 (cf. section 4.1.3). The air shower parameters (core position, arrival direction and primary energy), provided by the KASCADE(-Grande) reconstruction, are used as input parameters to generate CONEX (Pierog et al., 2006) showers. QGSJetII (Ostapchenko, 2006) and UrQMD (Bass et al., 1998) are used respectively as high and low energy interaction models. 200 CONEX showers for proton and 100 for iron (less fluctuations) are simulated.
Among these 300 showers, one CONEX shower for proton-primary and one for iron-primary which reproduces best the number of muons (N_μ) reconstructed by KASCADE are chosen. The selected CONEX showers are, then, reproduced with CORSIKA and REAS3.

In this new procedure, the parameter N_μ is fixed, but the number of electrons is still free to vary and the $X_{\max}$ of the shower still free to fluctuate.

8.1 Single component of the radio pulse amplitude

The total electric field $|\overrightarrow{\epsilon_{\mathrm{TOT}}}|$, simulated at each observer position, considered so far, can not be directly compared with the LOPES data.
In the LOPES30 and LOPESPol setups (cf. section 4.1.1) the antennas were suited for the detection of only one or two components of the total electric field, since they were oriented either to the east-west or to the north-south directions; only five antennas of the LOPESPol setup could measure two electric field components at the same position.

Therefore, LOPES can not generally determine the information of the total radio pulse. A comparison with a single electric field component simulated at each antenna position is, thus, demanded.

The selection for events in Selection2 (cf. section 4.1.3) was performed according to the radio pulse detected in the east-west (EW) direction, where the signal-to-noise ratio is expected, in average, higher compared to the north-south direction. An appropriate analysis with the REAS3 simulated LDF is accomplished with the single EW-component of the electric field: ϵ_{EW}.

A proper normalization of the electric field in EW is required and the single component $|\mathrm{P_{EW}}|$ is taken (cf. fig. 5.1).

Two assumptions were made in the previous ϵ_{TOT} study: One concerns the geomagnetic effect as the predominant emission mechanism. This allows the normalization for the sinus of the geo-magnetic angle α[1] (cf. Chapter 5).
The second regards the choice of the 1D-exponential fit for the lateral distribution function (cf. Chapter 6). Even though the charge excess contribution affects the radio lateral distribution in dependence on the azimuthal observer position, the effect is assumed to generally average out. The mean RMS spread of the residuals computed for the REAS3 simulated LDF is found of only few percent ($\sim 8\%$) (cf. Chapter 6).
For the events with a small contribution from the geomagnetic effect — i.e. small α — these two assumptions break when merely a single component, EW in this case, of the filtered electric field is considered.
For those events, the charge excess contribution becomes predominant when a single component of the radio pulse is taken, and the one-dimensional (one spatial dimension) fit seems not enough to properly describe the radio lateral distribution function.

As possible solutions to this problem are suggested both the use of a multi-dimensional (more than one spatial dimension) function for the radio LDF fit and/or the search for a reasonable normalization which would average out the charge excess effects on the different antennas.
These possibilities are not investigated in this dissertation but the problem is handled instead by using a further cut on the arrival direction of the events: Taking into account the considerations made in Chapter 5, a small part of the sky is cut away by limiting the east-west component of the Lorentz vector $\overrightarrow{\mathrm{P}}$ to a minimum value. $|\mathrm{P_{EW}}| > 0.2$ is considered to be a suitable limit to remove the non-normalizable lateral distribution functions.
9 events coming from the south out of 238 are removed (cf. section 4.1.3).

8.2 The $flat$ region

The same procedure used in the previous chapter (section 7.2) is applied also to the N_μ-preselected simulations, in order to identify the $flat$ region.

In fig.8.1, the relative RMS spread of the LDF fits, for the 114 events in the first zenith angle bin (0°-20°) - 57 protons and 57 irons - is presented. Only two energy

[1] $|\overrightarrow{\mathrm{P}}| = |\mathrm{Bxv}| \simeq \sin(\alpha)$

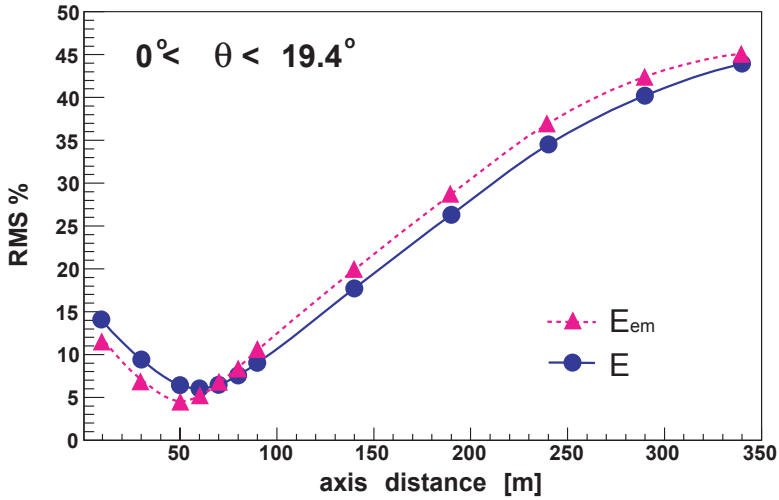

Figure 8.1: *RMS of the single component ϵ_{EW} at different distances from the shower axis. Two energy normalizations, the total (blue circles) and the electromagnetic (magenta triangles) energies, are considered.*

normalizations, precisely the total and the electromagnetic energy, are considered.
The usual twelve distance-bins (cf. section 7.2.1) are used, with the range of 10 meters between 50 m and 90 m from the core, which is the region where the minimum RMS is expected.
In Table 8.1 the values for the minimum RMS spread and the identified $flat$ region $\mathrm{d_{flat}}$ are reported for the whole zenith angle range in the selection.

Even with the higher statistics of Selection2 and the single electric field component in the east-west direction (ϵ_{EW}), similar values to section 7.2.1 are found:
On the one hand, the minimum RMS for the total energy normalization is between 6 % and 8 % (the largest values are characteristic of larger zenith angles). High resolution (directly) for the total energy reconstruction is, thus, predicted.
Moreover, the normalization for the electromagnetic energy has, as expected, the lowest RMS values (4 % on average). The predicted high resolution for the E_{em} reconstruction is of great importance: Once the electromagnetic energy is reconstructed with such low uncertainty, it is possible to yield the total energy by applying corrections for the "missing" energy.[2]
On the other hand, the $\mathrm{d_{flat}}$ presents a general constancy, even with different selections of the LOPES measurements. The maximum value is of 90 m from the shower axis, which corresponds to maximum 117 m in ground coordinate system, with the implication that the $flat$ region is again predicted inside the LOPES array.

[2]The missing energy is the fraction of the total primary energy carried away by neutrinos and high-energy muons, which do not interact in the atmosphere

Table 8.1: *Distance of the $flat$ region - Selection 2*

zenith angle		E		E_{em}	
$\Delta\theta$	entries	d_{flat} [m] $\pm$5 m	RMS % min	d_{flat} [m] $\pm$5 m	RMS% min
0.°-19.4°	114	60	6.0	50	3.7
19.4°-26.8°	110	70	6.2	60	4.7
26.8°-32°	102	70	6.4	60	4.8
32°-36.2°	80	90	7.6	70	6.3
36.2°-40°	48	90	8.0	80	6.3

8.3 Reconstruction of air shower parameters

With the identification of the $flat$ region for this specific selection of events also the $steep$ region is consequently identified. The d_{steep} is, again, set at 170 m distance from the $flat$ region.

The parameters necessary for the comparison and/or reconstruction of the primary energy and the shower maximum depth for the detected LOPES data (cf. Chapter 9) are determined below:

Primary energy determination

Only the total primary energy (E) normalization is considered, since it is the only quantity of interest for the following comparison with the LOPES data.

The filtered amplitude, simulated at the antenna position, is divided by the effective LOPES bandwidth (31 MHz), to make the values comparable to what is experimentally detected. Moreover, as previously discussed, the normalization to the arrival direction is performed by the single EW component of the **P** vector: P_{EW} (cf. Chapter 5).

Slightly different (larger) parameters for the linear (eq.7.1) and power-law (eq.7.4) correlations are expected. In fig.8.2 and in fig.8.3, respectively, the linear and the power-law fits, for the events in the first zenith bin, are presented. The figures relative to the energy correlation for Selection2, for the other zenith bins, are reported in Appendix C: section 13.2.1.

The k_l and k_{pl} parameters reconstructed for the linear and power-law fits are summarized in Table.8.2 as well as the RMS values of the relative spread from the fits.

Even for the single electric field component (ϵ_{EW}), the linear fit seems to well represent the correlation with the total primary energy.

The average intrinsic uncertainty on the primary energy reconstruction with the radio measurements is predicted around 7 %.

$X_{\max}$ determination

The filtered electric field ϵ in the $flat$ and in the $steep$ regions is extrapolated from the LDF fit values.

The correlation between the ratio $\epsilon_{\mathrm{flat}}/\epsilon_{\mathrm{steep}}$ and the $X_{\max}$ is again analyzed (Appendix

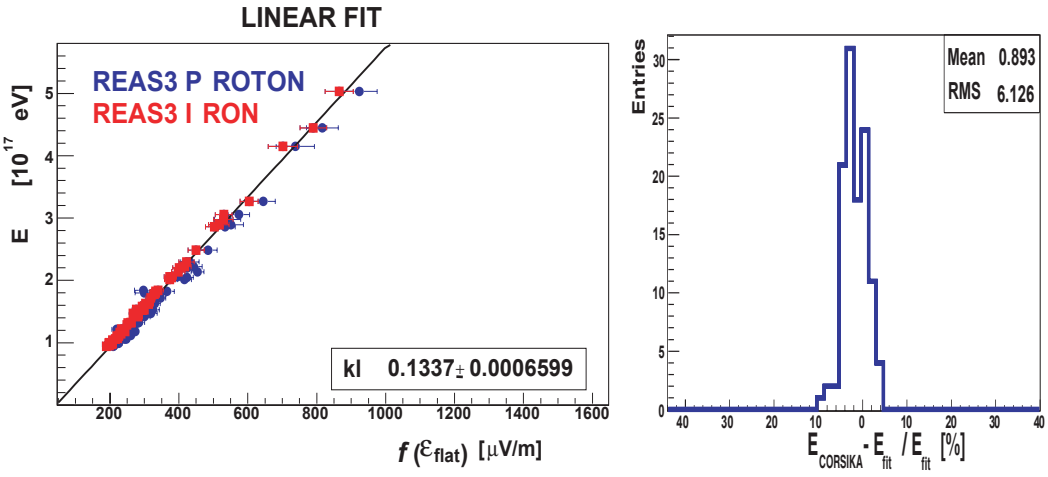

Figure 8.2: *Left: The correlation between the primary energy and the single electric field component in the $flat$ region is fit with a linear function. The energy is given by the KASCADE reconstruction. Only events in the first zenith angle bin, Selection2, are shown. Right: Relative dispersion around the fit gives the precision on the energy reconstruction achievable in the $flat$ region*

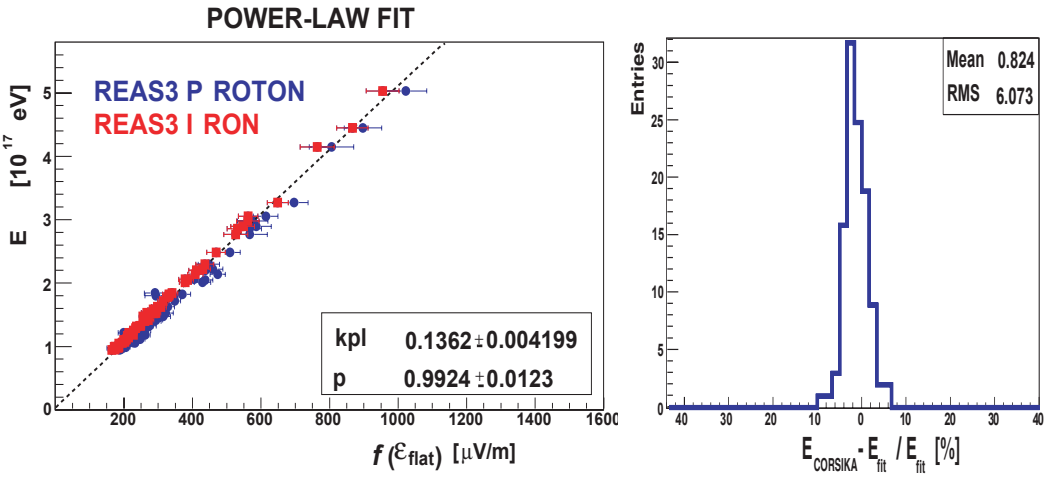

Figure 8.3: *The same correlation shown in fig.8.2 is now fit with a power-law*

B: fig.13.14). The X_{max} are directly given by CORSIKA (QGSJetII) and are considered as $true$ values.

Larger quantities for the $\epsilon_{flat}/\epsilon_{steep}$ ratio, i.e. steeper LDF slope, present also larger errors, derived with the Gaussian error propagation. These large uncertainties are due to both the value of σ_{R0} from the fitting procedure, which does not differ much among the events, and to the use of an exponential function. In general, this causes the proton events, i.e. steeper LDF slope, to be affected by a larger uncertainty compared to the iron events.

Table 8.2: *Energy fit parameters for the linear and power-law functions.*

	E				
	Linear fit		power-law fit		
$\Delta\theta$	k_l	RMS%	k_{pl}	p	RMS%
0.°-19.4°	0.13 ±0.66e-3	6.1	0.14 ±4.25e-3	0.99 ± 0.01	6.1
19.4°-26.8°	0.15 ± 0.68e-3	6.2	0.16 ±4.58e-3	0.98 ± 0.01	6.1
26.8°-32°	0.16 ± 0.60e-3	6.4	0.17 ±3.20e-3	0.98 ± 0.01	6.2
32°-36.2°	0.18 ± 0.68e-3	7.7	0.2 ±4.17e-3	0.95 ±0.01	7.0
36.2°-40°	0.19 ± 0.72e-3	8.1	0.2 ± 4.09e-3	0.97 ±0.01	7.8

Table 8.3: *X_{max} fitting function parameters and reconstruction uncertainty.*

	E_p			
$\Delta\theta$	a	b	c	ΔX_{max}
0.°-19.4°	200.0 ± 0.1	7.00 ± 0.01	0.871 ±1e-3	29.3
19.4°-26.8°	195.0 ± 0.1	6.90 ±0.01	0.943 ±1e-3	33
26.8°-32°	238.7 ±4.0	3.82 ±0.17	1.000 ±1e-3	35.4
32°-36.2°	220.0 ± 0.1	5.80 ±0.02	1.001 ±1e-3	37.5
36.2°-40°	88.0 ±0.1	20.00 ±1.75	1.450 ±1e-3	37

For the specific case of the mass sensitivity investigation through the slope method, the iron-simulated events, generally affected by lower uncertainties, will have a larger weight on the fit procedure - thus on the a, b and c parameters identification - compared to the proton simulated events.
Nevertheless, this may not be considered, in principle, as a limitation for the X_{max} investigation. Instead, even more realistic parameters (a, b and c) can be reconstructed if the expected mixed composition abundances are correctly taken into account for the primary energy range of the selection.
In this investigation, the simplest situation of 50% proton and 50% iron composition is considered.

The free parameters, a, b and c of the fitting function eq.7.6 reconstructed for this selection (Appendix B: fig.13.14) are summarized in Table 8.3.

The expected uncertainty (ΔX_{max}), defined as the difference between the $X_{\mathrm{max,true}}$ (points) and the $X_{\mathrm{max,fit}}$ values, is reported as well and it is referred to as the uncertainty (maximum of 37 g/cm^2) on the X_{max} reconstruction with the slope method for the LOPES events.
The parameters in Table 8.3 will be used to reconstruct the depth of the shower maximum for the LOPES events and compare with the REAS3 prediction.

8.4 Outlook

The slope method analysis has been investigated with REAS3 simulations of LOPES detected events based on a Nμ–pre-selection for the CORSIKA showers. In this way, the shower-to-shower fluctuations are reduced, and an analysis without fixing X_{max} is allowed.

The usual procedure discussed in Chapter 7 was applied to identify the $flat$ region. The general constancy of the $flat$ region range (60-90 m) over different selections and different hadronic interaction models used was noticed.
This allows us to employ the predicted d_{flat} to extrapolate the radio amplitude in the measured lateral distributions of LOPES.

The parameters necessary for the primary energy and X_{max} reconstruction are derived, after a proper normalization of the radio electric field amplitudes.
These parameters are directly exploited for the comparison and reconstruction of primary energy and X_{max} with the LOPES experimental data.

9 The slope method applied to the LOPES data and composition analysis

In the previous chapters it was discussed how the REAS3 simulations of the LOPES events have been employed to test the slope method.
The application to LOPES measurements is promising:
On the one hand, the good, but yet not complete, agreement in recent comparisons of the LDF between REAS3 simulations and LOPES data (Ludwig, 2011) suggests to apply the slope method also to the experimental data. On the other hand, for the primary energies of the analyzed selections, the $flat$ region, which is the distance to the shower core relevant for this method, is predicted inside the LOPES antenna array. Moreover, the range of the $flat$ region (Tables 7.1 and 7.2 and 8.1) appears quite stable over different event selections and almost independent of the hadronic interaction model used in the CORSIKA showers. Thus, it is reasonable to consider the distance predicted by the simulations as true $flat$ region also for the LOPES events (cf. Table 8.1).
The measured radio amplitude (ϵ) in the $flat$ and $steep$ (i.e. 170 m distance from $\mathrm{d_{flat}}$) distances are derived directly from the LDF fit.

In the next part, the direct application of the slope method to the LOPES measurements is discussed, which results in the reconstruction of the air shower parameters (energy and $\mathrm{X_{max}}$).

9.1 Primary energy and ϵ_{flat}

One of the fundamental purposes of a stand-alone radio experiment is to reconstruct the energy of the primary cosmic rays.
An important result achieved with the LOPES experiment is the clear dependence of the recorded radio pulse on the primary energy (Horneffer et al., 2007). The correlation between the measured CC-beam (cf. section 4.1.2) and the primary energy is parametrized as $\epsilon \simeq E^{0.95\pm0.04}$, where the primary energy is reconstructed by KASCADE-Grande.

One further argument is to be discussed here: the $flat$ region ($\mathrm{d_{flat}}$) is argued as the most suitable distance from the shower axis to look at the correlation between the radio electric field and the primary energy.
Instead of the calculated CC-beam pulse, the value of the LDF fit in the $flat$ region is considered.

The position of the $flat$ region used in the following has been previously determined with REAS3 simulations of the LOPES events (Table 8.1). This is allowed by a solidity

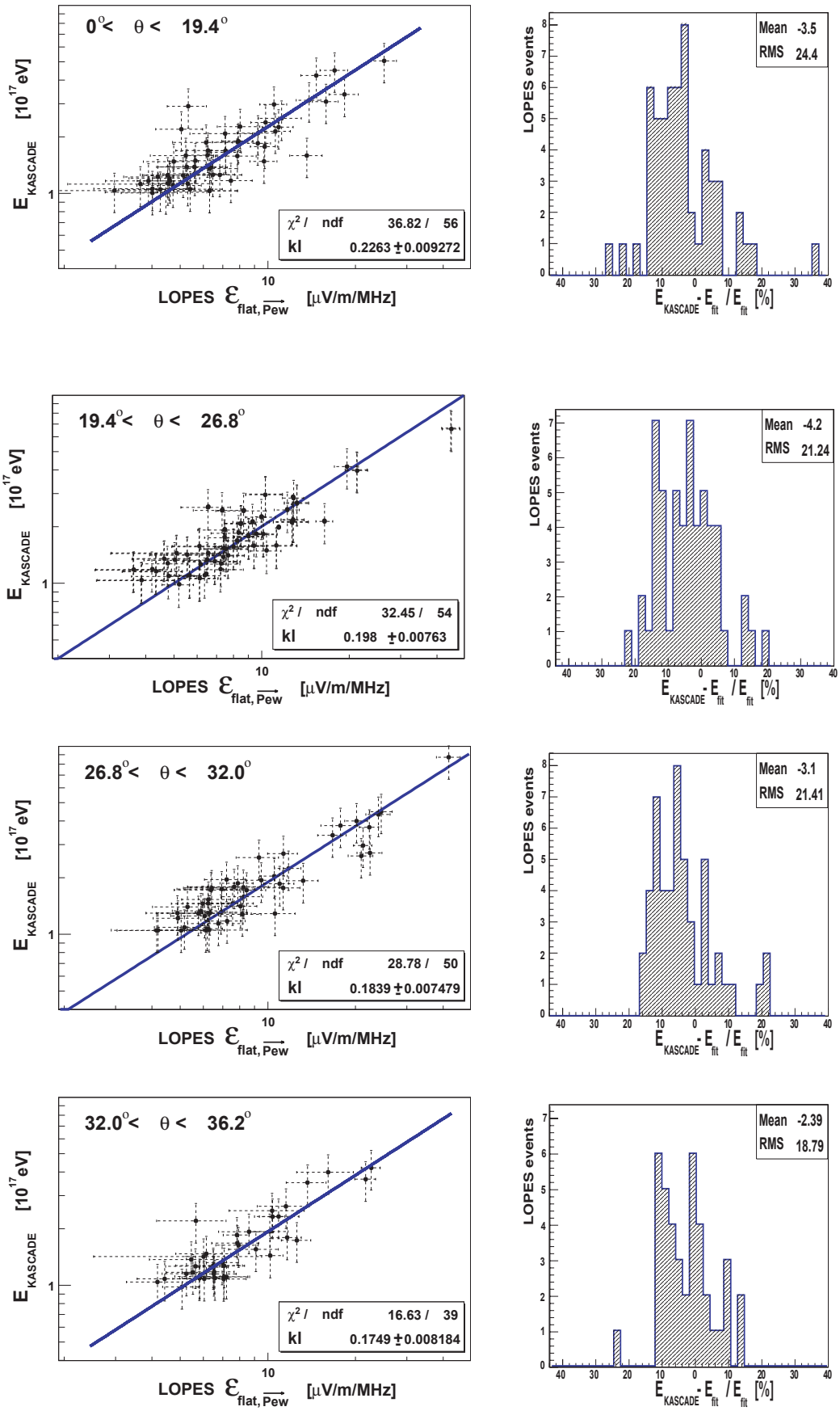

Figure 9.1: *to be continued in the next page.*

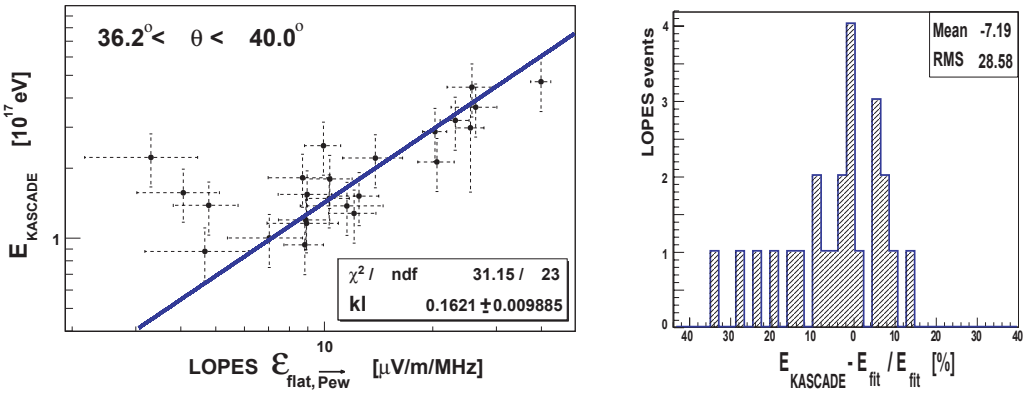

Figure 9.2: *(Continued) Linear correlation between the primary energy reconstructed by KASCADE-Grande and the filtered radio pulse detected in the $flat$ region. The position of the $flat$ region has been determined with REAS3 simulations (cf Chapter 8).From top to bottom, in order, events from the first to the fifth zenith angle bin are separately shown.*

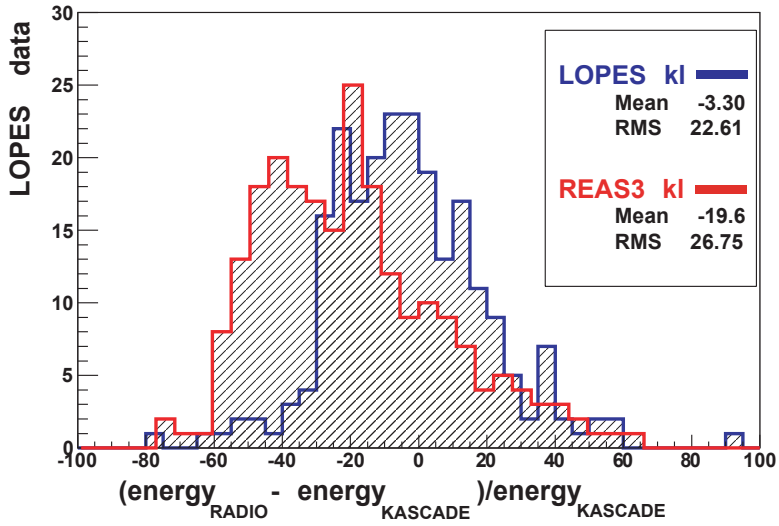

Figure 9.3: *Primary energy reconstructed by using the measured radio pulse in the $flat$ region, and the REAS3 (red) and the LOPES kl parameters of the linear fit (Table 8.2 for REAS3 kl, **fig.**9.2 for LOPES kl). The systematic deviation is due to the still existent discrepancy between simulations (REAS3) and measurements or due to a mis-reconstruction of the KASCADE energy.*

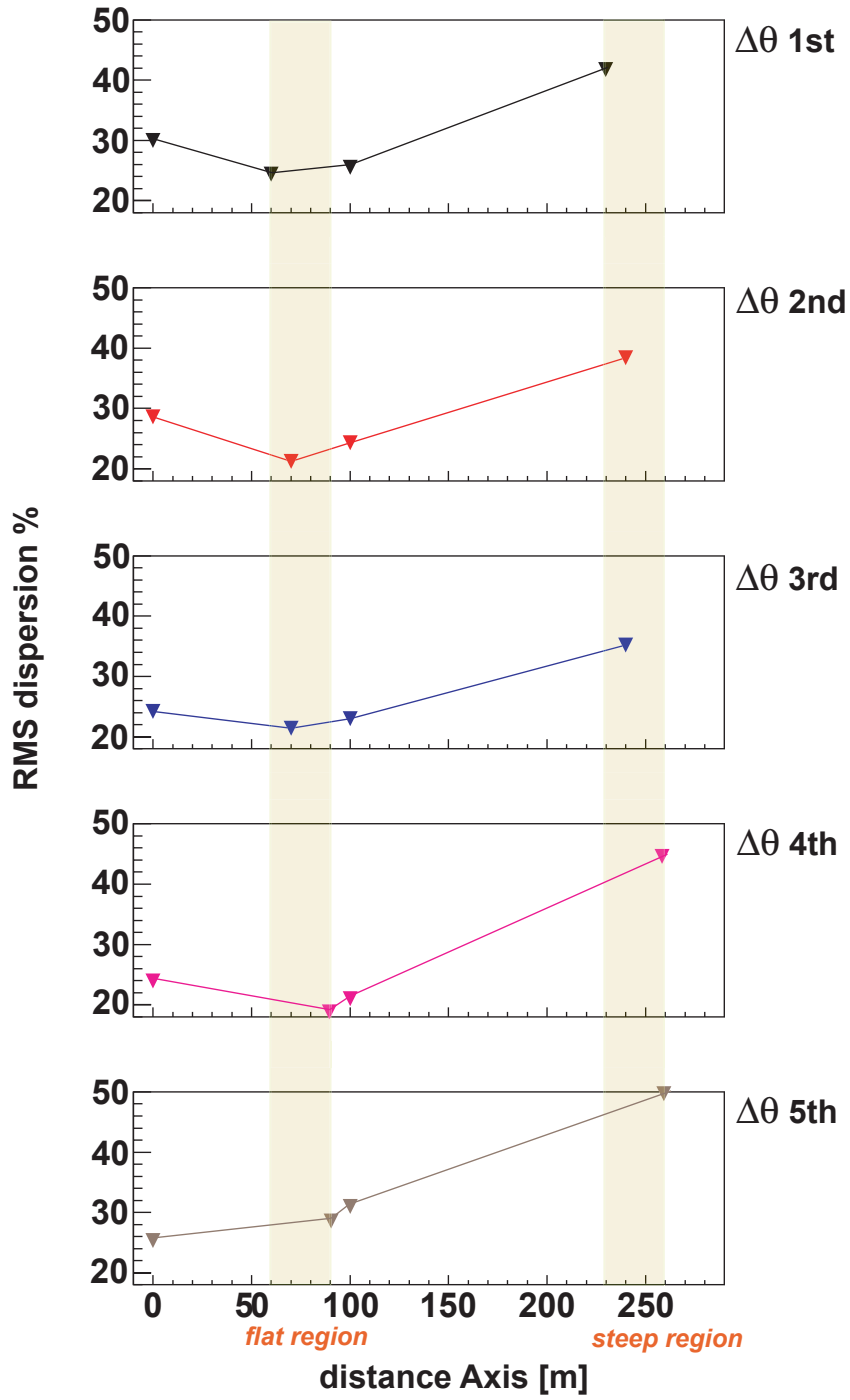

Figure 9.4: *The computed RMS spread from the linear fit (**fig.**9.2) at several distances from the shower axis. The distance-ranges where the $flat$ and $steep$ region are predicted by REAS3 simulations are highlighted. The primary energy correlation with the electric field in the $flat$ region shows a generally lower value.*

of the $flat$ region values shown over several event selections and hadronic interaction models (cf. Chapter 8).

REAS3 simulations adapted to a realistic case for the LOPES geometrical acceptance and setup, show a correlation of $\epsilon_{\rm flat}$ not only with the electromagnetic energy but also with the total energy of the air showers (cf. sections 7.4 and 8.3).
Both a power-law and a linear correlation are discussed in the previous chapter and only minor differences are noticed. Therefore, an investigation with the simpler linear fit is proposed here for the recorded LOPES electric field.

The primary energy values taken for this investigation are derived with the KASCADE (-Grande) reconstruction; information about the muons and electron number is derived from KASCADE (cf. section 4.1.3).
An overestimation of the muon number may be expected, due to the punch-through effect: The KASCADE experiment, in fact, is supposed to work up to a primary energy of 10^{17} eV. The muon detectors are shielded in order to avoid the electromagnetic component to penetrate. Nevertheless, for primary energy larger than $> 10^{17}$ eV, and for distance above 40 m from the core position, there is a high probability that electrons and positrons pass the shield and are counted as muons.
The reconstructed primary energy is considered with an uncertainty of 20 $\%$ up to 40 $\%$, on a per-event basis as reconstructed by KASCADE(-Grande).

The electric field in the $flat$ region, normalized for the arrival direction of the shower, is expressed as [1]

$$\epsilon_{\rm flat,|\overrightarrow{P_{EW}}|} = \epsilon_{\rm fit} \cdot \frac{\exp - \left(\frac{d_{\rm flat}}{R_0}\right)}{\mid \overrightarrow{P_{\rm EW}} \mid} \tag{9.1}$$

The $\mid \overrightarrow{P_{EW}} \mid$ is the $\overrightarrow{P}$ component along the east-west direction (cf. Chapter 5).

This is an approximation for mainly two reasons. First of all, as discussed in the previous chapters, the geomagnetic effect is considered to be the main, but not the unique, radio emission mechanism (cf. Chapter 5). Second, the LOPES antennas partially detect also the vertical component of the total electric field, due to their inverted V-shape.

The statistical uncertainties are calculated with the Gaussian error propagation formula

$$\sigma\epsilon_{\rm flat,|\overrightarrow{P_{EW}}|} = \sqrt{\left(\frac{\partial\epsilon_{\rm flat,|\overrightarrow{P_{EW}}|}}{\partial d}\sigma_d\right)^2 + \left(\frac{\partial\epsilon_{f\rm lat,|\overrightarrow{P_{EW}}|}}{\partial R_0}\sigma_{R_0}\right)^2 + \left(\frac{\partial\epsilon_{\rm flat,|\overrightarrow{P_{EW}}|}}{\partial\epsilon_{\rm fit}}\sigma_{\epsilon_{\rm fit}}\right)^2} \tag{9.2}$$

where the covariance terms are ignored.

Each zenith angle bin is separately looked at, since the $flat$ region values have been determined in this way.

[1] An exponential fit of the radio lateral distribution is considered

The data are fit with a linear function

$$\mathrm{E} = k_{\mathrm{l}} \frac{\epsilon_{flat,|\overrightarrow{P_{EW}}|}}{\mu\mathrm{V/m}} \tag{9.3}$$

with k_{l} [GeV] the only free fitting parameter.
In **fig.**9.2 a linear correlation is visible in each zenith angle bin, with a reduced χ^2 between 0.4 and 0.6 and a relative spread from the fit of less than 24 $\%$ for the first four zenith angle bins. In the last zenith angle bin ($\Delta\theta$=36°-40°) the values are larger, respectively 0.97 and $\sim$ 28 $\%$ also due to the lower statistics.

A first perception of the uncertainty on the primary energy reconstruction arises from **fig.**9.3, red line. The REAS3 parameters for the linear correlation (Table 8.2) are employed to reconstruct the energy. The radio amplitude in the $flat$ region is directly taken from the LOPES LDF. The clear systematic shift to negative values emphasize the above-discussed discrepancy between the measured and simulated radio amplitude in the $flat$ region.

A slight discrepancy between the REAS3 simulations and LOPES events is pointed out (please see **fig.**8.2 and Appendix B: **fig.**13.10): the k_{l} parameters, even though of the same order of magnitude, do not agree within the errorbars (cf. Table 8.2-*linear fit* and **fig.**9.2). An opposite tendency of the LOPES $\mathrm{k_l}$ to decrease with the shower zenith angle is clearly visible. Moreover, the ϵ_{flat} from the LOPES LDF tends to be smaller compared to the REAS3 values.

Two motivations come into question: first, the still remaining discrepancy between the REAS3 and the LOPES LDF and, as a consequence, the misidentification of the $flat$ region in the LOPES measurements. Second, the punch-through effect, in which the energetic electrons in the shower are mistaken as muons. An overestimation of the reconstructed primary energy, used as input for the simulations, could cause the divergences.
An update of the analysis with the latest version of the REAS code (REAS3.1) and the successor CoREAS is highly suggested.

9.1.1 Existence of the $flat$ region in LOPES data

Beside the linear correlation between the primary energy and the normalized electric field strength recorded by the LOPES experiment, the next step is to investigate whether the $flat$ region as determined with REAS3 simulations is the most appropriate distance from the shower axis to reconstruct the primary energy.
The smallest uncertainty on the radio-reconstructed energy, mainly due to the shower-to-shower fluctuations, is, in fact, predicted in this region.

For comparison, three other distances from the shower axis, of the same LDF fit, are considered: 0 m, 100 m and the steep region, i.e. between 230 m and 260 m for this specific selection (Selection2).
Plots similar to **fig.**9.2 for the other distances can be found in Appendix C: Chapter 14.

The RMS of the relative spread from the linear fit is used as comparison tool.
In $\mathrm{d_{flat}}$ the RMS is practically always the smallest (**fig.**9.4). At 100 m, so only at 40-10 m from the $flat$ region, the RMS increases on average less than 10 $\%$, while, in the

steep region, the RMS uncertainty grows, on average, of more than 80 $\%$.
At 0 m the RMS value varies quite a lot over the zenith angle range, and becomes comparable with the RMS uncertainty in the $flat$ region for the most inclined showers.
The RMS value for the complete zenith angle range is of $\sim$ 22.9 $\%$ (**fig.**9.3, blue line).
An upper limit on the precision for the energy reconstruction with the LOPES measurements is reached of circa 20 $\%$. This is comparable with the statistical uncertainty on the KASCADE(-Grande) energy reconstruction.

These results confirm the $flat$ region as the best distance for the primary energy investigation, especially for smaller zenith angles. On the one hand, the theoretical prediction concerning the existence of a characteristic distance at which the energy reconstruction works best, is experimentally verified. On the other hand, this measured distance agrees quite well with the REAS3 predicted distance.
For a more complete analysis, one may investigate further distances from the shower axis, especially in dependence on the shower inclination.

9.1.2 Outlook

Regardless of the minor divergences between the REAS3 simulations an the LOPES data, the main goal of the investigation is achieved: Also with measured data, the $flat$ region is confirmed to be the most suited distance for the primary energy reconstruction. An upper limit for the uncertainty ΔE reached with the LOPES measurement is of approximately 23 $\%$ - i.e. the RMS spread of the LDF fit in the $flat$ region.

For further investigations, an independent measurement at different distances, thus not using the same LDF fit, is suggested. For this, a high number of antennas are recommended. To answer this question the LOFAR experiment Falcke et al. (2006) is well suited, do to its high density of antenna stations.

9.2 X_{max} determination with the LOPES measurements

An indication for the primary cosmic ray mass is given by the atmospheric depth of its shower maximum (X_{max}): Heavier nuclei are characterized by a larger cross-section compared to the proton-like particles. Consequently, for the same primary energy and almost independent on the shower geometry, iron-like cosmic rays interact earlier in the atmosphere compared to light nuclei and the resulting air showers develop more rapidly. Due to a geometrical effect, this implies a flatter slope of the radio LDF for heavier nuclei (cf. Chapter 3).

Experiments which can have access to X_{max} are the ones where the detection method considers the air shower signal integrated over all the atmosphere, such as Cherenkov detectors and radio detectors, or the ones which can accurately measure the longitudinal development of the air shower, such as the fluorescence detectors.
While for both, the Cherenkov and the fluorescence detectors, the capability to measure X_{max} has been widely proven, reaching also quite low uncertainties [2], the radio detection only recently started to approach an X_{max} sensitivity investigation with experimental data (Apel et al., 2012a).

The radio detection offers two main methods for the determination of X_{max}: one by measuring the radio wavefront shape (cone method), the other by looking at the slope of the lateral distribution function (slope method).
The first method has been deeply investigated in the framework of the LOPES experiment (Schröder, 2010).

In this analysis the second method (slope method) will be applied to the LOPES data. Although the high environmental noise and the small LOPES array prevent the LOPES experiment to achieve precise X_{max}, it will be shown that not only quite reasonable values of X_{max} are reconstructed for each event, according to what is expected for the cosmic ray nuclei, but also quite low uncertainties can be obtained. Indeed, the slope method reaches a better precision for the LOPES measurements than the cone method.

9.2.1 X_{max} reconstruction

The reconstruction of X_{max} is performed by applying the slope method. The information about the ratio $\epsilon_{\mathrm{flat}}/\epsilon_{\mathrm{steep}}$ is provided by the LDF fit of the LOPES measurement. In this first step, the events in Selection2 (section 4.1.3) are taken into account.

The complete error propagation formula reported below, excluding only the negligible covariance terms, is used to compute the uncertainty of the $\epsilon_{\mathrm{flat}}/\epsilon_{\mathrm{steep}}$ (eq. 7.5).

$$\sigma\epsilon_{\mathrm{ratio}} = \sqrt{\left(\frac{\partial\epsilon_{\mathrm{ratio}}}{\partial d}\sigma_d\right)^2 + \left(\frac{\partial\epsilon_{\mathrm{ratio}}}{\partial R_0}\sigma_{R_0}\right)^2} \tag{9.4}$$

As expected and already discussed for the REAS3 simulations (cf. Chapter 7), also the $\epsilon_{\mathrm{flat}}/\epsilon_{\mathrm{steep}}$ for the LOPES experimental data shows a dependence on the cos(θ) (**fig.**9.5).

[2] 20 g/cm^2 (Abraham et al., 2010c) with the fluorescence detector at the Pierre Auger Observatory

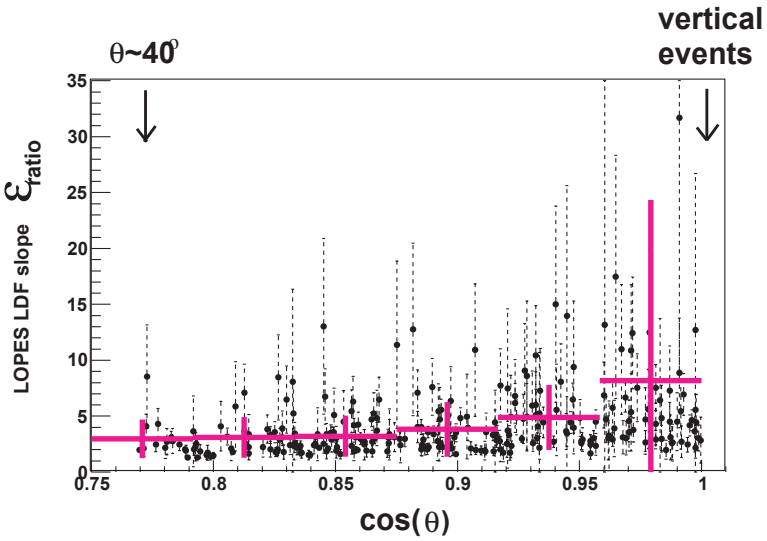

Figure 9.5: *Dependence of the $\epsilon_{\mathrm{flat}}/\epsilon_{\mathrm{steep}}$ ratio and the zenith angle, reconstructed for the LOPES events. Only for smaller zenith angle, the $\epsilon_{\mathrm{flat}}/\epsilon_{\mathrm{steep}}$ ratio presents also larger values, i.e. steeper slope of the LDF.*

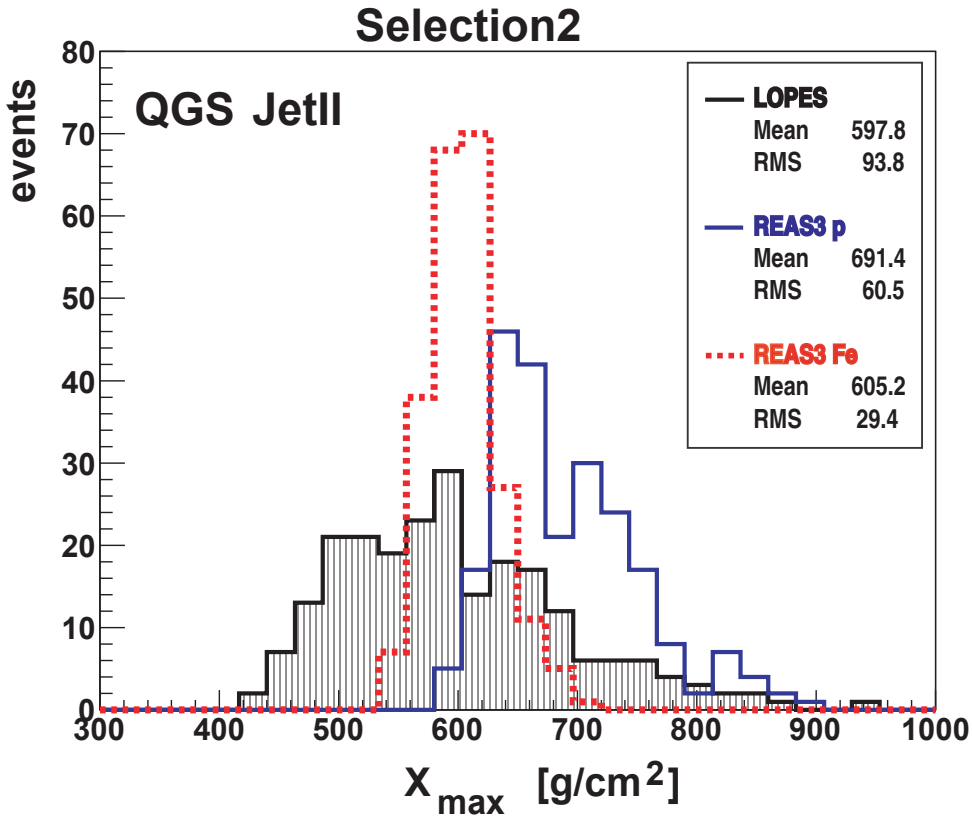

Figure 9.6: *Distribution of the reconstructed $X_{\max}$ with the slope method, for LOPES and the REAS3 simulations, using eq.9.5.*

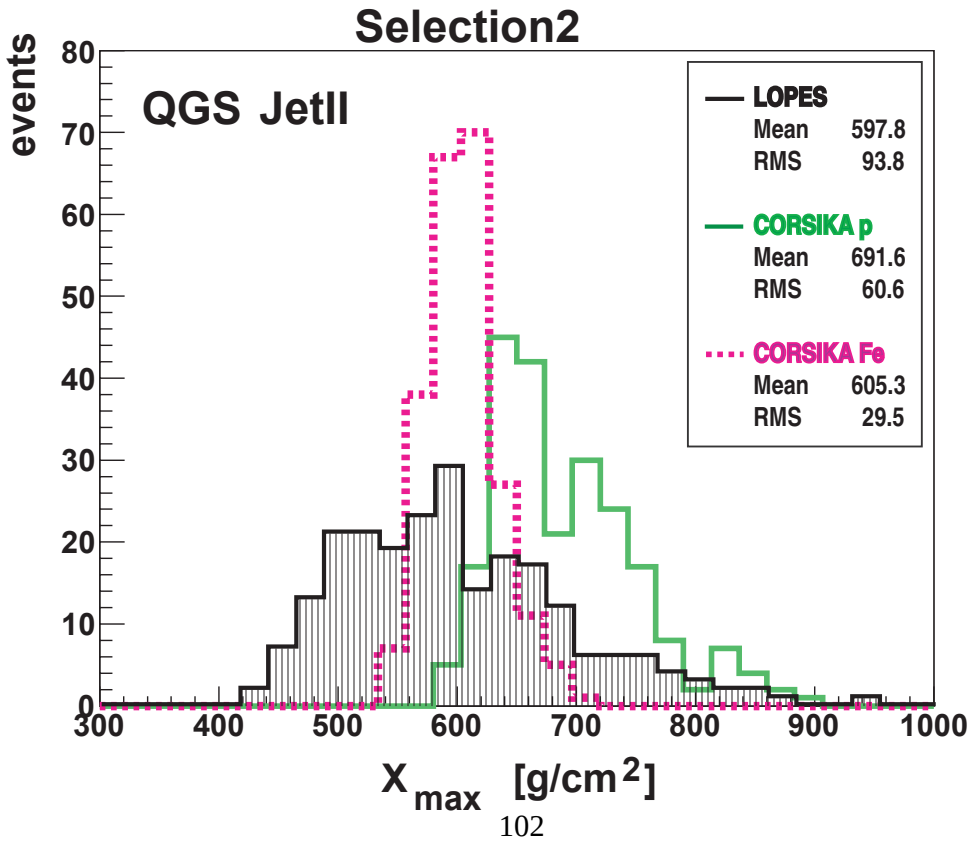

Figure 9.7: *Distribution of the LOPES reconstructed $X_{\max}$ (same as in **fig.**9.6), compared with the $true$ $X_{\max}$ values, directly given by the CORSIKA simulations.*

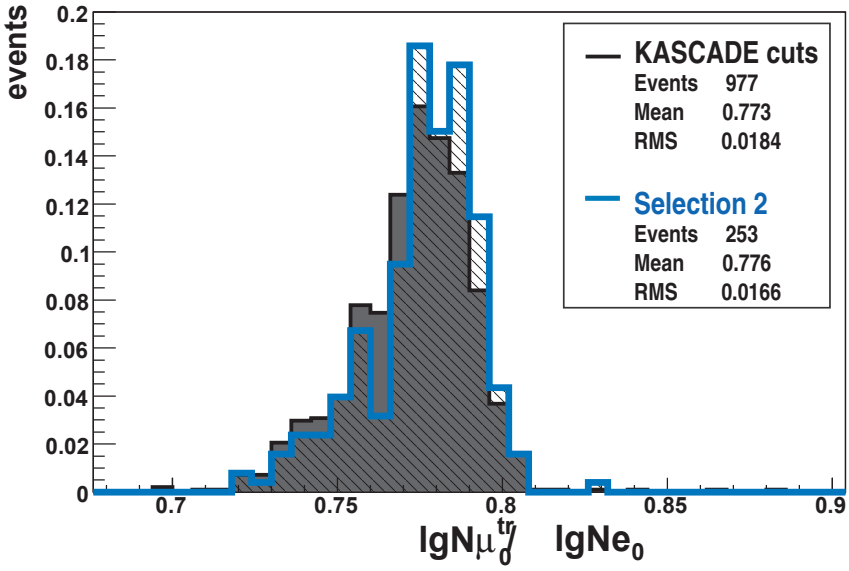

Figure 9.8: *No evident bias through an iron-preferred selection is noticed, by comparing the $lgN\mu_0^{tr}/lgNe_0$ for the events before and after the LOPES data selection.*

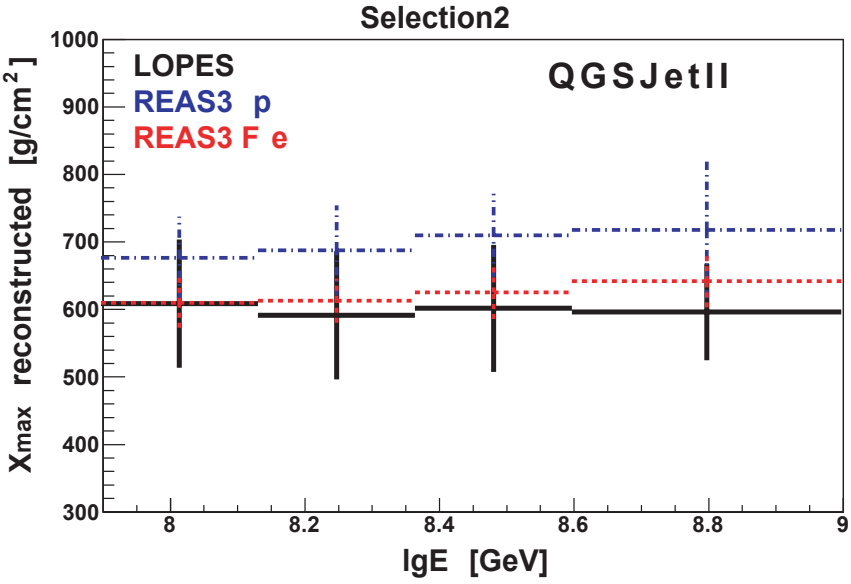

Figure 9.9: *The energy dependent X_{max} of the primary cosmic rays.*

The same kind of correlation $\sim$ 1+cos(θ)^j, with $j > 1$, is noticed. The big uncertainties on $\epsilon_{\mathrm{ratio}}$ do not allow a definitive conclusion concerning the value of j.
Due to the difficulties in properly defining a function for the zenith angle dependence, it remains difficult to correct for the shower inclination. Thus, the selected events are analyzed considering five zenith angle bins.

Simulations-derived parameters (*a, b* and *c*) are used in the following part: Table 8.3 provides all the information needed to reconstruct $\mathrm{X_{max}}$ per each zenith angle bin, minimizing the dependency of $\mathrm{X_{max}}$ on θ.

The experimental $\mathrm{X_{max}}$ is thus reconstructed, using the following formula

$$X_{max,\Delta\theta i} = a_{\Delta\theta i}\left[\ln\left(b_{\Delta\theta i}\frac{\epsilon_{\mathrm{flat}}}{\epsilon_{\mathrm{steep}}}\right)\right]^{c_{\Delta\theta i}} \tag{9.5}$$

In **fig.**9.6 the $\mathrm{X_{max}}$ distribution reconstructed for the complete zenith angle range is presented. For the LOPES events (black) the average $\mathrm{X_{max}}$ is 598 $\pm$ 94 gcm^{-2}, which are respectively the mean and the standard deviation of the distribution.
A comparison with the REAS3 simulations is shown as well. The $\mathrm{X_{max}}$ reconstructed with the slope method for the REAS3 proton showers and iron showers are represented respectively by the blue and red lines. In other words, these are the values on the fit of **fig.**13.14 corresponding to the slope ($\epsilon_{\mathrm{flat}}/\epsilon_{\mathrm{steep}}$) of the REAS3 lateral distributions.
The values obtained are $X_{max,REAS3,p}$ = 691 $\pm$ 61 gcm^{-2} and $X_{max,REAS3,Fe}$ = 605 $\pm$ 29 gcm^{-2}.

The whole $X_{max,LOPES}$ distribution generally covers the range of the values expected from cosmic ray nuclei. Nevertheless, a systematic shift to smaller $\mathrm{X_{max}}$ values (i.e. heavier particles) compared to the iron-like predictions is clearly visible (see also following discussion).

The same LOPES $\mathrm{X_{max}}$ (black) are also compared with the $true$ $\mathrm{X_{max}}$ values, directly given by the CORSIKA (QGSJetII) simulations (**fig.**9.7). Almost no difference is noticed.

The uncertainty on the $\mathrm{X_{max}}$ reconstruction partially comes from measurement uncertainties.
The RMS of the LOPES distribution (93.8 g/cm^2) includes both the width of a distribution of *true* $\mathrm{X_{max}}$ values – i.e. intrinsically due to shower fluctuations– and the uncertainty on the measurements. As worst case, the given value of 93.8 g/cm^2 can be considered itself as an upper-limit for the radio measurement uncertainty and it is, by now, the lowest available value for radio detection.
A step forward in the determination of LOPES measurement uncertainties concerns the comparison with REAS3-simulations predictions. In the worst (and not so realistic for such primary energy) case of pure iron-like composition, the squared difference between the REAS3–predicted-width (29 g/cm^2) and the LOPES width (93.8 g/cm^2) directly gives the measurements uncertainty. In such a case, the searched value is, again, almost 90 g/cm^2.
A better estimation would come from a comparison with REAS3-prediction for a mixed-composition-distribution expected in the energy range of the LOPES detection (around

10^{17} eV).

A noteworthy outcome of the slope method applied to the LOPES data is the reconstruction of more iron-like primaries; from one side this is in agreement with the theoretical expectation for the energy range of the considered selection 10^{17}-10^{18} eV, and with the recent KASCADE-Grande results (Apel et al., 2012d, 2011a).
However, a tendency to reconstruct $X_{max,LOPES}$ values even lower than for the iron-like predictions is clearly visible.

Different explanations are plausible for this effect:
From a technical point of view, it is known that the noise more likely increases the electric field in each antenna, thus flattening the LDF slope. An elaborate study on the error treatment in the radio antennas has already been investigated for the LOPES experiment (Schröder et al., 2010b), nevertheless possible other effects could have been missed.
The second possible explanation concerns the simulations, which could predict too steep LDF radio slopes compared to reality. On the one hand, the version of the REAS3 code used (REAS3.0) does not include yet a proper treatment of the refractive index, on the other hand, the hadronic interaction model employed has obviously a strong influence. Therefore, a comparison of the reconstructed X_{max} for, at least, the two interaction models considered so far, i.e. EPOS and QGSJetII, is mandatory (section 9.2.3).
Moreover, this might be an effect of a selection bias, in the sense that the radio detection of the signal and/or the selection of the radio data prefer iron-like more than proton-like events. By looking at **fig.**9.8, no clear bias in the selection appears. In the histogram the ratio $lgN\mu_0^{tr}/lgNe_0$ (i.e. ratio between the number of muons and electrons corrected for the zenith angle), given by the KASCADE reconstruction, is used as an indicator for the primary mass (Antoni et al., 2003b). The events which pass the KASCADE selection are compared with the events of Selection2 (cf. section 4.1.3). The two distributions have approximately similar shape, and also the mean and standard deviation values are comparable. Even if a significant difference existed, it would be small in comparison to the range of the distributions, thus it is considered not important.

In summary, no apparent bias through an iron-preferred selection is made in the LOPES detection method, neither in the reconstruction of the radio signal, nor in the selection of the radio events.

The next step is to compare the reconstructed X_{max}, for both LOPES events and REAS3 simulations, with the primary energy of the cosmic rays.
The X_{max} is predicted to be dependent on the primary mass and primary energy. Comparing the predictions from the simulations and the experimental data (**fig.**9.9), an energy dependent composition of the primary cosmic rays is obtained.
In fig. 9.9, each point represents the mean value of the X_{max} distribution for each energy bin, while the bars indicates the RMS-spread. This method offers reconstructed values for X_{max} quite comparable to the simulations, even though the tendency to reconstruct X_{max} even lower than the iron-like prediction is clearly visible in each energy bin.

The potential systematic uncertainties for the reconstruction of X_{max} are also investigated.
The reconstructions have been done taking the parameters a(θ), b(θ) and c(θ) per each zenith angle bin, so there should be no significant correlation with the incoming direc-

tion of the shower. This is crosschecked in **fig.**9.10. The plot on the bottom side is for REAS3 proton simulated events, and shows no evident correlation with θ. Since the parameters a(θ), b(θ) and c(θ) are the same for simulations and data, it shows that they do not bring any systematics to the reconstruction method. Also for the LOPES reconstructed X_{max} no clear correlation with the shower zenith angle is visible.

The potential dependence of X_{max} on the lateral mean distance was checked as well, and **fig.**9.11 shows no significant correlation.

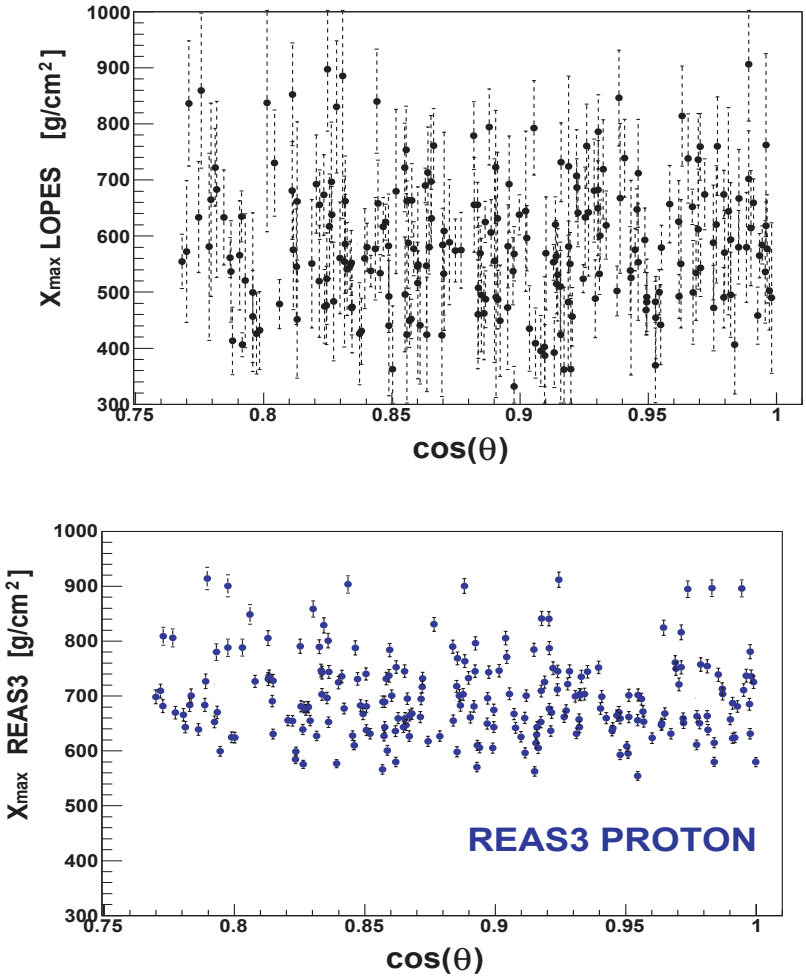

Figure 9.10: *Potential dependence of the reconstructed X_{max} values on the inclination of the shower, presented for the LOPES events (top) and for the REAS3 proton simulations (bottom). Similar behavior characterizes also the REAS3 iron simulations.*

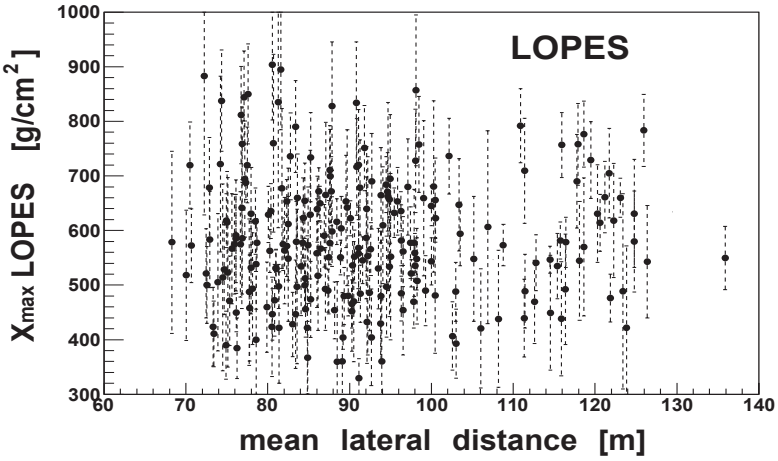

Figure 9.11: *Potential dependence of the reconstructed X_{max} values on the mean distance of the shower core, for the LOPES events.*

9.2.2 X_{max} resolution

Table 9.1: *Cone method cuts from Schröder (2010)*

Events 229	
	$\rho > 0.001$ and $\rho_{sim} > 0.001$
	lateral time fit $\chi^2 < 1.5$
	ρ relative error < 60 %
Events 118	

The aim of the present section is a qualitative study on the uncertainty of the X_{max} reconstruction, achievable with radio measurements. REAS3 simulations are considered for this investigation.
A combination of the two independent method (i.e. cone and slope method) for the reconstruction of X_{max} is discussed in the following.

As already mentioned, lighter nuclei interact deeper in the atmosphere and are characterized by a larger average X_{max} compared to the heavier particles. This implies a smaller distance between the radio source for proton-like cosmic rays and the observer. A large X_{max} means also a small curvature radius (i.e. large curvature) for a spherical shape of the radio wavefront and a small opening ρ-angle[3] for the conical wavefront. As a consequence, large ρ-angle are predicted for iron-like primaries, while small ρ-angle for light cosmic rays.

The shape of the wavefront has been studied for the LOPES events and a cone was found to approximate best the arrival time of the radio pulses (Schröder, 2010). The cone method obtains X_{max} values by looking at the wavefront shape determined with a fit of the total arrival time distribution of the radio pulses. The cone method investigation still needs improvement and is in continuous development. Here we will refer to values and formulas published in Schröder (2010).

In the following, REAS3 simulations of Selection2 are analyzed and further cuts (Table 9.1) required by the cone method, are applied. The number of events available for the comparison is reduced to 118.
The formula for estimating X_{max} in terms of the opening angle of the shower front, and published in Schröder (2010), is reported below:

$$X_{max} = c_{\mathrm{p}} \cdot \rho \cdot \cos(\theta)^{-3/2} \tag{9.6}$$

The proportionality constant c_p is arbitrarily set to 40500 g/cm^2 /rad[1] for this specific set of simulations. The value is chosen with the same methodology shown in Schröder (2010), thus to have the best mean value closest to zero in the $X_{max,true}$-$X_{\mathrm{max,REAS3}}$ distributions, for both iron and proton induced showers (**fig.**9.12, TOP).
The $\Delta\ X_{\mathrm{max}}$ distribution is derived also with the slope method, separately for proton

[3] ρ is the angle between the shower plane and the cone surface.

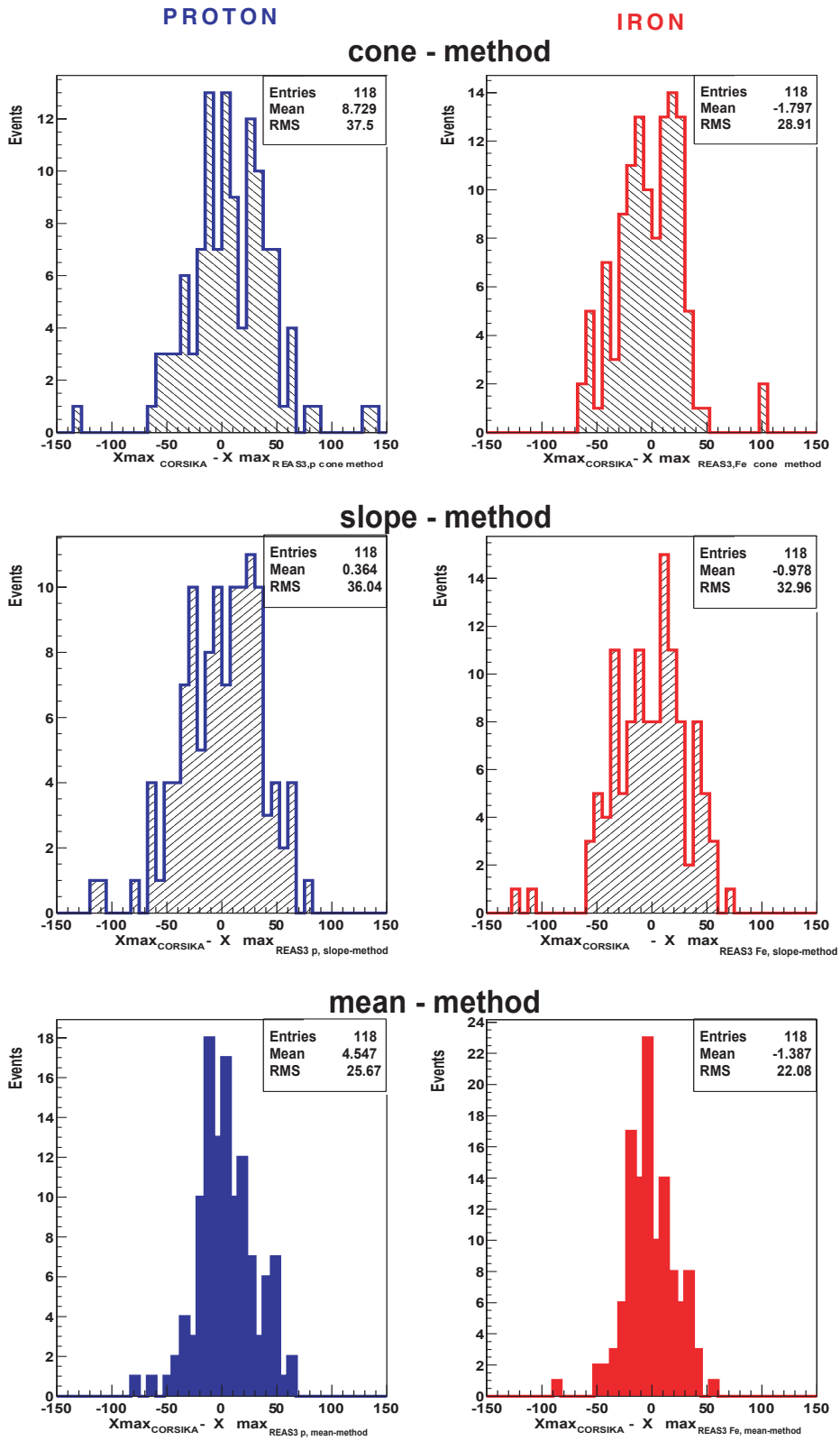

Figure 9.12: *Discrepancy between the* $true$ *(form CORSIKA) and the radio-reconstructed* X_{max} *values. TOP: cone method, MIDDLE: slope method, BOTTOM: mean method*

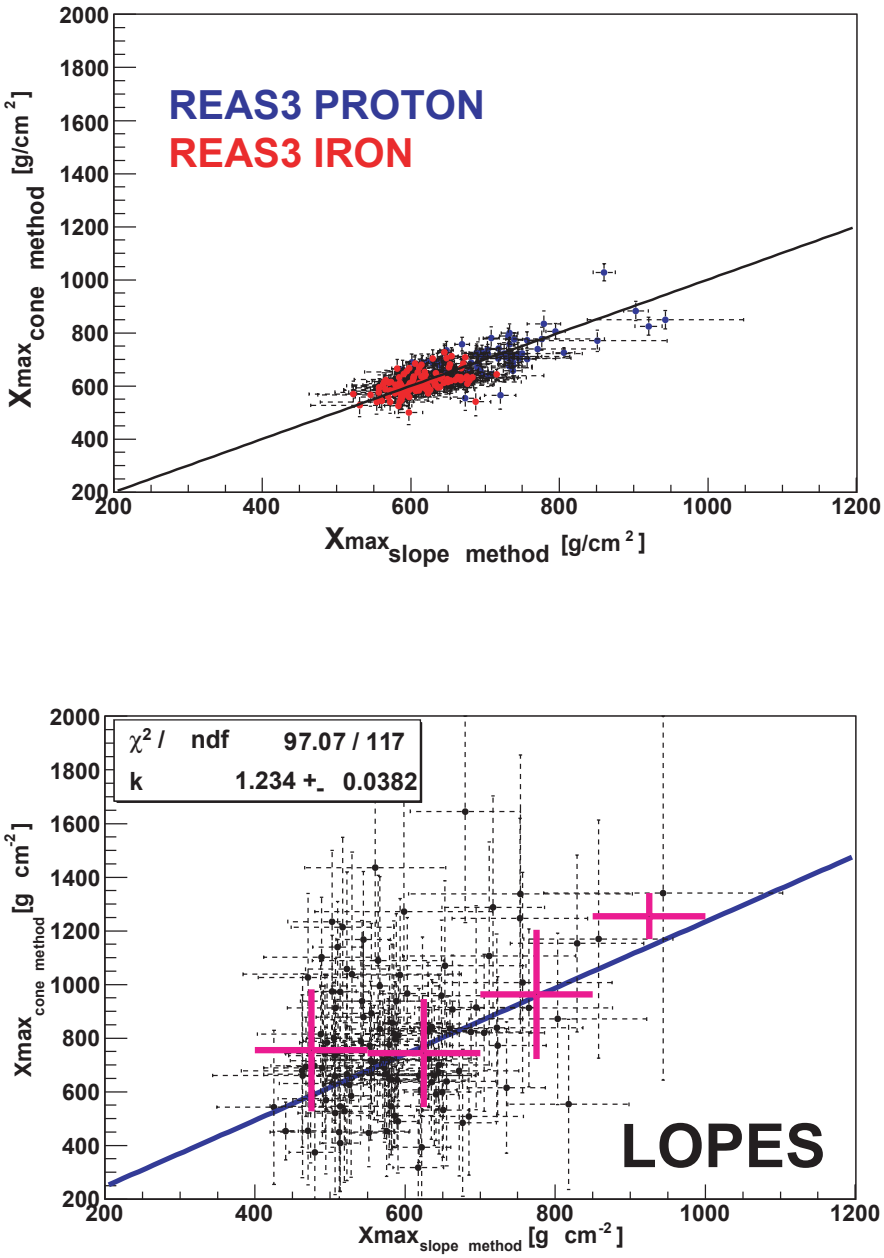

Figure 9.13: *Event by event comparison for the X_{max} reconstructed with the slope and the cone methods, for REAS3 simulations (top) and LOPES data (bottom). In the top figure, the continuous black line indicates the one-by-one correlation. In the bottom figure, the blue line is the linear fit.*

and iron showers.
For the complete zenith angle range and for both methods, the RMS uncertainties are $\sim$ 37 g/cm^2 and $\sim$ 30 g/cm^2 respectively for proton and iron primaries.
For the purpose of combining both methods, a mean $X_{\mathrm{max,REAS3}}$ between the slope- and cone- values is calculated for each event. The obtained $X_{\mathrm{max,mean-method}}$ is directly compared with the $true$ $\mathrm{X_{max}}$ from the CORSIKA simulations (**fig.**9.12, BOTTOM).

Narrower distributions compared to the single methods are clearly visible. The RMS values are smaller by $\sim$ 20 % (for iron) and $\sim$ 30 % (for proton) compared to the lowest RMS of the single methods.
The values for the combined method are, moreover, compatible with expectations from two completely independent methods used to yield X_{max}: in such a case, the error is expected to scale with the inverse squared sum (i.e. Gaussian error propagation).

A direct, event by event, comparison of the two reconstructed $\mathrm{X_{max}}$, is shown in **fig.**9.13 for both simulations and LOPES data. The errors are obtained with the Gaussian error propagation formula.
REAS3 simulations show no bias in the 1 to 1 event comparison for the two independent methods. This is not the case for the LOPES reconstructed $\mathrm{X_{max}}$, in which the points are shifted to larger reconstructed values for the cone method. The LOPES values (**fig.**9.13, bottom) are fitted with a linear function (blue line). The resulting proportionality constant k is more than 6 σ away from the unity. Nevertheless, the calculated $\mathrm{R^2}$ coefficient, already largely used in section 6.3.1, confirms the compatibility of the points distribution with a linear fit at 99.99 $\%$, thus with a horizontal line only at 0.01 $\%$.
The $\mathrm{X_{max}}$ values obtained with the two independent methods are, thus, compatible.

The purpose of the study is fully achieved and a quantitative value on the expected uncertainty of $\mathrm{X_{max}}$ is obtained. With complementary information from the two independent methods, a better precision for the $\mathrm{X_{max}}$ reconstruction is gained than with each of the method alone.
With the resulting $\Delta \mathrm{X_{max}} \simeq$ 30 g/cm^2, the radio detection method may attempt to reach almost the precision of the FD at the Pierre Auger Observatory (almost 20 g/cm^2 (Abraham et al., 2010c))

9.2.3 Interaction model dependence of the X_{max} reconstruction

The discrepancy between the EPOS 1.99 and QGSJetII predictions for X_{max} is of almost 10 g/cm^2 in the energy range of interest for the LOPES experiment (10^{17}-10^{18} eV).
The influence of the interaction models on the X_{max} reconstruction with the LOPES measurements is investigated below.
Although the slope of the radio LDF did not show to be largely influenced by the interaction models in use (cf. section 7.3), the slope method, precisely the a, b and c parameters (Tables 7.4 and 7.5), appear to be slightly dependent on the choice of model (EPOS or QGSJetII), for the X_{max} investigation.

Simulations of both the interaction models were performed for the LOPES events of Selection1 (cf. section 7.3).
The parameters necessary for the reconstruction are available in Table 9.2, where the single EW component of the radio pulses - and not the total as discussed in section 7.3 - has been considered in the X_{max}-$\epsilon_{\mathrm{ratio}}$ correlation fit.

Table 9.2: *X_{max} fit: a, b, c parameters for Selection 1, EW component of the radio pulse*

	EPOS			QGSJetII		
$\Delta\theta$	a	b	c	a	b	c
0.°-19.4°	414±27	1.2±0.17	0.6±0.04	69.7±17.4	21.7±7.1	1.4±0.09
19.4°-26.8°	282±15	3.0±0.3	0.84±0.03	523±2	1±0.02	0.5 ±0.01
26.8°-32°	19±3	85.9±15.3	2±0.06	560±1.5	1±0.02	0.48±0.01
32°-36.2°	303±18	3±0.2	0.91±0.04	601±1.9	1±0.45	0.48±0.01
36.2°-40°	12.7±2	47.4±6	2.5±0.07	8.1±1.8	45.8 ±4.9	2.84 ±0.11

Using the a, b and c parameters for each of the two models, the X_{max} distribution of the LOPES events in Selection1 is reconstructed.
At first glance, the distributions (**fig.** 9.14) for EPOS 1.99 and for QGSJetII look very similar:
An average $X_{max,LOPES,EPOS}$ = 571 ± 98 g/cm^2 and an average $X_{max,LOPES,QGSJet}$ = 575 ± 87 g/cm^2 (mean and standard deviation) are found for the LOPES reconstructed values (black). Similarly, the depth of the shower maximum reconstructed for the REAS3 simulations, i.e. $X_{max,REAS3,EPOS}$ and $X_{max,REAS3,QGSJet}$, look almost the same for both protons and irons.

This result is not surprising if one considers that the largest divergence between the two interaction models happens for primary energy larger than 10^{18} eV (Pierog et al., 2009).

Nevertheless, some minor divergences in the distributions of the REAS3 simulations may be noticed: Concerning the iron primaries, QGSJetII predictions are slightly shifted to larger X_{max} values compared to EPOS; on the other hand, for proton primaries, the EPOS predictions show larger X_{max} values. This is in perfect agreement with the mod-

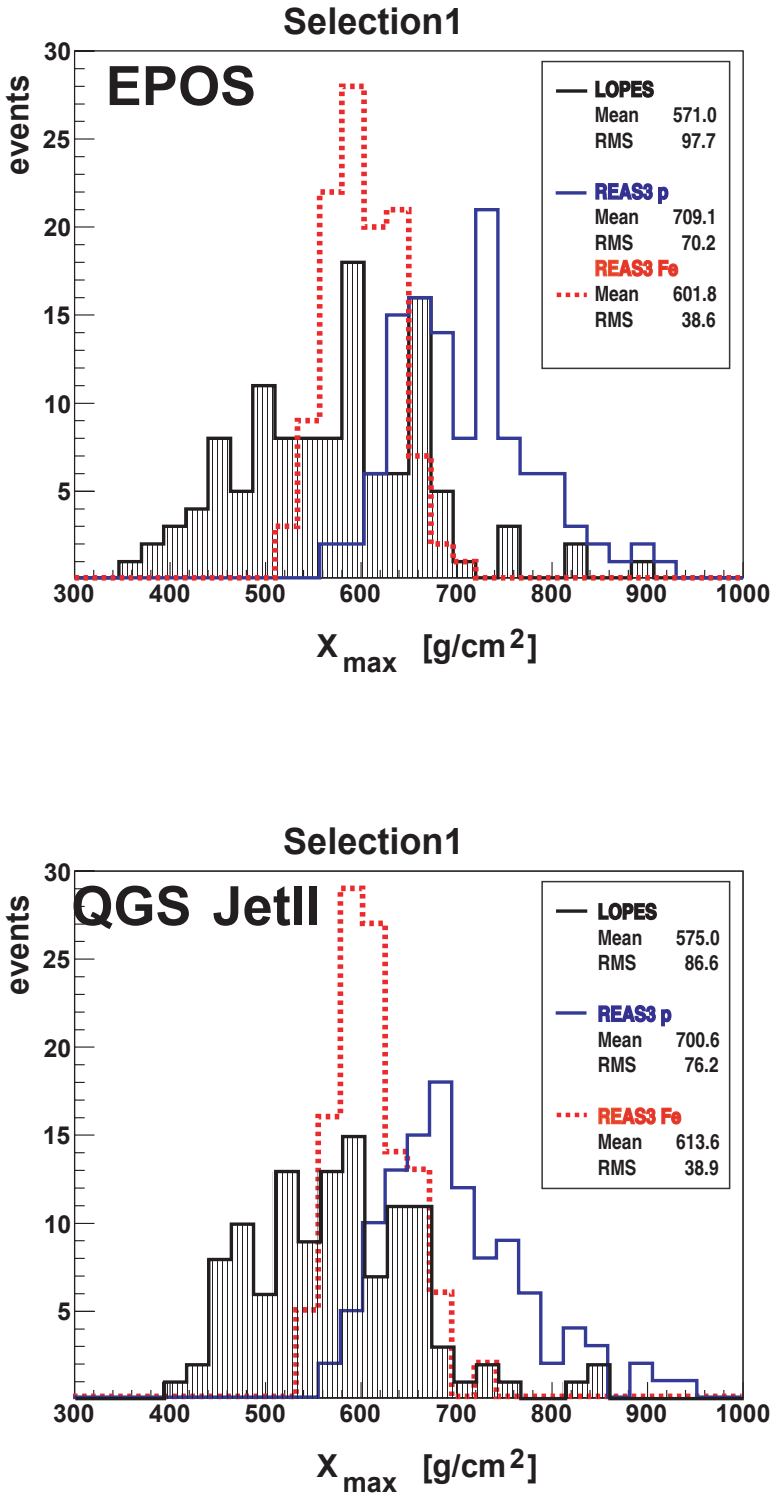

Figure 9.14: *Distribution of the reconstructed X_{max} with the slope method. On the top for EPOS and on the bottom for QGSJetII hadronic interaction models, for the events in Selection1. The EW-component of the radio pulse is considered.*

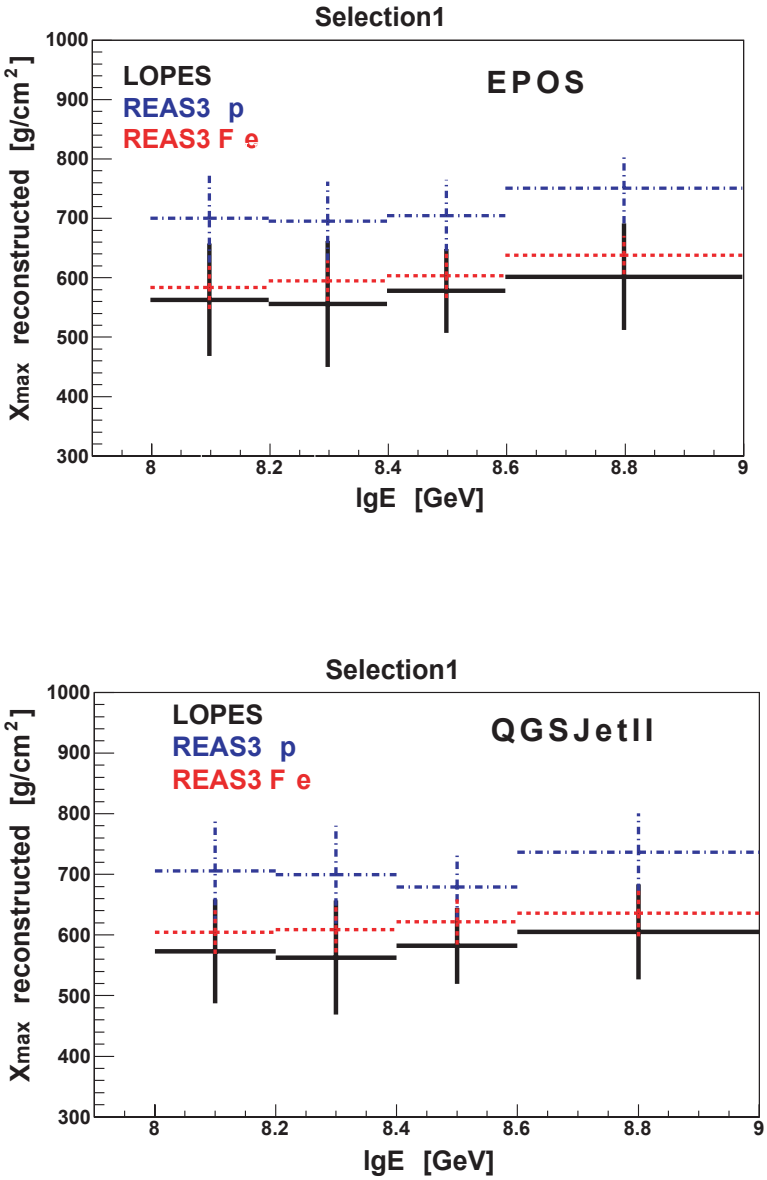

Figure 9.15: *The energy dependent X_{max} reconstructed with the slope method for Selection1 (EW-component of the radio pulse). On the top for EPOS and on the bottom for QGSJetII hadronic interaction models.*

els' expectations (Pierog et al., 2009). Indeed, in the primary energy range of 10^{17}-10^{18} eV, EPOS proton primaries interact slightly deeper in the atmosphere while the EPOS irons interact earlier compared to QGSJetII.

The reconstructed $X_{max,LOPES}$ is looked at in dependence on the primary energy (**fig.**9.15). A comparison with the REAS3 predictions for proton (blue) and iron (red) primaries is shown as well. The EPOS 1.99 interaction model is presented in the top figure, while the QGSJetII model is in the bottom figure.
In each energy bin, no large differences due to the hadronic interaction models is visible. Moreover, a tendency to reconstruct $X_{max,LOPES,EPOS}$ smaller even than the iron-like nuclei (cf. section 9.2.1) is clearly visible also for the EPOS interaction model.

In summary, the hadronic interaction models (EPOS 1.99 and QGSJetII) used to simulate the air showers do not largely influence the X_{max} reconstruction with the slope method. This outcome is valid for REAS3 simulations of the LOPES events, thus in a specific range of the primary energy, in which the predictions on X_{max} of EPOS 1.99 and QGSJetII do not widely differ.

9.3 Composition study

X_{max} is a well-known indicator for cosmic ray composition. The application of a simulation-based procedure (slope method) for a per-event reconstruction of X_{max} with the radio measurement has been developed.

The comparison of the reconstructed X_{max} from at least two different detection methods is of fundamental importance and it will be possible at the Pierre Auger Observatory, where the radio information from AERA can be easily compared with the Fluorescence Detector measurements, in the so-called super-hybrid environment (cf. Chapter 4).

For the LOPES experiment, the direct comparison of the reconstructed X_{max} is not possible:
The KASCADE-Grande experiment can not directly access the air shower X_{max} but has information about the cosmic ray composition through the ratio $\lg N\mu_0/\lg Ne_0$ (Antoni et al., 2004).
The muon-electron ratio is, indeed, the most common indicator of the primary mass in particle detector experiments (Gaisser, 1990).

For better accuracy the KASCADE experiment does not use the total reconstructed $N\mu$, but the truncated muon number ($N\mu^{tr}$), that is the integrated value between 40 m and 200 m from the shower core. In the following analysis $N\mu$ is referred to as the truncated muon number.

The $N\mu/Ne$ ratio must be corrected for the air shower zenith angle. The electron number and the truncated muon number are zenith-angle-corrected to θ=0° — thus the appendix 0 in the $lgN\mu/lgNe$— using the attenuation law reported below (Antoni et al., 2003a):

$$\mathrm{Ne}_0 = \mathrm{Ne} \cdot \exp\left[\mathrm{X}_0/\Lambda e(\sec(\theta) - 1)\right]$$
$$\mathrm{N}\mu_0 = \mathrm{N}\mu \cdot \exp\left[\mathrm{X}_0/\Lambda\mu(\sec(\theta) - 1)\right]$$

with the attenuation lengths Λe = 175 gcm^{-2} and $\Lambda\mu$ = 823 gcm^{-2}. X_0 = 1022 gcm^{-2} is the vertical atmospheric depth at the KASCADE observation level.

The value given by the KASCADE experiment as threshold between light, i.e. proton-like, and heavy, i.e. iron-like, elements is $\lg N\mu_0/\lg Ne_0 \sim 0.74$ (Antoni et al., 2004).

As for the reconstructed primary energy, it must be kept in mind that all the KASCADE parameters (such as Λe and $\Lambda\mu$) have been mainly investigated for primary energies in the range 10^{14}-10^{16} eV.
The LOPES detected events used for the composition analysis have primary energy values around 10^{17} eV. Consequently, it is important to look at the possible dependence on the zenith angle and primary energy of the $lgN\mu_0/lgNe_0$ for such events:

A dependence of the, already zenith-angle corrected, mass indicator $\lg N\mu_0/\lg Ne_0$ with the shower inclination is presented in **fig.**9.16. A correlation, almost linear, is clearly visible. The points are fitted with a power-law function a+(cos(θ))^c.
Since proton and iron primaries are expected to arrive isotropically, the dependence on the zenith angle (**fig.**9.16) could be attributed to an attenuation formula that is not completely appropriate. Probably the parameters used (Λe and $\Lambda\mu$) should be particularly examined for such high energies.
Another already discussed motivation for such a behavior is the punch-through effect:

The KASCADE muon detectors are shielded enough to avoid the electromagnetic component to penetrate, but only for energies up to 10^{17} eV. For the energy range of the used selection (Selection2) and especially for almost vertical showers, larger amount of energetic electrons and positrons penetrate the shield and are detected as muons.

The dependence on the primary energy is looked at in **fig.** 9.17. The $N\mu_0$ can be used as indicator for the primary energy, since muon in air showers do not multiply but only lose their energy by ionization (Gaisser, 1990).
The ratio $\lg N\mu_0/\lg Ne_0$ shows here a slight dependence also on the primary energy.
The energy dependence of the muon-to-electron ratio has already been studied for another energy range (Obenland, 2005); nevertheless a clear correlation has not been established.

The $lgN\mu_0/lgNe_0$ correlations respectively with the inclination and the primary energy of the shower must be taken into account for any conclusion in the following analysis.

9.3.1 Comparison of the radio lateral slope and the muon-electron ratio from KASCADE

The most general indicator of the slope for the radio LDF, independent of the fitting function in use, is the ratio $\epsilon_{\rm ratio}$ [4]. For this specific case, where the LDF is fit with a 1D-exponential (cf. Chapter 6), also the parameter R_0 could be similarly used.
In the following part, both R_0 and $\epsilon_{\rm ratio}$ in correlation with the primary mass indicator $\lg N\mu_0/\lg Ne_0$ will be analyzed.

An overview of these two parameters for the complete selection (Selection2) is shown in **fig.**9.18 in black, compared with the expectations from the REAS3 simulations, for both proton (blue) and iron (red) initiated showers. The simulations are based on the QGSJetII interaction model.
Small values of $\epsilon_{\rm ratio}$ indicate flatter slopes of the radio lateral distribution.
The range of the R_0 parameter is much larger and, opposite to $\epsilon_{\rm ratio}$, small R_0 means steep LDF slope.

As previously discussed, the LOPES LFD slope (**fig.**9.18) appears to flatten even more than the REAS3 predicted LDF for the iron-like nuclei. Indeed, the LOPES $\epsilon_{\rm ratio}$ values, are generally shifted to values smaller then the REAS3 iron $\epsilon_{\rm ratio}$.

The distributions for the REAS3 simulated irons (red) and protons (blue) largely overlap for both R_0 and $\epsilon_{\rm ratio}$ quantities. Thus, both the parameters are expected not to be strong discriminators between proton and iron primaries.

A direct per-event correlation between the KASCADE $\lg N\mu_0/\lg Ne_0$ and the LOPES LDF slope parameters is presented in **fig.**9.20 (for $\epsilon_{\rm ratio}$) and in **fig.**9.22 (for R_0). Both the parameters R_0 and $\epsilon_{\rm ratio}$ and the muon-electron ratio are not corrected for the shower inclination (see previous discussion of **fig.**9.16) and the usual 5 zenith angle bins are separately considered.

[4] ratio of the radio amplitudes at two different distances from the shower axis

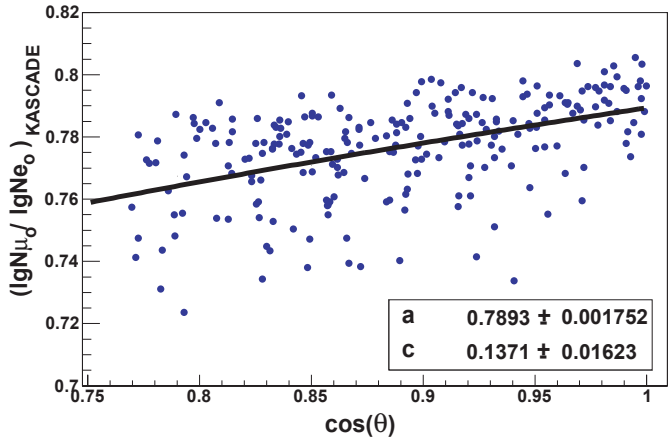

Figure 9.16: *The already corrected primary mass indicator $lgN\mu_0/lgNe_0$ continues to show a zenith angle dependence.*

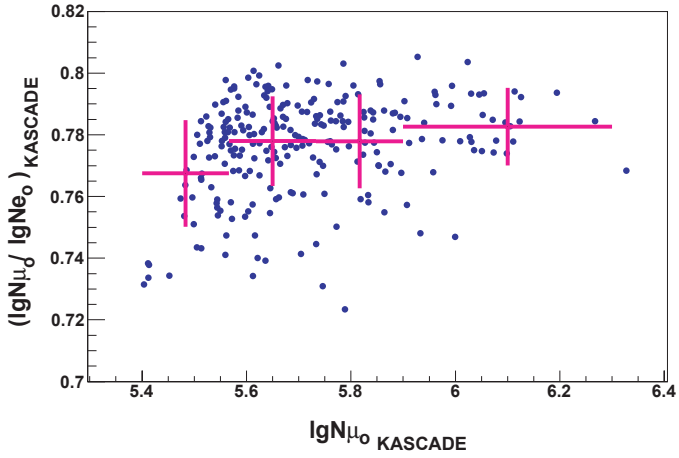

Figure 9.17: *A slight dependence on the primary energy of the zenith angle corrected primary mass indicator $lgN\mu_0/lgNe_0$ is visible.*

While for the simulated $\lg N\mu_0/\lg Ne_0$ there is a sharp separation between the two primaries at around 0.76, for ϵ_{ratio} (and for R_0) the delimitation between primaries is not well defined.
Nevertheless, analyzing the REAS3 simulations, a region can be identified where circa 90% of events may be expected to be proton-like.
ϵ_{ratio} dependence on the zenith angle is discussed (section7.5.1) as $\sim [\cos(\theta)]^j$, with a j value possibly between 3 and 5. If, as example, j is set to 5 (**fig.**9.5), the value $\epsilon_{\text{ratio,B,corr}} \simeq 12$ can be considered an indicative border line for such region, where

$$\epsilon_{\text{ratio,B,corr}} = \epsilon_{\text{ratio,B}} \cdot \cos(\theta)^{-5}$$

with B stands for border and corr. for zenith angle corrected.
The border line in each zenith angle bin is marked with the dotted line. The right part from the line is the 90 $\%$-proton-like nuclei zone.

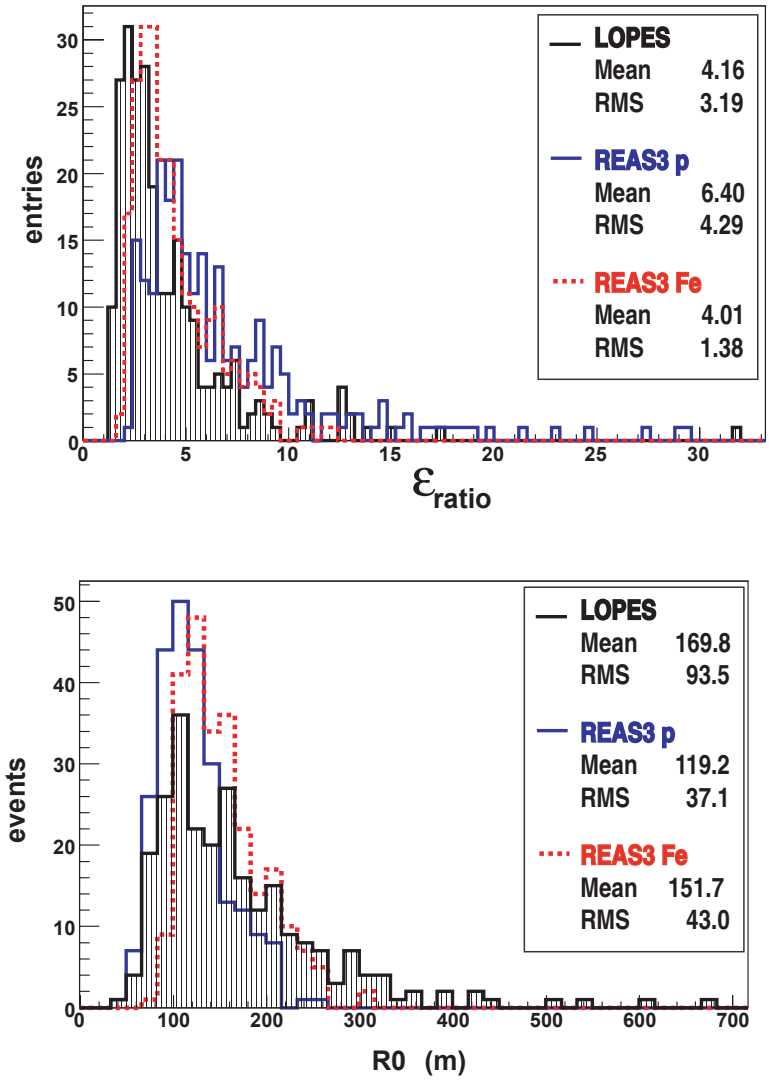

Figure 9.18: *LDF slope for all events in Selection 2, compared with values for the REAS3 simulated LDF.*

Concerning the R_0 parameter, a similar approach could be applied. Nevertheless, the R_0 parameter seems an even weaker indicator for the primary mass compared to $\epsilon_{\mathrm{ratio}}$. This is also due to the large uncertainty on the reconstructed LDF fit parameter R_0.

By looking at the LOPES data comparison (**fig.** 9.20 and 9.22), the reconstructed $\lg N\mu_0/\lg Ne_0$ does not seem to be a reliable parameter. Especially in the first zenith angle bin, too large values are shown, which would stress once more an increment of the count for muon-like particles due to the punch-through effect discussed above.
The punch-through effect and the zenith angle dependence seem to play a fundamental role in the composition analysis for the specific case of the LOPES experiment.
Due to these limitations, no firm and clear conclusions on the cosmic ray composition

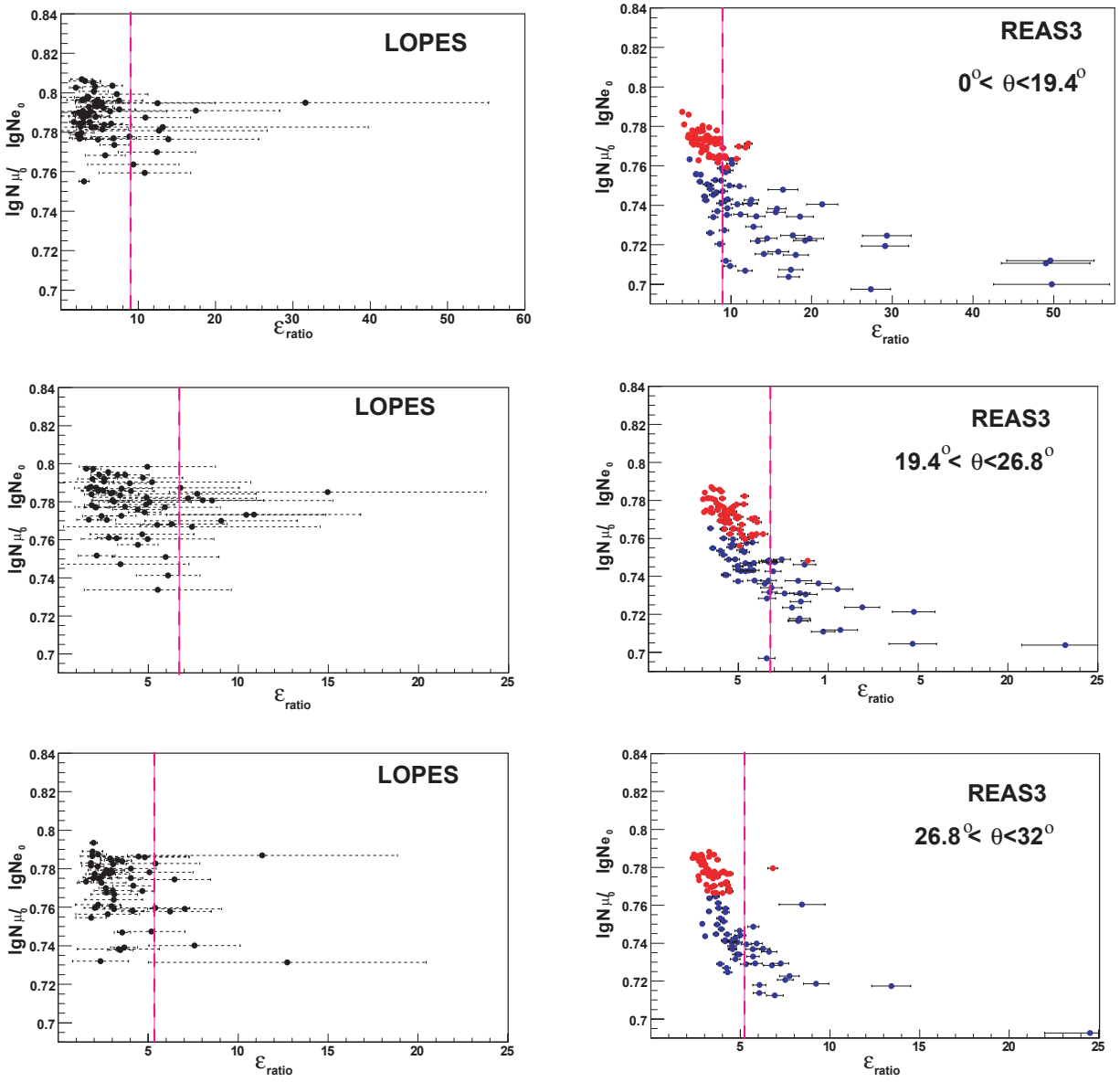

Figure 9.19: *to be continued in the next page*

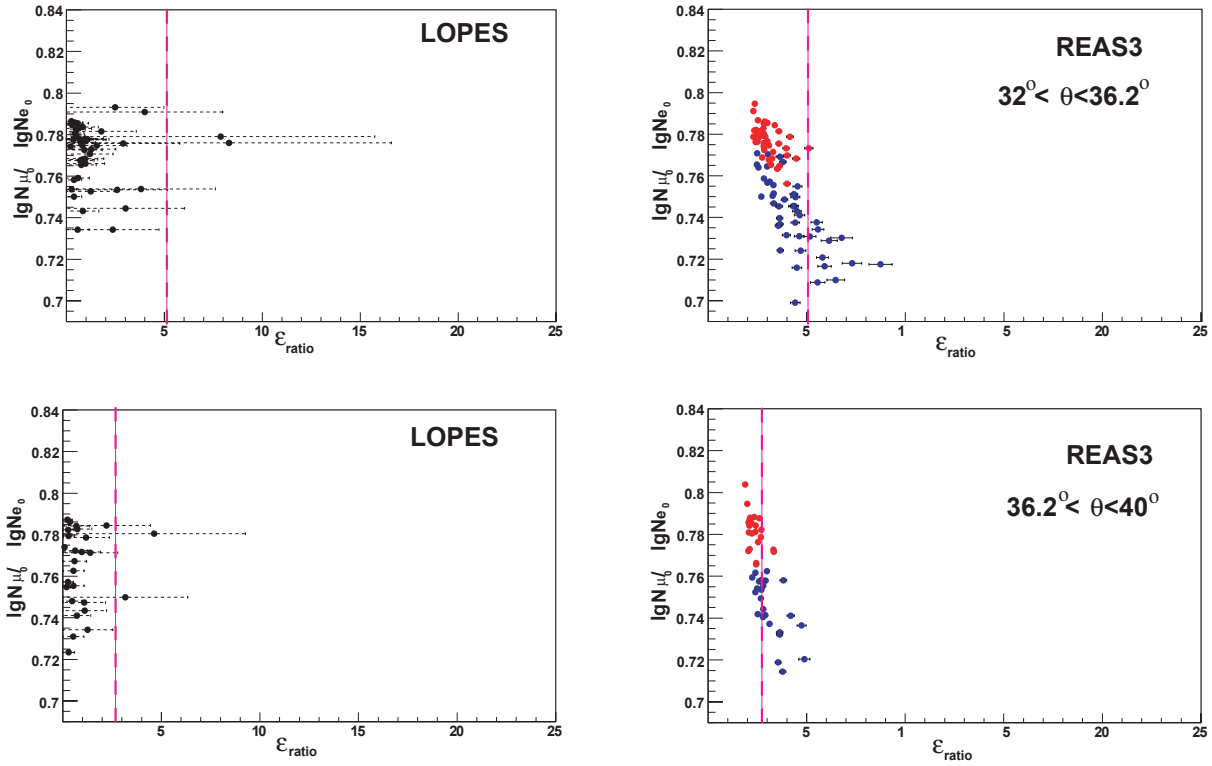

Figure 9.20: *(continued) Sensitivity of the LDF slope, $\epsilon_{\mathrm{ratio}}$, to the mass of the primary particle, expressed with the ratio of muon number and electron number detected by KASCADE, for both detected (left) and REAS3 simulated (right) data. The region of 90% expectation for light primaries is on the right part of the dotted line.*

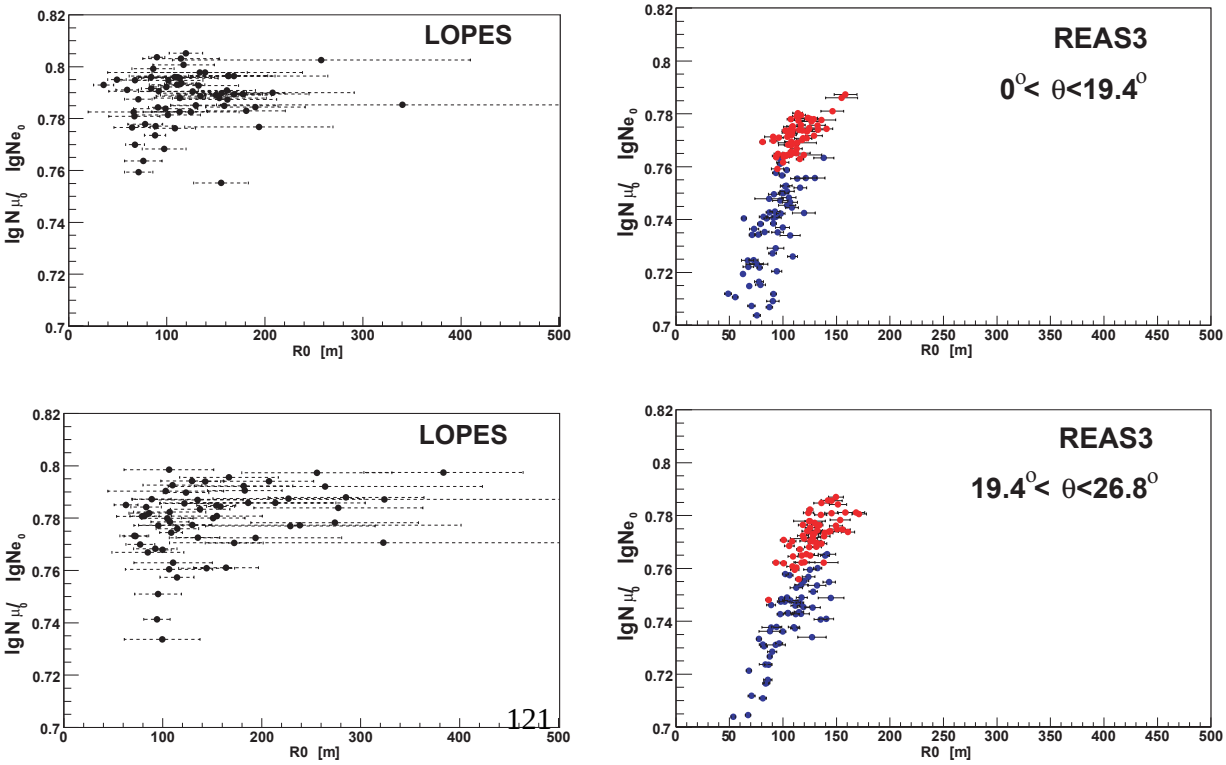

Figure 9.21: *to be continued in the next page*

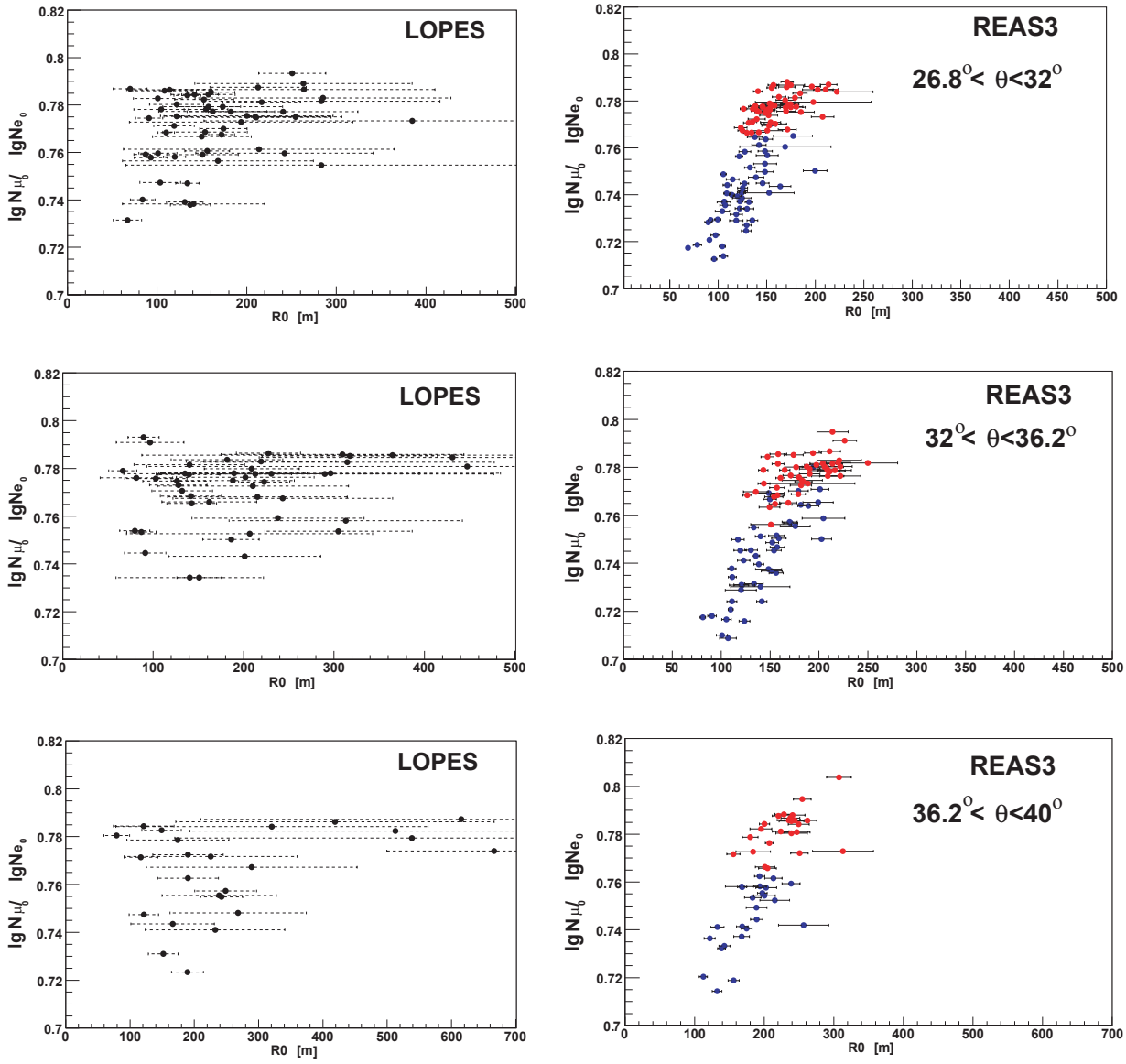

Figure 9.22: *(continued) Sensitivity of the LDF fitting parameter R_0 to the mass of the primary particle, expressed with the ratio of muon number and electron number detected by KASCADE.*

can be reached with the analyzed selection of LOPES events.

9.4 Discussion

In the following several limitations which had influence on the slope method analysis as well as possible refinements are discussed.

The precision on the energy reconstruction with the LOPES measurements ($\sim$ 23 %) was affected by mainly two factors: first, the uncertainty on the R_0 parameter of the LDF fit, which is determined by both the random noise recorded at each antenna station and the LDF-fitting procedure.
Second, the KASCADE(-Grande) uncertainty on the energy reconstruction, which is, by all means, of the same order of magnitude of the predicted LOPES-energy uncertainty, i.e. 20 $\%$-40 $\%$.
Aiming to reach the uncertainty on the primary energy predicted by the slope method of only 6 $\%$-8 $\%$ (an even of $\sim$ 4 % for the energy due to the electromagnetic part of the air shower), an investigation on radio measurements gathered in a low-noise environment is strongly suggested.

Concerning the $X_{\max}$ investigation, several limitations are pointed out:
First, the a, b and c parameters for the $X_{\max}$ reconstruction are obtained on the basis of (REAS3)-simulations of the LOPES events applied to a 50 $\%$-proton and 50 $\%$-iron composition: indeed, the same LOPES event is simulated as both iron and proton primaries. An analysis on a more realistic mixed-composition expected in the energy range 10^{17}-10^{18} eV is highly suggested in order to obtain more precise a, b and c parameters, thus more precise $X_{\max}$ reconstruction. Moreover, with a realistic cosmic-ray-composition, a more realistic determination of the measurement uncertainty is achievable.

The second limitation is connected to the employment of REAS3 simulations, which do not include a proper treatment of the atmospheric-refractive index. Willing to smooth the still existing discrepancy between simulated and recorded LDFs, such as the clear tendency of the LOPES data to present flatter LDF-slope, an application of the slope method on the more complete REAS3.1 and CoREAS simulations (only recently available) is strongly advised.

The third restriction concerns the deliberate exclusion of the detector-simulation in the investigation. A more realistic comparison with the measurements may include both simulations of detector properties as well as simulated transient noise typical of the specific experiment site.

9.5 Conclusion

The parameters derived in the previous chapters from a simulations-based procedure (slope method), have been directly applied to LOPES measurements for the reconstruction of both energy and $X_{\max}$ of air showers.
Despite the high level of man-made noise at the LOPES experiment, important outcomes are:

- The $flat$ region is confirmed to exist in data and proven to be the most appropriate distance from the shower axis for the primary energy investigation with radio

measurements.

- By means of LOPES measurements, an upper-limit on the uncertainty for the energy reconstruction is provided ($\sim$ 23 %). This value is consistent with the statistical energy uncertainty of the KASCADE(-Grande) experiment.

- X_{max} is reconstructed with the information from the measured radio LDF. The resulting values are reasonable and comparable with expectations from cosmic ray nuclei.
  By merging information from two different radio methods which provide X_{max} values, the quite low uncertainty $\Delta X_{max} \simeq 30$ g/cm^2 is predicted.

  A better resolution for the radio reconstructed X_{max} and a ΔX_{max} comparable with the smallest FD uncertainties ($\Delta X_{max} = 20$ g/cm^2) may be achievable at the Pierre Auger site, where the environmental noise is lower compared to Karlsruhe (i.e. LOPES experiment).

  A noteworthy issue is the tendency of a LOPES reconstructed X_{max} to be lower (even) compared to iron-like primary predictions. In other words, the LOPES events exhibit a slope of the radio lateral function which is on average flatter compared to what is predicted by REAS3 simulations. Possible explanations were also discussed.

- A composition analysis for the LOPES experiment turned out to be difficult to investigate for two main reasons: first, the punch-through effect which affects the KASCADE measurements of the muon-to-electron ratio.
  Second, the prediction of mostly heavy particles (iron) and only a small fraction of protons in the cosmic rays flux in the primary energy range of interest for LOPES (Apel et al., 2011b).

In the next chapter, the slope method will be investigated on REAS3 simulations of events detectable with the AERA setup. An investigation of the predictions for the $flat$ region and, thus, the possibilities to apply the slope method to the future AERA events will be discussed.

10 The slope method applied to AERA

The slope method has been successfully tested, so far, on the LOPES simulated and measured data.
The values found for the $flat$ region and the parameters used to reconstruct energy and X_{max} of a primary are all specific for the LOPES setup and selection, thus not directly usable for other experiments.

AERA, located at the Pierre Auger Observatory, will investigate the radio detection from cosmic ray air shower with respect to the next generation of large scale surface detectors (Fliescher (2010) and cf. Chapter 4).
The AERA array will include about 160 stations distributed over a total area of 20 km^2, featuring three different spacings (cf. section 4.2). A sketch of the completed AERA setup is presented in **fig.**10.1, where each triangle is an AERA station.

Verifying the applicability of the slope method in particular on the AERA experiment is of great interest for several reasons: on the one hand, located in an area with lower human-made noise compared to LOPES, this experiment could highly improve the resolution on X_{max}, thus the sensitivity to the primary type.
On the other hand, AERA will take advantage of the super-hybrid detection mode (Fliescher, 2010) and it will cross-check the radio reconstructed X_{max} with the FD values, which have an uncertainty of only $\sim$ 20 g/cm^2 (Abraham et al., 2010a).
Moreover, the application of the slope method to the simulated events for AERA can put a limit on the spacing of the antennas which ensures a sensitivity of the radio lateral distribution function slope to the mass of the primary.

10.1 REAS3 simulations

The AERA experiment is characterized by different spacings of the antennas (**fig.**10.1). As a consequence, two sets of REAS3 simulations have been performed: one including 200 simulated events with the core position in the dense region (blue, small, circle in **fig.**10.1), while the second has 250 events with the core in the surrounding area, with 250 m of distance between the antennas (red, bigger circle). We will refer to them respectively as Set-phase1 and Set-phase2.

For each event, one CORSIKA shower is prepared, using QGSJetII (Ostapchenko, 2006) and UrQMD (Bass et al., 1998) as high and low energy interaction models. No typical shower is pre-selected, thus, the shower-to-shower fluctuations are included in the investigation.
Unlike the procedure shown in Chapter 7, not each event is simulated as both proton

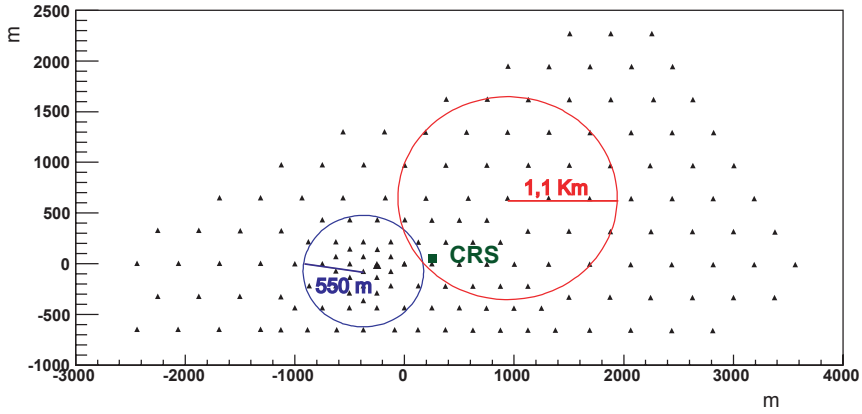

Figure 10.1: *Mape of the AERA site. The core positions for the events in Set-phase1 and in Set-phase2 are delimited respectively with the blue and the red circles.*

and iron primaries, but 100 protons and 100 heavy-like nucleons [1] for Set-phase1 (and 125 protons and 125 heavy-like nucleons for Set-phase2) are generated, with energy and arrival direction randomly chosen in the respective ranges of 10^{17}-10^{19} eV, 0-60 degrees for the zenith angle and 0-360 degree for the azimuth angle.
The primary energy and arrival direction distributions are shown in **fig.**10.2 separately for the two primary types, for both Set-phase1 (right side) and Set-phase2 (left side).

10.2 Lateral distribution function fit

The analysis of the radio data detected with AERA is fully implemented into the $\overline{\text{Off}}\underline{\text{line}}$ standard software framework of the Pierre Auger Observatory (cf. section 4.2).
Nevertheless, to be consistent with the previous analysis on the LOPES events, the simulated response of the radio detector is not taken into account here. Instead, the REAS3 simulated electric field in the north-south, east-west and vertical directions is directly taken at the position of the AERA antennas.
Again, the amplitude is determined as the maximum of each electric field component.

Due to the possibility offered by $\overline{\text{Off}}\underline{\text{line}}$ to reconstruct the total electric field strength at each antenna station, the ϵ_{TOT} given by the REAS3 simulations are considered.

The simulated radio pulses are filtered with an ideal rectangular filter of 30-80 MHz, nominal frequency-bandwidth of AERA (cf. Chapter 4).

These sets of REAS3 simulations can exhibit a significant level of numerical noise (Huege et al., 2010), especially for near-vertical air showers and for the electric field signal far away from the shower core. Thus, it is mandatory to exclude in each individual event all the antennas where the numerical noise becomes predominant.

A cut on the number of events is applied: each LDF must involve at least four antennas which provide radio information not affected by the numerical noise. This re-

[1] At the time of writing the thesis, a mistake in the configuration of CORSIKA showers was found: not iron nuclei but 26 neutrons only were set.

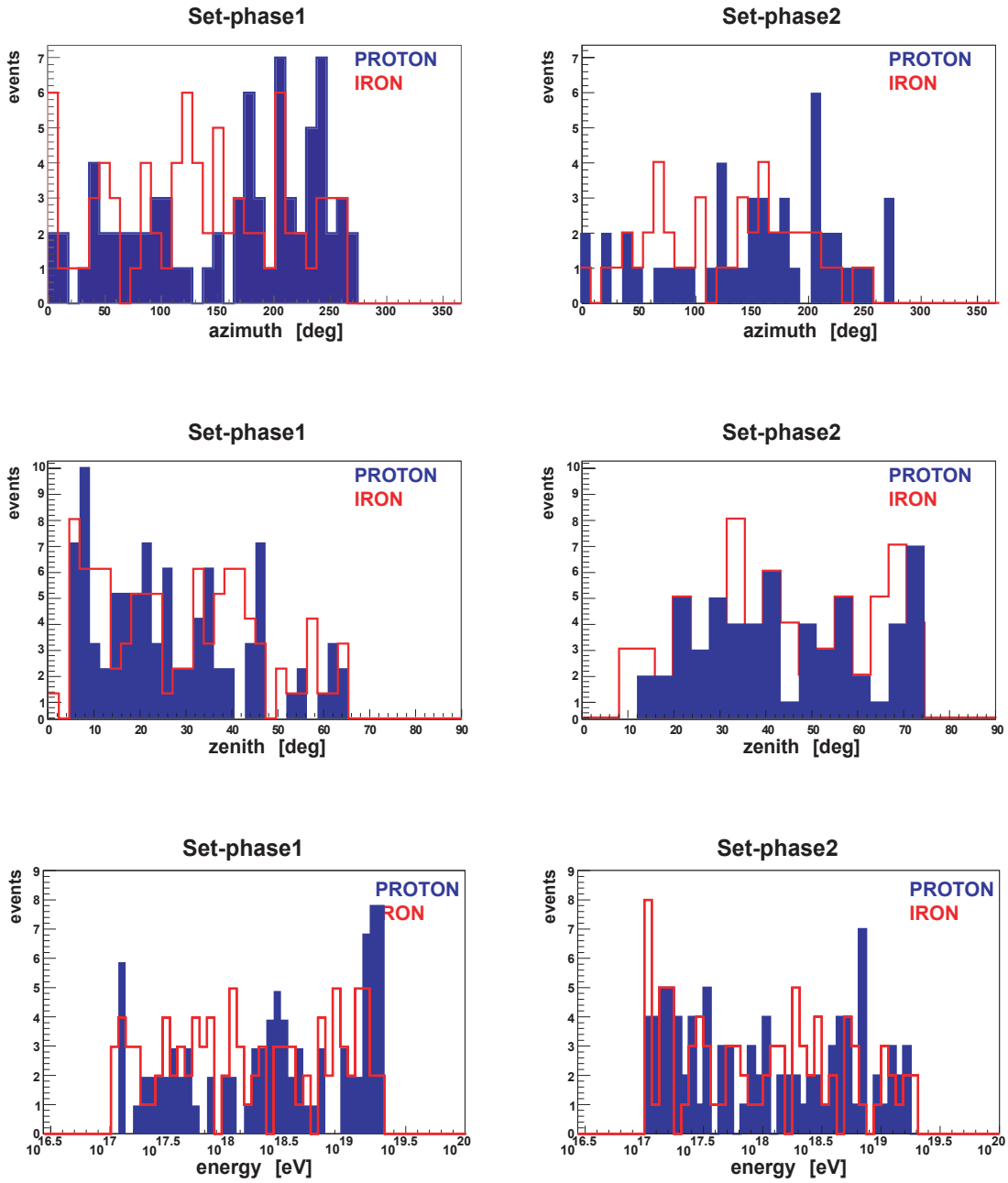

Figure 10.2: *Azimuth angle, zenith angle and primary energy distributions for the 200 events in Set-phase1 (left) and 250 events in Set-phase2 (right).*

quirement drops the number of events available for the analysis to 188 (98 heavy-like nucleons and 90 protons) for Set-phase1 and to 178 (86 heavy-like nucleons and 92 protons) for Set-phase2.

As already discussed in Chapter 6, the exponential fit does not properly describe the radio lateral behavior for distances larger than circa 200 m.

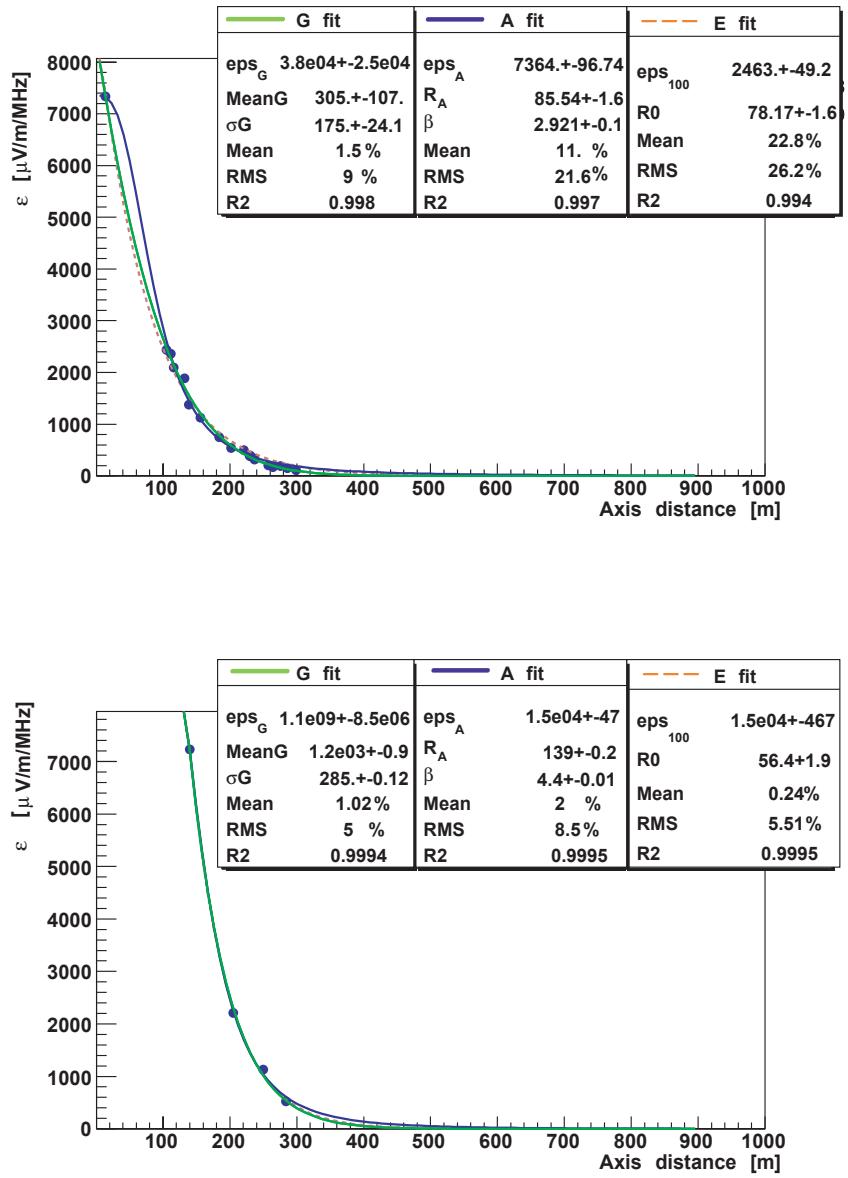

Figure 10.3: *Examples of the radio lateral distribution function fits with the a Gaussian, an exponential and a power-law functions, for one event in Set-phase1 (top) and one event in Set-phase2 (bottom).*

Before applying the slope method to the AERA simulated events and individualizing the typical distance for the $flat$ region, the fitting function for each LDF must be investigated in light of the AERA specific characteristics (i.e. antenna spacing and distance range from the shower axis).

Also in this case, three fitting functions are compared with each other, the exponential E fit and A fit functions already used in section 6.3 and a Gaussian function, with zero as the mean value, and the standard deviation (σ) and the amplitude (ϵ_G) as the two free fitting parameters.

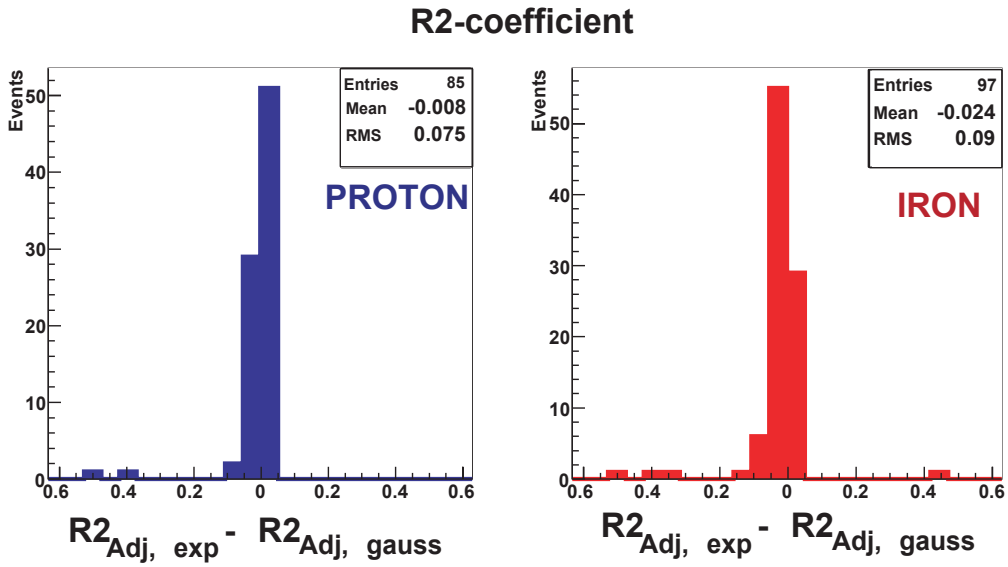

Figure 10.4: *Comparison between the adjusted R2 coefficient for the exponential (E fit) and the Gaussian function fit, for the events in Set-phase1*

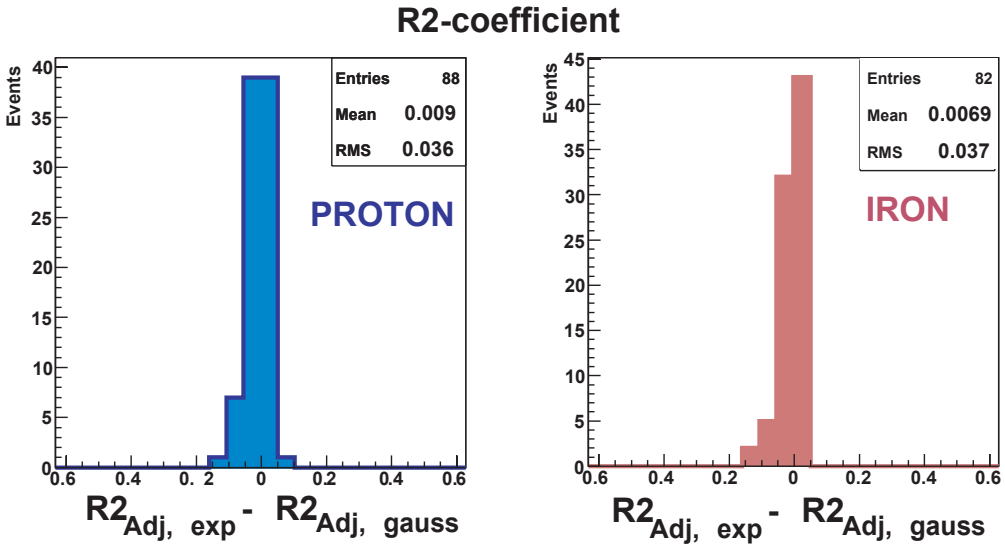

Figure 10.5: *Same as in 10.4, but for the events in Set-phase2*

As example, the LDF of a typical event from Set-phase1 (primary energy $2{\cdot}10^{18}$ eV, zenith 40.3° and azimuth 279°, coming from the south) and from Set-phase2 (primary energy $1.4{\cdot}10^{19}$ eV, zenith 16.7° and azimuth 3°, coming from the south) are presented in **fig.**10.3. For each, the three functions are fitted and the relative spread point–fit (i.e. Mean and RMS values) is computed as well.

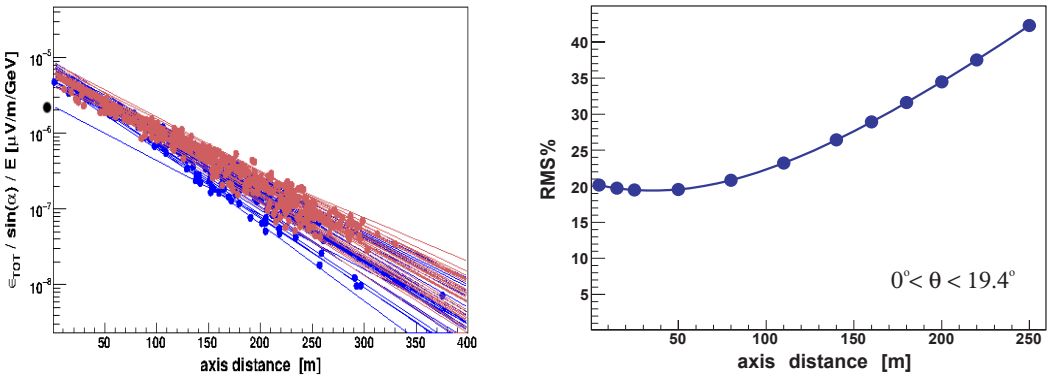

Figure 10.6: *Left: LDF for proton (blue) and heavy-like nucleons (red) REAS3 simulations of AERA events (Set-phase1) in the first zenith bin. The normalization for the total primary energy is shown. The exponential function is used as fit. Right: RMS spread of the LDF fits calculated at 12 distances from the shower axis.*

The A fit, which at larger distances reduces to a simple power-law function, is the most unstable among all, due to three fitting parameters. The Gaussian function seems to well describe the electric field strength even at distances larger than 300 m from the shower axis.

The adjusted R2-coefficient[2] is proposed again as comparison tool, separately for the two sets of simulations (**fig.**10.4 and **fig.**10.5).
The discrepancy between the Gaussian end the exponential fits is, on average, less then 10 $\%$.

The largest values are found for Set-phase1, with an RMS of $\sim$ 7 % and $\sim$ 9 %, respectively for proton and heavy-like nucleons events. Thus, noteworthy is the influence of the *number of antennas* involved in the LDF analysis: with a minor number of antennas - such as the case of Set-phase2 - both the exponential and the Gaussian functions can be equally considered to interpret the radio lateral behavior.

In the following analysis, aiming at a first indication about the functionality of the slope method applied to the AERA simulations, the exponential function can still be employed to fit the radio LDF.

10.3 The $flat$ region and X_{max} reconstruction

LDFs from proton and heavy primaries are plotted together to allow the identification of the $flat$ region, which is the distance from the shower axis where the radio pulse is independent of X_{max}, and where the LDF fits intersect. In other words, in the $flat$ region, the RMS spread of the fits is at the minimum value (cf. section 7.2.1).

In order to reduce the dependence of the LDF slope on the shower zenith angle, the

[2]For details please refer to section 6.3.1

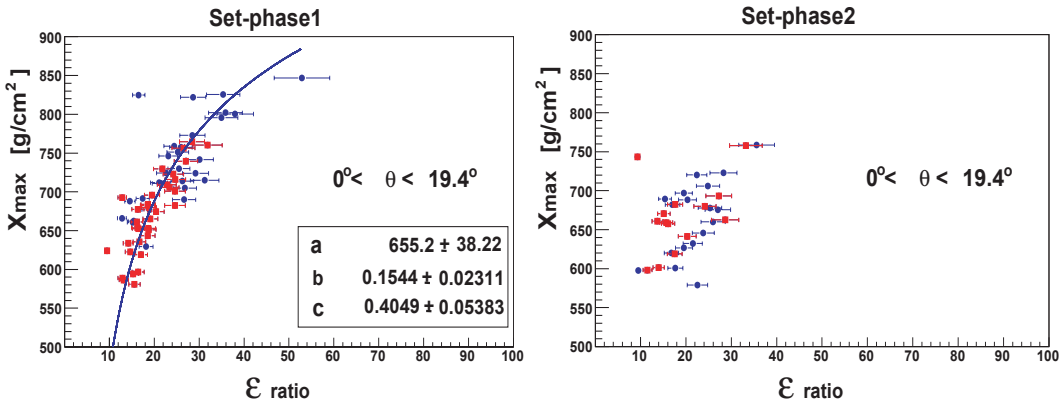

Figure 10.7: *Correlation between the X_{max} from the CORSIKA simulations and the slope of the radio LDF, fit with an exponential function ($\epsilon_{\mathrm{ratio}}$), for the AERA simulated events (Set-phase1-left part, Set-phase2, right part) in the first zenith angle bin. The blue points and the red squares represent respectively the proton and the heavy-like simulated events.*

simulated AERA events are subdivided into several zenith angle bins ($\Delta\theta$). Compared to section 7.2.1, 3 more zenith bins are available, but the statistics is remarkably reduced.

The total electric field strength in the antennas is divided by the AERA effective frequency bandwidth (50 MHz).

Normalizations concerning the arrival direction and the energy are needed. Indeed, the events of both Set-phase1 and Set-phase2 are simulated with an isotropic incoming direction and with the primary energy varying in the range 10^{17}-10^{19} eV. For already discussed reasons (cf. Chapter 7), the $\sim$sin(α), with α the geomagnetic angle[3], seems an appropriate approximation for the incoming direction normalization when the total electric field strength ϵ_{TOT} is considered. The energy normalization is performed with the total (E), the calorimetric ($\mathrm{E_{cal}}$) and the electromagnetic ($\mathrm{E_{em}}$) energies here as well (cf. Chapter 7 and Huege et al. (2008)).

In **fig.**10.6 (left side), the events in the first zenith bin of the selection Set-phase1 are presented. Only the total energy normalization is shown, since all three energy normalizations present almost the same behavior. The radio LDFs are fitted with the exponential eq.6.1.
On the right side, the corresponding RMS spread of the fits is displayed at twelve distances from the shower axis.

The $\mathrm{d_{flat}}$ is identified at the distance with the minimum RMS spread. The values for both the selections are listed in Table 10.1 and Table 10.2, respectively for Set-phase1 and Set-phase2. Some zenith angle bins are excluded from the investigation of the $flat$ region since the statistics are too low.
Nevertheless, by looking at **fig.**10.6 (left side), the LDF fits clearly do not intersect all at one distance from the shower axis. Moreover, the minimum value of the RMS spread

[3] **P** = **v**x**B** $\simeq$sin(α)

Table 10.1: *Distance of the $flat$ region - Set-phase1*

		E_{cal}		E_{em}		E	
$\Delta\theta$	entries	d_{flat} [m]	RMS % min	d_{flat} [m]	RMS% min	d_{flat} [m]	RMS% min
0.°-19.4°	64 (p 29, Fe 35)	20	16.5	15	16.7	30	16.4
19.4°-26.8°	23 (p 11, Fe 12)	10	12.9	5	13.3	20	12.1
26.8°-32°	9 (p 4, Fe 5)	//	//	//	//	//	//
32°-36.2°	19 (p 10, Fe 9)	5	18.6	5	19.4	30	19.5
36.2°-40°	11 (p 3, Fe 8)	30	22.2	20	22.5	50	22
40°-42.7°	9 (p 8, Fe 1)	//	//	//	//	//	//
42.7°-45.2°	7 (p 3, Fe 3)	//	//	//	//	//	//
$> 45.2°$	7 (p 22, Fe 25)	//	//	//	//	//	//

remains constant for a wide range of distances (0-50 m) with a value well away from the expectation, i.e. almost 20 % (cf. LOPES events show a minimum RMS of circa 6-8 %).

Before any hasty hypothesis on the non-existence of the $flat$ region, one may consider possible other explanation for such a behavior of the LDF fits. Plausible motivations are connected to:
a) the inaccuracy of the LDF fit, b)the improper normalization used, i.e. the geomagnetic as predominant effect assumption, c)the missing statistics and to d)the low number of the antennas which pass the cuts.
a) An appropriate analysis on the LDF fitting function different from a 1D-exponential is strictly required before applying the slope method on the AERA events, since the, apparently small, discrepancy between the exponential function and the correct radio lateral distribution seems to have a big impact on the whole analysis.
b) The charge excess effect gets important at the AERA site while the geomagnetic contribution diminishes (**fig.**5.2). The need to average out the charge excess contribution in the radio LDF is of fundamental importance for the application of the slope method.
d) Apparently, the number of antennas available for the analysis is not adequate . More antenna-points would help the identification of the correct fitting-function for the radio LDF. Moreover, a larger number of antennas may help in averaging out the charge excess effect.

Despite the large values of the RMS spread in the $flat$ region, one could look at the correlation between the slope $\epsilon_{\mathrm{ratio}}$ (see Chapter 7) and X_{max} from the CORSIKA simulations (**fig.**10.7). Only the events in the first zenith bin (Set-phase1, left part, Set-phase2, right part) are shown.
Only for the first set of data it is possible to apply the usual fit eq.7.6.

The dependence of $\epsilon_{\mathrm{ratio}}$ on X_{max} is clearly attenuated by increasing the spacing of the antennas and proton and heavy-particle initiated showers show quite similar slope of the LDF, i.e.$\epsilon_{\mathrm{ratio}}$.

Table 10.2: *Distance of the $flat$ region - Set-phase2*

		E_{cal}		E_{em}		E	
$\Delta\theta$	entries	d_{flat} [m]	RMS % min	d_{flat} [m]	RMS% min	d_{flat} [m]	RMS% min
0.°-19.4°	33 (p 18, Fe 15)	140	23	150	23.9	150	22
19.4°-26.8°	31 (p 14, Fe 17)	125	21.2	125	21.6	135	20.3
26.8°-32°	14 (p 7, Fe 7)	135	13.5	125	14	140	12.5
32°-36.2°	14 (p 7, Fe 7)	105	18	105	18.3	125	17.7
36.2°-40°	10 (p 2, Fe 8)	//	//	//	//	//	//
40°-42.7°	17 (p 10, Fe 7)	175	16.5	175	16.7	175	16
42.7°-45.2°	8 (p 6, Fe 2)	//	//	//	//	//	//
$> 45.2°$	7 (p 28, Fe 23)	//	//	//	//	//	//

10.4 Conclusion

The slope method is applied to REAS3 simulations for two sets of AERA events.

Several points are discussed as possible motivations for a mis-identification of the $flat$ region and an apparently weaker sensitivity of the LDF-slope to X_{max}:

The 1D-exponential is not adapted to describe the radio LDF for mean distances antenna-shower core of a typical AERA event. In contrast to LOPES, the discrepancy between the exponential function and the correct lateral-behavior can no longer be ignored.

A detailed investigation on other possible fitting functions, either multi-dimension (more than one spatial dimension) functions or the suggested Gaussian, is strongly recommended.

The assumption for the geomagnetic effect as the predominant emission mechanism, thus the use of the factor sin(α) for the radio pulse normalization, could partially affect the analysis. Indeed, in contrast to the LOPES site, the geomagnetic field strength in Argentina is quite low (cf. Chapter 5). With a small contribution to the radio signal from the geomagnetic effect, the charge excess effect becomes important and the need to average it out in the LDF analysis is fundamental.

Also the spacing between the antennas may strongly cause the loss in composition sensitivity for this selection of simulated events. The differences between the two sets of events considered so far, suggests that a large number of antennas allows a better identification of the LDF-fitting function and, in principle, allows to average out the charge-excess-effect.

Further investigations on the LDF fit function and the position of the $flat$ region for the AERA simulated events are, thus, necessary.

Larger statistics for the REAS3 simulated events, in each zenith angle bin, will surely improve the analysis on the mass sensitivity of the radio LDF-slope.

A simulated finer grid of antenna positions is strongly suggested in order to more precisely identify the LDF fitting-functions and the $flat$ region distances. Moreover, a finer grid helps to define the minimum spacing between the antenna for which the slope

method is applicable for the mass-sensitivity investigation.

11 Conclusion

In the last years the detection of radio emission from cosmic ray air showers, in the MHz regime, reached impressive results.
Eager to become competitive with the already well-established detection methods, the radio detection aims to achieve the information of primary cosmic-ray parameters with reasonably low uncertainties.

With a probe into the features of the radio lateral distribution (LDF), this work explored the possibility for a precise reconstruction of two fundamental air-shower parameters: the primary energy and the depth of the shower maximum $X_{\max}$.
The investigation was developed on a (REAS3-)simulation-based method, afterwards it was applied to LOPES measurements.

Even with the high level of man-made noise at the LOPES site, a precision of almost 20 $\%$ is reached for the primary energy reconstruction. Moreover, a promising low $X_{\max}$ uncertainty ($\sim$ 30 g/cm^2), almost comparable with the highest reachable accuracy of the fluorescence detectors, is predicted by merging radio information from two independent $X_{\max}$-reconstruction methods (slope- and cone-method).

Significant results emerge from this dissertation and are summarized in the following:

- The slope method requires a precise fit of the radio lateral distribution.
  The radio LDF profile shows to be more complex than a one-dimension (1D)-function. Moreover, the homogenous 1D-exponential, already in use for the LOPES measurements, obviously fails at certain distances from the shower axis. However, both a statistical analysis on the residuals and a comparison with expectations from REAS3 simulations established that the 1D-exponential function can be still considered a good approximation of the individual LOPES LDF.

  Fluctuations in the electric field, most probably connected to the charge excess contribution, are also evident. Due to the antenna spacing of the LOPES experiment, this effect is averaged out and has almost no influence on the slope of the lateral distribution function fit, and thus on the slope method.

- A certain distance from the shower axis ($flat$ region) was identified on a simulation-based method. This $flat$ region was confirmed to exist in (LOPES) data and it was proven to be the best place for a primary energy reconstruction. Indeed, in the $flat$ region, the analysis is affected by the lowest uncertainty, almost exclusively due to the shower-to-shower fluctuations.
  Even with the high level of man-made noise which affects the LOPES data, an accuracy on the energy reconstruction of $\sim$ 20 $\%$ is reached, almost independent on the shower inclination.

- A reconstruction of X_{max} for the events detected by the LOPES experiment was successfully carried out. The obtained values are comparable with the expectations for the cosmic ray nuclei.

  Remarkable is the tendency of a flatter slope of the radio lateral distribution for LOPES compared to REAS3 simulations. This is reflected in a mean reconstructed X_{max} smaller than for the iron-like nuclei.
  Possible reasons which may cause the divergences between measurements and simulations were discussed. Among them, the refractive index of the atmosphere, properly treated in the simulations only in the next version REAS3.1 and CoREAS.

  By itself, the slope method predicts a precision on X_{max} of only 20-40 g/cm^2, in dependence on the zenith angle of the event. This is the smallest uncertainty reachable with a stand-alone method applied on radio measurements.

X_{max} is the principal indicator for the cosmic ray composition, and the possibility to reconstruct it with radio-only data was demonstrated, using a simulation-based procedure applied to the LOPES data.
Comparisons of the reconstructed X_{max} with values determined independently by, at least, one other detection method are essential, but not possible in the framework of the KASCADE-Grande experiment.
This opportunity is offered at both the TUNKA-Rex experiment and at the Pierre Auger Observatory, where the next generation radio antenna array AERA will cross check the radio reconstructed X_{max} with the experimental values obtained respectively with the Cherenkov and the fluorescence detector.

A first attempt to apply the slope method to the AERA simulated events reveals the necessity to further investigate on the fitting function for the lateral distribution. Possible alternative functions - primarily the Gaussian function - are proposed and a methodology to approach the investigation is discussed.

12 Appendix A

The geo-magnetic radiation, which results from time-varying electrons and positrons drifted in the atmosphere, is considered to be the main contribution to the radio emission from air showers (cf. Chapter 5). The analysis presented in the following, on both LOPES and Auger measurements, aims to verify the statement above with a look at the sign and the polarization of the detected radio data. The results are brought to discussion in section 5.2.

12.1 Polarity of the signal

The expectations for a pure geo-magnetic contribution have been presented in Chapter 5, for both the LOPES and the Auger site. The individual **P** vector components (fig.5.2 and fig.5.1) flip the sign according to both the direction of the magnetic field and the arrival direction of the air shower.
The agreement in the first order between measurements and the geo-magnetic emission (**P**) (Horneffer et al., 2007, Isar et al., 2009, Ardouin et al., 2009, Revenu, 2010b) implies a sign dependence of the unlimited bandwidth radio pulse, for each individual component of the electric field. In fig.5.3 a REAS3 simulated radio pulse is taken as example. The component in the EW direction of the total radio pulse shows a positive sign, while in the NS and VE directions the pulse has a negative sign according to the specific arrival direction of the event.
No clear motivation supports the idea of a sign preserved also in the pass-band filtered signal. In fig. 5.4 the signal in the EW components of fig.5.3 is filtered with an ideal rectangular filter 43-74 MHz .
CODALEMA claimed to have seen in the detected radio pulse, i.e. filtered pulse with 23-83 MHz pass-band filter, a correlation between the incoming direction of the events and the sign of the signal recorded in the EW polarization (Ardouin et al., 2009), namely pulses from showers coming from the north are generally *positive* -see definition below - while signals from the south are generally *negative*. Further studies on the polarity, also on the NS polarization, are presented in (Riviere et al., 2009). In the CODALEMA analysis, the signal in each antenna was defined as the extremum of the filtered signal; the sign of the event was simply defined as the sign of the extremum (Ardouin et al., 2009). For the events detected by more than one antenna in a specific direction, i.e. east-west or north-south, the sign of the event was chosen as the majority of the signs among the several antenna traces (Ardouin et al., 2009).

A similar investigation is proposed here for both the EW and NS polarization signals detected by the LOPES experiment. A simplified expectation for the sign of both the **P** components along the north-south (NS) and east-west (EW) directions expected at the Karlsruhe site are presented in fig.12.1. According to the analysis in (Riviere et al.,

2009), the coordinate system is chosen so to have the positive sign (blue part) associated to the showers coming from the north for the EW component. Therefore, events coming from the east for the NS component have a positive value.

The radio events analyzed in the following are processed with the CR-tools pipeline (svn revision 6250). High coherency is required by setting the fraction of the correlated power larger than 80 $\%$, as it was already discussed for Selection1 and Selection2 in section 4.1.3. To increase the signal-to-noise ratio, a signal larger than 5 μV/m/MHz in, at least, one antenna per event is required. For each event detected by LOPES, the trace at the single antenna at the time of the CC-beam (cf. section 4.1.2, **The interferometric analysis**) is considered for the analysis. The sign of the trace is set to be positive if the absolute value of the maximum amplitude peak is larger than the absolute negative peak value.

In order to establish the polarity of each LOPES event and to equally take into account all the antennas which participate in the CC-beam procedure, the signal in each individual antenna is weighted with the corresponding signal-to-noise ratio (SNR), as described by eq.12.1

$$s = \frac{\sum_{\mathrm{i}=1}^{\mathrm{Nant}} (-1)^{\mathrm{m}} \mathrm{SNR_i}}{\sum_{\mathrm{i}=1}^{\mathrm{Nant}} \mathrm{SNR_i}} \tag{12.1}$$

The exponent m is 2 if $\mid \mathrm{positive_{MaxPeak}} \mid > \mid \mathrm{negative_{MaxPeak}} \mid$ while m=1 if $\mid \mathrm{positive_{MaxPeak}} \mid < \mid \mathrm{negative_{MaxPeak}} \mid$. Antennas with larger SNR have the biggest influence in the determination of s. For each individual radio event, the value of s gives the sign of the event. Moreover, larger absolute values of s generally mean that antennas with larger SNR present also the same sign of the trace. For the first part of the investigation, s is set to be larger than 40 $\%$.

A total of 572 events (381 for the EW polarization and 191 for the NS polarization) are selected.

The resulting signs of all the events are presented in fig.12.2, respectively for the EW polarization (top figure) and the NS polarization (bottom figure). The positive events are in total $\mathrm{N}_{positive}$=361 $\pm$ 17, while the negative are $\mathrm{N}_{negative}$=267 $\pm$ 16.

The dependence of the number of events with the direction of the shower which appears also in fig.12.2 reconfirms, also here, the predominance of the geo-magnetic emission mechanism, for both EW and ND detections.

A quantity r, defined as

$$r = \frac{\mathrm{N_{POSITIVE}}}{\mathrm{N_{NEGATIVE}}} \tag{12.2}$$

thus, the ratio between the positive and the negative events, is computed separately for the EW and for the NS signals.

Apparently a correlation between the incoming direction and the polarity of the LOPES detected signals is shown, for both the polarizations:

The EW oriented antennas, and the fraction of events coming from the south, thus expected to have a negative sign (RED region in fig.12.1 left), is considered at first.

Only a few percent of the total positive-signs is found in this region, with a significance of 2.25 - i.e. ($positive_{RED-EW}/positive_{total-EW}$). In contrast, the significance for the negative-signs, in the same region, is of more than 5.

The r quantity, for the EW oriented antennas, is considered as well. In the red region, $r_{\mathrm{ew.red}}$ is 0.62 $\pm$ 0.2, while, in the blue region, where the positive signals are expected,

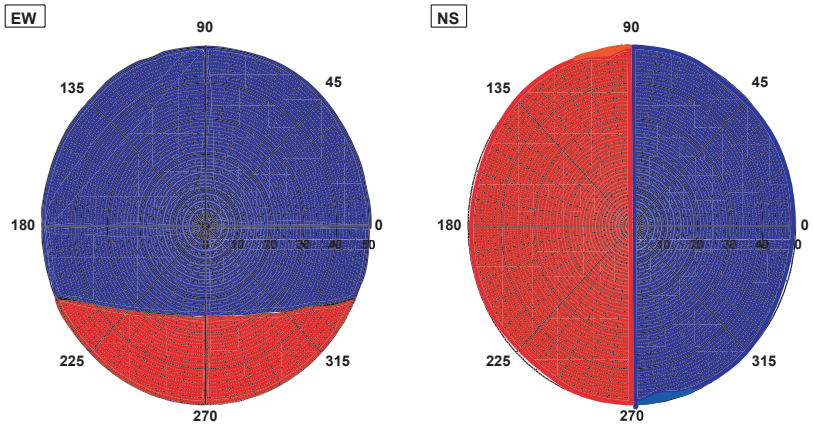

Figure 12.1: *Sign of the EW (left side) and NS (right side) components of the* P *vector calculated for the LOPES experiment site. Blue indicates the positive part, while red the negative.*

the ratio more than doubles, up to $r_{\mathrm{ew.blue}}$ =1.44 $\pm$ 0.2.
Regarding the NS oriented antennas a similar conclusion is argued: in the positive-sign region (fig.12.1, right, blue side), a larger fraction of positive-sign events with a significance of 56 is found compared to the negative-sign events (significance of 33). The calculated r quantities are $r_{\mathrm{ns.red}}$ = 0.5 $\pm$ 0.2 and $r_{\mathrm{ns.blue}}$ = 1.2 $\pm$ 0.2.
This would confirm the results found with the CODALEMA experiment and would lead us to declare a visible polarity of the signal even in the filtered LOPES traces.
Nevertheless, if a further cut on the events is applied, requiring s larger than 65 $\%$, in other words imposing that the selected events have a clearer sign, only few events are left and the dependence sign-arrival direction is no more evident.
Thus, no conclusive statement about the signal-sign in the LOPES data is possible.

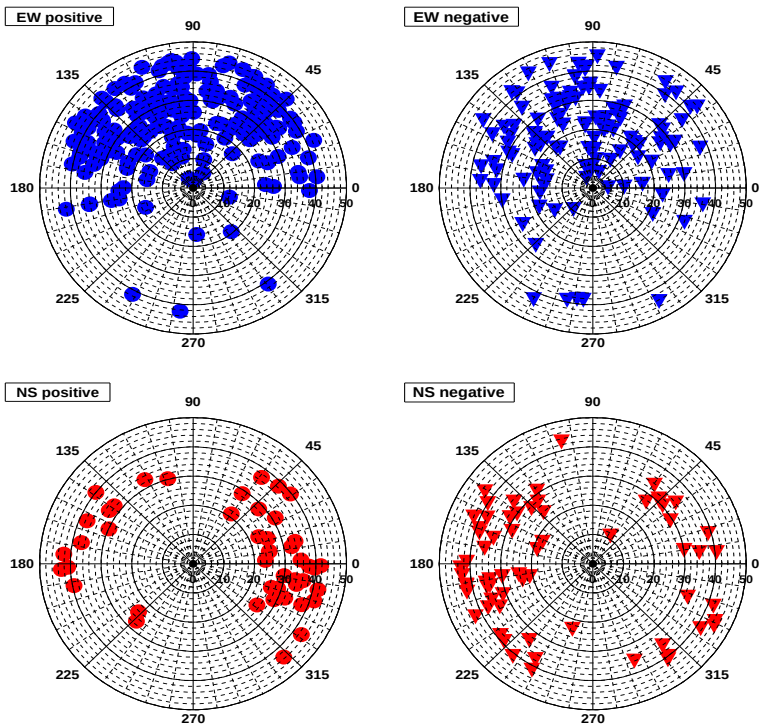

Figure 12.2: *Distributions of the sign recorded in the LOPES traces, for the signal in the EW polarized antennas (blue) and in the NS aligned antennas (red). On the left side only the positive sign ($s > 0$) (circles), while on the right only the negative sign (triangles) are plotted.*

12.2 Polarization analysis of the BLS-Auger data

An analysis of LOPES data presented in Isar (2010) argued interesting correlations of the radio pulse polarization with air shower parameters, in particular with the shower azimuth angle.
Taking into account the LOPES results, a similar investigation on one of the first radio data sets collected within the Pierre Auger Observatory is proposed.
In 2007 three antenna stations (Pole1, Pole2 and Pole3) were operating at the BLS (Coppens, 2009) with antennas aligned in both east-west and north-south directions (for further details please see section 4.2.2).
Only the radio events recorded in coincidence with the surface detector SD are considered. The search for coincidences is performed by looking at the GPS timestamps for both SD and radio setup (cf. section 4.2.2). A total of 313 events were recognized as coincident events and among these, only 234 had a detected radio signal in all three antenna stations (cf. section 4.2.3).
For the purpose of this investigation, REAS3 simulations for the 313 recorded events are performed, taking into account the environmental parameters of the Pierre Auger Observatory site, such as the altitude, the geomagnetic field strength and inclination.
For each event, 250 CONEX (Pierog et al., 2006) showers induced by proton primaries are prepared, using QGSJetII (Ostapchenko, 2006) and UrQMD (Bass et al., 1998) respectively as high and low energy interaction models. Among all the 250 showers, a typical [1] shower is selected. Finally, 26 REAS3 simulations for each typical shower are performed, one for the exact reconstructed core position and the other 25 for core locations randomly picked within the RMS uncertainty of the core position reconstruction (Asch et al., 2008).
Both simulated and recorded events are processed with the RDAS (Radio Detector Array Simulation) code (cf. section 4.2.2, **"RDAS"** and (RDAS Software, 2008)), in order to simulate the antennas response. A specific module is used, with the characteristics of the LPDA (Logarithmic Periodic Dipole Antenna) antenna which were employed at the BLS site during 2007.
RDAS functions and parameters are carefully set; for more details about the software modules and the BLS data selection we refer to section 4.2.2.

12.2.1 Recorded events

The recorded events are processed with RDAS and, after a quality cut selection, only 21 radio events are available for the analysis (see section 4.2.3).
Since the configuration of Pole3 changed during the data acquisition, its measurements are excluded from the investigation. The radio pulse information provided only by Pole1 and Pole2 is analyzed.
The peak of the electric field amplitude in the two east-west and north-south channels is taken into account and we will simply refer to them respectively as EW and NS.
In order to look simultaneously at the signal in both the north-south and east-west direction for the same event, the logarithm of the ratio of the peak amplitudes in the channels

[1] a shower with the shower maximum depth X_{max} close to the average X_{max} value of the 250 simulated primaries.

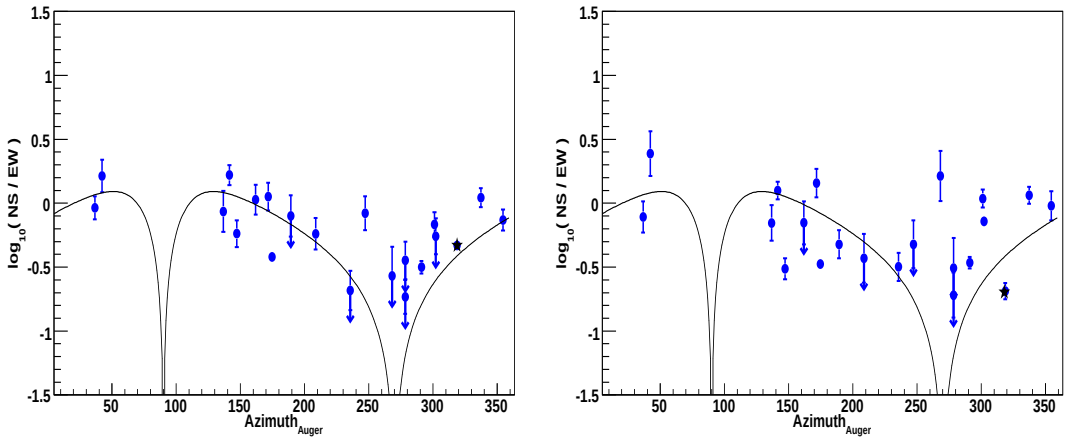

Figure 12.3: *Ratio of the maximum amplitude of the electric field measured in the north-south and east-west channels, for the BLS data, detected respectively at Pole1 (left) and Pole2 (right). The azimuth angle is provided by the SD reconstruction. The black star is the event recorded during a thunderstorm. The continuous line aims to be a guideline and represents the mean expected behavior, i.e. the* ***P*** *vector components ratio, calculated for the mean zenith angle (45.6°).*

is considered

$$\log_{10}\left(\frac{\mid \mathrm{NS} \mid}{\mid \mathrm{EW} \mid}\right) \tag{12.3}$$

and the correlation with the incoming direction of the shower is presented in fig.12.3 for both Pole1 and Pole2.
The signal-to-noise (SNR) is defined as a power quantity, thus the ratio of the squared signal-amplitude and the squared noise standard deviation σ^2. As a consequence, for each individual channel, the uncertainty on the pulse is estimated as:

$$\sigma_{\mathrm{EW}} = \sqrt{\frac{(\mathrm{EW})^2}{\mathrm{SNR}_{\mathrm{EW}}}} \quad ; \quad \sigma_{\mathrm{NS}} = \sqrt{\frac{(\mathrm{NS})^2}{\mathrm{SNR}_{\mathrm{NS}}}} \tag{12.4}$$

where the signal-to-noise (SNR) is directly given by the RDAS tool.
Since one of the event selection criteria described in the previous Chapter was to require a SNR larger than 14 in at least one of the two channels per antenna station (see section 4.2.3), some of the 21 selected events present a SNR lower than the chosen limit for the NS or the EW. In such a channel, no clear detection of the radio pulse is established and the recorded signal could be due to pure noise. In order to take into account these partially detected signals, upper and lower limits of the eq.12.3 can be stated. These are represented by arrows in the plots and an upper-limit (arrow pointing downwards) indicates no detection in the north-south channel while a lower-limit (arrow pointing upwards) stands for no detection in the east-west channel.
In fig.12.3 the azimuth angle is shown with the Auger convention, i.e. 0° means a shower coming from East and 90° from North.
A slight correlation of the BLS data polarization and the arrival direction of the primary

is presented, which would be a sign for the geomagnetic emission component.
Moreover, in black, a possible thunderstorm event is marked (Melissas et al., 2010). We decided to reject this event for the next comparison with the REAS3 simulations, since the electric field measured could have been strongly influenced by the high atmospheric electric field.
Using the information about the arrival direction reconstructed by the SD, the expectations for the **P** vector values along the north-south and east-west direction (eq.5.2) of the 21 events are estimated.
In fig. 12.4 the ratio of eq.12.3, now calculated for the **P** vector components

$$\log_{10}\left(\frac{\mathrm{P_{NS}}}{\mathrm{P_{EW}}}\right) \tag{12.5}$$

of each individual event (magenta triangles) are presented.
The colored lines represent the same **P** vector components ratio but calculated not for specific directions, but for constant values of the zenith angle (10°, 45° and 60°) and varying the azimuth angle in the range 0°-360°.
Eq.12.5 is not dependent on the observer position with regard to the shower core, thus the 21 expectations for the pure geomagnetic component can be directly compared with the electric field value recorded in both Pole1 and Pole2. The results are shown in fig.12.5.
The continuous line represents the ratio (eq.12.5) calculated for the constant zenith angle of 45.6°, which is the mean among the zenith values of the 21 selected events.
A general agreement between the recorded data (points) and the **P** vector expectation is visible in both the antenna stations. Nevertheless a strong deviation is noticed around 270°, which means, in the Auger coordinate system, events coming from the south, and for one point coming from the north (azimuth $\sim 40°$, zenith $\sim 60°$).
Theoretically, for these incoming directions and for an experiment in the Southern hemisphere, as in the case of the Pierre Auger Observatory, **P** is almost completely aligned in the east-west direction, thus the north-south component is null. This creates the expectation for eq.12.5 to drop to infinitely negative values, which is impossible for physically detected signals.
However, most of these events with azimuth angle value around 270° present upper-limits, which would indicate not real signal but pure noise detection in the north-south channel.
This could partially solve the visible discrepancy.

12.2.2 REAS3 simulated events

The necessary air shower parameters reconstructed by the SD, such as primary energy, core position and arrival direction of the 313 measured radio events are used as input parameters for CORSIKA (Heck et al., 1998) and REAS3 (Ludwig and Huege, 2011b). The observer position is simulated in order to represent the three antenna stations of the BLS setup in relation to the core of the shower and the frequency pass-band filter from 25 to 70 MHz [2] is applied to the simulated radio pulse.

[2] 50-70 MHz is the pass-band filter used in 2007 for the BLS setup

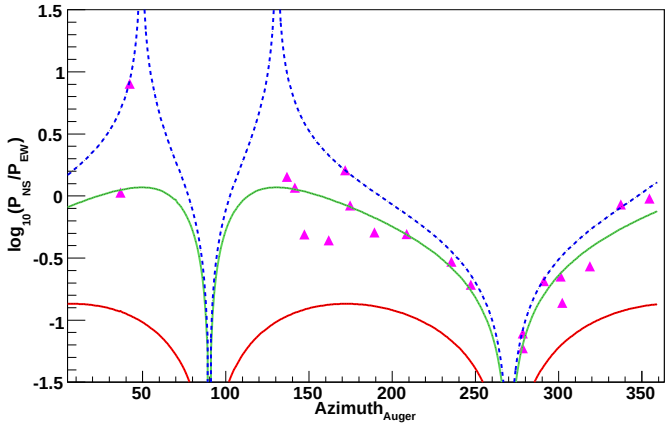

Figure 12.4: *Pure geomagnetic component expectation for the 21 selected events. Due to the chosen axis range for the next comparison, one point with azimuth $\sim 280^\circ$ and ratio -1.8 is not displayed. The* ***P*** *components ratio calculated for constant zenith angle is also shown, with a red line for 10°, green line for 45° and dotted blue line for 66°.*

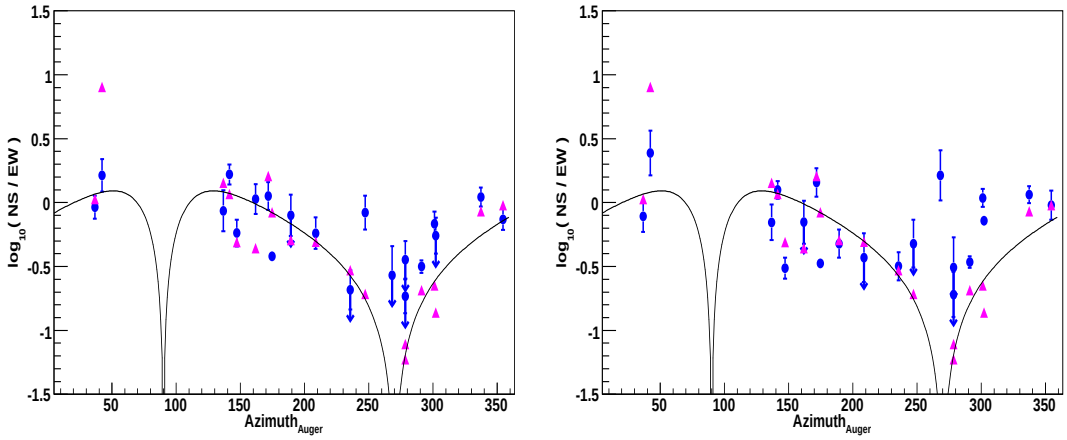

Figure 12.5: *Direct comparison between the data (circles) and the pure geomagnetic expectations (triangles) for both Pole1 (left) and Pole2 (right).*

The filtered radio pulse is taken and the polarization behavior analyzed before applying the detector response, thus before processing the simulations with the RDAS tool.
For the 21 previously selected events, the maximum peak amplitude in the east-west and north-south channel is taken and the logarithm of the ratio is shown in fig.12.6 (red crosses) for one antenna station. In the same figure, the REAS3 simulations are directly compared to the 21 previously calculated expectations for the **P** components ratio (purple x). Similar behavior is seen also in the second antenna station (Pole2).
A large discrepancy is visible again for azimuth angle around 270° and for one point with azimuth angle $\sim 40^\circ$.

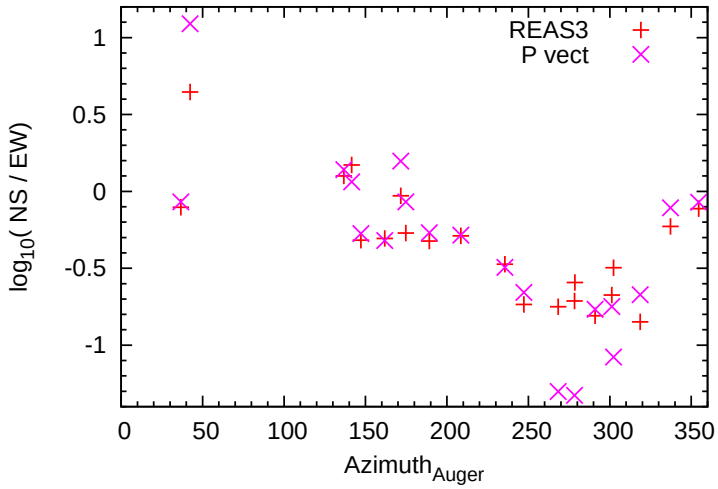

Figure 12.6: *The electric field information at the Pole1, taken directly from the REAS3 simulations of the 21 selected events (red crosses). A direct comparison with the* ***P*** *vector expectations of the same events is also shown (purple x).*

A first possible explanation is connected to a weak geomagnetic contribution in one of the two channels. Taking as reference the plot fig.5.2, the event with zenith angle $\sim 40^{\circ}$, i.e. coming from the north, and zenith of $\sim 66^{\circ}$ exhibits a geomagnetic component in the east-west channel close to zero. Since REAS3 included also the non-geomagnetic contribution, this discrepancy can be fully justified.
The same explanation might be used for the discrepancy of the events which have a southern arrival direction ($\sim 270^{\circ}$ azimuth angle), for which the P_{NS} component is supposed to be extremely small.
Nevertheless, a closer investigation revealed that some of these REAS3 simulated events are characterized by weaker signals in both the channels. Consequently, numerical noise in the REAS3 simulations becomes, for these events, unusually strong, leading to a logarithmic ratio of the pulses close to zero.
For such events, a proper treatment of the experimental background noise becomes absolutely mandatory.
In a second step, the 21 REAS3 simulated events are processed with the RDAS modules, and the galactic noise is added in each channel. This is simulated with a specific RDAS module (GalacticNoise module), based on the noise model of Cane (Cane, 1979), in which the intensity of the radio background towards the Galactic pole is parametrized. To properly take into account the noise influence on the simulated traces, each of the 21 REAS3 events is processed 30 times with RDAS, obtaining 30 different representations of the noise. The reason for such procedure was mainly due to the low statistics, since only 21 events passed the quality cuts.
Afterwards, for each simulated event, the distribution of the 30-times calculated eq.12.3 is considered and the Mean and RMS values are taken respectively as the value and the error bars presented in figure 12.7 as red squares, for both Pole1 and Pole2.

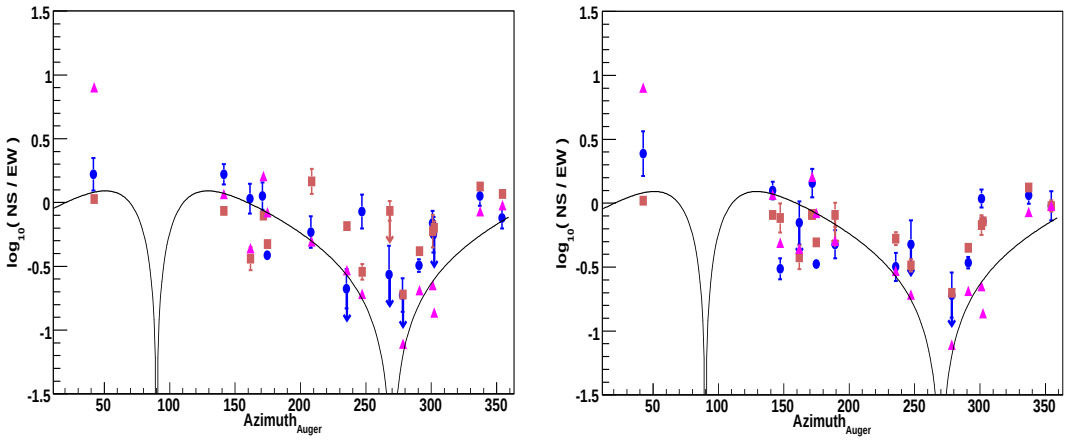

Figure 12.7: *Direct comparison between recorded data (circles), REAS3 simulations (squares) and the pure geomagnetic expectation (triangles) of the polarization behavior. The continuous line gives a trend of the mean expected behavior for the pure geomagnetic emission (**P** component calculated for 45.6° inclined events).*

Only events with SNR larger than 14 in at least one channel are shown and, with such criteria, 5 events are rejected in each antenna station since their simulated field strengths are too low to pass the cut.
As in the previous plots, the arrows represent the upper- and lower-limit for the signal partially detected.
As expected, some discrepant points previously discussed (cf. fig.12.6) drop out. This is a clear indication for a small signal but large noise in both the channels for these removed events.
A direct comparison between **P** vector calculated expectation (triangles), REAS3 simulations (squares) and recorded data (points) (fig.12.7) for both stations is presented. Again, as guideline, the **P** vector components ratio, calculated for the mean zenith angle (45.6°) is drawn.
Even with a slight disagreement between recorded data and REAS3 simulations, a general trend which follows the geomagnetic component expectation is seen.
On the other hand, the discrepancy with the **P** vector prediction becomes large, for both data and REAS3 events, when a pure geomagnetic component is expected to be weak in one of the two channels. In other words, for those events which come from the south (small or null P_{NS} signal) and from the north (small or null P_{EW} signal).

13 Appendix B

13.1 Selection1

13.1.1 REAS3 simulations: energy determination for Selection1

The correlation between the electric field in the $flat$ region and the calorimetric energy (fig.13.2) is shown for all the zenith angle bins (cf. section 7.4). The correlation is fitted with the linear function (left side) and with a power-law function (right side).
In fig. 13.4 the correlation between the electric field in the $flat$ region and the electromagnetic energy is shown as well.

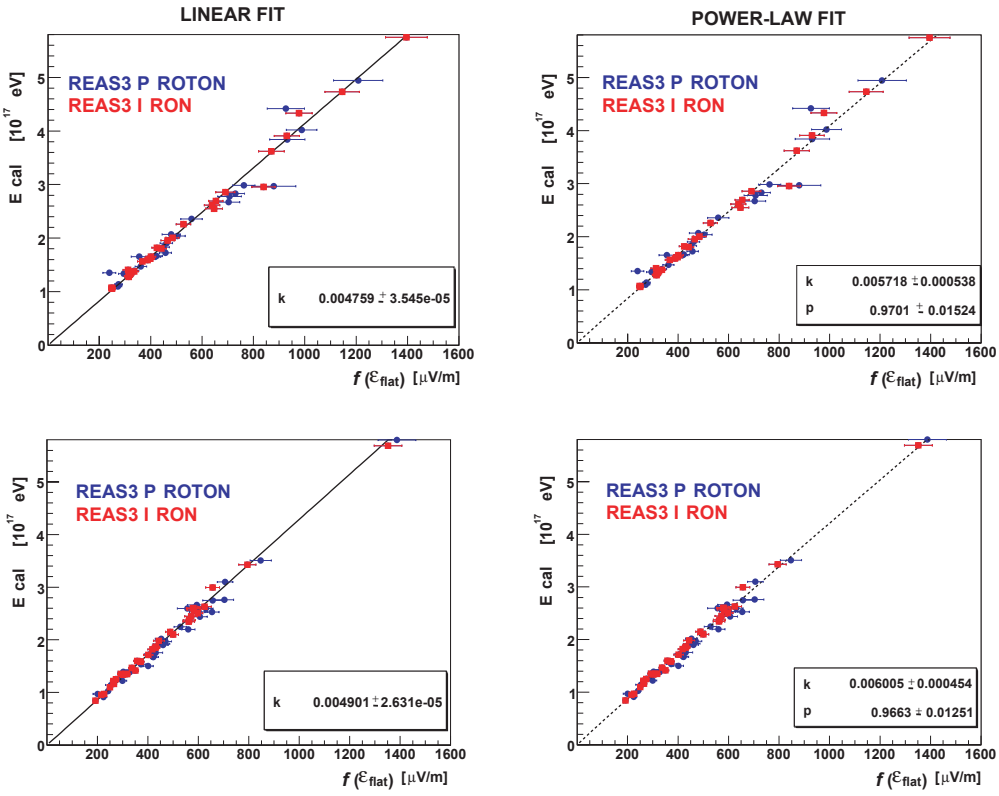

Figure 13.1: *to be continued in the next page*

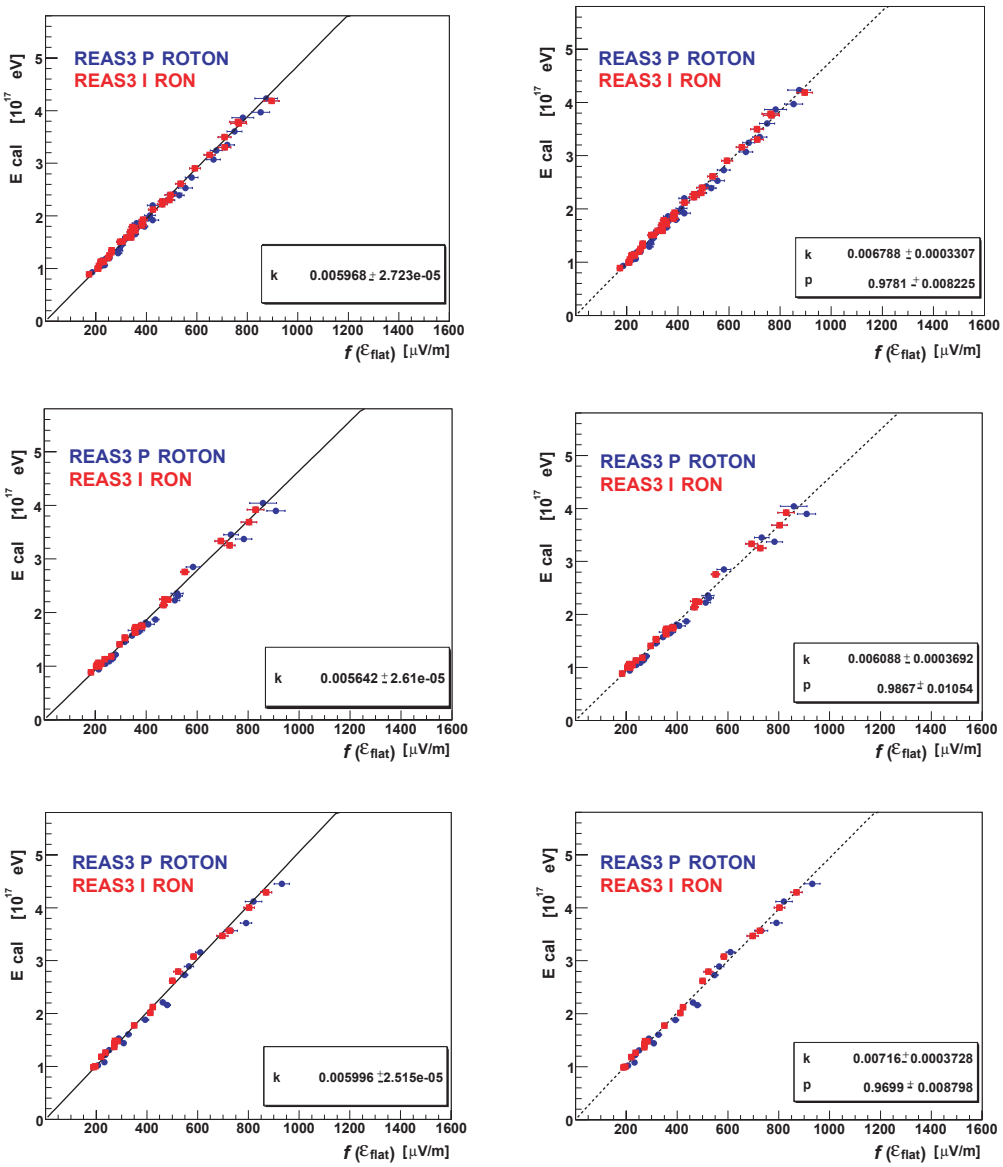

Figure 13.2: *(continued) Linear correlation between the electric field in the $flat$ region and the calorimetric energy for the events, from top to bottom, in all the five zenith angle bins. Both proton (points) and iron (squares) primaries are simulated. Both the linear fit (left side) and the power–law fit are shown.*

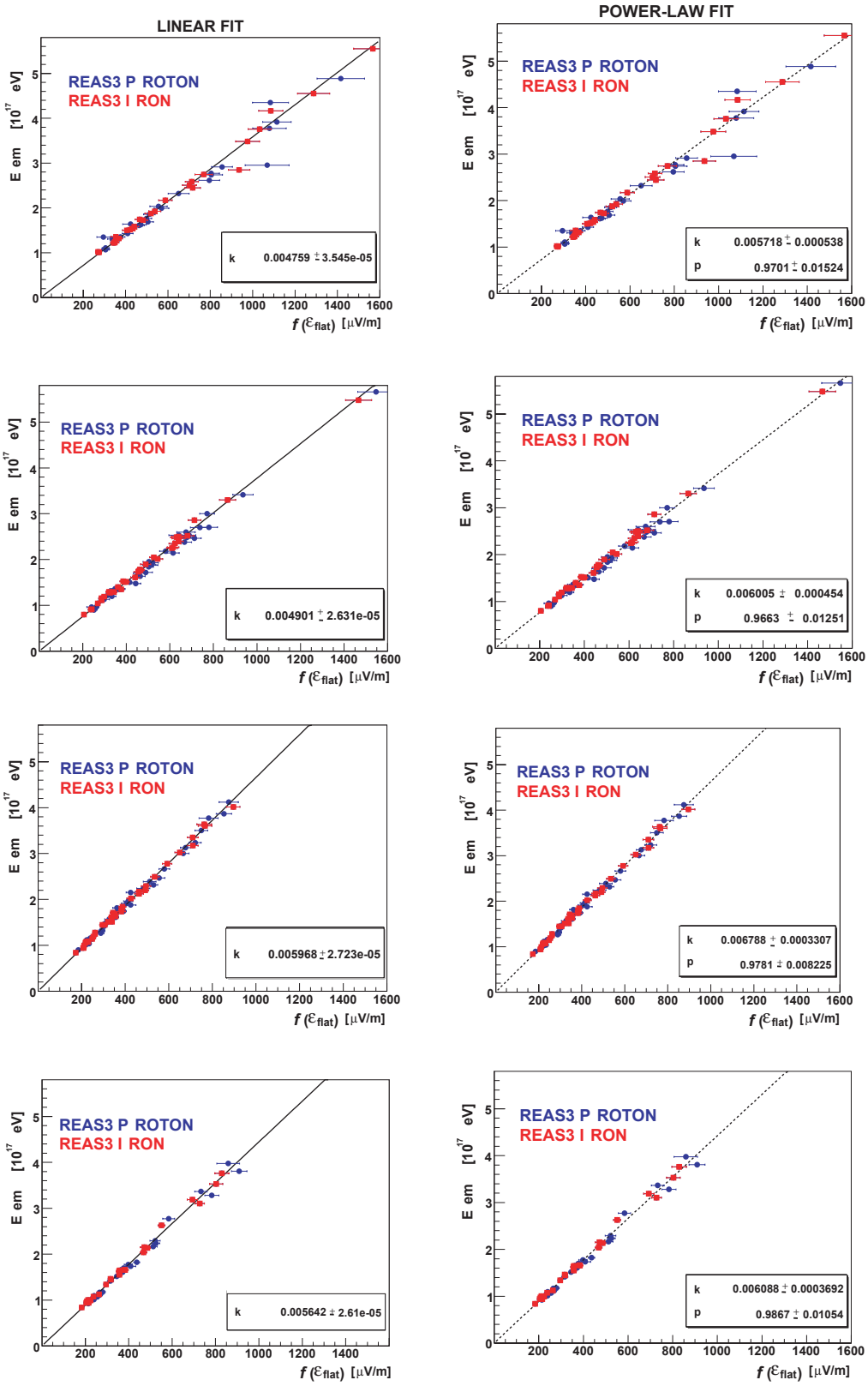

Figure 13.3: *to be continued in the next page*

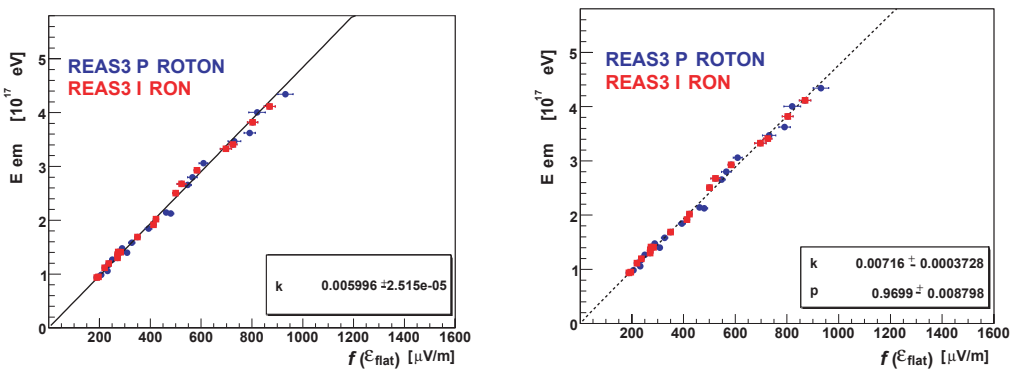

Figure 13.4: *(continued) Linear correlation between the electric field in the $flat$ region and the electromagnetic energy for the events, from top to bottom, in all the five zenith angle bins. Both proton (points) and iron (squares) primaries are simulated. Both the linear fit (left side) and the power–law fit are shown.*

13.1.2 REAS3 simulations: $X_{\max}$ determination for Selection1 - QGSJetII

The ratio of the REAS3-simulated radio amplitudes ϵ_{TOT} in the $flat$ and $steep$ regions provides the slope of the LDF. QGSJetII is used as interaction model in CORSIKA in order to reproduce the air shower particles in the atmosphere.
A correlation between the `true` X_{max} (from CORSIKA) and the radio LDF slope, discussed in section 7.5, is clearly visible in all the zenith angle bins. The function 7.6 is used to fit the protons (points) and the irons (square) simulated events. From top to bottom are presented, in order, the events in the second (19.4°-26.8°), third (26.8°-32°), forth (32°-36.2°) and fifth (36.2°-40°) zenith angle bins.

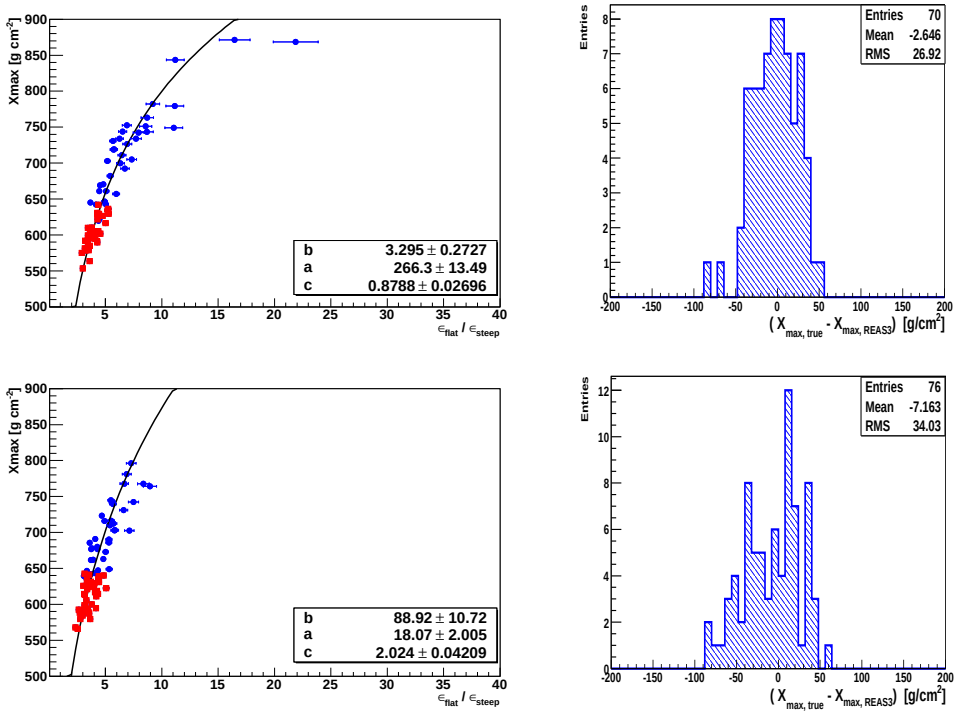

Figure 13.5: *to be continued in the next page*

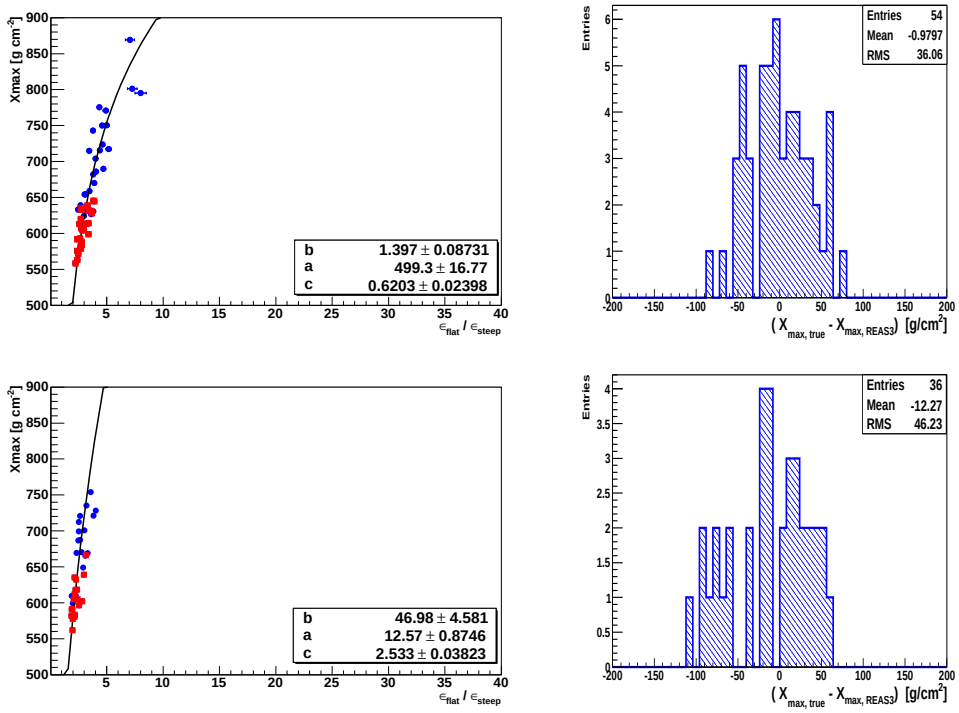

Figure 13.6: *(continued) Ratio of the simulated filtered radio pulse in the $flat$ and $steep$ region in relation to the depth of the shower maximum. In order from top to bottom the proton (points) and iron (squares) simulations for the events from the second to the fifth zenith bin.*

13.1.3 REAS3 simulations: $X_{\max}$ determination for Selection1 - EPOS

I the following, the EPOS interaction model is used to generate the air-shower particles. The same kind of correlation between the $X_{max,CORSIKA}$ and the radio LDF slope, discussed in section 7.5, is clearly visible in all the zenith angle bins. The function 7.6 is used to fit the protons (points) and the irons (square) simulated events. From top to bottom are presented, in order, the events in the second (19.4°-26.8°), third (26.8°-32°), forth (32°-36.2°) and fifth (36.2°-40°) zenith angle bins.

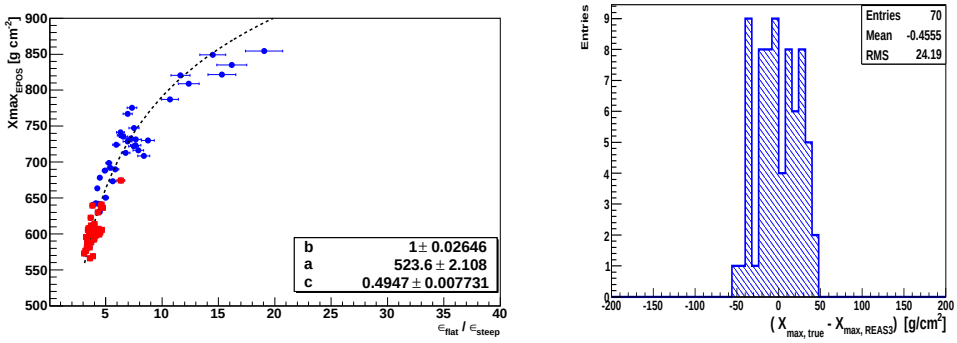

Figure 13.7: *to be continued in the next page*

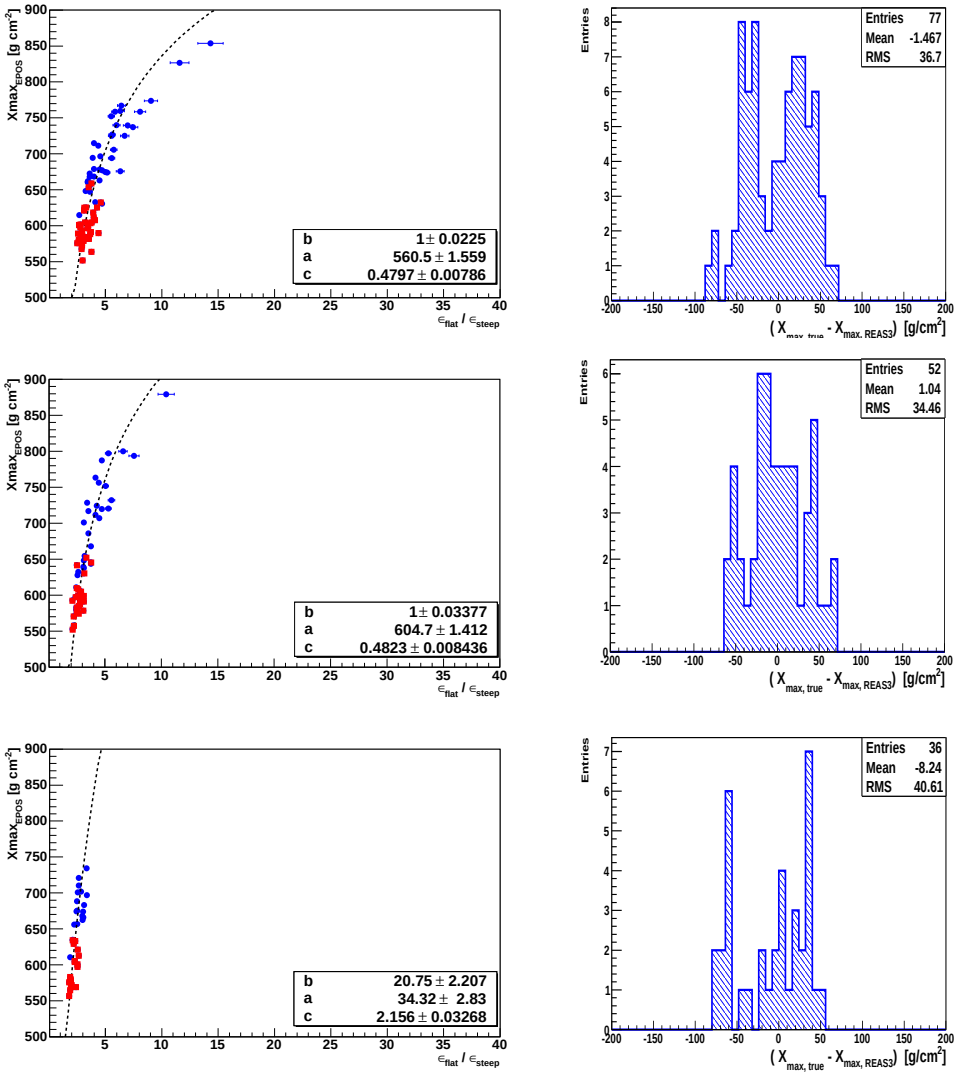

Figure 13.8: *(continued) Same as fig.13.6 but with EPOS interaction model simulations.*

13.2 Selection2

13.2.1 REAS3 simulations: energy determination for Selection2

The correlation between the electric field in the $flat$ region and the total energy of the air shower is shown below for the events in Selection2 (cf . section 8.3). The correlation is fitted with both a linear function (fig.13.10) and with a power-law function (fig. 13.12). On the right part of the figure, the relative spread from the fit, defined as (energy$_{point}$-energy$_{fit}$/energy$_{fit}$), is presented.
From top to bottom, in order, the events in the first (0°-19.4°), second (19.4°-26.8°), third (26.8°-32°), forth (32°-36.2°) and fifth (36.2°-40°) zenith angle bins are shown.

13.2.1.1 Linear fit

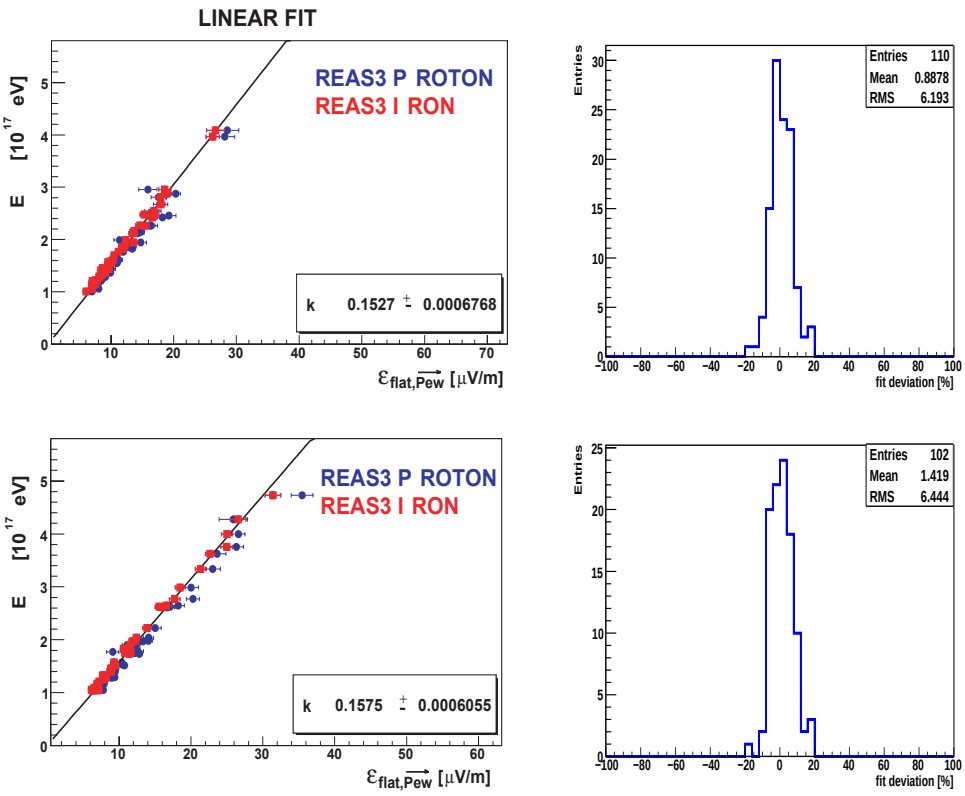

Figure 13.9: *to be continued in the next page*

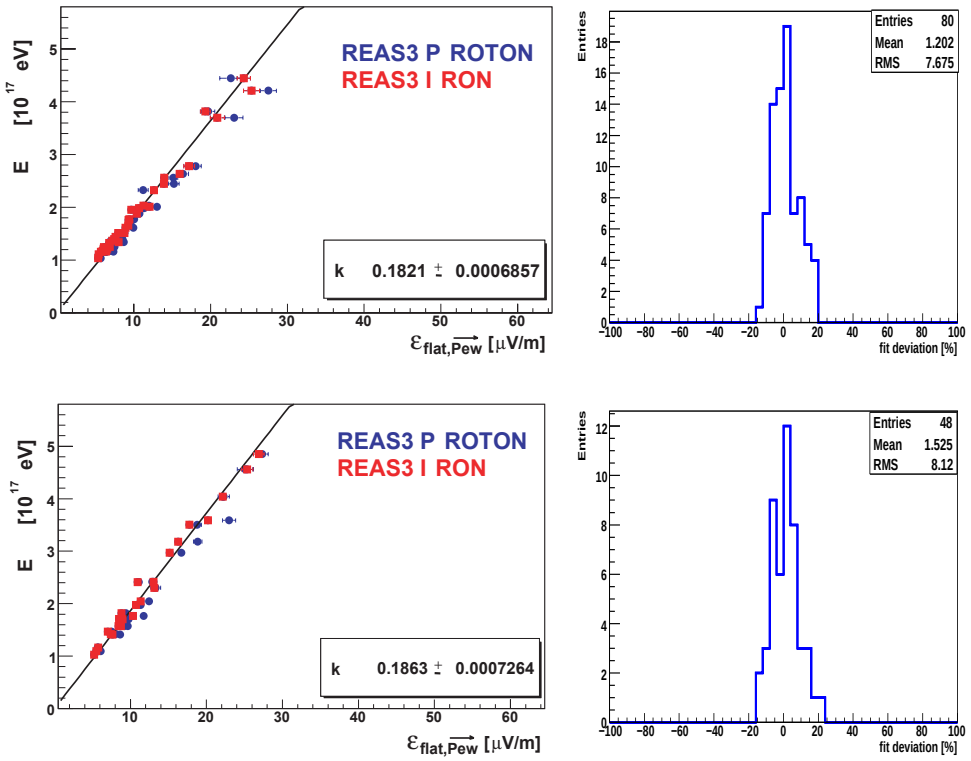

Figure 13.10: *(continued) Linear fit for the total primary energy correlation with the single component of the electric field in the $flat$ region. From top to bottom events from the first to the fifth zenith angle bin.*

13.2.1.2 Power-law fit

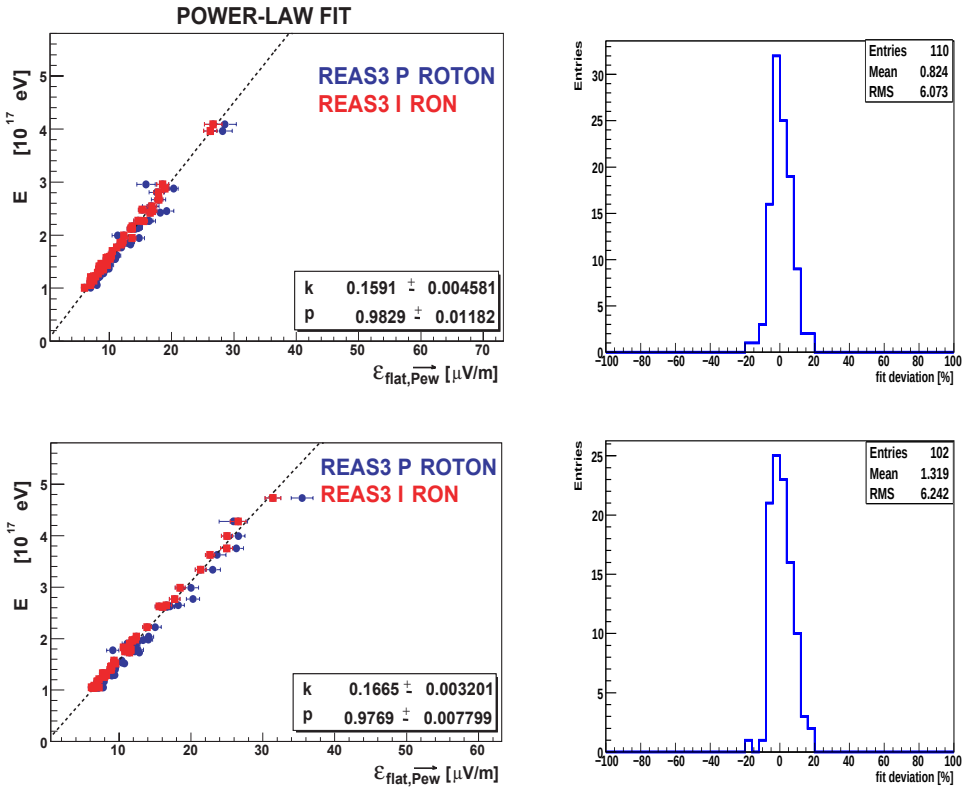

Figure 13.11: *to be continued in the next page*

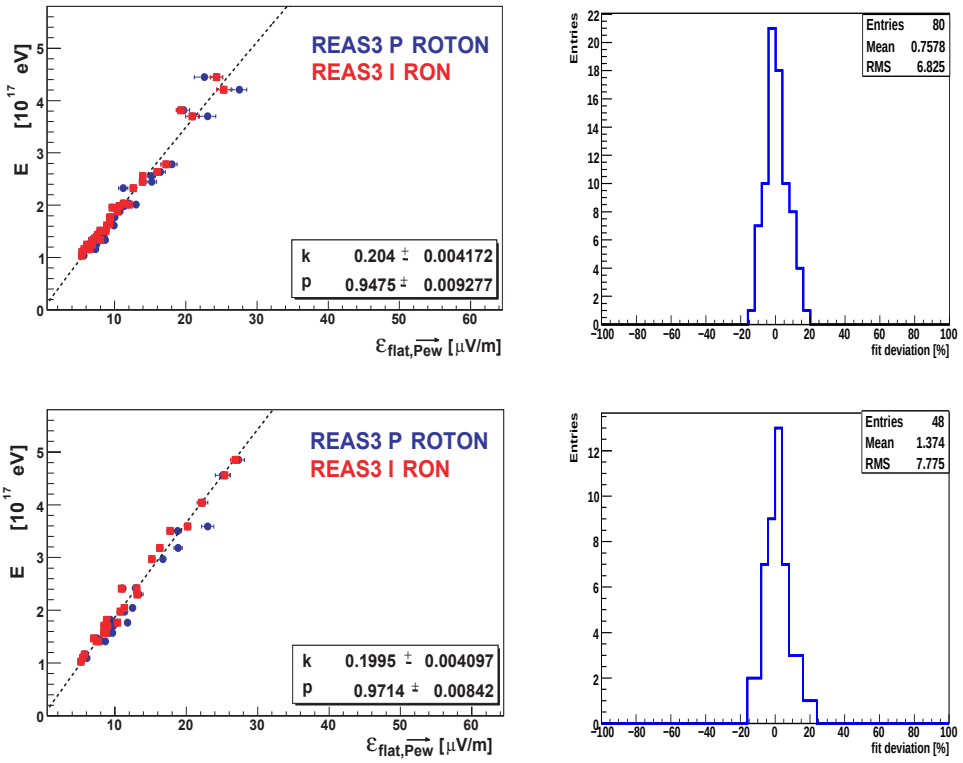

Figure 13.12: *(continued) Power-law fit for the total primary energy correlation with the single component of the electric field in the $flat$ region. From top to bottom events from the first to the fifth zenith angle bin.*

13.2.2 REAS3 simulations: X_{max} determination for Selection2

In fig.13.14, the correlation between X_{max} and the radio LDF slope is presented for all the events in Selection2(cf . section 8.3). On the right part of the figure, the relative spread from the fit.
From top to bottom, in order, the events in the first (0°-19.4°), second (19.4°-26.8°), third (26.8°-32°), forth (32°-36.2°) and fifth (36.2°-40°) zenith angle bins are shown.

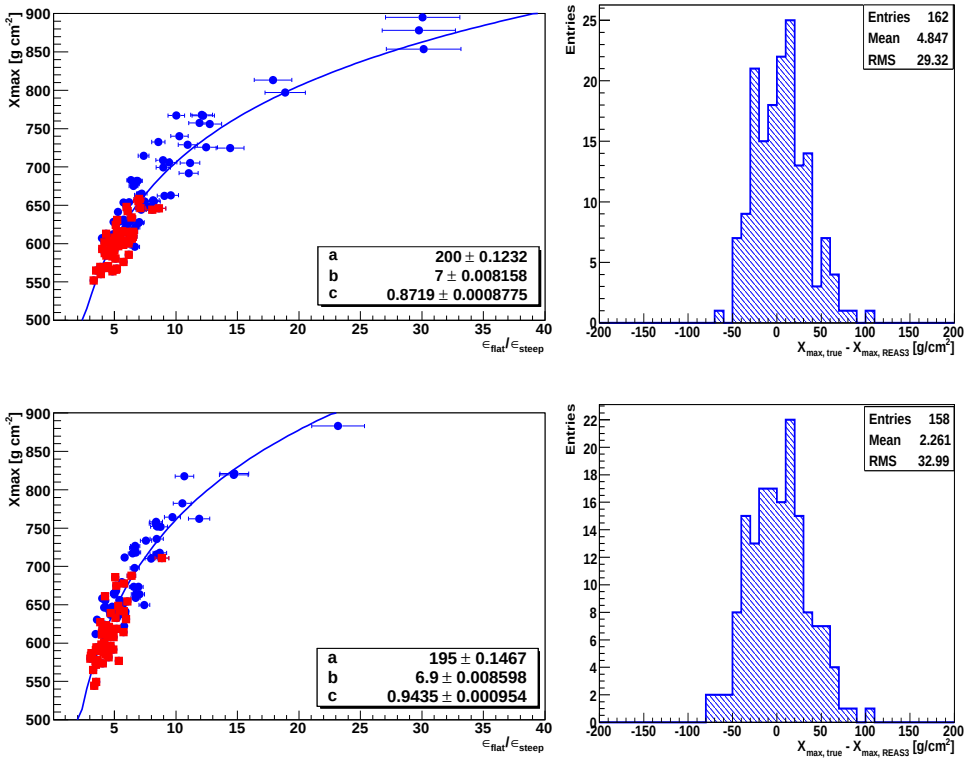

Figure 13.13: *to be continued in the next page*

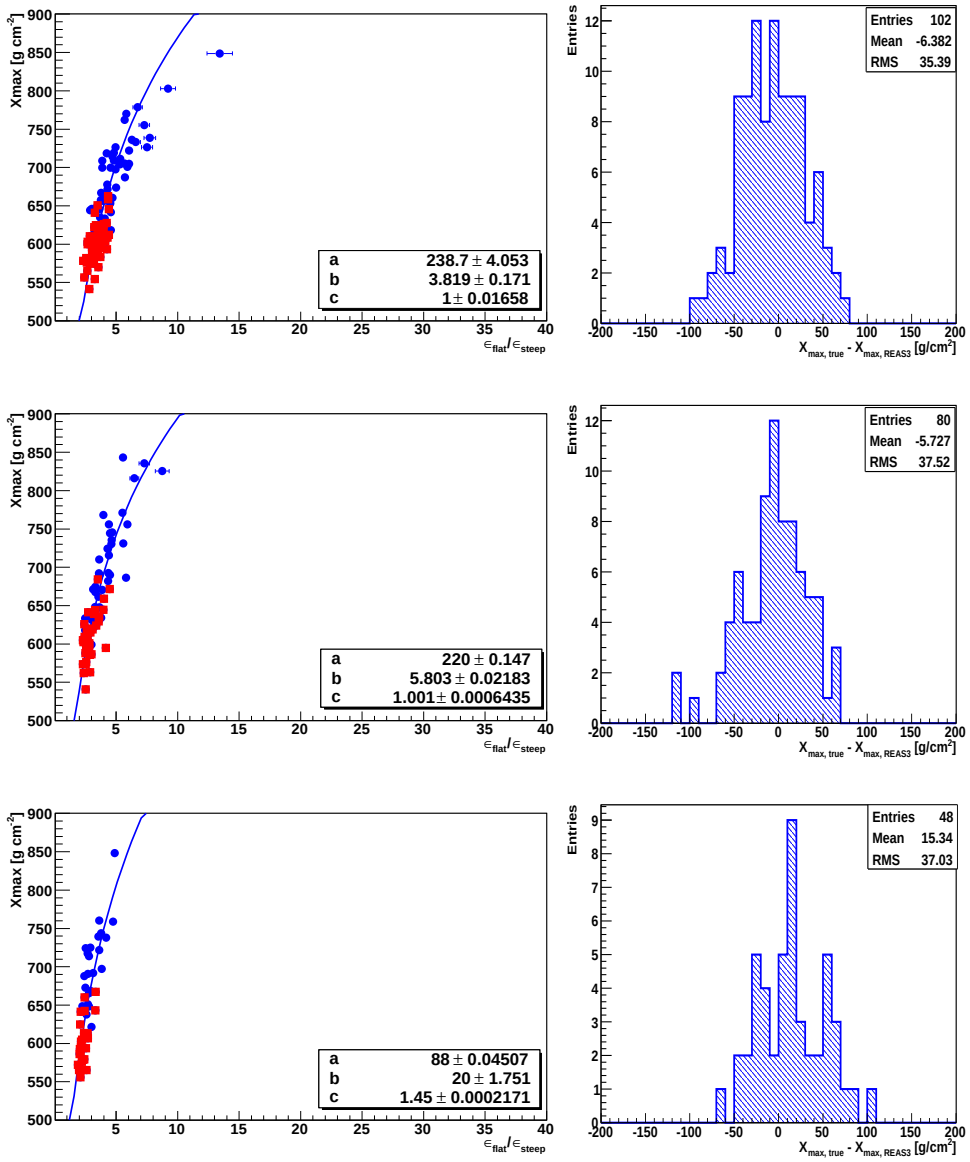

Figure 13.14: *(continued) LDF slope for the single electric field component (EW) in relation to the depth of the shower maximum, given by the CORSIKA simulations. From top to bottom, events in the first up to the fifth zenith angle bin. On the right, distribution of the points (*$X\mathrm{max}, \mathrm{CORSIKA}$*) around the fit (*$X\mathrm{max}, \mathrm{REAS3}$*) value.*

14 Appendix C

In section 9.1.1 is investigated whether the $flat$ region is the most appropriate distance from the shower axis to reconstruct the primary energy. Indeed, the smallest uncertainty on a radio-reconstructed energy, mainly due to the shower-to-shower fluctuations, is predicted in this region.
A linear correlation between the energy given by KASCADE-Grande reconstruction and the LOPES amplitude in the $flat$ region (ϵ_{flat}) is shown in fig.9.2, where the normalization to the east-west component of the **P** vector (cf. Chapter5) is considered.
For comparison, the same linear correlation is investigated at three other distances from the shower axis, of the same LDF fit. Namely at 0 m, 100 m and at the steep region, i.e. between 230 m and 260 m for this specific selection (Selection2).

The RMS of the relative spread from the linear fit is used as comparison tool (fig.9.4 and, in the $flat$ region, the RMS is practically always the smallest.

14.1 Primary energy and ϵ_0

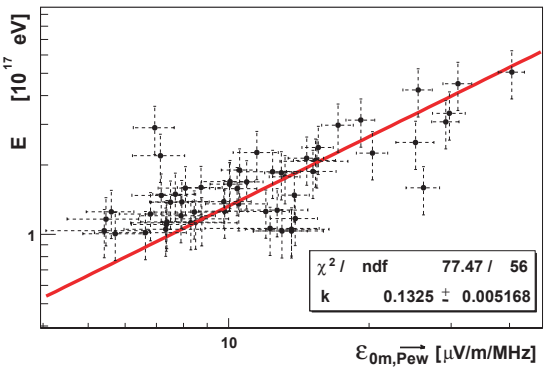

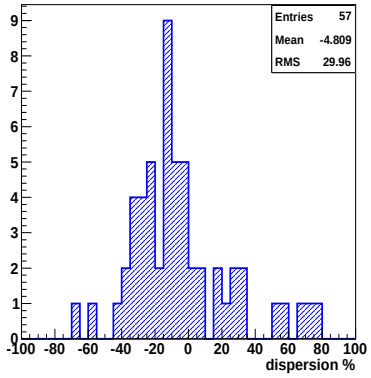

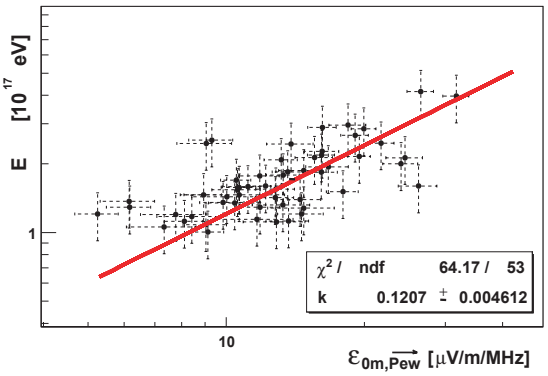

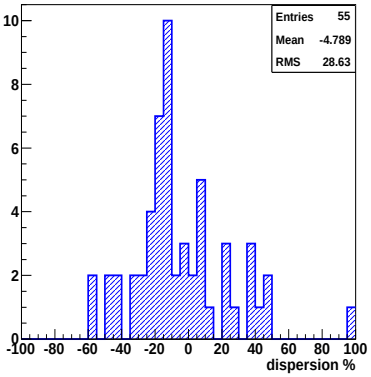

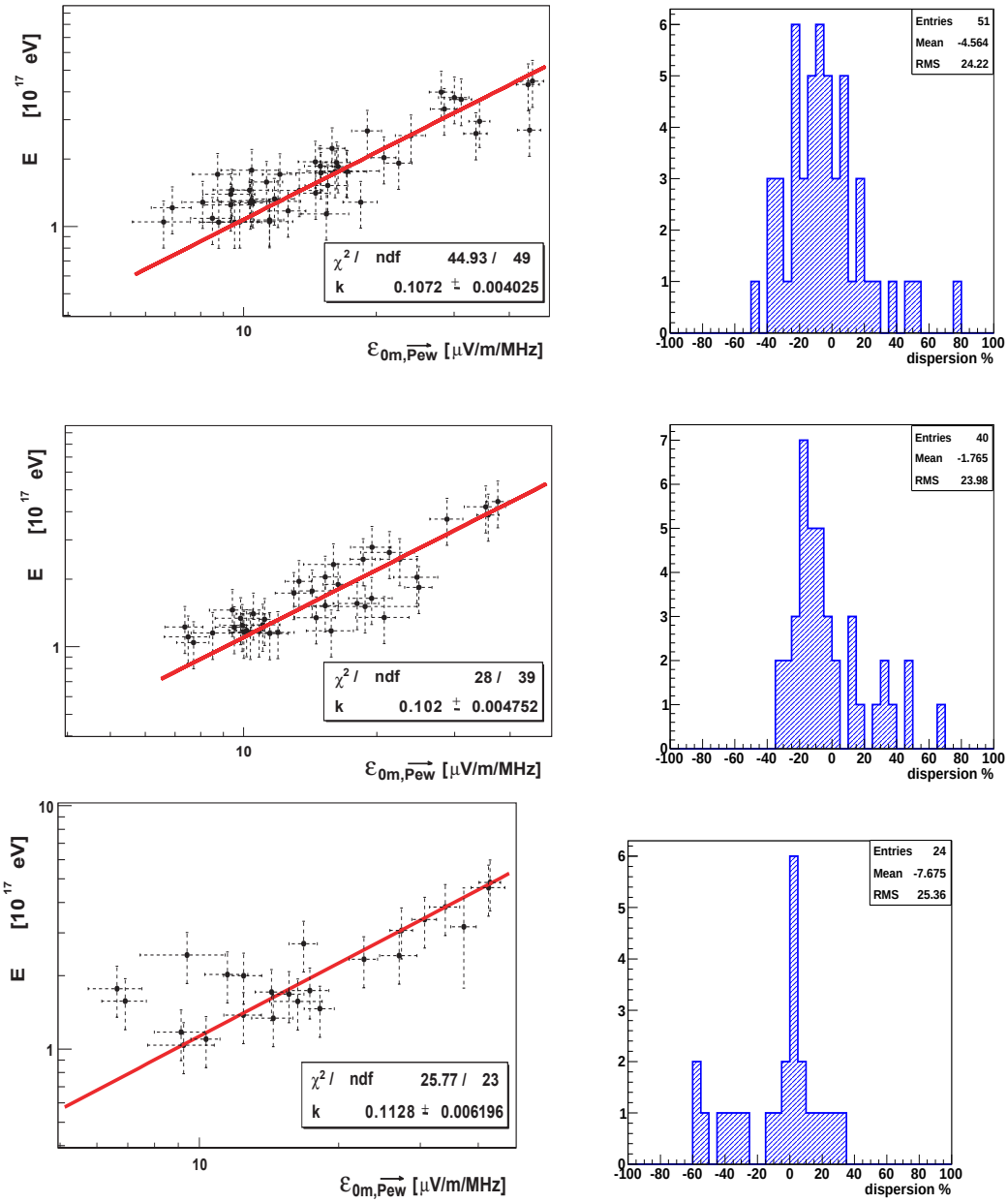

Figure 14.1: *Linear correlation between the primary energy reconstructed by KASCADE-Grande and the filtered radio pulse detected at 0 m from the shower axis. From top to bottom, in order, events from the fist to the fifth zenith angle bin are separately shown.*

14.2 Primary energy and ϵ_{100}

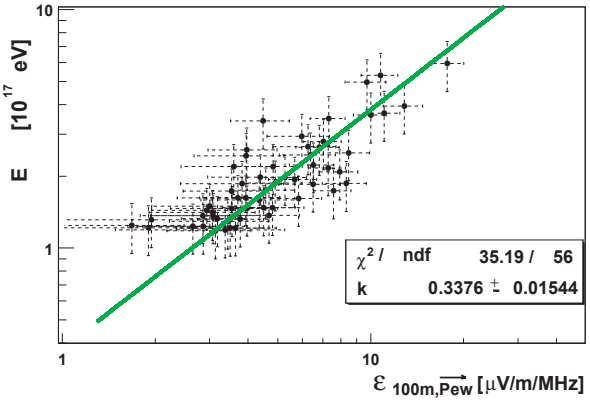

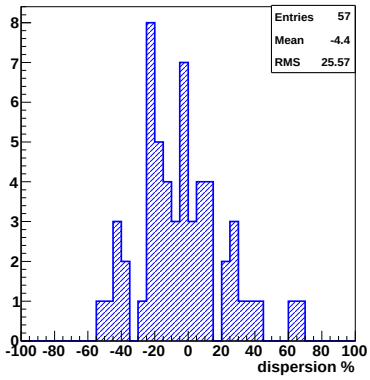

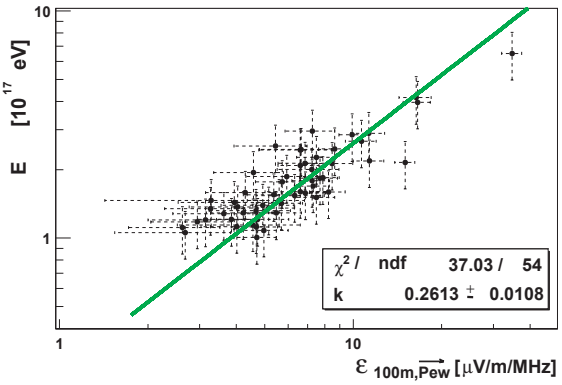

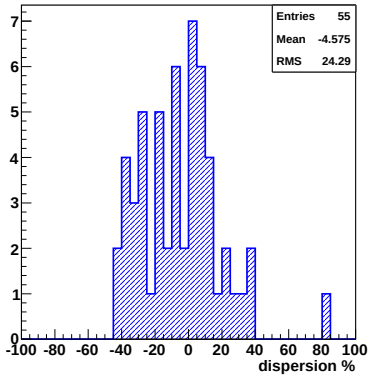

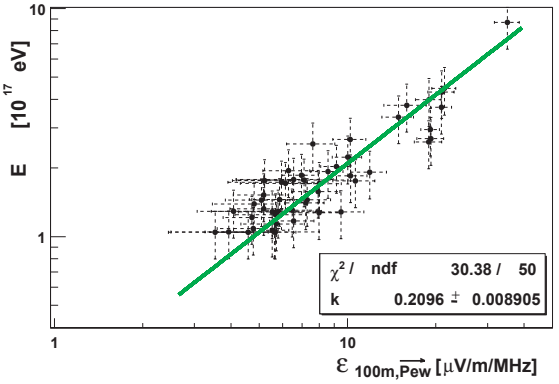

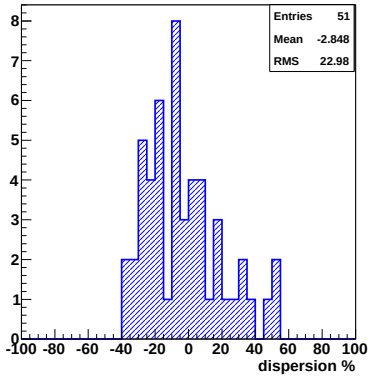

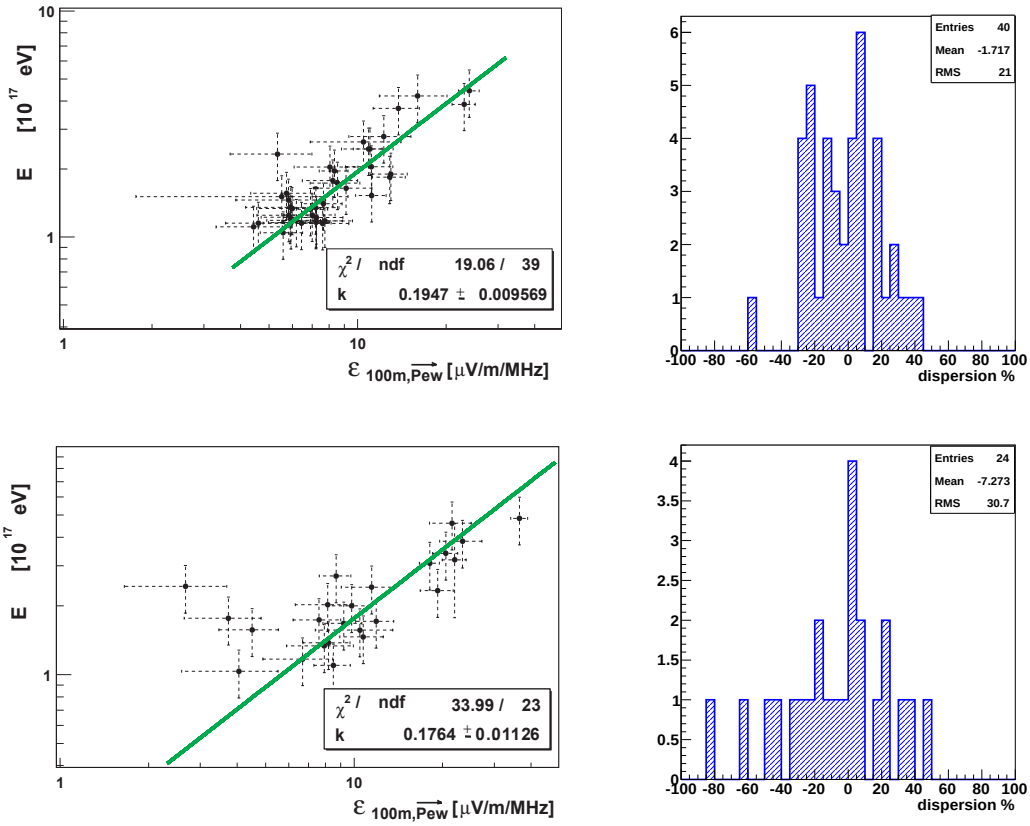

Figure 14.2: *Linear correlation between the primary energy reconstructed by KASCADE-Grande and the filtered radio pulse detected at 100 m from the shower axis. From top to bottom, in order, events from the fist to the fifth zenith angle bin are separately shown.*

14.3 Primary energy and $\epsilon_{\mathrm{steep}}$

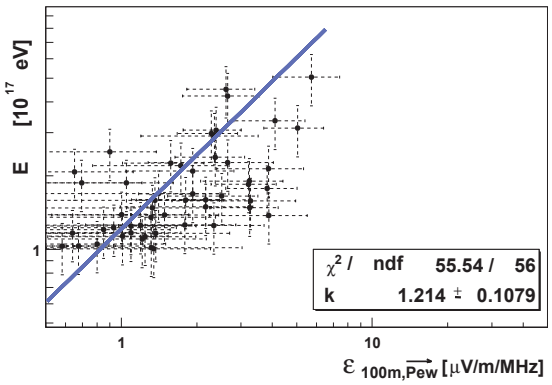

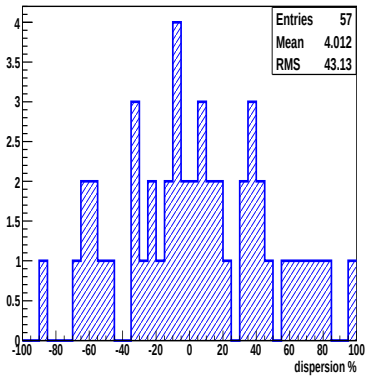

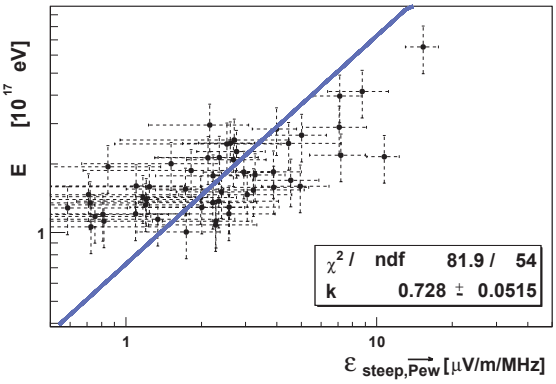

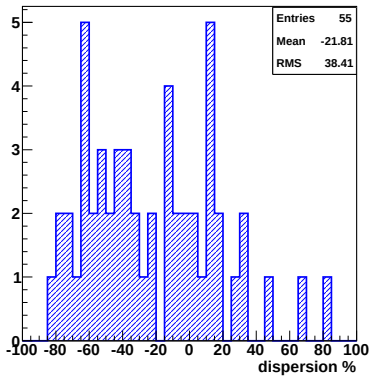

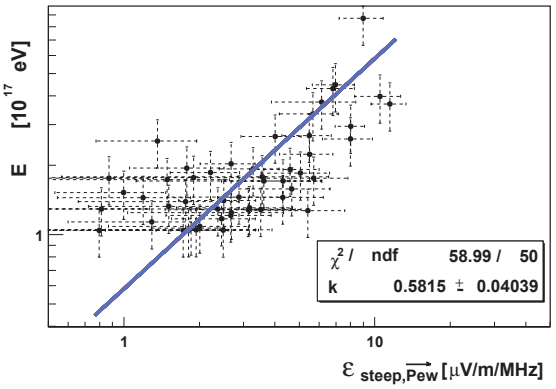

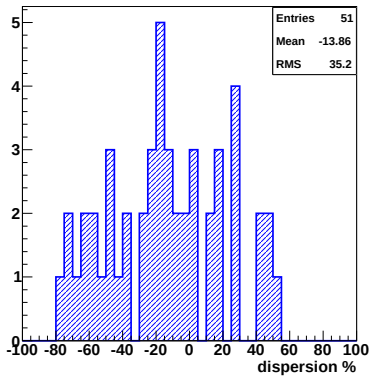

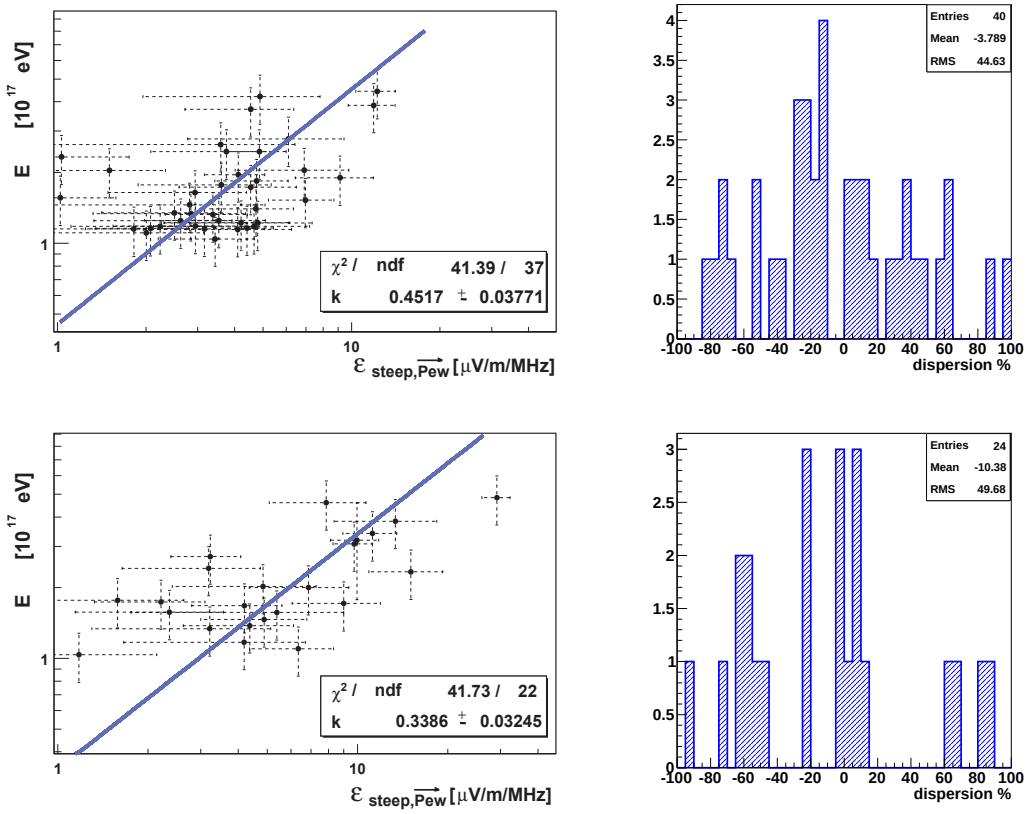

Figure 14.3: *Linear correlation between the primary energy reconstructed by KASCADE-Grande and the filtered radio pulse detected in the* $steep$ *region. From top to bottom, in order, events from the fist to the fifth zenith angle bin are separately shown.*

Bibliography

Abraham, J. et al. (Pierre Auger Collaboration) (2004a). *Properties and performance of the prototype instrument for the Pierre Auger Observatory*. Nucl. Instr. and Meth. in Phys. Res. A, 523 (1-2): 50–95. doi:DOI:10.1016/j.nima.2003.12.012.

Abraham, J. et al. (Pierre Auger Collaboration) (2004b). *Properties and performance of the prototype instrument for the Pierre Auger Observatory*. Nuclear Instruments and Methods, A523: 50. doi:10.1016/j.nima.2003.12.012.

Abraham, J. et al. (Pierre Auger Collaboration) (2010a). *Measurement of the Depth of Maximum of Extensive Air Showers above* 10^{18} *eV*. Physical Review Letters, 104 (9): 91–101. doi:10.1103/PhysRevLett.104.091101.

Abraham, J. et al. (Pierre Auger Collaboration) (2010b). *Measurement of the energy spectrum of cosmic rays above* 10^{18} *eV using the Pierre Auger Observatory*. Physics Letters B, 685 (4-5): 239 – 246. doi:DOI:10.1016/j.physletb.2010.02.013.

Abraham, J. et al. (Pierre Auger Collaboration) (2010c). *The fluorescence detector of the Pierre Auger Observatory*. Nuclear Instruments and Methods in Physics Research A, 620 (2-3): 227 – 251. doi:DOI:10.1016/j.nima.2010.04.023.

Abreu, P. et al. (Pierre Auger Collaboration) (2011). *Advanced functionality for radio analysis in the Offline software framework of the Pierre Auger Observatory*. Nuclear Instruments and Methods in Physics Research A: Accelerators, Spectrometers, Detectors and Associated Equipment, 635 (1): 92 – 102. doi:10.1016/j.nima.2011.01.049.

Allan, H. R. (1971). *Radio Emission From Extensive Air Showers*. Progress in Elementary Particle and Cosmic Ray Physics, 10: 171–302.

Allard, D., Parizot, E., Olinto, A. V. et al. (2005). *UHE nuclei propagation and the interpretation of the ankle in the cosmic-ray spectrum*. Astronomy & Astrophysics, 443 (3): L29–L32. doi:10.1051/0004-6361:200500199. URL `http://dx.doi.org/10.1051/0004-6361:200500199`.

Aminaei, A. (Pierre Auger Collaboration) (2010). *An introduction to the Auger Engineering Radio Array (AERA)*. In ISKAF2010 Science Meeting.

Antoni, T. et al. (KASCADE Collaboration) (2003a). *Measurements of attenuation and absorption lengths with the KASCADE experiment*. Astrop. Phys., 19 (6): 703 – 714. doi:10.1016/S0927-6505(03)00116-6.

Antoni, T. et al. (KASCADE Collaboration) (2003b). *The Cosmic-Ray Experiment KASCADE*. Nuclear Instruments and Methods in Physics Research A, 513: 490–510.

Antoni, T. et al. (KASCADE Collaboration) (2004). *Large scale cosmic-ray anisotropy with KASCADE*. Astrophysics, 604: 687–692. doi:10.1086/382039. ArXiv:astro-ph/0312375v1.

Antoni, T. et al. (KASCADE Collaboration) (2005). *KASCADE Measurements of energy spectra for elemental groups of cosmic rays: Results and open problems*. Astrop. Phys., 24 (1-25). doi:doi:10.1016/j.astropartphys.2005.04.001.

Apel, W. D. et al. (KASCADE Collaboration) (2009). *Energy spectra of elemental groups of cosmic rays: Update on the KASCADE unfolding analysis*. Astroparticle Physics, 31 (2): 86 – 91. doi:DOI:10.1016/j.astropartphys.2008.11.008.

Apel, W. D. et al. (LOPES Collaboration) (2010a). *Lateral distribution of the radio signal in extensive air showers measured with LOPES*. Astroparticle Physics, 32: 294–303. doi:10.1016/j.astropartphys.2009.09.007.

Apel, W. D. et al. (KASCADE-Grande Collaboration) (2010b). *The KASCADE-Grande experiment*. Nuclear Instruments and Methods in Physics Research A, 620: 202–216. doi:10.1016/j.nima.2010.03.147.

Apel, W. D. et al. (KASCADE-Grande Collaboration) (2011a). *KASCADE-Grande - Contributions to the 32nd International Cosmic Ray Conference, Beijing, August, 2011*. ArXiv:1111.5436v1 [astro-ph.HE].

Apel, W. D. et al. (KASCADE-Grande Collaboration) (2011b). *Kneelike Structure in the Spectrum of the Heavy Component of Cosmic Rays Observed with KASCADE-Grande*. Phys. Rev. Lett., 107. doi:10.1103/PhysRevLett.107.171104.

Apel, W. D. et al. (LOPES Collaboration) (2011c). *Thunderstorm observations by air-shower radio antenna arrays*. Advances in Space Research, 48: 1295. doi:10.1016/j.asr.2011.06.003.

Apel, W. D. et al. (LOPES Collaboration) (2012a). *Experimental evidence for the sensitivity of the air-shower radio signal to the longitudinal shower development*. Technical report. ArXiv:1203.3971v1.

Apel, W. D. et al. (LOPES Collaboration) (2012b). *Radio lateral distribution of cosmic ray air showers - a comparison of LOPES measurements and REAS3 simulations*. In preparation.

Apel, W. D. et al. (KASCADE-Grande Collaboration) (2012c). *The spectrum of high-energy cosmic rays measured with KASCADE-Grande*. submitted to Elsevier.

Apel, W. D. et al. (KASCADE-Grande Collaboration) (2012d). *The spectrum of high-energy cosmic rays measured with KASCADE-Grande*. Astrop. Ph. doi:10.1016/j.astropartphys.2012.05.023.

Ardouin, D. et al. (CODALEMA Collaboration) (2005). *Radio-detection signature of high-energy cosmic rays by the CODALEMA experiment*. Nuclear Instruments and Methods in Physics Research A, 555: 148–163. doi:10.1016/j.nima.2005.08.096.

Ardouin, D. et al. (CODALEMA Collaboration) (2006). *Radioelectric field features of extensive air showers observed with CODALEMA.* Astrop. Phys., 26 (4-5): 341–350. doi:DOI:10.1016/j.astropartphys.2006.07.002.

Ardouin, D. et al. (CODALEMA Collaboration) (2009). *Geomagnetic origin of the radio emission from cosmic ray induced air showers observed by CODALEMA.* Astrop. Phys., 31: 192–200. doi:10.1016/j.astropartphys.2009.01.001.

Ardouin, D. et al. (TIANSHAN Collaboration) (2011). *The TIANSHAN Radio Experiment for Neutrino Detection*. Astrop. Phys., 34: 717–731. doi:10.1016/j.astropartphys.2011.01.002.

ARENA (2010). *Proceedings of the 4th international workshop on acustic and radio eev neutrino detection activities*. doi:http://arena2010.in2p3.fr/. Nantes, France.

Argirò, S., Barroso, S. L. C., Gonzalez, J. and others (2007). *The offline software framework of the Pierre Auger Observatory*. Nuclear Instruments and Methods in Physics Research A, 580 (3): 1485 – 1496. doi:DOI:10.1016/j.nima.2007.07.010.

Arqueros, F., Hoerandel, J. R. and Keilhauer, B. (2008). *Air Fluorescence Relevant for Cosmic-Ray Detection - Review of Pioneering Measurements.* Nucl.Instrum.Meth., A597: 23–31. doi:10.1016/j.nima.2008.08.055.

Asch, T. (2009). *Self-Triggering of Radio Signals from Cosmic Ray Air Showers*. FZKA Report 7459, Forschungszentrum Karlsruhe.

Asch, T. et al. (Pierre Auger Collaboration) (2008). *Simulation of an array of antenna detectors*. GAP note 2008-177, Pierre Auger Observatory.

Askaryan, G. A. (1962). *Excess negative charge of an electron-photon shower and its coherent radio emission*. Soviet Physics JETP, 14: 441.

Askaryan, G. A. (1965). *Coherent radio emission from cosmic showers in air and in dense media*. Soviet Physics JETP, 21: 658.

Auger, P. (1938). *Grandes gerbes cosmiques atmosphériques contenant des corpuscoles ultra pénétrantes.* Comptes rendus, Académie des Sciences, 206: 1721.

Baade, W. and Zwicky, F. (1934). *Remarks on Super-Novae and Cosmic Rays*. Physical Review, 46: 76–77. doi:10.1103/PhysRev.46.76.2. URL `http://link.aps.org/doi/10.1103/PhysRev.46.76.2`.

Badescu, A. (2010). *private communication*.

Bass, S. A., Belkacem, M., Bleicher, M. et al. (1998). *Microscopic models for ultrarelativistic heavy ion collisions*. Progress in Particle and Nuclear Physics, 41: 255 – 369. doi:DOI:10.1016/S0146-6410(98)00058-1.

Bellètoile, A. (COSALEMA Collaboration) (2011). *The Standalone Antenna Array of the CODALEMA Radio Detection Experiment*. In Proceedings of the 32nd International Cosmic Ray Conference, Beijing (China), volume V1, 23. www.ihep.ac.cn/english/conference/icrc2011/paper/proc/.

Berezinsky, V., Gazizov, A. Z. and Grigorieva, S. I. (2005). *Dip in UHECR spectrum as signature of proton interaction with CMB.* Phys.Lett. B, 612: 147–153. doi:10.1016/j.physletb.2005.02.058.

Berezinsky, V., Kachelriess, M. and Vilenkin, A. (1997). *Ultrahigh Energy Cosmic Rays without Greisen-Zatsepin-Kuzmin Cutoff.* Phys. Rev. Lett., 79: 4302–4305. doi:10.1103/PhysRevLett.79.4302. URL `http://link.aps.org/doi/10.1103/PhysRevLett.79.4302`.

Blümer, J., Engel, R. and Hörandel, J. R. (2009). *Cosmic rays from the knee to the highest energies*. Progress in Particle and Nuclear Physics, 63: 293–338. doi:10.1016/j.ppnp.2009.05.002. `0904.0725`.

Bracewell, R. N. (1986). The Fourier Transform and Its Applications (Second Edition, Revised). McGraw-Hill Book Company. ISBN 0070070156.

Budnev, N. M. et al. (Tunka Collaboration) (2009). *The Tunka-133 EAS Chrenkov array - status, first results and plans.* In Proceedings of the 31st ICRC, Łódź, Poland. http://icrc2009.uni.lodz.pl/proc/html/, astro-ph/1003.0089.

Buitink, S. et al. (LOPES Collaboration) (2007). *Amplified radio emission from cosmic ray air showers in thunderstorms*. Astronomy & Astrophysics, 467: 385–394. doi:10.1051/0004-6361:20066006.

Burke, G. J. and Poggio, A. J. (1977). *Numerical electromagnetis code (nec) method of moments, parts i*. Technical report, Lawrence Livermore National Laboratory.

Burke, G. J. and Poggio, A. J. (1981). *Numerical electromagnetis code (nec) method of moments, parts ii*. Technical report, Lawrence Livermore National Laboratory.

Burke, G. J. and Poggio, A. J. (1983). *Numerical electromagnetis code (nec) method of moments, parts iii.* Technical report, Lawrence Livermore National Laboratory.

Cane, H. V. (1979). *Spectra of the non-thermal radio radiation from the galactic polar regions.* Royal Astronomical Society, Monthly Notices, 189: 465–478.

CDAS (Pierre Auger Coll.) (2008). URL `http://www.auger.org.ar/CDAS-Public/`.

Coppens, J. (for the Pierre Auger Observatory) (2009). *Observation of radio signals from air showers at the Pierre Auger Observatory*. Nuclear Instruments and Methods in Physics Research Section A: Accelerators, Spectrometers, Detectors and Associated Equipment, 604 (1-2, Supplement 1): S41 – S43. doi:DOI:10.1016/j.nima.2009.03.119. ARENA 2008.

CR-Tools (2004). *LOFAR software package*. URL `http://usg.lofar.org/`.

de Vries, K. D., van den Berg, A. M., Scholten, O. and Werner, K. (2010). *The Lateral Distribution Function of Coherent Radio Emission from Extensive Air Showers; Determining the Chemical Composition of Cosmic Rays*. Astropart.Phys., 34: 267–273. doi:DOI:10.1016/j.astropartphys.2010.08.003.

de Vries, K. D., van den Berg, A. M., Scholten, O. and Werner, K. (2012). *Coherent Cherenkov Radiation from Cosmic-Ray-Induced Air Showers*. Phys. Rev. Lett., 107. doi:10.1103/PhysRevLett.107.061101.

d'Enterria, D. et al. (2011). *Constraints from the first lhc data on hadronic event generators for ultra-high energy cosmic-ray physics*. Astrop. Phys., 35: 98–113. doi:http://dx.doi.org/10.1016/j.astropartphys.2011.05.002.

DuVernois, M. A., Cai, B. and Kleckner, D. (2005). *Geosynchrotron radio pulse emission from extensive air showers: Simulations with AIRES*. In 29th International Cosmic Ray Conference Pune, volume 8, 311–314.

Ender, M. (2009). *Radiodetektion von Luftschauern unter dem Einfluss starker elektrischer Felder in der Atmosphäre*. FZKA Report 7506, Forschungszentrum Karlsruhe.

Facal San Luis, P. et al. (2012). *Status of the microwave detection of cosmic rays program at the Pierre Auger Observatory*. In Proc. of the Int. Symposium on Future Directions in UHECR Physics (CERN).

Falcke, H. and Gorham, P. W. (2003). *Detecting radio emission from cosmic ray air showers and neutrinos with a digital radio telescope*. Astroparticle Physics, 19: 477–494.

Falcke, H. et al. (LOPES Collaboration) (2005). *Detection and imaging of atmospheric radio flashes from cosmic ray air showers*. Nature, 435: 313–316. doi:10.1038/nature03614. `astro-ph/0505383`.

Falcke, H. et al. (LOFAR) (2006). *A very brief description of LOFAR - the Low Frequency Array*. In IAU GA 2006, Highlights of Astronomy, volume 14. Astro-ph/0610652, URL `http://adsabs.harvard.edu/abs/2006astro.ph.10652F`.

Fermi, E. (1949). *On the Origin of the Cosmic Radiation*. Phys. Rev., 75: 1169–1174. doi:10.1103/PhysRev.75.1169. URL `http://link.aps.org/doi/10.1103/PhysRev.75.1169`.

Fliescher, S. (for the Pierre Auger Observatory) (2008). *Radio detector array simulation: A full simulation chain for an array of antenna detectors*. Nucl. Instr. and Meth., 604 A: S225. doi:http://dx.doi.org/10.1016/j.nima.2009.03.068.

Fliescher, S. (for the Pierre Auger Observatory) (2010). *Radio detection of cosmic ray induced air showers at the Pierre Auger Observatory*. In Nucl. Instr. and Meth. A; Proceedings of the ARENA 2010 conference, Nantes, France. doi:DOI:10.1016/j.nima.2010.11.045. DOI: 10.1016/j.nima.2010.11.045, in press.

Fliescher, S., Fraenkel, D., Fuchs, B. et al. (Pierre Auger Collaboration) (2010). *The radio extension of Auger Offline*. GAP note 2010-056.

Fuchs, B., Fraenkel, D., Huege, T. and Melissas, M. (Pierre Auger Collaboration) (2011). *A comparison of the reconstructed E-field from BLS radio data with simulations based on Offline* . GAP note 2011-135.

Gaisser, T. K. (1990). Cosmic Rays and Particle Physics.

GraphPad (2011). *A complete guide to nonlinear regression*. URL `http://www.graphpad.com/curvefit/goodness_of_fit.htm`.

Greisen, K. (1966). *End to the cosmic-ray spectrum ?* Phys. Rev. Lett., 16 (17): 748–750.

Haungs, A., Rebel, H. and Roth, M. (2003). *Energy spectrum and mass composition of high-energy cosmic rays*. Reports on Progress in Physics, 66 (7): 1145. URL `http://stacks.iop.org/0034-4885/66/i=7/a=202`.

Heck, D., Knapp, J., Capdevielle, J. N. et al. (1998). *CORSIKA: A Monte Carlo Code to Simulate Extensive Air Showers*. FZKA Report 6019, Forschungszentrum Karlsruhe.

Heitler, W. (1944). Quantum Theory of Radiation. Oxford, 2nd edition.

Hess, V. F. (1912). *Observation of Penetrating Radiation in Seven Balloon Flights*. Physikalische Zeitschrift, 13: 1084.

Hill, T. (1983). *Monopolonium*. Nucl. Phys. B, 224: 469–490. doi:10.1016/0550-3213(83)90386-3.

Hinton, J. A. (HESS Collaboration) (2004). *The Status of the H.E.S.S. Project*. New Astron.Rev., 48: 331–337. doi:10.1016/j.newar.2003.12.004.

Horneffer, A. (2006). *Measuring Radio Emission from Cosmic Ray Air Showers with a Digital Radio Telescope*. PhD Thesis, Rheinische Friedrich-Wilhelms-Universität Bonn, Germany. URL `http://nbn-resolving.de/urn:nbn:de:hbz:5N-07819`.

Horneffer, A. et al. (LOPES Collaboration) (2007). *Primary Particle Energy Calibration of the EAS Radio Pulse Height*. In Proceedings of the 30th ICRC, Merida, Mexico, volume 4, 83–86.

Horneffer, A. et al. (LOPES Collaboration) (2009). *The LOPES System for the Detection of Radio Pulses from Air Showers*. Nucl. Instrum. Meth. Suppl., A604: 20–23.

Huber, D. (LOPES Collaboration) (2011). *LOPES 3D reconfiguration and first measurements*. In Proceedings of the 32nd International Cosmic Ray Conference, Beijing (China), volume 3, 72–75.

Huege, T. (2004). Radio Emission from Cosmic Ray Air Showers. Ph.D. thesis, Rheinische Friedrich-Wilhelms-Universität Bonn, Germany. URL `http://hss.ulb.uni-bonn.de/2004/0479/0479.htm`.

Huege, T. (for the Pierre Auger Coll.) (2009a). *Radio detection of cosmic rays in the Pierre Auger Observatory*. Nucl. Instr. and Meth, A (617): 484–487.

Huege, T. (2009b). *Simulations and theory of radio emission from cosmic ray air showers.* Nucl. Instr. and Meth. in Phys. Research, A (604): S57–S63.

Huege, T. (LOPES Collaboration) (2010). *The LOPES experiment — recent results, status and perspectives*. In Nucl. Instr. and Meth. A; Proceedings of the ARENA 2010 conference, Nantes, France. doi:DOI:10.1016/j.nima.2010.11.081.

Huege, T. (2011). *REAS Manual*. URL `http://www.timhuege.de/reas`.

Huege, T. (2012). *Simulation der Radioemissionen von Luftschauern mit CoREAS.* Technical report. Deutsche Physikalische Gesellschaft (DPG) Fruehjahrstagung, March 2012.

Huege, T. and Falcke, H. (2003). *Radio emission from cosmic ray air showers. Coherent geosynchrotron radiation*. Astronomy & Astrophysics, 412: 19–34. doi:10.1051/0004-6361:20031422.

Huege, T. and Falcke, H. (2005a). *Radio emission from cosmic ray air showers. Monte Carlo simulations*. Astronomy & Astrophysics, 430: 779–798. doi:10.1051/0004-6361:20041873.

Huege, T. and Falcke, H. (2005b). *Radio emission from cosmic ray air showers: Simulation results and parametrization*. Astroparticle Physics, 24: 116. doi:10.1016/j.astropartphys.2005.05.008.

Huege, T., Ludwig, M., Scholten, O. and de Vries, K. D. (2010). *The convergence of EAS radio emission models and a detailed comparison of REAS3 and MGMR simulations*. In Nucl. Instr. and Meth. A; Proceedings of the ARENA 2010 conference, Nantes, France. DOI:10.1016/j.nima.2010.11.041, in press.

Huege, T., Ulrich, R. and Engel, R. (2007). *Monte Carlo simulations of geosynchrotron radio emission from CORSIKA-simulated air showers*. Astroparticle Physics, 27: 392–405. doi:10.1016/j.astropartphys.2007.01.006.

Huege, T., Ulrich, R. and Engel, R. (2008). *Dependence of geosynchrotron radio emission on the energy and depth of maximum of cosmic ray showers*. Astroparticle Physics, 30: 96–104. doi:10.1016/j.astropartphys.2008.07.003.

Isar, P. G. (2010). *Polarization Measurements of Radio Emission of Cosmic Ray Air Showers with LOPES*. PhD Thesis, Karlsruhe Institute of Technology.

Isar, P. G. et al. (LOPES Collaboration) (2009). *Polarization studies of the EAS radio emission with the LOPES experiment*. In Proceedings of the 31st ICRC, Łódź, Poland, 1128. http://icrc2009.uni.lodz.pl/proc/html/.

Jackson, J. D. (1975). Classical Electrodynamics. John Wiley & Sons, New York, second edition.

James, C. W., Falcke, H., Huege, T. and Ludwig, M. (2010). *An 'endpoint' formulation for the calculation of electromagnetic radiation from charged particle motion*. submitted to: Physical Review E. astro-ph/1007.4146, 1007.4146.

Jelley, J. V., Fruin, J. H., Porter, N. A. et al. (1965). *Radio Pulses from Extensive Cosmic-Ray Air Showers*. Nature, 205: 327–328. doi:doi:10.1038/205327a0.

Kahn, F. D. and Lerche, I. (1966). *Radiation from cosmic ray air showers*. In Proceedings of the Royal Society of London. Series A, Mathematical and Physical Sciences, volume 289, 206.

Kazanas, D. and Nicolaidis, A. (2003). *Cosmic Rays and Large Extra Dimensions*. Gen. Rel. Grav., 35: 1117–1123.

Kelley, J. (for the Pierre Auger Coll.) (2011). *AERA: the Auger Engineering Radio Array*. In 32nd International Cosmic Ray Conference, Beijing, volume V3, 112. www.ihep.ac.cn/english/conference/icrc2011/paper/proc/.

Knapp, J. et al. (2003). *Extensive Air Shower Simulations at the Highest Energies*. Astropart.Phys., 19: 77–99. doi:10.1016/S0927-6505(02)00187-1.

Konzack, M., Bozdog, H., Haungs, A. and Schröder, F. G. (2010). *Specifications of the AERA Beacon and its Software*. GAP note 2010-099, Pierre Auger Observatory.

Krömer, O. (2008). *Empfangssystem zur Radioobservation hochenergetischer kosmischer Schauer und sein Verhalten bei Selbsttriggerung*. FZKA Report 7396, Forschungszentrum Karlsruhe.

Krömer, O. et al. (LOPES Collaboration) (2009). *New Antenna for Radio Detection of UHECR*. In Proceedings of the 31st ICRC, Łódź, Poland, 1232. http://icrc2009.uni.lodz.pl/proc/html/.

Lafèbre, S. et al. (2009). *Universality of electron-positron distributions in extensive air showers*. Astroparticle Physics, 31: 243–254.

Lecacheux, A. and Bellètoile, A. (CODALEMA Collaboration) (2009). *Radio signature of extensive air showers observed with the Nançay Decameter Array*. In Proceedings of the 31st ICRC, Łódź, Poland, 1508. http://icrc2009.uni.lodz.pl/proc/html/.

LHC (2008). *The large hadron collider*. Http://public.web.cern.ch/public/en/lhc/lhc-en.html.

Lidvansky, A. S. (2005). *Air Cerenkov methods in cosmic rays: A Review and some history*. Radiat.Phys.Chem. astro-ph/0504269.

Link, K. (for the LOPES Collaboration) (2011). *The LOPES experiment*. In Nuclear Physics B Proceedings Supplements, volume 212, 323–328. doi:10.1016/j.nuclphysbps.2011.03.043.

Ludwig, M. (2011). Modelling of radio emission from cosmic ray air showers. Ph.D. thesis, Karlsruhe Institute of Technology.

Ludwig, M. and Huege, T. (2011a). *Analysis of air shower radio signals with REAS3*. In 32nd International Cosmic Ray Conference, Beijing, volume V2, 19. www.ihep.ac.cn/english/conference/icrc2011/paper/proc/.

Ludwig, M. and Huege, T. (2011b). *REAS3: Monte Carlo simulations of radio emission from cosmic ray air showers using an 'end-point' formalism*. Astroparticle Physics, 34 (6): 438 – 446. doi:DOI:10.1016/j.astropartphys.2010.10.012.

Marin, V. (CODALEMA Coll.) (2011). *Charge excess signature in the CODALEMA data. Interpretation with SELFAS2*. In 32nd International Cosmic Ray Conference, Beijing, volume V1, 291. www.ihep.ac.cn/english/conference/icrc2011/paper/proc/.

Mathes, H. (for the Pierre Auger Observatory) (2011). *The HEAT Telescopes of the Pierre Auger Observatory. Status and first data*. In 32nd International Cosmic Ray Conference, Beijing, volume V3, 149. www.ihep.ac.cn/english/conference/icrc2011/paper/proc/.

Matthews, J. N. (2005). *A Heitler model of extensive air showers*. Astroparticle Physics, 22: 387–397. doi:10.1016/j.astropartphys.2004.09.003.

Matthews, J. N. et al. (Telescope Array Coll.) (2009). *Overview of the Telescope Array Experiment*. In Proceedings of the 31st ICRC, Łódź, Poland, 1386. http://icrc2009.uni.lodz.pl/proc/html/.

Medvedev, M. V. (2007). *Extragalactic shocks as cosmic accelerators*. Highlights of Astronomy, 14: 95–96. doi:10.1017/S1743921307009970.

Melissas, M. (Pierre Auger Coll.) (2012). *Measurement of cosmic rays events with new AERA electronic*. Technical report. Deutsche Physikalische Gesellschaft (DPG) Fruehjahrstagung, March 2012.

Melissas, M., Huege, T. and Haungs, A. (2010). *Measurements of high amplitude radio events during thunderstorms-auger internal: Auger-gap 2010-065*.

Melissas, M., Huege, T. and Schieler, H. (2011). *Weather monitoring at the central radio station*. Auger internal: Auger-GAP 2011-066.

Menjo, H. et al. (2011). *Monte Carlo study of forward π^o production spectra to be measured by the LHCf experiment for the purpose of benchmarking hadron interaction models at 10^{17} eV*. Astroparticle Physics, 34: 513–520. doi:DOI:10.1016/j.astropartphys.2010.11.002.

Nehls, S. (2008). *Calibrated Measurements of the Radio Emission of Cosmic Ray Air Showers*. FZKA Report 7440, Forschungszentrum Karlsruhe.

Nehls, S., Hakenjos, A., Arts, M. J. et al. (2008). *Amplitude calibration of a digital radio antenna array for measuring cosmic ray air showers*. Astronomy & Astrophysics, 589 (3): 350 – 361. doi:DOI:10.1016/j.nima.2008.02.092.

Nigl, A. et al. (LOPES Collaboration) (2008). *Direction identification in radio images of cosmic-ray air showers detected with LOPES and KASCADE*. Astronomy & Astrophysics, 487: 781–788. doi:DOI:10.1051/0004-6361:20079218.

NOAA (2011). *Earth's magnetic field calculation*. URL `http://www.ngdc.noaa.gov/geomag/magfield.shtml`.

Nyquist, H. (1928). *Certain Topics in Telegraph Transmission Theory*. American Institute of Electrical Engineers, Transactions of the, 47 (2): 617 –644. doi:10.1109/T-AIEE.1928.5055024.

Obenland, R. (2005). Verbesserung der Winkelauflösung des Myonspurdetektors von KASCADE und Bestimmung von Myonproduktionshöhen. Master's thesis, Universität Karlsruhe. FZKA Report.

Ostapchenko, S. (2006). *QGSJET-II: results for extensive air showers*. Nuclear Physics B - Proceedings Supplements, 151 (1): 147–150. doi:DOI:10.1016/j.nuclphysbps.2005.07.027.

Pierog, T., Engel, R. and Heck, D. (2009). *3D Air Shower Simulations Using CONEX in CORSIKA*. In Proceedings of the 31st ICRC, Łódź, Poland. Http://icrc2009.uni.lodz.pl/proc/html/.

Pierog, T. and Werner, K. (2009). *EPOS Model and Ultra High Energy Cosmic Rays*. Nuclear Physics B - Proceedings Supplements, 196: 102 – 105. doi:10.1016/j.nuclphysbps.2009.09.017.

Pierog, T. et al. (2006). *First results of fast one-dimensional hybrid simulation of EAS using CONEX*. Nuclear Physics B - Proceedings Supplements, 151 (1): 159 – 162. doi:DOI:10.1016/j.nuclphysbps.2005.07.029. VERY HIGH ENERGY COSMIC RAY INTERACTIONS.

Platino, M. (for the Pierre Auger Observatory) (2009). *AMIGA - Auger Muons and Infill for the Ground Array of the Pierre Auger Observatory*. In Proceedings of the 31st ICRC, Łódź, Poland, 0184. http://icrc2009.uni.lodz.pl/proc/html/, astro-ph/0906.2354, `0906.2354`.

Ravel, O. (CODALEMA Collaboration) (2010). *The CODALEMA experiment*. Nucl. Instr. and Meth. in Phys. Research Section A: Accelerators, Spectrometers, Detectors and Associated Equipment In Press. doi:DOI:10.1016/j.nima.2010.12.057.

RDAS Software (2008). *Radio Detector Array Simulation*. URL `http://web.physik.rwth-aachen.de/fliescher/doc2/html/`.

Revenu, B. (for the Pierre Auger Observatory) (2010a). *Radio-detection of cosmic ray air showers by the RAuger experiment, a fully autonomous and self-triggered system installed at the Pierre Auger Observatory*. In Nucl. Instr. and Meth. A; Proceedings of the ARENA 2010 conference, Nantes, France, In Press. doi:DOI:10.1016/j.nima.2010.11.087.

Revenu, B. (for the Pierre Auger and CODALEMA Coll.) (2010b). *Radio detection of cosmic ray air showers by the RAuger experiment, a fully autonomous and self-triggered system installed at the Pierre Auger Observatory*. Nucl. Instr. and

Meth. in Phys. Research Section A: Accelerators, Spectrometers, Detectors and Associated Equipment, In Press. doi:DOI:10.1016/j.nima.2010.11.087.

Revenu, B. (for the Pierre Auger Coll.) (2011). *Autonomous detection and analysis of radio emission from air showers detected at the Pierre Auger Observatory*. In 32nd International Cosmic Ray Conference, Beijing, volume V3, 172. www.ihep.ac.cn/english/conference/icrc2011/paper/proc/.

Risse, M. and Heck, D. (2004). *Energy release in air showers*. Astrop. Phys., 20: 661–667.

Riviere, C. et al. (CODALEMA Collaboration) (2009). *Radio emission of extensive air shower at CODALEMA: Polarization of the radio emission along the v∗B vector*. Http://icrc2009.uni.lodz.pl/proc/html/.

Röttgering, H. et al. (2003). *LOFAR: a new radio telescope for low frequency radio observations: science and project status*. In Texas in Tuscany. XXI Symposium on Relativistic Astrophysics, 69–76.

Scholten, O., Werner, K. and Rusydi, F. (2008). *A macroscopic description of coherent geo-magnetic radiation from cosmic-ray air showers*. Astroparticle Physics, 29: 94–103. astro-ph/0709.2872.

Schröder, F. G. (2010). Instruments and Methods for the Radio Detection of High Energy Cosmic Rays, Ph.D. thesis. Ph.D. thesis, Karlruhe Institute of Technology (KIT), Germany. URL `http://www.astro.ru.nl/lopes/publications/phd_theses/`.

Schröder, F. G., Asch, T., Bähren, L. et al. (2010a). *New method for the time calibration of an interferometric radio antenna array*. Nuclear Instruments and Methods in Physics Research Section A: Accelerators, Spectrometers, Detectors and Associated Equipment, 615 (3): 277 – 284. doi:DOI:10.1016/j.nima.2010.01.072.

Schröder, F. G., Bozdog, H. and Krömer, O. (2009). *Test Measurements for the Time Calibration of AERA with a Beacon*. GAP note 2009-085, Pierre Auger Observatory.

Schröder, F. G. et al. (LOPES Collaboration) (2010b). *On noise treatment in radio measurements of cosmic ray air showers*. In Nucl. Instr. and Meth. A - Proceedings of the ARENA 2010 conference, Nantes, France, In Press. doi:DOI:10.1016/j.nima.2010.11.009.

Schroeder, F. (2011). Private communication.

Seeger, O. (for the Pierre Auger Coll.) (2010). *Logarithmic periodic dipole antennas for the Auger engineering radio array*. Nucl. Instr. and Meth. in Physics Research Section A: Accelerators, Spectrometers, Detectors and Associated Equipment, In Press. doi:DOI:10.1016/j.nima.2010.10.140.

Settimo, M. (for the Pierre Auger Coll.) (2011). *An update on a search for ultra-high energy photons using the Pierre Auger Observatory*. In Proceedings of the 32st ICRC, Beijing, China, volume V2, 55–59. www.ihep.ac.cn/english/conference/icrc2011/paper/proc/.

Šmída, R. et al. (2011). *First results of the CROME experiment*. In Proceedings of the 32st ICRC, Beijing, China, volume V3, 17–20. www.ihep.ac.cn/english/conference/icrc2011/paper/proc/.

Šmída, R. et al. (2012). *Microwave emission from extensive air showers as seen by CROME*. In Proc. of the Int. Symposium on Future Directions in UHECR Physics (CERN).

Sommers, P. (for the Pierre Auger Observatory) (2005). *First estimate of the primary cosmic ray energy spectrum above EeV from the Pierre Auger Observatory*. In Proceedings of the 29st ICRC, Pune.

Sparvoli, R. (2008). *Direct measurements of cosmic rays*. Il Nuovo Cimento, 123 B, 6-7 (908). doi:DOI:10.1393/ncb/i2008-10592-8.

Stecker, F. W. and Salamon, M. H. (1999). *Photodisintegration of Ultra-High-Energy Cosmic Rays: A New Determination*. Astrop. J., 512: 521–526.

Stephan, M. (for the Pierre Auger Coll.) (2010). *Antennas, filters and preamplifier designed for the radio detection of ultra-high-energy cosmic rays*. In Proc. of Asia-Pacific Microwave Conference, 1455–1458.

Toma, G. (KASCADE-Grande Collaboration) (2010). *Primary Energy Spectrum as Reconstructed from S(500) Measurements by KASCADE-Grande*. AIP Conference Proceedings, 1203 (1): 145–150. doi:DOI:10.1063/1.3322394. URL `http://link.aip.org/link/?APC/1203/145/1`.

van den Berg, A. (for the Pierre Auger Observatory) (2009). *Radio detection of high-energy cosmic rays at the Pierre Auger Observatory*. In Proceedings of the 31st ICRC, Łódź, Poland, 0232. http://icrc2009.uni.lodz.pl/proc/html/.

Weber, J. H. et al. (KASCADE Collaboration) (1999). *Analysis of the muon / electron ratio in EAS*. In 26th ICRC, Salt Lake City, Utah, USA, volume 1, 341.

Werner, K. and Scholten, O. (2008). *Macroscopic Treatment of Radio Emission from Cosmic Ray Air Showers based on Shower Simulations*. Astroparticle Physics, 29: 393–411. doi:DOI:10.1016/j.astropartphys.2008.04.004.

Wommer, M. (2007). Bestimmung des Energiespektrums und der mittleren Masse kosmischer Strahlung mit dem KASCADE-Grande-Experiment. Master's thesis, Universität Karlsruhe.

Zatsepin, G. T. and Kuzmin, V. A. (1966). JETP Lett., 4: 78.

List of Figures

List of Tables

Acknowledgements

The experience at KIT made me growing on both human and professional side.
I would like to express my deep gratitude to all who have supported me in the last years.

First thanks to Professor Johannes Blümer, who gave me the opportunity to work on this project, and to Professor Michael Feindt who accepted to be my co-referent.

Many thanks to Andreas Haungs and Tim Huege, who accompanied and guided me to accomplish this work. Thanks for the fruitful ideas and discussions, especially for motivating me when the scientific aim seemed difficult to achieve.
Special thanks to professor Gianni Navarra, who encouraged me to set out on the endeavour of the PhD in Germany.

Furthermore, I would like to thank all my colleagues for both their assistance and the nice moments spent together. In particular I would like to say thanks to Frank, who always found the time to discuss with me doubts and improvements for the analysis, and Marianne for providing me with the simulations. Special thanks go to all who read this thesis and gave me essential comments.

I would like to thank all the people who supported me in the easy and less easy moments, and who encouraged me to always stand in front of the reality and search for the truth of the things. So many thanks to Stefan, my family and my friends. Last, but not least, thanks Iddu (as Paolino would say!) for all.